Using multiplexers to study the statistics of quantum phenomenon in one-dimensional wires

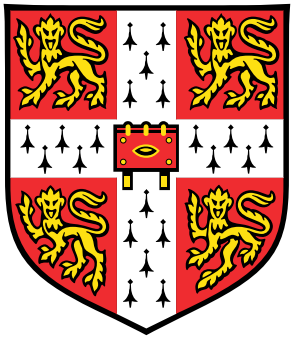

Pengcheng Ma

Cavendish Laboratory

University of Cambridge

Dissertation submitted for the degree of
Doctor of Philosophy

Churchill College

December 2017

Declaration

This dissertation is the result of my own work and includes nothing which is the outcome of work done in collaboration except where specifically indicated in the text. It has not been submitted in whole or in part for any degree at this or any other university and is less than 60,000 words.

Pengcheng Ma
December 2017

Acknowledgements

First and foremost, my sincere gratitudes go to my supervisor, Prof. Charles Smith, who gives me this precious opportunity to pursue a Ph.D. at the Cavendish Laboratory and brings me into the fantastic multiplexing one-dimensional world. His support, patience, encouragement and knowledge have been very valuable to me. Discussions with him always have significant impacts on my understandings in theories and experiments.

My heartfelt thanks also to Dr Reuben Puddy for his constant guidance, enthusiasm and great humour. It was a great pleasure to learn the techniques of cleanroom fabrication and cryogenic measurement from him. His design in the mask layout has been invaluable to this Multiplexer project.

Thanks are also extended to Prof. Michael Kelly for his collaboration on the project, Prof. Dave Ritchie, Dr Harvey Beere and Dr Ian Farrer for growing the world-class wafers used in this project, Prof. Chris Ford for his data acquisition software-CryoMeas, Dr Kaveh Delfanazari for his collaboration and engagement in the 40 mK measurements for several month, particularly during the whole Christmas holiday, Dr Luke Smith and Dr Haider Al-Taie for their pioneering contributions for realising the Multiplexer with 256 QPCs, Mr Jon Griffiths and Mr Tom Mitchell for e-beam lithography, Mrs Melanie Tribble for the cleanroom organisation and insulator deposition, Dr Joanna Waldie for her assistance in the cryostat measurements, Mr Moda Cao for his continuing valuable suggestions and discussions in theories, Mr Teng Yi for his help in the Multiplexer programming and data processing. Many thanks to all the colleagues in the Semiconductor Physics Group, who are generous with their time and advices.

I am most grateful to the financial support of my Ph.D. from the China Scholarship Council and the Cambridge Commonwealth, European and International Trust. Thanks to the Engineering and Physical Sciences Research Centre for funding the project.

Finally, I must express the appreciation to my parents, for their everlasting love and support to this 10th year of my lifetime in universities.

Abstract

The quantum point contact (QPC) is a one-dimensional constriction with the differential conductance quantised in units of $G_Q = 2e^2/h$. However, the transport behaviour below the first plateau is still not fully understood, including the 0.7 anomaly and the 0.25 anomaly in the linear and non-linear transport regimes respectively.

In this work, we utilise a multiplexing technique and statistically investigate the 0.7 anomaly observed on the first three plateaus respectively in 571 QPCs, fitting well the van-Hove model. The 0.7 anomaly shows the transconductance suppression due to the effective electron interactions which are modified by the local density of states (LDOS). At the maximum of LDOS, the interaction strength becomes strongest, resulting in the strongest transconductance suppression. The strongest interaction strength is determined by the ratio of transverse confinement curvature and longitudinal barrier curvature.

Moreover, we realise measurements of the effective g factor (g^*) and high-field offset (ΔE^{hfo}) in numerous devices in a single cooldown at T=40 mK. The statistical results show both the g^* and ΔE^{hfo} increase with the potential confinement, which supports the predictions about the role of interaction strength on g^* and ΔE^{hfo} in a 1D tight-binding model. We explore the origin of ΔE^{hfo} and find that it is only considerable for the first plateau. Using a short and narrow QPC could result in a stronger potential confinement and thus a higher g^*, which could be beneficial for its use in spintronic applications.

Last, we investigate the formation and development of the DC-bias-induced 0.75 and 0.25 anomalies for 402 QPCs. We find the anomalies evolve similarly in a magnetic field. To explain the anomaly behaviours, we propose a phenomenological DC-bias-induced spin-splitting model. In the model, with the increasing DC bias (V_{DC}), the 0.75 anomaly occurs first at a differential conductance of 0.75 G_Q, while the 0.25 anomaly is formed at a differential conductance of 0.5 G_Q and moves to 0.375 G_Q. The spin gap of the first subband opens to be $e|V_{DC}|$, which enables an all-electric manipulation of spin polarisation simply by applying a DC bias.

The work in this thesis is being prepared as follows for submission:

P. C. Ma, R. K. Puddy, K. Delfanazari, M. D. Cao, T. Yi, J. P. Griffiths, H. E. Beere, D. A. Ritchie, M. J. Kelly and C. G. Smith, *'Statistical measurements of 571 GaAs/AlGaAs quantum point contacts showing the 0.7 anomaly suppression utilising an on-chip multiplexing scheme'*, in preparation (2017).

P. C. Ma, K. Delfanazari, R. K. Puddy, M. D. Cao, T. Yi, J. P. Griffiths, H. E. Beere, D. A. Ritchie, M. J. Kelly and C. G. Smith, *'On-chip multiplexer addressed effective g-factors in split-gate transistors'*, in preparation (2017).

P. C. Ma, R. K. Puddy, K. Delfanazari, M. D. Cao, T. Yi, J. P. Griffiths, H. E. Beere, D. A. Ritchie, M. J. Kelly and C. G. Smith, *'Statistical measurements of the DC-bias-induced 0.75 and 0.25 anomalies in 402 quantum point contacts'*, in preparation (2017).

Table of contents

List of figures

Nomenclature

$\downarrow$	spin-down, with lower energy
$\uparrow$	spin-up, with higher energy
1D	one-dimensional
2D	two-dimensional
2DEG	two-dimensional electron gas
α	lever arm
$\alpha_{N,N+1}$	first three lever arms
B	magnetic field
$B_{\perp(\parallel)}$	in-plane B field perpendicular (parallel) to the 1D transport direction
$\widetilde{B}$	$= g^0\mu_B B$ ($g^0 = 1$ in our calculations, μ_B is Bohr magneton)
$B_*(\kappa)$	quadratic dependence coefficient of S_B on B
B_*^{min}	minimum B_* (decreases with U_{eff}^{max})
B_{rs}	magnetic field at which the risers start splitting for transconductance
B_{ls}	magnetic field at which ΔE_{rs} starts splitting linearly with B fields
D(row,column)	256 device coordinates using addressed row and column in a MUX
DOS	density of states
E_F	Fermi energy
E_N	subband edge energy/central barrier height
E_x	$= \hbar\omega_x$ longitudinal potential barrier curvature
E_x^N	E_x of the first three subbands
E_y	$= \hbar\omega_x$ transverse potential confinement curvature
$\Delta E_{N,N+1}$	first three subband spacings
ΔE_{rs}^{0T}	$\alpha\Delta V_G$ of the spontaneous splitting risers at 0 T
ΔE_Z	$= g^*\mu_B B$, Zeeman energy
ΔE_{ss}	$= \Delta E_Z + \Delta E^{hfo}$, subband splitting energy
ΔE_{rs}	$\alpha\Delta V_G$ of the splitting risers for transconductance ($\approx \Delta E_{ss}$)
ΔE^{hfo}	high-field offset (intercept of the linear fitting of ΔE_{rs} with B fields)
$\Delta E_{\perp(\parallel)}^{hfo}$	ΔE^{hfo} in the $B_{\perp(\parallel)}$ fields

ΔE_{drop} swift decrease of the first subband energy once it crosses the higher μ_s

ΔE_{DC} DC-bias-induced spin gap due to the pinning mechanism ($\approx e|V_{DC}|$)

ΔE_{DC}^{end} final ΔE_{DC} after releasing the pinning energy ($\approx \Delta E_{drop}$)

forward (backward) sweep sweep V_G to decrease (increase) conductance

G_Q $= 2e^2/h$

$G^0(\kappa, E_x, \widetilde{T})$ conductance (superscript 0 represents non-interacting variables)

$G_{SD}(G_{ac})$ $= dI/dV_{ac}$, source-drain differential conductance

G_d definition conductance

$G_{TC}^{0.7}$ conductance at the strongest S_{TC}

$G^{0.7}$ conductance at the strongest S_G

G_{0T} zero-B-field G_{SD}

G_B magnetoconductance

G_{dc} source-drain dc conductance

$G_{ac(dc)}^{0.75}$ $G_{ac(dc)}$ for the 0.75 anomaly at minimum of $dG_{ac(dc)}/dV_G$

$G_{ac(dc)}^{0.75s}$ $G_{ac(dc)}$ for the 0.75 anomaly when it starts showing up

$G_{ac(dc)}^{0.25}$ $G_{ac(dc)}$ for the 0.25 anomaly at minimum of $dG_{ac(dc)}/dV_G$ ($G_{ac}^{0.25} \approx 0.375 G_Q$)

$G_{ac(dc)}^{0.25s}$ $G_{ac(dc)}$ for the 0.25 anomaly when it starts showing up ($G_{ac}^{0.25s} \approx 0.5 G_Q$)

g^* effective g factor (gradient of the linear fitting of ΔE_{rs} with B fields)

$g_{\perp(\parallel)}^*$ g^* in $B_{\perp(\parallel)}$ fields

KQD Kondo quantum dot

κ $= (\mu - E_N)/E_x = \alpha(\widetilde{V}_G^{riser} - \widetilde{V}_G)/E_x$, V_G axis is transformed into κ

$\kappa_{LDOS_{max}}$ κ position of $LDOS_{max}$ (increases with U_{eff}^{max}, characterised by $\kappa_{TC}^{0.7}$)

$\kappa_{TC}^{0.7}$ κ position at the strongest S_{TC} (increases with U_{eff}^{max})

$\kappa^{0.7}$ κ position at the strongest S_G

$\kappa_{B_*^{min}}$ κ position at the minimum of B_* (increases with U_{eff}^{max})

L QPC length

l_y transverse harmonic oscillator length

$LDOS(\kappa)$ effective local density of states (characterised by $1 - S_{TC}$)

$LDOS_{max}$ maximum LDOS ($\propto 1/\sqrt{E_x}$, characterised by $1 - S_{TC}^{0.7}$)

μ_s higher chemical potential at source

μ_d lower chemical potential at drain

MUX type 1 multiplexer with length varying at fixed width 0.6 and 0.4 μm

MUX type 2 multiplexer with fixed L/W ratio (width=0.4, 0.8, 1.2, 1.6 μm)

MUX sample 1 type 1 multiplexer, QPC length=0.1-2 μm

MUX sample 2 type 1 multiplexer, QPC length=0.4, 0.7, 1, 1.3 μm

MUX sample 3 type 2 multiplexer, QPC length/width=1

MUX sample 4 type 2 multiplexer, QPC length/width=2
MUX sample 5 type 2 multiplexer, QPC length/width=2
S1-T1-1 sample 1-at 40 mK-in the 1st cooldown
S2-T2-2i sample 2-at 1.4 K-in the 2nd cooldown after illumination
n_{2D} 2D carrier density
n^{1D} 1D carrier density
n_p count of pinch-off devices for a MUX in a cooldown
n_{1D} count of 1D devices for a MUX in a cooldown
$n_{0.7}$, $n_{1.7}$, $n_{2.7}$ count of 1D devices that show a parabolic potential barrier and show the 0.7 anomaly for the first three plateaus respectively, for a MUX in a cooldown
n_{DC} count of DC spectroscopies for a MUX in a cooldown
N subband index/plateau number
QPC quantum point contact
R_s constant series resistance
R_s^N variable series resistance at Nth subband index
ρ(A,B) Pearson product-moment correlation coefficient of A with B
$S_{TC}(\kappa)$ $= TC_{SD}/TC^0$, transconductance suppression ($\approx 1 - U_{eff}(\kappa)$)
$S_{TC}^{0.7}$ 0.7 anomaly transconductance suppression ($\approx 1 - U_{eff}^{max}$)
S_G $= G_{SD}/G^0$, conductance suppression
$S^{0.7}$ 0.7 anomaly conductance suppression
$S_B(B)$ $= G_B/G_{0T}$, magnetoconductance suppression (decreases with U_{eff}^{max})
T temperature
$\widetilde{T}$ $= k_BT$ (k_B is Boltzmann's constant), thermal energy
T_K Kondo temperature
$T_r(E)$ transmission probability
TC_{SD} source-drain transconductance
τ hopping amplitude
U interaction strength in a 1D tight-binding model ($\propto \sqrt{E_y}$)
$U_{eff}(\kappa)$ $= U \cdot LDOS(\kappa)$, LDOS modified effective interaction strength
U_{eff}^{max} $= U \cdot LDOS_{max} \propto \sqrt{E_y/E_x}$, strongest effective interaction strength
U_E $= E_y/E_x$, measure of U_{eff}^{max}
V_G split-gate voltage
V_p pinch-off voltage
V_d definition voltage ($\approx n_{2D}$)
V_{ac} source-drain ac excitation voltage
V_{DC} applied DC bias voltage

V_{SD} corrected source-drain DC bias voltage

$V_{DC}^{0.75s}$ DC bias when the 0.75 anomaly starts showing up ($e|V_{DC}^{0.75s}| \approx \Delta E_{drop}/2$)

$V_{DC}^{0.25s}$ DC bias when the 0.25 anomaly starts showing up ($e|V_{DC}^{0.25s}| \approx \Delta E_{drop}$)

W QPC width

$Y_{R_s^N}$ yield of devices showing a variable R_s^N in all 1D devices

$Y_{TC}^{0.7}$ yield of devices showing transconductance suppression in all 1D devices

$Y_{rs}^{0.7}$ yield of the devices showing the spontaneous risers-splitting in all 1D devices

$Y^{0.25}$ yield of the 0.25 anomaly in DC spectroscopies

ZBA zero-bias anomaly

1

Introduction

1.1 Background

In 1958, Jack Kilby, from Texas Instruments in the USA, invented the first transistor, which has been considered as one of the greatest inventions in the 20th century. Afterwards, the integrated circuit industry has been developing with ever smaller features. In 1965, Gordon Moore, the co-founder of Intel, asserted that, the amount of transistors on one chip doubles in every 18 months, while the price remains unchanged [8]. Moore's Law has profoundly pushed forward the development of modern electronic research and technology, including the advancement of semiconductor manufacturing techniques. The industry has started focusing on the nano-fabrication process and the feature size of lithography has entered into the nano-range, which also propels the research in nano-science.

As the integrated level of the transistors becomes higher and higher, the transistor dimensions are now of the order of nanometres. When devices operate at such dimensions, quantum physics starts to dominate the device behaviours instead of classic physics. Also leakage and heat issues are becoming more and more serious, which makes Moor's law start to fail inevitably. To cope with the dilemma, the semiconductor industry may transit from an all-Si technology to a composite III-V/Si technology for

the next generation of transistors. Simultaneously, the conventional digital computing architecture may experience a revolution and may be substituted ultimately by a new computing architecture based on quantum computing. The quantum computing speed is faster by several orders of magnitude for some computing problems, which will drastically improve the modern computational ability and solve many important issues.

Classical computing is based on the transistor-based binary digits (bits), which are always in two definite states (0 or 1). A similar principle applies to quantum computing with quantum states. The building block is called a 'quantum bit' (qubit), which can be any quantum superposition and entanglement of '0' and '1' [9]. Today, although people have executed some quantum computations successfully using a very small number of qubits, the normal operations of quantum devices are still very difficult. It is still necessary to devote a significant amount of research into quantum devices, before any possible realisation of large-scale quantum integrated circuits. In particular, Al-Taie et al. first realised the application of an on-chip quantum multiplexer, and studied the reliability and scalability of 256 split-gate devices in just one cooldown [10]. This enlightens the further development of more advanced quantum circuits.

1.2 Non-interacting electron transport in 1D systems

1.2.1 Low-dimensional systems

In a bulk semiconductor, electrons can freely move in three dimensions and have a drift velocity when an electric field is applied. In a semiconductor heterostructure, the movement of electrons is restricted in the two-dimensional (2D) quantum well at the interface of different semiconductors, forming a two-dimensional electron gas (2DEG). The 2D systems bring about a variety of interesting quantum discoveries, including the quantum Hall effect (Nobel Prize in Physics, 1985) [11] and the fractional quantum Hall effect (Nobel Prize in Physics, 1998) [12]. In the quantum Hall effect, the Hall resistance shows plateaus as a function of the perpendicular magnetic field, due to the 2D density of states transforming into the discrete Landau levels.

Quantum wires and quantum dots can be realised by the further confinement of one-dimensional (1D) and zero-dimensional (0D) systems respectively. More quantum phenomena are exhibited, including the conductance quantisation in discrete units in 1D systems [13, 14], and Coulomb blockade in 0D systems [15]. To realise 1D systems, the quantum wires can be defined by a split-gate [16]. The quantum dots can be achieved through an assembly of split-gates, which can be used to trap and manipulate single electrons.

1.2.2 Ballistic transport

As is known, when an electron moves through a conductor from source (S) to drain (D) under an applied potential, the scattering occurs randomly, which is called 'diffusive transport'. This conductance is described by Ohm's law

$$G = \frac{\sigma A}{L} \tag{1.1}$$

where σ is the Drude conductivity to describe the diffusive transport, A is the cross-sectional area (for 2DEG, A is equal to the sample width) and L is the length of the conductor. The Drude conductivity is given by

$$\sigma = en\mu; \mu = \frac{e\tau}{m^*}; \tag{1.2}$$

where n is the electron density, μ is the electron mobility, m^* is the electron effective mass (m^*=0.067 m_e for GaAs, m_e is the electron mass) and τ is the relaxation time (the average time between scattering events).

In particular, for 2DEG, the transport is still diffusive since the sample is much larger than the electron's mean free path (the average distance between scattering events). In contrast, for the QPC constriction at sufficiently low temperatures, the channel from S to D is shorter than the mean free path, and electrons can transport directly from S to D without scatterings happening. This is called 'ballistic transport' in which the Drude model is no longer valid.

1.2.3 Density of states

For 2D or 1D systems, the density of states (DOS) is the number of available states per unit area (2D) or per unit length (1D) in a given energy range, given by

$$\rho(E) = \frac{\mathrm{d}n}{\mathrm{d}E} \tag{1.3}$$

For the 2DEG in which only the lowest 2D subband is occupied, the 2D DOS is constant, given by

$$\rho_{2D}(E) = \frac{m^*}{\pi\hbar^2} \tag{1.4}$$

With the states occupied up to wave vector k, the dispersion relation of each 1D subband is given by

$$E_{k,N} = E_N + \frac{\hbar^2 k^2}{2m^*} \tag{1.5}$$

where N is the subband index and E_N is the energy at bottom of the N^{th} subband (subband edge). The carrier density of the N^{th} subband is given by

$$n^{1D} = \frac{2}{\pi\hbar}\sqrt{2m^*(E - E_N)} \tag{1.6}$$

where the states are occupied up to energy E and the factor of 2 accounts for the spin degeneracy of the subband. By differentiating n^{1D} with energy, the 1D DOS is given by

$$\rho_{1D}(E) = \frac{\sqrt{2m^*}}{\pi\hbar}\frac{1}{\sqrt{E - E_N}} \tag{1.7}$$

The total DOS is the sum of ρ_{1D} of all subbands below the Fermi energy, which is illustrated in Fig. 1.1 for a case of four subbands populated in a square well. We can see the van Hove singularity at each subband edge ($E = E_N$).

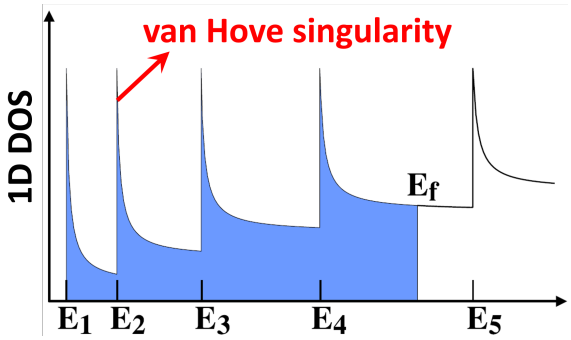

Figure 1.1: 1D DOS in a square well with four subbands populated. The van Hove singularity is pointed with an arrow. Adapted from Ref. [2].

1.2.4 Conductance quantisation

In a semiclassical picture, at 0 K, the net current flowing through a 1D subband is given by

$$I_{1D} = e\rho_{1D}(E_F)v(E_F)(\mu_s - \mu_d) = \frac{2e^2}{h}V \tag{1.8}$$

where $\rho_{1D}(E_F)$ and $v(E_F)$ are the 1D DOS and group velocity at the Fermi energy E_F, μ_s and μ_d are the chemical potentials at source and drain, and eV is the small potential difference applied between source and drain ($\mu_s - \mu_d$=eV). Then the differential conductance of 1D subband is given by

$$G_Q = \frac{dI_{1D}}{dV} = \frac{2e^2}{h} \tag{1.9}$$

which shows remarkably that the 1D conductance is quantised in units of G_Q. This indeed arises from the fact that the group velocity is inversely proportional to the 1D DOS.

1.2.5 Landauer-Büttiker formula

In experiments, the electrostatic potential induced by the split-gate voltage V_G varies as a function of position. Büttiker used a saddle-point potential $\widetilde{V}(x,y)$ ($\widetilde{V} = -|e|V$) to simulate the transmission through a 1D channel [17]

$$\widetilde{V}(x,y) = \widetilde{V}_0 - \tfrac{1}{2}m^*\omega_x^2x^2 + \tfrac{1}{2}m^*\omega_y^2y^2 \tag{1.10}$$

where the electron transport is along the x-direction and the quantised energy levels form in the transverse y-direction, $\widetilde{V}_0$ is the potential at the saddle point, and ω_x and

ω_y are the potential curvatures in the x and y directions respectively. Typically, the longitudinal barrier curvature and the transverse confinement curvature are expressed in terms of the harmonic-oscillator energies $E_x = \hbar\omega_x$ and $E_y = \hbar\omega_y$ respectively. A schematic of the saddle-point potential is shown in Fig. 1.2.

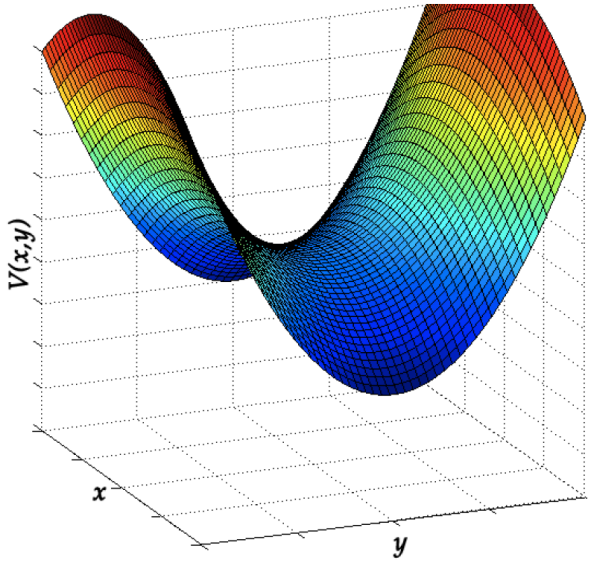

Figure 1.2: A schematic of the saddle-point potential. Adapted from Ref. [1].

For a parabolic confinement, based on Eq. 1.5, there are N 1D subbands with the transverse modes E_N equally spaced:

$$E_N = \widetilde{V}_0 + E_y(N - \tfrac{1}{2}) \tag{1.11}$$

where the subband spacing is equal to E_y. When applying a negative split-gate voltage, the discrete 1D subbands will move above the Fermi energy one by one and thus the transport conductance diminishes in steps of G_Q.

Thus, the effective potential barrier along the transport direction can be written as

$$\widetilde{V}_N(x) = E_N - \tfrac{1}{2}m^*\omega_x^2 x^2 \tag{1.12}$$

where the central barrier height $\widetilde{V}_c$ is equal to E_N. For a potential barrier, there are probabilities that an electron could be reflected or tunnel through it. Therefore, there is a transmission probability $T_r(E)$ for electrons with energy E across the barrier:

$$T_r(E) = \frac{1}{1 + e^{-2\pi(E-E_N)/E_x}} \tag{1.13}$$

This saddle-point model is accepted as a good approximation for a QPC near pinch off [18, 19], and we assume it applies in the first three plateaus. We use the Landauer-Büttiker formula to calculate the non-interacting conductance G^0, where non-interacting variables are marked with the superscript 0. In our calculations, we choose the chemical potential μ as the reference frame, thus the electron energy E' is equal to $E - \mu$ and Eq. 1.13 is written as

$$T_r^0(E') = \frac{1}{1 + e^{-2\pi(\kappa + E'/E_x)}}; \tag{1.14}$$

where $\kappa = (\mu - E_N)/E_x$. Typically, at the plateau riser with the transmission equal to 0.5, the central barrier height E_N^{riser} just intercepts μ. Thus, substituting Eq. 1.11 into the κ expression, we have

$$\kappa = \frac{\mu - E_N}{E_x} = \frac{E_N^{riser} - E_N}{E_x} = \frac{\widetilde{V}_0^{riser} - \widetilde{V}_0}{E_x} = \frac{\alpha(\widetilde{V}_G^{riser} - \widetilde{V}_G)}{E_x} \tag{1.15}$$

where α is the geometric conversion factor-lever arm between the applied split-gate voltage V_G and the electrostatic potential energy; V_G^{riser} is the split-gate voltage at the plateau riser with a conductance 0.5 G_Q. In this work, we will commonly convert V_G into κ using Eq. 1.15.

Considering the Fermi distribution, G^0 at a temperature (T) is given by

$$G^0(\kappa, E_x, \widetilde{T}) = G_Q \int T_r^0(E', \kappa, E_x)(-\frac{\partial f}{\partial E'})\mathrm{d}E'; f = \frac{1}{1 + \mathrm{e}^{E'/\widetilde{T}}} \tag{1.16}$$

where f is the Fermi function and $\widetilde{T}$ is the thermal energy $k_B T$ (k_B is the Boltzmann's constant). We can see G^0 is a function of κ, E_x and $\widetilde{T}$. Typically, based on Eq. 1.14, at T=0 K with $E' = 0$, the conductance G_0 is

$$G_0(\kappa) = G_Q T_r^0(0) = G_Q \frac{1}{1 + e^{-2\pi\kappa}}; \tag{1.17}$$

We can see $G_0(\kappa = -0.5)$=0.041 G_Q, $G_0(\kappa = 0)$=0.5 G_Q, and $G_0(\kappa = 0.5)$=0.959 G_Q. The step width has a κ range of 1 (i.e. a potential range equal to E_x), over which G_0 rises from zero to G_Q basically.

1.3 1D transport in an in-plane magnetic field

Based on Eq. 1.16, non-interacting magnetoconductance G_B^0 is

$$G_B^0 = G_\downarrow^0 + G_\uparrow^0; \qquad G_{\downarrow(\uparrow)}^0 = \frac{1}{2} G_Q G^0(\kappa \pm \frac{\widetilde{B}}{2E_x}, E_x, \widetilde{T}) \tag{1.18}$$

where the electron energy over the central barrier height decreases for spin-down $G_\downarrow^0$ and increases for spin-up $G_\uparrow^0$ symmetrically by half the Zeeman energy ($\widetilde{B} = g^0 \mu_B B$, non-interacting effective g factor $g^0 = 1$ is used in our calculations, μ_B is the Bohr magneton).

In a pioneering work by Graham et al., Fig. 1.3 (1) and (2) show transconductance dG_B/dV_G as a function of V_G and B fields, under in-plane magnetic fields parallel ($B_\parallel$, (1)) and perpendicular ($B_\perp$, (2)) to the transport direction respectively, for a same device in different cooldowns at 50 mK [2]. Fig. 1.3(3) and (4) shows a schematic diagram illustrating main features in Fig. 1.3 (1) and (2). The lines correspond to the transconductance peaks in dark in Fig. 1.3 (1) and (2). Blue lines are spin-down subband edges, and red lines are spin-up subband edges.

For similaritits between Fig. 1.3(1) and (2), first, the arrow in Fig. 1.3(b) shows the second crossing occurs at a B field less than twice that at first crossing. Second, the arrow in Fig. 1.3(d) shows the first spin-up subband is discontinuous at first crossing. For disparities between Fig. 1.3(1) and (2), first, the arrow in Fig. 1.3(a) shows spin-down subbands converge in V_G and shift to leftward with increasing B fields in Fig. 1.3(1), while the arrow in Fig. 1.3(e) shows spin-down subbands diverge in V_G and shift to rightward with increasing B fields in Fig. 1.3(2). Second, the arrow in Fig. 1.3(c) shows the triangle in grey shifts to leftward with increasing B fields in Fig. 1.3(1), while the arrow in Fig. 1.3(f) shows the triangle in grey shifts to rightward with increasing B fields in Fig. 1.3(2).

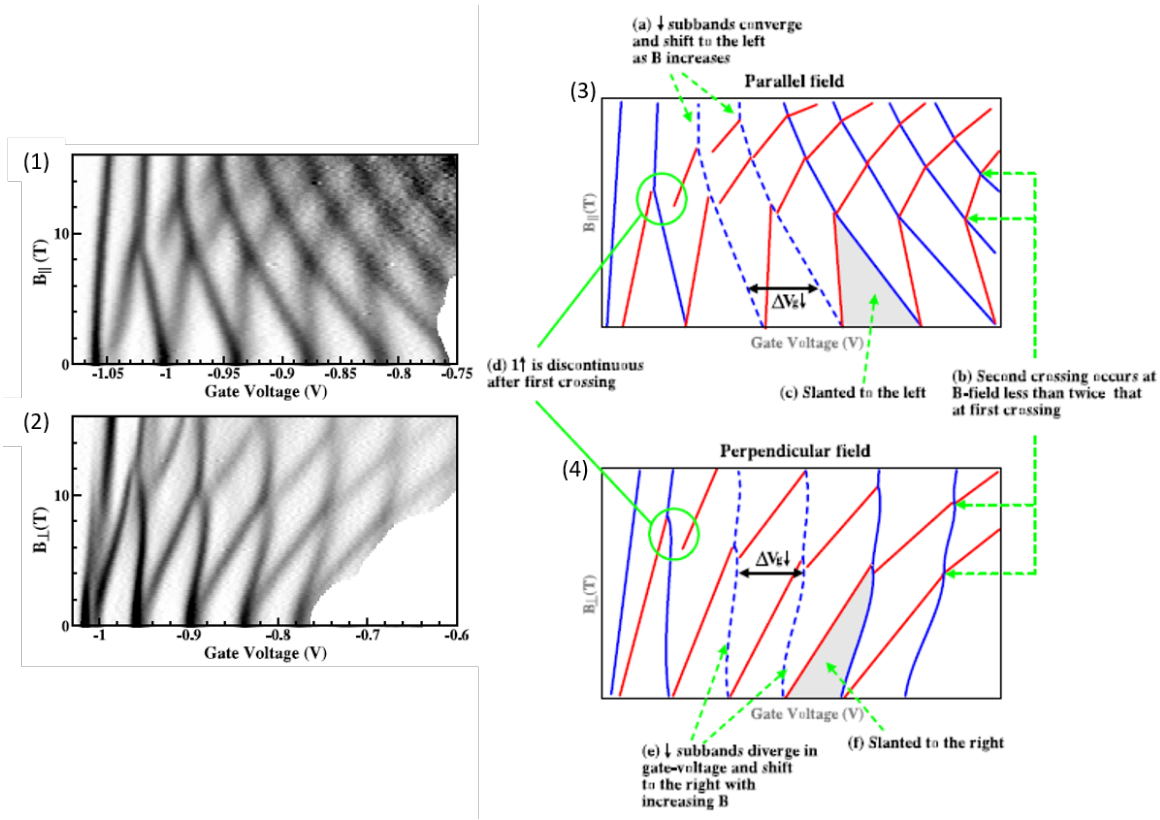

Figure 1.3: (1,2), Transconductance dG_B/dV_G as a function of V_G and B, under in-plane magnetic fields perpendicular ($B_\perp$, (1)) and parallel ($B_\parallel$, (2)) to the transport direction respectively. (3,4), Schematic diagram illustrating main features in (1,2). The lines correspond to the transconductance peaks in dark in (1,2). (a-f) shows similarities and disparities between Fig. 1.3(1) and (2). Adapted from Ref. [2].

1.4 Physical realisation of a QPC

1.4.1 Modulation-doped GaAs/AlGaAs heterostructures

2D systems were first investigated using Si-MOSFET (metal-oxide-field-effect-transistor), and 1D transport was first measured using a n-channel Si-MOSFET. However, this was in a diffusive regime, since the channel length was of the order of 10 μm [20, 21]. Afterwards, the $GaAs/Al_xGa_{1-x}As$ HEMT (high-electron-mobility-transistor) became an ideal semiconductor material for 2D system research, since its first realisation in the laboratory in 1979 [22]. HEMT has advantages over Si-MOSFET. The lattice constants of GaAs and AlGaAs only differ by 0.025 Å, resulting in negligible lattice strain and mismatch at interfaces. HEMT also exhibits a superior electron mobility, which is of the order of $1 \times 10^6 cm^2 V^{-1} s^{-1}$ for the wafers we use.

Fig. 1.4 shows the energy band structure for a GaAs/AlGaAs heterostructure we use. Compared with GaAs that has a 1.4 eV band gap (the energy discrepancy between the valence and conduction band), $Al_xGa_{1-x}As$ has a wider band gap described as $E = (1.424 + 1.247x)eV$ [23], which is 1.8 eV for the $GaAs/Al_{0.3}Ga_{0.7}As$ wafers we use. As E_F must remain constant through two materials with different band gaps, electrons of the donor layer move to the GaAs/AlGaAs interface. The positive charges left behind at the doped layer cause the band structure to bend, in order to keep the charges in equilibrium again. Thus a dipole layer appears at the interface, similar to a P-N junction. At low temperatures (<4 K), electrons only occupy the ground state in the potential well (the lowest 2D subband). As a result, a sheet of electrons is confined parallel to the interface in an approximately triangular potential well where the conduction band E_c bends below E_F, forming the 2DEG.

The wafers we use are grown by molecular beam epitaxy (MBE) at the Cavendish Laboratory. MBE can realize high quality wafers and sharp interfaces between different semiconductors by depositing one layer at a time. For GaAs/AlGaAs heterostructures, there are four sources: gallium, arsenic, aluminium and silicon (used for doping), which are evaporated from separate heated crucibles in the MBE chamber [24]. To reduce impurities, the chambers must operate in an ultra-high vacuum.

Fig. 1.5 illustrates the GaAs/AlGaAs heterostructure we use. Different semiconductors are grown on each other with little lattice strain, among which the doped AlGaAs layer and the GaAs sheets are most essential. The high quality 1 μm GaAs buffer is grown onto a relatively low quality substrate, to ensure a perfect crystalline structure [25]. These slightly variant layers of GaAs stacking on each other helps to achieve

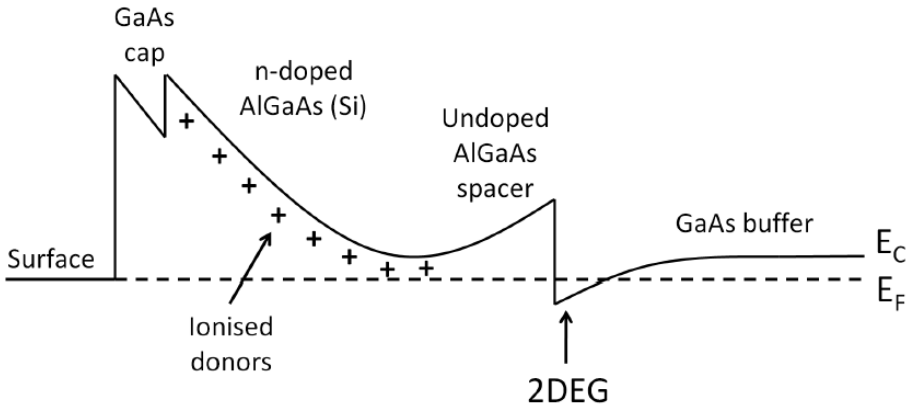

Figure 1.4: A schematic of the band structure for the GaAs/AlGaAs heterostructure we use.

the maximum electron mobility. Then a 40 nm AlGaAs spacer is grown and a 40 nm n-doped (doped with Si) AlGaAs is grown on top of the spacer. The spacer keeps the donor ions away from the 2DEG, which helps reduce the scatterings between electrons and ionised dopants and thus increases the mobility. Typically, by using a thinner spacer layer could achieve a higher carrier density, since the 2DEG is nearer to the donor layer. However, this causes more scattering and reduces the mobility. Finally, a final 10 nm GaAs cap is grown as the outer layer, since Al element may react with oxygen resulting in the layer degradation. The 2DEG is formed at 90 nm below the substrate surface, which is pointed with an arrow in Fig. 1.5.

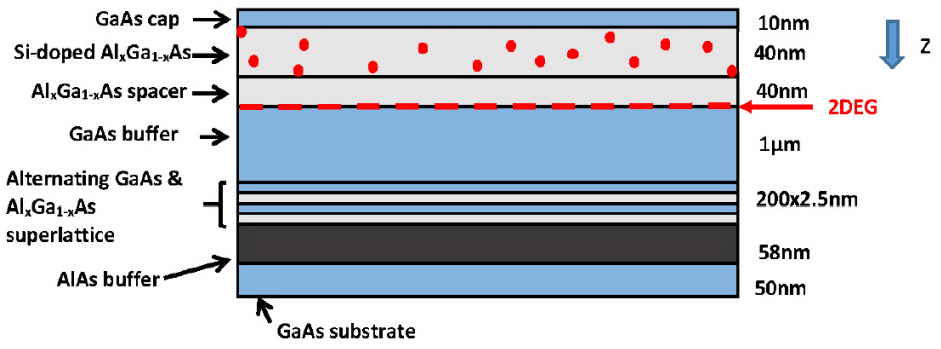

Figure 1.5: A schematic of the GaAs/AlGaAs heterostructure we use. The 2DEG is formed at 90 nm below the substrate surface. Adapted from Ref. [26].

1.4.2 The split-gate device

The first split-gate device was fabricated by Thornton et al. in 1986 [16]. A diagram of the split-gate is shown in Fig. 1.6. It is made of two leads which are separated by a gap and deposited onto the semiconductor heterostructure. Applying a negative voltage on the Schottky gates will shift the entire band structure upward and push the triangle edge of the conduction band above E_F, resulting in the depletion of 2DEG underneath, and the formation of a quasi-1D channel.

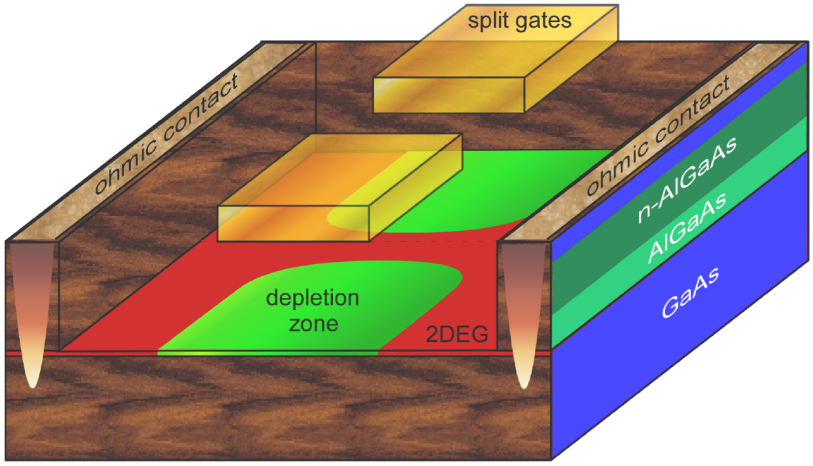

Figure 1.6: A diagram of the split-gate device. Adapted from Ref. [3].

Considering the gates and 2DEG as two plates of a capacitor, the relation of V_G changing the electron density can be described as

$$|e|\Delta n = C\Delta V_G; C = \varepsilon/d \tag{1.19}$$

where C is the capacitance per unit area between the gates and 2DEG, ε is the permittivity and d is the 2DEG depth.

Though Thornton et al. first measured a split-gate, they did not observe quantised plateaus, because their device had a length 15 μm which is longer than the electron mean-free path, and the electron transport is indeed diffusive. Two years later, van Wees et al. [13] and Wharam et al. [14] independently realised ballistic electron transport and discovered conductance quantisation, by using a short split-gate with a length of 0.5 and 1 μm respectively. To make the 1D ballistic transport come into being, we use electron-beam (e-beam) lithography to pattern the split-gate with nano-scale features.

1.5 Multiplexer technique

The mass production of quantum devices is becoming an attractive topic, for example for a fabrication of a few Si/SiGe electron double quantum dots on a single chip in Ref. [27]. However, the number of devices producible on one single chip is limited by the electrical contact pads. In addition, if the measurement of each device is from a different fabrication run and different cool down, then it is difficult to make a clear comparison. Therefore it would be extremely useful if a large number of devices can be fabricated on a single chip. With this purpose, an on-chip multiplexer with 256 split-gate devices has been realised by Al-Taie et al. [10].

For the standard LCC chip package we use with 20 contact pads, we can achieve a multiplexer with a maximum of 256 addressable devices. This is a matrix of 16×16 QPCs using two 16-branch multiplexers. 19 contacts are required: 8 contacts for addressing gates of the Source-Drain MUX, 8 contacts for addressing gates for the Gates MUX, 2 contacts for source and drain, and 1 contact for gate voltage V_G. Fig. 1.7a shows a Scanning Electron Microscope (SEM) image of a MUX sample. The selected area in Fig. 1.7a is enlarged in Fig. 1.7b showing three split-gate transistors in a row. Fig. 1.7c shows one QPC with width and length labelled. Fig. 1.7d shows an optical micrograph. The Source-Drain MUX is on the left to select the desired row from source to drain, and the Gates MUX is on the top to direct V_G to the selected column.

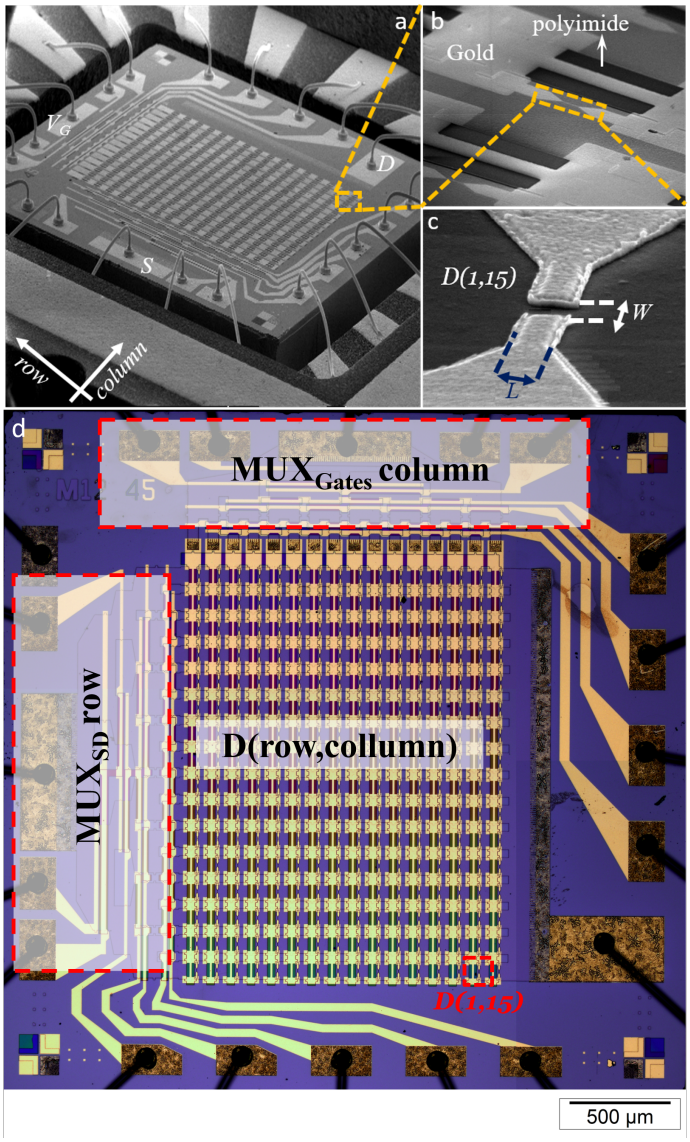

Figure 1.7: (a-c), SEM images of an on-chip quantum multiplexer. (a), A MUX sample consisting of 256 QPCs that are externally controlled by only 19 wire contacts. Each QPC is measured by addressing the row of Source-Drain MUX (S-D contacts are labelled in the figure) and the column of Gates MUX (V_G contact is labelled in the figure), and is called in terms of the coordinate-'D(row,column)'. (b), The enlarged area of the dashed-square in (a) showing three split-gate transistors in the first row-D(1,14), D(1,15) and D(1,16). (c), The device D(1,15) with width W and length L labelled. (d), An optical micrograph of a multiplexer. The position of D(1,15) is shown with a red dashed square in the bottom-right.

Fig. 1.8 is a diagram of the addressing principle for Gates MUX. The green arrow illustrates how the input gate voltage V_G is directed to the output path 6 in 16 paths (labelled 1 to 16), through a two-way 'tree-like' mesa. The operation of Gates MUX requires 8 'addressing gates', called G_1 to G_8. Each of the 16 paths is addressed by a combination code of 'on' or 'off' for the addressing gates.

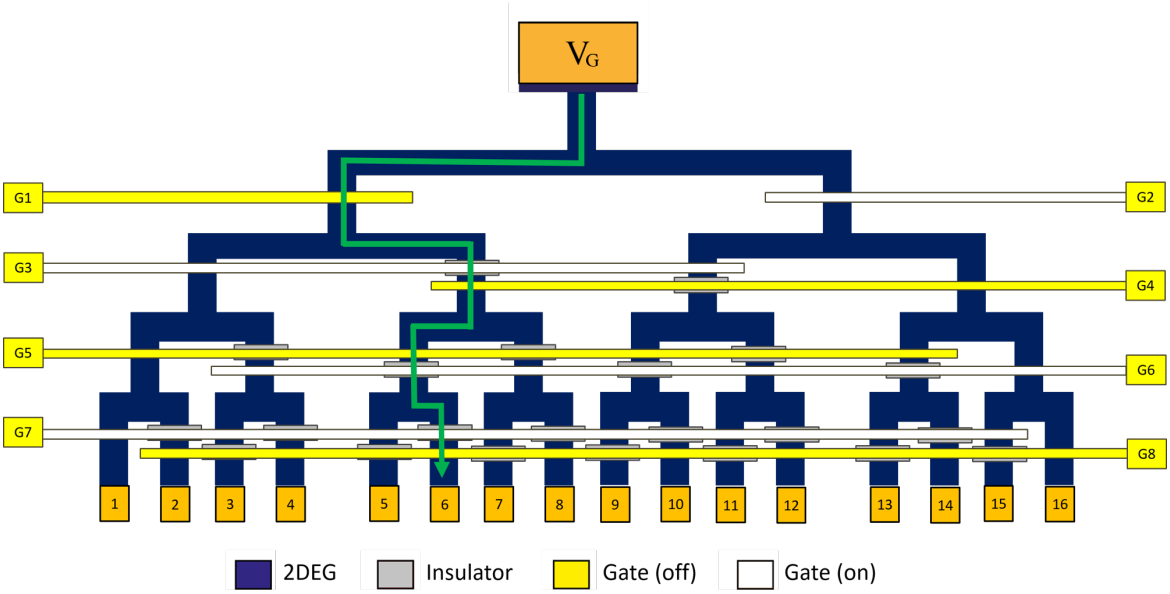

Figure 1.8: A diagram of the addressing principle for Gates MUX. To select the output path 6, addressing gates G_2, G_3, G_6 and G_7 are turned 'on' by applying a negative voltage to deplete the 2DEG under the bar gate, and addressing gates G_1, G_4, G_5 and G_8 are turned 'off' with no voltage applied. Adapted from Ref. [10].

In this work, we design two types of QPC geometries (type 1: varying length L with width W fixed; type 2: fixed geometrical aspect ratio L/W), and fabricate five MUX samples (called sample 1-5: sample 1 and 2 have the type 1 QPC geometry; sample 3-5 have the type 2 QPC geometry). Sample 1 is fabricated using W552 wafer, for which the carrier density and mobility are $1.71 \times 10^{11} cm^{-2}$ and $1.59 \times 10^{6} cm^{2} V^{-1} s^{-1}$ with the 2D mean free path ($l = \mu\sqrt{2\pi n}\hbar/e$) being 10.8 μm. After illumination, the carrier density and mobility are $3.39 \times 10^{11} cm^{-2}$ and $3.82 \times 10^{6} cm^{2} V^{-1} s^{-1}$. Sample 2-5 are fabricated using W922 wafer, for which the carrier density and mobility are $2.08 \times 10^{11} cm^{-2}$ and $3.06 \times 10^{6} cm^{2} V^{-1} s^{-1}$ with the 2D mean free path being 23 μm. After illumination, the carrier density and mobility are $3.06 \times 10^{11} cm^{-2}$ and $5.15 \times 10^{6} cm^{2} V^{-1} s^{-1}$.

1.6 Summary

In this Chapter, first, we introduce 1D transport in the non-interacting regime. The equation of non-interacting conductance G^0 as a function of κ, E_x and $\widetilde{T}$ is given, based on the Landauer-Büttiker formula assuming a saddle-point potential. Then the equation of non-interacting magnetoconductance G_B^0 is given. A pioneering work by Graham et al. is then introduced, for measurements of magnetoconductance in $B_\perp$ and $B_\parallel$ fields respectively. Second, we introduce the physical realisation of a split-gate device on a GaAs/AlGaAs heterostructure, and the principle of multiplexing technique.

2

Overview of the 0.7 anomaly

2.1 The 0.7 anomaly behaviours

Below the first plateau in the 1D conductance, it is common to see an unexpected shoulder at around 0.7 G_Q, called the 0.7 anomaly or 0.7 structure. In fact, the anomaly is not always at 0.7 G_Q, but located in the range of 0.5-0.9 G_Q. This phenomenon was first studied by Thomas et al. in 1996 [28, 29]. In Fig. 2.1a, they found the 0.7 structure evolves into a spin-split plateau with increasing in-plane magnetic fields from 0 to 16 T. In addition, the 0.7 anomaly exists not only for the first plateau, but also for the second plateau although with a much weaker suppression. This can be called the 1.7 anomaly, as shown in Fig. 2.1a. In Fig. 2.1b, they measured the development of the 0.7 anomaly with the increasing temperature. Commonly, the conductance plateau should become more evident at a lower temperature due to the weakened thermal broadening. However, they found it is the opposite case for the 0.7 anomaly, which becomes less pronounced as temperature decreases. Moreover, they found the 0.7 anomaly is not related with the impurity effect, since the 0.7 anomaly remains unaffected after they laterally shifted the 1D channel by asymmetrically biasing the two split gates.

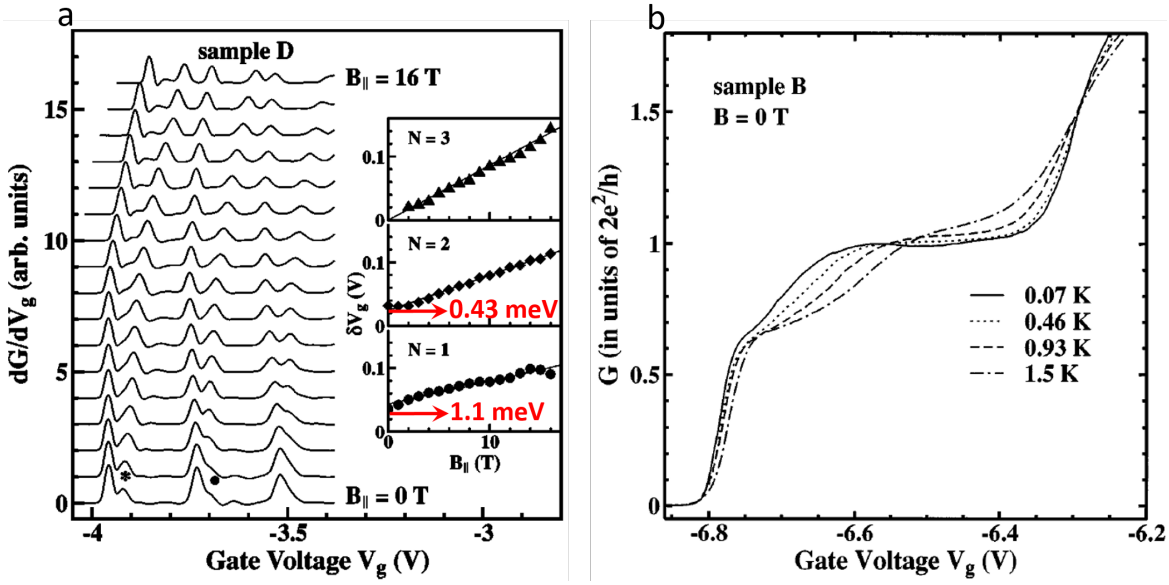

Figure 2.1: a, The development of the 0.7 anomaly with increasing in-plane magnetic fields from 0 to 16 T. The star and dot shows the 0.7 and 1.7 anomaly for the first and second plateau respectively. Adapted from Ref. [29]. b, The temperature dependence of the 0.7 anomaly. The 0.7 anomaly becomes more pronounced as temperature increases. Adapted from Ref. [28].

Since then, researchers have proposed a variety of theories and experiments to explain the 0.7 anomaly in this simplest nanostructure. For a detailed review, see Ref. [30, 31]. However, over twenty years, people have only considered the 0.7 structure to be a result of electron interactions and the underlying origin is still a mystery. In particular, in 2013, two papers in Nature provide new insights into it [7, 32]. In Ref. [7], Bauer et al. attributed the 0.7 anomaly to the van Hove ridge-like 1D LDOS without evoking spontaneous spin polarisation (their calculations set the magnetisation to be exactly zero at zero magnetic field) or quasi-bound states. In Ref. [32], Iqbal et al. provided the experimental evidence of a quasi-bound state in the QPC. Strikingly, comparing these two scenarios of a van Hove ridge or a quasi-localised state, Bauer et al. argued that they are compatible for explaining the low-energy behaviours of the 0.7 anomaly or the Kondo effect respectively [33].

2.2 Theories of the 0.7 anomaly

2.2.1 Spontaneous spin polarisation

In the first experiment on the 0.7 anomaly, Thomas et al. speculated it is caused by a spontaneous spin polarisation. Soon Wang and Berggren used a density functional theory (DFT) in both infinite [34] and finite long 1D wires [35], and proposed that the exchange interactions are strong when the Fermi energy crosses a subband edge, which causes spontaneous subband splitting. That only the spin-down electrons transmit through the quantum wires gives rise to a spin-polarised 0.5 G_Q plateau. In a saddle-point potential, a plateau at 0.5 G_Q is expected to appear at a larger value, since the exchange interactions result in a difference of the effective barrier height for spin-down ($\downarrow$, lower energy) and spin-up ($\uparrow$, higher energy) electrons. Thus, $\downarrow$ electrons are transmitted while $\uparrow$ electrons tunnel through the barrier, raising the feature from 0.5 G_Q to 0.7 G_Q. This model covers the magnetic field dependence of the 0.7 anomaly, but does not explain the temperature dependence.

2.2.2 Pinning of the subband

Bruus et al. proposed a phenomenological model based on spontaneous spin polarisation, to explain the temperature dependence of the 0.7 anomaly [36]. This model assumes $\uparrow$ subband 'pins' to the chemical potential and is followed by spin-splitting as the 1D channel widens. The model predicts a plateau at 0.75 G_Q exists for a range of temperatures and this plateau becomes more pronounced with increasing temperature. Afterwards, experimental evidences for the pinning model were provided. For instance, Graham et al. explained the DC bias dependence behaviours with the highest-energy spin-polarised subband pinning to the source chemical potential over a range of V_G [37]. A disadvantage of Bruus's model is that it also predicts a plateau at 0.5 G_Q besides the 0.7 anomaly at low temperatures.

In Bruus's model, the spin splitting is instantaneous. Reilly et al. modified it and proposed a density-dependent spin-gap model [38, 39]. They assumed the 1D subbands remain spin degenerate until they are populated, and then the subbands split linearly with the electron density. This model predicts a feature between 0.5 G_Q and G_Q, the position of which depends on the opening rate of the spin-gap γ, and the thermal energy k_BT. With the appropriate γ and k_BT, this model could predict the magnetic field and temperature dependence of the 0.7 anomaly. They attributed γ to the 1D electrostatic profile, which further depends on the wire length, split gates geometry

and 2D reservoir density. However, with the density increasing further, the spin-gap is assumed to close again, which is not included in Reilly's model.

2.2.3 Wigner crystallisation

In an electron system with an extremely low carrier density ($n \ll a_B^{-1}$, a_B is the Bohr radius), the Coulomb interactions dominate over the kinetic energy between electrons so that electrons can be regarded as classical particles. Their mutual Coulomb repulsions render their positions to be equally apart, forming a Wigner crystal [40, 41]. A study of the spin properties related with different types of Wigner crystals was reported by by Klironomos et al. in Ref. [42, 43]. A Wigner crystal is formed and develops into a zigzag chain as a function of the electron density. Different exchange processes between neighbouring electrons could determine different spin phases, including partial spin polarisation, ferromagnetism, antiferromagnetism and dimer order.

Spivak and Zhou first provided an explanation of the 0.7 anomaly based on Wigner crystallisation [44]. It is assumed an anti-ferromagnetic Wigner crystal is formed and pinned at extremely low carrier densities in the channel. A conducting channel of a ferromagnetic ground state is formed via the hopping of point defects through the crystal, which gives a conductance of 0.5 G_Q. This plateau at 0.5 G_Q is predicted to be stronger as temperature increases, consistent with the 0.7 anomaly. However, this model does not explain why the 0.7 anomaly is not at the 0.5 G_Q position.

2.2.4 Spin incoherent Luttinger liquid

A Luttinger liquid could be formed in 1D systems with strong electron interactions, which is very different from a Fermi liquid [45, 46]. In a Luttinger liquid, the spin and charge modes transport through the quantum wire separately with different group velocities, which is called 'spin-charge separation'. If the characteristic energy of the spin excitation E_{spin} is exponentially suppressed relative to that of the charge excitation E_{charge}, k_BT could lie between these two energies: $E_{spin} \ll k_BT \ll E_{charge}$. Thus, only the charge excitations are transmitted, forming a spin-incoherent Luttinger liquid, which has distinct characteristics from a normal Luttinger liquid.

Matveev et al. first studied the spin-incoherent Luttinger liquid and also explained the 0.7 anomaly [47, 48]. They adopted the Wigner crystal model with an exchange coupling J of neighbouring electrons ($n \ll a_B^{-1}$) near the QPC centre, which are connected to the non-interacting Fermi-liquid leads ($n \gg a_B^{-1}$). In this regime, the conductance remains at G_Q at a low temperature with $k_BT \ll J$, and drops to 0.5

G_Q at $k_BT \gg J$. This is similar to the temperature behaviour of the 0.7 anomaly, though the conductance tends to saturate at 0.5 G_Q when only charge excitations are transmitted.

2.2.5 The Kondo effect

Similar to a QPC, a quantum dot also exhibits an anomalous conductance feature-the Kondo effect, which was first observed in 1998 [49–51]. When an odd number of electrons occupy the dot, the highest energy level contains an unpaired electron with a localised spin. This spin can form a singlet state with the electrons in the leads, resulting in a peak in the DOS at the chemical potential and an increase of conductance at low temperatures. When applying a DC bias across the dot, the Kondo correlation will be destroyed quickly, resulting in a drop of the Kondo-enhanced conductance. Thus, a zero-bias peak appears in the conductance. For a review of the Kondo quantum dot (KQD), see Ref. [52].

Cronenwett at al. first proposed the Kondo effect could be responsible for the 0.7 anomaly [53]. They observed an anomalous peak of the conductance in a QPC when sweeping the DC bias through zero, known as the zero-bias anomaly (ZBA). The 0.7 anomaly and the Kondo effect do have similar behaviours at low excitation energies below the Kondo temperature (T_K): the linear conductance both strongly decreases with increasing B and T, while the nonlinear conductance both shows a zero-bias peak and the peak splits into two peaks with increasing B. Later, Meir et al. presented a theoretical model using spin-DFT and attributed the Kondo-like anomalies to a 'quasi-bound state' with a localised spin in the QPC [54–57]. However, up to now, it is still unknown that whether a Kondo impurity could be formed possibly in a QPC as an open system.

In Ref. [32], Iqbal et al. used six gates to tune the QPC length. With the increasing length, the 0.7 anomaly rises to merge with the first plateau, and then re-appears at the 0.7 G_Q position. This period repeats three times as the length increases from 180 to 610 nm. Furthermore, the ZBA has a single, double and triple peaks, which is strongly correlated with the periodic length. They proposed that these are due to the increasing number of spontaneously localised states which are formed in the longer QPC.

2.2.6 Smeared van Hove singularity

In Ref. [7], Bauer et al. used a 1D tight-binding model with short-ranged interactions, and advocated the 0.7 anomaly is a result of the van Hove ridge for the local density of states LDOS.

The interaction term in the Hamiltonian is given by Eq. 3.17 in Ref. [6], which is written here:

$$H_{int} = \sum_{j} n_{j\uparrow} n_{j\downarrow} \tag{2.1}$$

where $n_{j\uparrow(\downarrow)}$ counts the number of electrons with spin $\uparrow$ ($\downarrow$) at the site j; the on-site interaction strength U_j is constant as U on sites in the central constriction region, and drops to zero on outer sites.

For the local density of states LDOS, the potential barrier and electron–electron interactions combine to modify the van Hove singularity to be an extended and curved ridge. LDOS is a function of κ defined in Eq. 1.15. As mentioned before, the velocity of an electron is inversely proportional to LDOS. Thus, electrons are being slowed down where LDOS is high and experience an enhanced effective interaction strength: $U_{eff}(\kappa) = U \cdot LDOS(\kappa)$ (see Eq. S36 in Ref. [7]). When the central barrier height lies just below the chemical potential during sweeping V_G, $LDOS(\kappa)$ has its maxima ($LDOS_{max}$), which results in the strongest U_{eff} (U_{eff}^{max}) there:

$$U_{eff}^{max} = U \cdot LDOS_{max} \tag{2.2}$$

.

The 0.7 anomaly depends on U_{eff}^{max}, and can be found where the conductance lies between 0.5 and 0.9 G_Q, called the 'sub-open regime' in Ref. [7]. In particular, the van Hove scenario can be extended to explain the 0.7 anomaly for the second and third plateaus (called the 1.7 and 2.7 anomaly respectively), since the sub-open regime has an analogy in each plateau and so shows the suppression anomaly.

Moreover, they continuously measured the transition from a QPC to a quantum dot by using side gates, and attempted to unify the van Hove scenario with the Kondo physics in Ref. [33]. They attributed similar low-energy behaviours between the 0.7 anomaly and the Kondo effect to the spatially confined spin fluctuations in both a QPC and a Kondo quantum dot KQD. For a KQD, the spin fluctuations result from the screening of a truly localized spin (the similarities cease at high energies where the Kondo effect is governed by an unscreened local moment), whereas for a QPC, they result from the van Hove ridge including a large number of spins. These spin

fluctuations are characterised by small energy scales: the Kondo temperature T_K for a KQD, and so-called B_* in Ref. [7] for a QPC , both of which are inversely proportional to the local spin susceptibility.

The local spin fluctuations are inherited from the non-interacting LDOS at the chemical potential related with the sample geometry, and are enhanced by strong interactions in spaces with slow electrons. For a KQD, the odd electron is slow simply because it is really trapped inside the dot, whereas for a parabolic QPC, slow electrons are just above the barrier top in the QPC centre.

In addition, they noted a long QPC naturally has a flatter-than-parabolic barrier top. It could be expected to show more interesting behaviours in this regime, like the formation of a Wigner crystal. In this regard, they pointed out the experimental results by Iqbal et al. in Ref. [32, 58] are probably related with a wide and flat barrier in a long QPC as tuned.

2.3 Previous statistical study on the role of barrier curvature on the 0.7 anomaly

Previous statistical studies on the 0.7 anomaly by Smith et al. using multiplexers can be found in Ref. [59–61]. In Fig. 2.2a, Smith et al. plot together G_{SD} curves as a function of κ for multiplexed devices (with width=0.4 μm and length=0.4 μm) at 1.4 K. Fig. 2.2b shows G_{SD} as a function of E_x at fixed κ positions for the devices in Fig. 2.2a. As E_x decreases, G_{SD} decreases, showing a stronger conductance suppression of the 0.7 anomaly. This agree with the role of E_x on the 0.7 anomaly as predicted in the van Hove model.

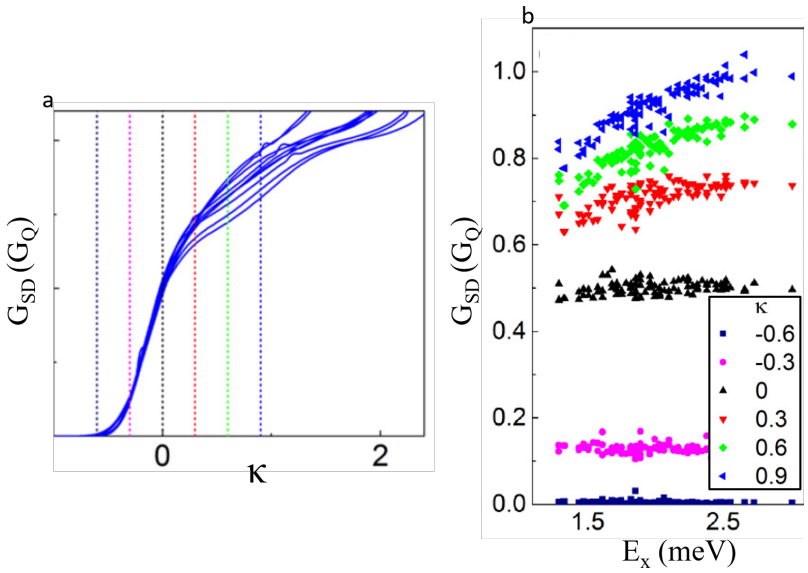

Figure 2.2: (a), G_{SD} curves as a function of κ (in our symbols) for multiplexed devices at 1.4 K. V_G axis is transformed into κ using Eq. 1.15. (b), G_{SD} as a function of E_x for the devices in (a), at fixed κ positions (vertical dotted lines in (a)). Adapted from Ref. [60].

In our work, the multiplexing technique allows us to use a statistical approach to study the physics of QPCs. Our results appear to match well with the van Hove scenario.

2.4 Summary

In this Chapter, first, we introduce the typical 0.7 anomaly characteristics. Second, we introduce a variety of models to explain the 0.7 anomaly. Third, we make a detailed introduction of a recent van Hove model, and make a comparison to the Kondo model. The van Hove model stresses the role of $LDOS$ on the 0.7 anomaly. Fourth, we introduce previous statistical study on the 0.7 anomaly using multiplexers by Smith et al.. These results initially verify the van Hove model, regarding the role of barrier curvature on the 0.7 anomaly.

3

Device Fabrication and Measurement Methods

3.1 Device fabrication

3.1.1 Optical and e-beam lithography

This chapter will introduce the standard semiconductor fabrication techniques in a 100/1000 clean room at the Cavendish Laboratory, used to fabricate a multiplexer. The sequential fabrication recipe includes the mesa pattern, Ohmic contacts, insulators, gate contacts and device bonding.

The MUX layout for the photomask is designed by AutoCAD. The photomask is a piece of transparent glass with patterned chromium on one side. The MUX layout is on the chromium and will be transferred to the sample. We scribe and cleave one manageable piece of material from a GaAs/AlGaAs wafer, and clean the sample. Spin Shipley 1805 (negative photoresist) at 5500 rpm for 30 seconds and bake at 115 °C for 60 seconds to ensure resist uniformity. The resist always becomes thicker at the sample edge, forming an edge bead. Since the edge bead may cause the sample to be

displaced when doing alignment of the device pattern, it should be cleared away first by exposing and developing those edges using an edge-bead-cleaning pattern.

We use the mask aligner to make the alignment. First, we expose the edge bead with ultra-violet (UV) light for 100 seconds and develop in MF319 developer solvent for about 60 seconds to remove the edge bead. Then we repeat the exposure for 3.5 seconds and develop to realise the MUX pattern as Fig. 3.1(a) shows. The UV exposure weakens the chemical bonds of the resist and the exposed parts are removed after developing, leaving the remaining patterned resist shown in Fig. 3.1(b).

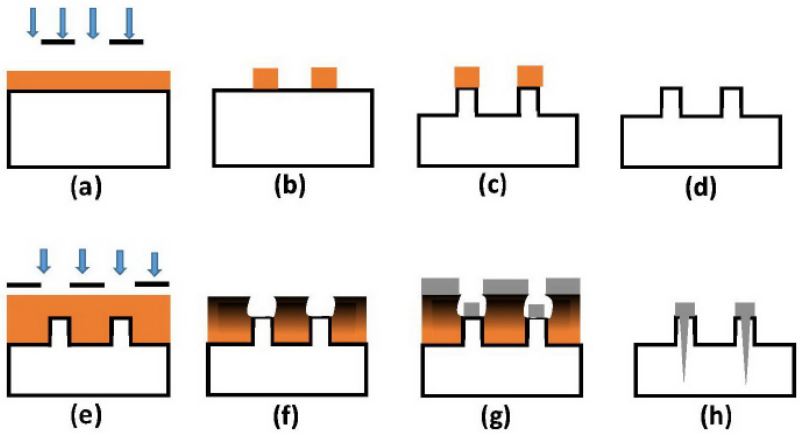

Figure 3.1: The schematic of the Ohmic contacts deposition on a GaAs/AlGaAs heterostructure.

In our clean room, the smallest feature size realised by optical lithography is about 1 μm, so we use e-beam lithography to pattern the QPC. The e-beam resist is a double-layer: the first layer is a 1:1 mixture of A6-100k PMMA (Polymethyl Methacrylate) with Anisole and the second layer is a 1:5 mixture of A11-950k PMMA and MIBK (Methyl Isobutyl Ketone). We spin the first layer at 6000 rpm for 60 seconds and bake at 125°C for 2 minutes, and repeat this for the second layer, which makes each layer have a 50 nm thickness. The developer solution is a 1:3 mixture of Isopropanol and MIBK, and the developing time should be much shorter (8 seconds) for the fine features. The e-beam instrument in our clear room is a LEICA VB6 UHR, which can achieve a reliable resolution of 10 nm.

3.1.2 Mesa patterning

After optical patterning, we immerse the sample into an acid solution, which is made of $H_2SO_4 : H_2O_2 : H_2O$=1:8:1600, for 150 seconds to realise an etching depth of about

100 nm. The raised area on the sample is called a mesa, as Fig. 3.1(c) shows. Here H_2O_2 is used to oxidise the exposed GaAs surface and H_2SO_4 is used to dissolve the oxide. Note that GaAs cannot be etched solely in H_2O_2 or H_2SO_4 solutions. Next, we remove the resist with acetone. Rinse in isopropyl alcohol (IPA) and dry with nitrogen (N_2), as Fig. 3.1(d) shows.

The etching should ensure the Si-doped AlGaAs layer are etched away, however, the mesa should be not be etched too deep, in case the gate would not be able to climb the mesa. A dilute acid solution is used to let the mesa edge have a sloped profile for a better metal deposition. The DEKTAK surface profiler is used to measure the mesa depth.

3.1.3 Ohmic contacts and gate contacts

As Fig. 3.1(e) shows, we coat the sample with 1813 resist (thicker than 1805), and bake at 90 °C for 1 minute, then expose in UV for 6 seconds. Prior to developing, remember to dip the sample into Chlorobenzene (C_6H_5Cl) for 3 minutes to harden the surface of the unexposed resist. Then after developing, the 'undercut' profile can be formed for a good lift-off of the metal deposition, as shown in Fig. 3.1(f). The metallic gates are deposited using a thermal metallisation. Before the metallisation, we put the sample into an RF asher for 45 seconds (or a microwave asher for 100 seconds), to remove any residual resist in the developed area with the oxygen plasma. After the ashing procedure, put the sample into 20 % HCl solution ($HCl : H_2O$=1:4) for 30 seconds to remove any oxide caused by the oxygen plasma.

Then, in a thermal evaporator with a low-pressure chamber ($< 2 \times 10^{-6}$ mbar), we deposit about 100 nm of gold-germanium-nickel (AuGeNi, about 0.5 grams in the evaporator boat) onto the sample, as Fig. 3.1(g) shows. AuGeNi alloy is chosen, as Au is a good conductor, and Ge serves as an n-dopant to make a good contact with GaAs, while Ni sticks the metal film onto the substrate. After the evaporation, soak the sample into acetone to lift-off the remaining resist along with the unwanted metals. Finally, anneal the sample at 430 °C for 80 seconds to diffuse the patterned metal into the 2DEG and establish the Ohmic contact between them, as Fig. 3.1(h) shows. The Ohmic contact obeys Ohm's law, which exhibits a low resistance and a linear current-voltage (I-V) curve.

For the gate contacts, a Schottky barrier is formed at the interface between metal and semiconductor. A Schottky barrier has a non-linear I-V curve with a rectification property, which can be used as a diode. The gate processing is similar to the Ohmic processing. However, if the sample has a thick insulator on it like Polyimide, a dual-

layer resist is needed to create a steep undercut for an easy lift-off of the gate metal. For the first layer, spin LOR 7B onto the sample at 3000 rpm for 50 seconds and bake at 175 °C for 10 minutes. For the second layer, spin 1805 at 5500 rpm for 30 seconds and bake at 115 °C for 1 minute. In the evaporation, a double layer of 10/100 nm titanium/gold (Ti/Au) is deposited for the optical gates, or 10/60 nm Ti/Au is deposited for e-beam gates with the fine features. Ti is used for a good adhesion of metal to the surface. Again, for the sample with a insulator, use a rotating disc that holds the sample at 45° to the metal boat, to ensure the deposition is continuous over the raised mesa and insulator. After the metallisation, use a hot solution of SVC-14 photoresist stripper to do the lift-off.

3.1.4 Insulator

Polyimide is a liquid polymer with the high thermal stability and chemical resistivity [62]. We use the 2:1 mixture of polyimide and T9039 as the insulator between gates and mesa. As polyimide absorbs moisture from the surroundings and the water-polymer interactions may impair the insulating properties [63], first the sample needs to be baked at 125 °C for 3 minutes to remove any moisture on the sample. Also the humidity should be reduced to less than 50 % inside the spinner, by flushing the spinner cabinet with N_2. During the spinning, first set the speed at 5000 rpm for 50 seconds and then ramp it up gradually to 7500 rpm within 10 seconds. The following bake is as follows: bake the sample at 60 °C for 2 minutes and then at 90 °C for 3 minutes; align the desired pattern with the mask aligner and expose for 70 seconds; wait for at least 5 minutes and bake again at 80 °C for 1 minute. To develop, put the sample into HD Microsystems PA401D developer for about 40 seconds to dissolve the unexposed polyimide, and then rinse in PA400R solution. Next, do RF ashing for 2 minutes to remove any residual unexposed polyimide. Finally, the polyimide is cured by baking in an N_2 atmosphere at 350 °C. The oven temperature ramps up slowly to 350 °C and holds for 1 hour, and then ramps down slowly to room temperature. The moisture absorbed by polyimide is driven out, causing the polyimide thickness to shrink by 40 % [63].

3.1.5 Bonding and packaging

The packaging is used in order to mount the device onto a measurement probe. Fig. 3.2 shows a bonded up package. First, the sample is diced and glued using GE varnish onto a standard LCC chip carrier. The gold-ball thermosonic bonder is used to bond

the Ohmic contacts to the carrier pads with a gold thread. During the bonding, remember to ground the sample, especially for the samples with e-beam features which are sensitive to static charge. After each bonding, wait for 60 seconds to let the tip discharge.

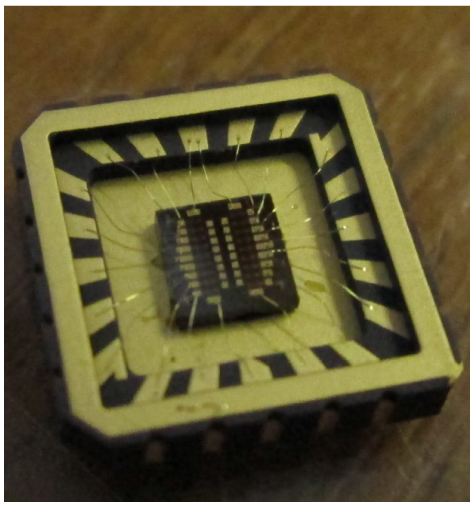

Figure 3.2: Picture of a bonded-up package.

3.2 Low-temperature measurements

3.2.1 4 K ^{4}He dip station

To study quantum transport, measurements must be performed at very low temperatures, which ensures k_BT is much smaller than the 1D subband spacing and allows individual subband levels to be resolved. The MUX samples are tested preliminarily in the ^4He dip station at 4 K, although this temperature is too high to see the 1D plateau.

Load a MUX sample onto the sample holder in the probe which has 20 BNC connectors connected to the package using wires. Before loading the sample, ground all connectors with grounding plugs (which can also act as a ground terminal) to dissipate any floating charges. First, check the resistance of Ohmic contacts at low temperatures. Second, test the 16 addressing bar gates of the MUX sample one by one. Third, address several QPCs and measure the pinch-off curves, to ensure the Source-Drain MUX and Gates MUX all function well. The MUX samples that operate well at 4 K will be further measured at lower temperatures.

3.2.2 1.4 K ^{4}He cryostat

Simply by pumping the vapour of ^4He liquid to a very low pressure, a lower temperature of 1.4 K can be reached. 1D plateaus can be observed at this temperature. In particular, it is interesting to investigate the 0.7 anomaly at this temperature since the 0.7 anomaly is stronger at 1.4 K than 40 mK. In this work, MUX sample 1-5 are measured at 1.4 K. MUX sample 1 is also measured at magnetic fields below 7 T. By pumping the liquid helium bath around a superconducting magnet, the liquid helium can be cooled from approximately 4.2 K to a temperature near the lambda point of helium (approximately 2.17 K, at which temperature normal fluid helium I transits to superfluid helium II), and a lower magnetic field 10 Tesla can be achieved. However, to observe the Zeeman splitting and measure the effective g factor (g^*) in a magnetic field, this temperature is still too high, since the thermal energy is larger than the Zeeman energy, even at a magnetic field 10 Tesla.

3.2.3 40 mK dilution refrigerator

When cooling the mixture of ^4He and ^3He below a critical temperature, two phases will be separated-the concentrated phase rich in ^3He and the dilute phase rich in ^4He.

The concentration of ^3He in each phase is temperature dependent. As the enthalpy of ^3He in two phases is different, ^3He diffusing from the concentrated phase into the dilute phase provides a high cooling power.

In this work, MUX sample 1 is measured at 40 mK in an Oxford Instruments Kelvinox 100 dilution refrigerator. The base temperature is measured using a calibrated ruthenium oxide thermometer on the mixing chamber. The device electron temperature is around 70 mK at a base temperature 40 mK. The magnetic fields can be achieved up to 16 T using a superconducting magnet.

3.3 Conductance measurements

Two-terminal conductance measurements are performed in this work, the circuit of which is shown in Fig. 3.3. The split-gate voltage V_G is applied using National Instruments (NI) 9269 isolated analog output modules, which are capable of supplying $\pm 40V$ to 20 connectors simultaneously. We set the source-drain ac excitation voltage V_{ac}=0.1 mV using a potential divider. A current pre-amplifier J883 with a gain of 10^6 or 10^7 A/V is used to transform the measured current into a large voltage which will be read by a Stanford SR830 DSP lock-in amplifier. The ac signal frequencies should not be close to the main frequency (50 Hz) or its harmonics or any other significant noise frequencies. We choose 77 Hz to give the best signal-to-noise ratio (SNR), which can be analysed using an oscilloscope to perform a real-time Fourier transform of the signal. The instruments are connected to the computer through a General Purpose Interface Bus (GPIB) or Universal Serial Bus (USB). The multiplexing platform is controlled by MATLAB to realise the automatic addressing of 256 split-gates.

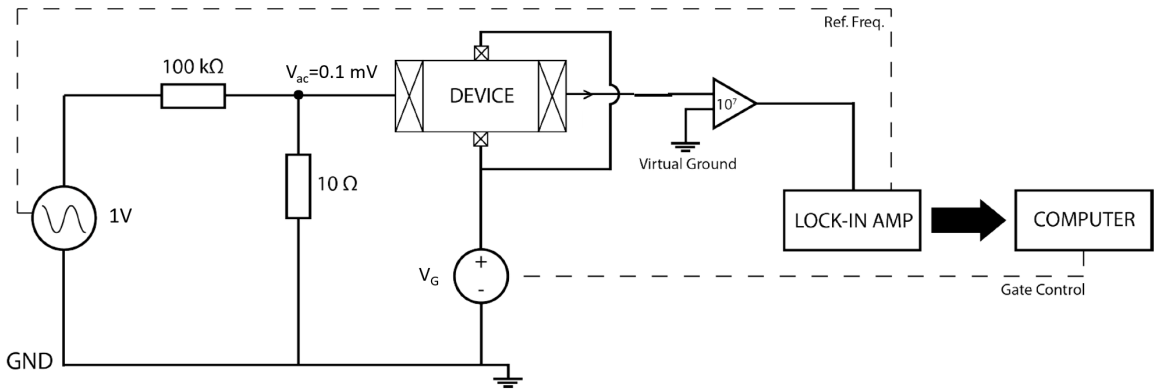

Figure 3.3: The electrical circuit of two-terminal measurements. Adapted from [4].

The measured differential conductance G_m is in series with the whole circuit including the 2DEG region, Ohmic contacts and wires. The probe wires for the 1.4 K cryostat is about 100 Ω at room temperature. After removing the series resistance R_s, we get the corrected source-drain differential conductance G_{SD} in units of $G_Q = 2e^2/h$=77.48 μS

$$G_{SD} = \frac{1}{77.48(1/G_m - R_s)} \tag{3.1}$$

When applying a DC bias voltage V_{DC}, there is a drop on the series resistance. We correct the series resistance R_s by aligning the first plateau to G_Q. By integrating G_m,

we get the corrected source-drain *dc* conductance G_{dc} , which has been used to track the subband energy by Chen et al. [64–66].

$$G_{dc} = \frac{1}{\frac{1}{\int_0^{V_{DC}} G_m dV} - R_s} \tag{3.2}$$

The corrected source-drain DC bias V_{SD} is

$$V_{SD} = V_{DC} - V_{DC} R_s \int_0^{V_{DC}} G_m dV \tag{3.3}$$

3.4 Summary

In this Chapter, first, we introduce the fabrication process of our multiplexer sample. Second, we introduce the setup of low-temperature measurements at a 1.4 K cryostat and a 40 mK dilution rerigerator. Third, we introduce the electrical circuit of our measurements. Fourth, we show the correction of differential conductance by removing the series resistance. We also give the correction of applied DC bias voltage by removing the voltage drop on the series resistance.

4

The 0.7 Anomaly

4.1 Introduction

To explain the 0.7 anomaly, researchers proposed a variety of models including spontaneous spin polarisation [28, 34, 36, 38], Wigner crystallisation [47, 58], Kondo effect [53, 54, 57] and smeared van-Hove singularity [6, 7, 33, 67]. In this chapter, we focus on the 0.7 anomaly by taking advantage of a multiplexing technique [10], which will allow the measurements of hundreds of QPCs in one single cooldown. In particular, the higher plateaus also show the 0.7 anomaly, although much weaker, since the screening increasingly limits the interactions for higher subband index values. Here we systematically investigate the 0.7 anomaly for the first three plateaus respectively.

4.2 Depletion voltage and pinch-off voltage

Fig 4.1 illustrates the 1D conductance properties-definition voltage (V_d), definition conductance (G_d), and pinch-off voltage (V_p), for uncorrected conductance curves before and after illumination (using a red LED) respectively at 1.4 K, for a long channel device D(2,13) (length L=1.8 μm) for sample 1. Sweeping split-gate voltage V_G to decrease (increase) the conductance is called forward (backward) sweeping. In this work, the results are in the forward sweeping if not specified. V_d and G_d are found at the sharp rise of transconductance ($TC_{SD} = dG_{SD}/dV_G$). After illumination, V_d and V_p get more negative, and G_d increases.

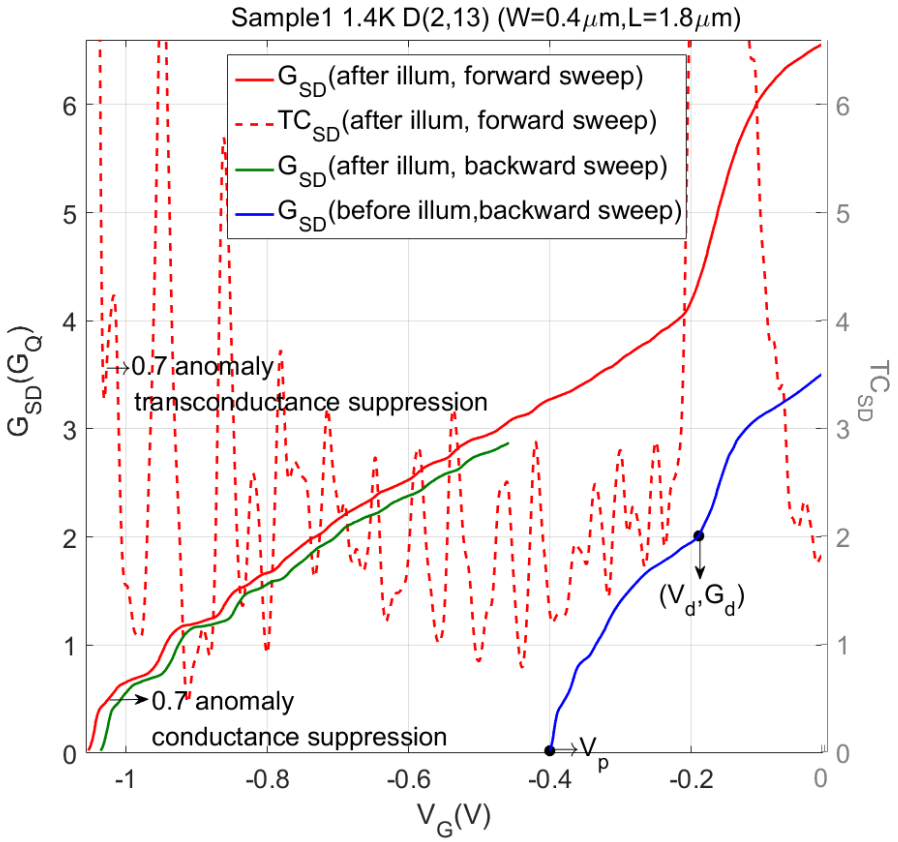

Figure 4.1: Forward and backward conductance curves for a device D(2,13) in sample 1 before and after illumination respectively at 1.4 K. The device has width W=0.4 μm and length L=1.8 μm. Definition voltage V_d, definition conductance G_d and pinch-off voltage V_p are arrowed for G_{SD} (blue curve), in the backward sweep before illumination. The 0.7 anomaly suppressions are pointed out for G_{SD} (red solid line) and TC_{SD} (red dashed line, differential of smoothed G_{SD}, read the right axis) respectively, in the forward sweep after illumination.

For a MUX sample in a cooldown, the quantised 1D devices with the formation of good plateaus are identified, and the number of these is called n_{1D}. Fig. 4.2 shows the statistics of G_d and V_p using error-bars for sample 1-4 in 9 cooldowns at 40 mK or 1.4 K, in the order of decreasing values of mean V_d (V_d^{mean}). The cooldowns with a more negative V_d commonly have a larger G_d and therefore a more negative V_p.

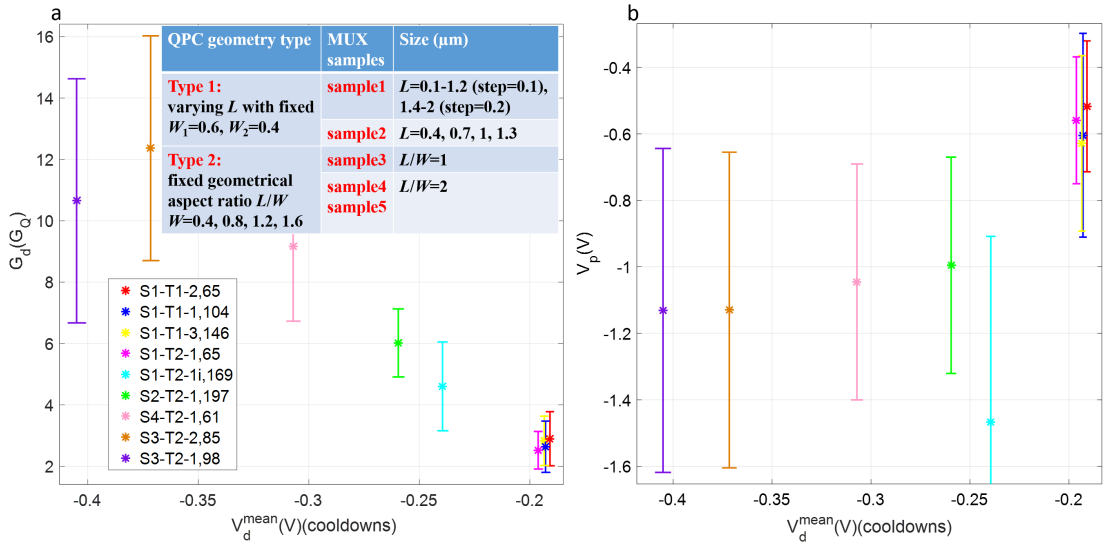

Figure 4.2: The statistics of G_d and V_p for MUX sample 1-4 in 9 cooldowns at 40 mK or 1.4 K, in the order of decreasing V_d^{mean}. The error bar represents the mean $\pm$ standard deviation for each cooldown. The legend in (a) shows each cooldown information. For instance, for the red error-bar, the symbol 'S1-T1-2, 65' refers to sample 1-at 40 mK-in the 2^{nd} cooldown in the dark-with n_{1D} =65 1D devices. For the cyan error-bar, the symbol 'S1-T2-1i, 169' refers to sample 1-at 1.4 K-in the 1^{st} cooldown after illumination-with 169 1D devices. The table in (a) records the QPC geometry information for MUX sample 1-5. MUX sample 1-2 have QPCs with varying length at fixed width. MUX sample 3-5 have QPCs with fixed ratio of length with width.

Considering the capacitance between the split-gates and 2DEG, V_d is proportional to the 2D carrier density (n_{2D}):

$$V_d \approx n_{2D} \frac{ed}{\epsilon_r \epsilon_0} \tag{4.1}$$

where e is the electronic charge, d is the depth of 2DEG, ϵ_r is the relative permittivity, and ϵ_0 is the vacuum permittivity. For the MUX samples, d=90 nm and $\epsilon_r \approx 12$ for $x = 0.33$ in $Al_xGa_{1-x}As$.

Fig. 4.3a shows the V_d histogram of 65 1D devices for sample 1 at 1.4 K before illumination. The mean and standard deviation is -0.196 V and 0.0088 V respectively, which gives $n_{2D} \approx 1.46 \pm 0.07 \times 10^{11} cm^{-2}$ based on Eq. 4.1. The inset shows the V_d map of those devices in the MUX sample, which can be used to approximate the distribution of carrier density. Fig. 4.3b shows the V_d histogram of 169 1D devices for sample 1 at 1.4 K after illumination. The mean and standard deviation is -0.239 V and 0.0803 V respectively, which gives $n_{2D} \approx 1.78 \pm 0.6 \times 10^{11} cm^{-2}$. For comparison, conventional Hall bar measurements shows the carrier density is $1.71 \times 10^{11} cm^{-2}$ and $3.39 \times 10^{11} cm^{-2}$ before and after illumination respectively for the W552 wafer used for sample 1. For another four histograms of V_d for sample 1-3 at 40 mK or 1.4 K, see the Appendix Fig. A.1.

Fig. 4.3c shows the scatter plot of V_d between before and after illumination with 57 devices for sample 1 at 1.4 K. The dashed line with gradient=1 provides a guide to eye. V_d gets more negative due to the increased carrier density after illumination. Fig. 4.3d shows the scatter plot of V_d between the 1^{st} and 3^{rd} cooldowns with 82 devices for sample 1 at 40 mK, showing a repetitive distribution of carrier density in a re-cooldown from room temperature to 40 mK.

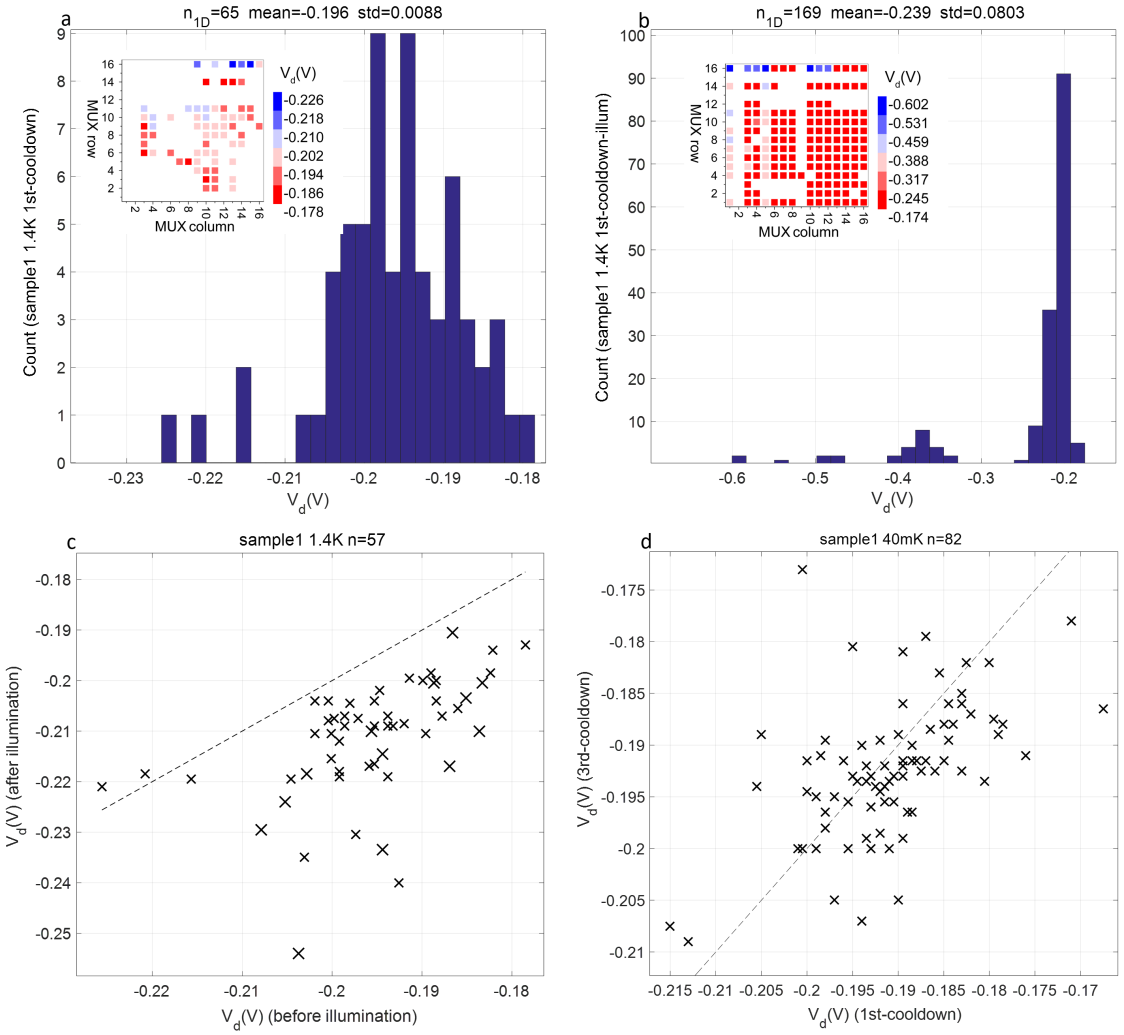

Figure 4.3: (a,b), V_d histograms for sample 1 at 1.4 K before (a) and after (b) illumination respectively. In (a), for n_{1D}=65 1D devices, the V_d mean and standard deviation (abbreviated as 'std') is -0.196 V and 0.0088 V respectively. The inset shows the V_d map of 1D devices achieved in the MUX sample. (c), Scatter plot of V_d between before (X axis) and after (Y axis) illumination with n=57 devices for sample 1 at 1.4 K. (d), Scatter plot of V_d between the 1^{st} (X axis) and 3^{rd} (Y axis) cooldowns with n=82 devices for sample 1 at 40 mK. The dashed line (gradient=1) provides a guide to eye in scatter plots.

Fig. 4.4a,b shows the scatter plots of G_d (a) and V_p (b) respectively between the 1^{st} and 3^{rd} cooldowns for sample 1 at 40 mK, both of which show repeatability. Fig. 4.4c,d shows the scatter plots of G_d (c) and V_p (d) respectively between before and after illumination for sample 1 at 1.4 K. G_d almost doubles and V_p more than doubles after illumination.

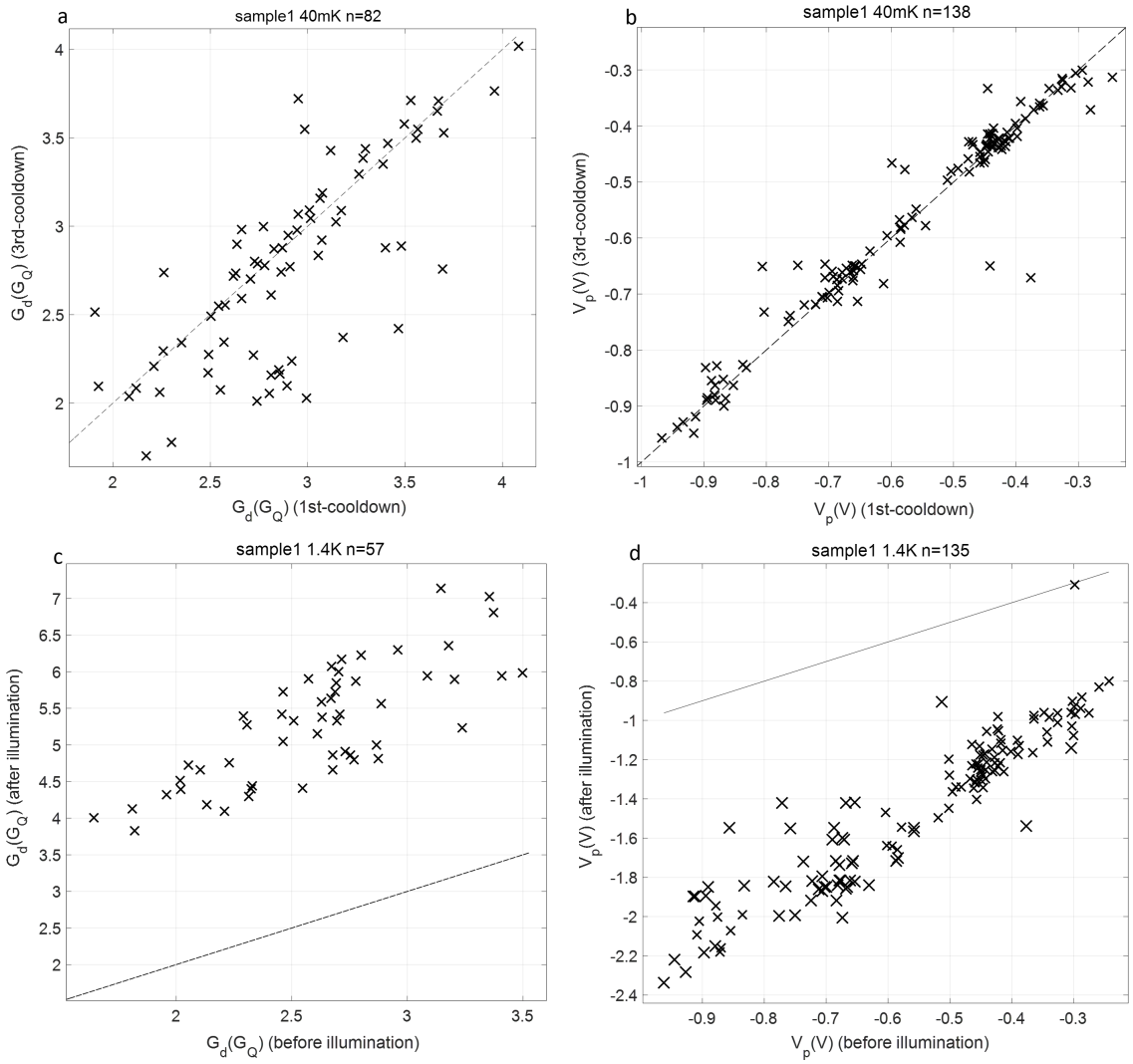

Figure 4.4: (a,b), Scatter plots of G_d (a, with n=82 devices) and V_p (b, with n=138 devices) between the 1^{st} (X axis) and 3^{rd} cooldowns (Y axis) for sample 1 at 40 mK. (c,d), Scatter plots of G_d (c, with n=57 devices) and V_p (d, with n=135 devices) between before (X axis) and after (Y axis) illumination for sample 1 at 1.4 K. The dashed line (gradient=1) provides a guide to eye in each panel.

Fig. 4.5 shows the dependences of V_p on length and G_d respectively, for sample 1 at 40 mK (a,b), and sample 2 at 1.4 K (c,d). Fig. 4.5a,c clearly shows that at a fixed length, the devices with width $W_1 = 0.6\mu m$ (red dots) have a more negative V_p than the devices with width $W_2 = 0.4\mu m$ (blue crosses), and at a fixed width, the devices with smaller length have a more negative V_p. Fig. 4.5b,d shows that the devices with a larger G_d need a more negative V_p to pinch off. For the dependences of V_p on length and G_d for MUX sample 3,4, see the Appendix Fig. A.2.

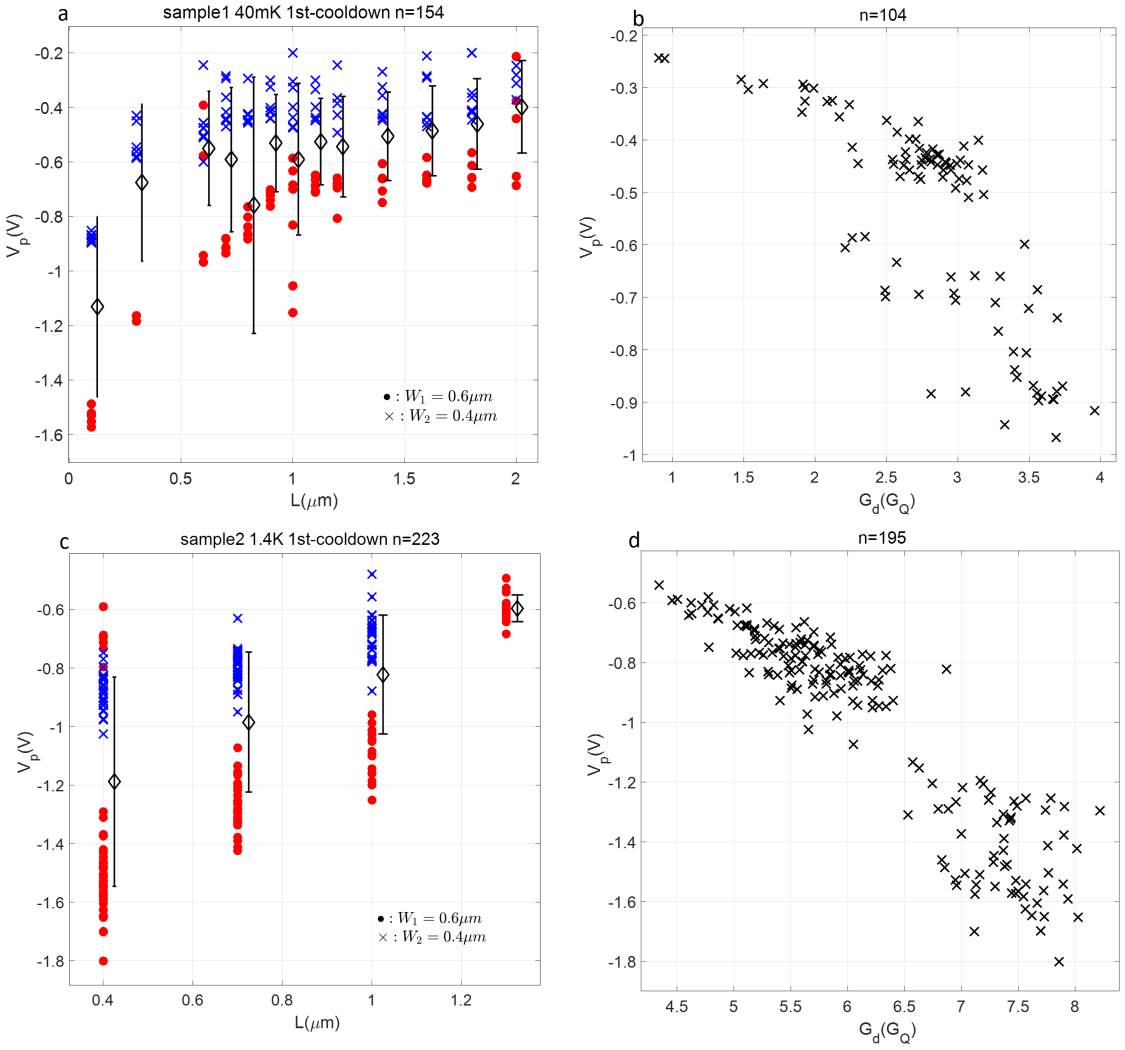

Figure 4.5: Dependences of V_p on length and G_d respectively for sample 1 at 40 mK in the first cooldown (a,b), and sample 2 at 1.4 K in the first cooldown (c,d). n counts the device number in each panel. In geometry-dependence panels (a,c), the error bar represents the mean ± standard deviation of V_p for the devices at each length, and is offset horizontally by 0.025 for clarity. The red dots and blue crosses represent the devices with width $W_1 = 0.6\mu m$ and $W_2 = 0.4\mu m$ respectively, for the geometry type 1 MUX-sample 1, 2.

4.3 Variable series resistance

For some devices in a MUX sample, we find the series resistance R_s is not the same but increases with decreasing subband index N. We acquire the variable series resistance R_s^N for the N^{th} plateau by correcting the N^{th} plateau to the integer quantised position. We call the percentage of the devices showing a variable R_s^N, $Y_{R_s^N}$, for all 1D devices in one cooldown. For instance, for 65 1D devices achieved for sample 1 at 1.4 K, there are 54 devices showing a constant R_s as shown in Fig. 4.6a, and 11 devices showing a variable R_s^N as shown in Fig. 4.6b, which gives a yield $Y_{R_s^N} = 16.92\%$. Fig. 4.6a shows the histogram of constant R_s for those 54 devices, which gives the typical value of series resistance $R_s = 5.03 \pm 3.46k\Omega$ for sample 1. The inset shows the map of constant R_s for those 54 devices. Fig. 4.6b shows the variable R_s^N as a function of subband index N for those 11 devices. The inset shows the map of $R_s^{N=1}$ for the first plateau for those 11 devices. By contrast, for 166 1D devices achieved for sample 1 at 1.4 K after illumination, there are 81 devices showing a constant R_s as shown in Fig. 4.6a, and 85 devices showing a variable R_s^N as shown in Fig. 4.6b, which gives a yield $Y_{R_s^N} = 50.89\%$. We can see $Y_{R_s^N}$ greatly increases from 16.92% to 50.89% after illumination. For the variable R_s^N for sample 1 at 40 mK before and after illumination respectively, see the Appendix Fig. A.3.

In a similar way, Fig. 4.7 shows the histogram of constant R_s, and variable R_s^N as a function of N, for sample 3 at 1.4 K in the first (a,b) and second (c,d) cooldowns respectively. For a comparison, the Appendix Fig. A.4 shows the variable R_s^N for sample 1 at 40 mK in the first and third cooldowns respectively. Appendix Fig. A.5 shows the variable R_s^N for sample 2 at 1.4 K in the first cooldown.

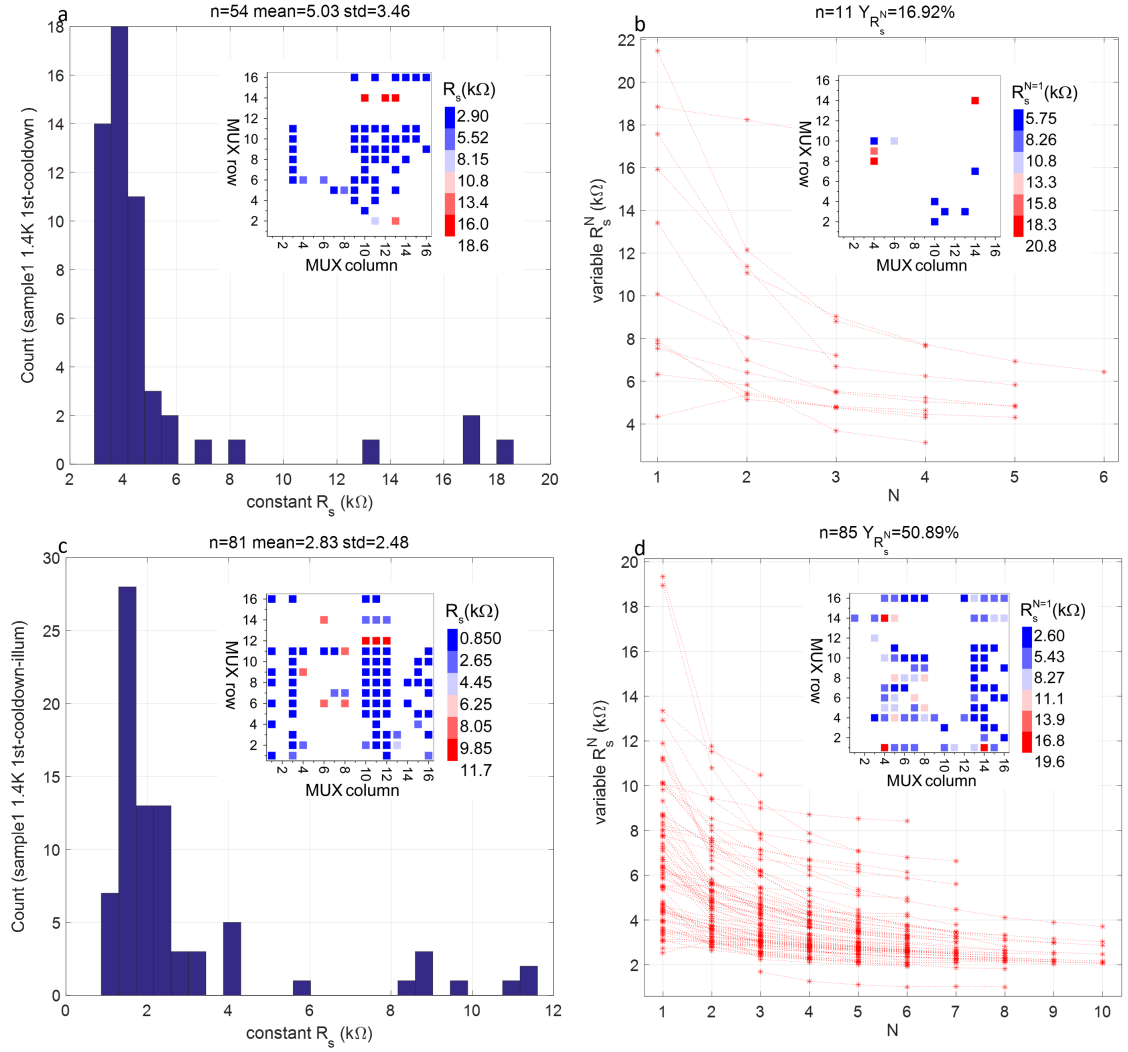

Figure 4.6: (a), Histogram of the constant series resistance R_s ($= 5.03 \pm 3.46k\Omega$) for 54 1D devices for sample 1 at 1.4 K. The inset shows the map of constant R_s for those 54 devices. (b), variable R_s^N as a function of subband index N for 11 1D devices for sample 1 at 1.4 K. The percentage of such devices $Y_{R_s^N} = 16.92\%$ in all 1D devices. The inset shows the map of $R_s^{N=1}$ for the first plateau for those 11 devices. (c), Histogram of constant R_s for 81 1D devices for sample 1 at 1.4 K after illumination. (d), variable R_s^N as a function of N for 85 1D devices for sample 1 at 1.4 K after illumination. Sample 1 has the QPC geometry with length varying from 0.1 to 2 μm at fixed width 0.4 or 0.6 μm.

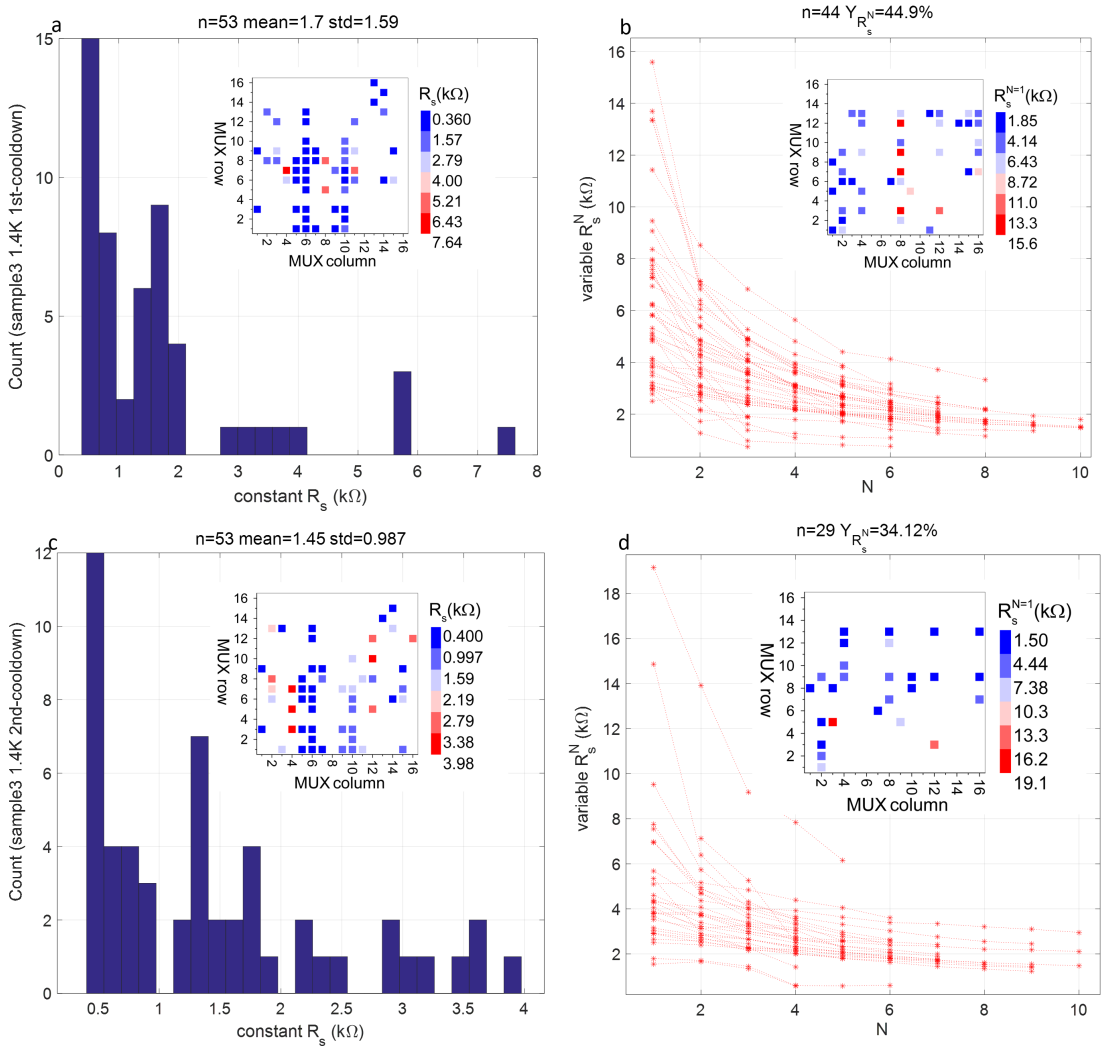

Figure 4.7: (a), Histogram of the constant series resistance R_s ($= 1.7 \pm 1.59k\Omega$) for 53 1D devices for sample 3 at 1.4 K in the first cooldown. The inset shows the map of constant R_s for those 53 devices. (b), variable R_s^N as a function of subband index N for 44 1D devices for the same cooldown with (a). The percentage of such devices $Y_{R_s^N} = 44.9\%$ in all 1D devices. The inset shows the map of $R_s^{N=1}$ for the first plateau for those 44 devices. (c), Histogram of constant R_s for 53 1D devices for sample 3 at 1.4 K in the second cooldown. (d), variable R_s^N as a function of N for 29 1D devices for the same cooldown with (c). Sample 3 has the QPC geometry with fixed length/width ratio (L/W=1, with W=0.4, 0.8, 1.2, 1.6 μm).

To explain the variable series resistance for some QPCs, it may be because that for that QPC the polyimide as arrowed in Fig. 4.8 has a bad insulation of the gate on top. The source-drain 2DEG conductance is affected by the gate voltage and decreases with decreasing V_G, which results in the increase of series resistance as a function of subband index.

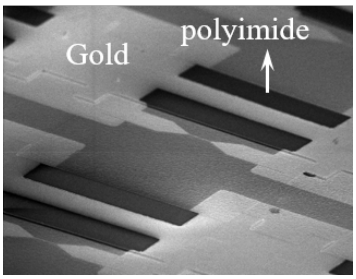

Figure 4.8: SEM image of a QPC in a multiplexer sample. The polyimide as arrowed is underneath the collumn gate.

In addition, there is also a possibility that the variable series resistance may be caused by an impurity in the channel. We propose an impurity-caused wide-narrow-wide model in Fig. 4.9. An impurity (red dot) in the channel results in a narrower QPC (with width W_i) in series with two QPCs (with width W). For a QPC showing a variable series resistance, we are indeed measuring the narrower QPC, and the series resistance measured is an sum of the 2D reservoir resistance and the resistance of two wider QPCs. As the subband index decreases, the quantised conductance of three QPCs decreases. This means the resistance of two wider QPCs increases, and the total series resistance as measured increases with decreasing subband index.

To deal with the devices showing a variable series resistance, first, to acquire the barrier curvature for the first three plateaus, the series resistance is corrected by aligning each plateau to its integer position respectively. Second, for a DC-bias spectroscopy, the drop of applied DC bias voltage on series resistance is corrected by aligning the first plateau to G_Q using Eq. 3.2, since we most care about the DC-bias-induced anomalies below the first plateau. In this way, the first subband spacing is properly acquired, but the second and third subband spacings and thus corresponding lever arms are underestimated, since a larger $R_s^{N=1}$ is used rather than $R_s^{N=2}$ ($R_s^{N=3}$) for the second (third) plateau. Third, for the effective g factor, its value relies on the individual lever arm for each subband index. Therefore, we only process normal devices that show a constant series resistance.

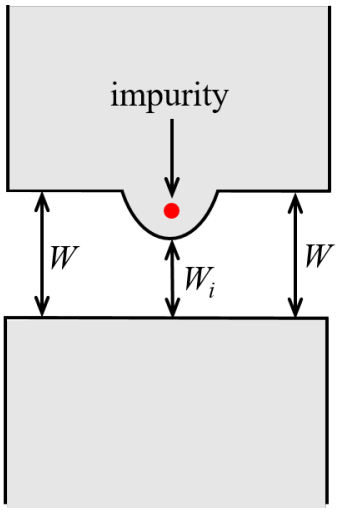

Figure 4.9: An impurity-caused wide-narrow-wide model. An impurity (red dot) happens to be in the channel, resulting in a narrower QPC (with width W_i) in series with two wider QPCs (with width W).

4.4 Potential barrier curvature

Based on Eq. 2.2, U_{eff}^{max} is governed by the product of interaction strength U and effective $LDOS_{max}$. On the one hand, $LDOS_{max}$ scales with $1/\sqrt{E_x}$ [7]. Decreasing $E_x(=\hbar\omega_x)$ can enhance $LDOS_{max}$ and thus U_{eff}^{max}. On the other hand, a stronger confinement $E_y(=\hbar\omega_y)$ decreases the transverse harmonic oscillator length l_y (smaller channel width) and causes the transverse wave functions to be more localised, which can increase U itself directly. Lunde et al. state that U scales with $1/l_y$ $(\sqrt{E_y})$ within a saddle-point potential [68]. Combining both relations, we have

$$U_{eff}^{max} \propto \sqrt{E_y/E_x} \tag{4.2}$$

U_{eff}^{max} depends on both the potential curvatures-E_x and E_y, although in different ways. In experiments, we define $U_E = E_y/E_x$ to characterise U_{eff}^{max}. To explore the interaction effects, we will investigate the statistics of E_x and E_y and how to tune them by geometry.

To get E_x, we fit the lower half step of G^0 with that of the corrected G_{SD} using Eq. 4.3:

$$G^0(\kappa, E_x, \widetilde{T}) = G_Q \int_{-50\widetilde{T}}^{50\widetilde{T}} \frac{1}{1+e^{-2\pi(\kappa+E'/E_x)}} \frac{e^{E'/\widetilde{T}}}{\widetilde{T}(1+e^{E'/\widetilde{T}})^2} dE' \tag{4.3}$$

where we integrate the Fermi distribution in Eq. 1.16 between $\pm 50\widetilde{T}$.

First, we only acquire E_x for those devices that have a good fitting of G_0 with G_{SD} to guarantee that the potential barrier is parabolic, which is a precondition of the van Hove scenario. Second, we only acquire E_x for those devices that show the 0.7 anomaly conductance suppression ($S^{0.7}$) smaller than 99%, since we are interested in the devices that show the 0.7 anomaly. The E_x^N for the first three subbands are acquired in the forward (to decrease the conductance) and backward V_G sweep directions respectively. The number of E_x^N acquired counts the number of devices that have a parabolic potential barrier and show the 0.7 anomaly for the first three plateaus respectively (called $n_{0.7}$, $n_{1.7}$, $n_{2.7}$).

Fig. 4.10a shows the statistics of E_x^N in the forward or backward sweep for the first three plateaus respectively, for sample 1-5 in 12 cool-downs at 40 mK or 1.4 K. The means of E_x^N for each plateau in total 1188 1D curves are: E_x=1.43 (1.29) meV ($E_x^{N=1}$ is abbreviated as E_x); and $E_x^{N=2}$=1.32 (1.27) meV; and $E_x^{N=3}$=1 (1.06) meV for the forward (backward) V_G sweep. The table in Fig. 4.10b records the numbers of pinch-off devices (called n_p), quantised 1D devices (called n_{1D}), and $n_{0.7}$, $n_{1.7}$, $n_{2.7}$ for each multiplexer sample in 12 cooldowns (see the legend in (a) for each cooldown information) respectively. $n_{1.7}$ and $n_{2.7}$ are less than $n_{0.7}$, showing a lower probability of showing the 0.7 anomaly for higher plateaus.

Fig. 4.11a-c provides a way to test the accuracy of fitted E_x^N, by comparing E_x^N between the forward and backward V_G sweeps for sample 1 at 1.4 K after illumination. Fig. 4.11d compares E_x between the first and third cooldowns for sample 1 at 40 mK, showing a poor repeatability. This indicates that E_x is highly influenced by the random fluctuations of electrostatic potential background when sweeping V_G, and is distinct in different cooldowns. Therefore, to investigate the role of E_x on the 0.7 anomaly, measurements should be performed in a single cooldown, which highlights the advantage of multiplexering technique.

Fig. 4.12 shows the geometry dependence of E_x^N for the first three plateaus respectively, for sample 1 (a-c) and 2 (d-f) at 1.4 K. We can see E_x^N is almost independent of length for each plateau, which is same as the results found by Smith et al. in Ref. [61]. The red dots (devices with width $W_1 = 0.6\mu m$) and blue crosses (devices with width $W_2 = 0.4\mu m$) mix together on average, showing E_x^N is also independent of width. This suggests E_x^N is dominated by the disorder-modified potential landscape and is hardly tunable by geometry. For more evidences, see the geometry dependence of E_x for sample 1 at 40 mK, and sample 3, 4 at 1.4 K in Appendix Fig. A.6.

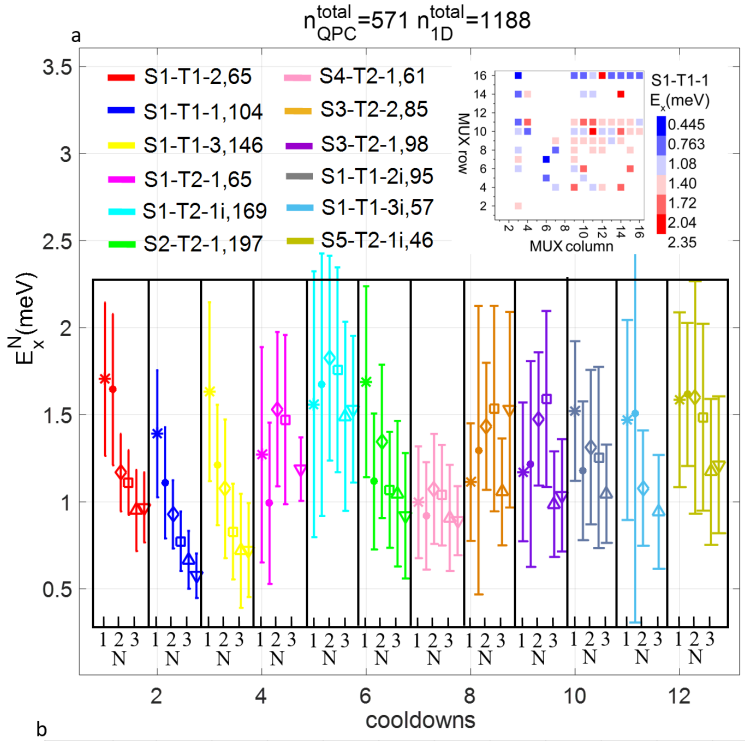

cool-down	1	2	3	4	5	6	7	8	9	10	11	12
n_p	93	154	174	135	203	223	101	85	98	181	176	48
n_{1D}	65	104	146	65	169	197	61	85	98	95	57	46
$n_{0.7}$	54	62	65	47	81	135	54	66	74	65	33	31
$n_{1.7}$	18	37	60	28	79	87	37	45	43	60	33	30
$n_{2.7}$	16	15	29	3	74	40	13	12	15	37	15	16

Figure 4.10: (a), Statistics of E_x^N for the first three plateaus for MUX sample 1-5 in 12 cooldowns at 40 mK or 1.4 K (in the order of decreasing V_d^{mean}). In the legend, for instance, the symbol 'S1-T1-2, 65' refers to sample 1-at 40 mK-in the 2^{nd} cooldown in the dark-with n_{1D} =65 1D devices. The symbol 'S1-T2-1i, 169' refers to sample 1-at 1.4 K-in the 1^{st} cooldown after illumination-with 169 1D devices. In 12 cooldowns, the measurements before and after illumination respectively in the same cooldown are counted as two cooldowns, like the 1st and 10th cooldowns ('S1-T1-2' and 'S1-T1-2i' in the legend). We measured a maximum of $n^{total}_{QPC} = 571$ 1D QPCs at 1.4 K: 169, 197, 98, 61 and 46 for MUX sample 1-5 respectively. In total, 1188 1D curves have been measured ($n^{total}_{1D} = 1188$ is the sum of n_{1D} in 12 cooldowns). In the sub-plot for each cooldown, the error-bars in the same colour show the statistics of E_x^N as a function of N in the forward sweep. Statistics of E_x^N in the backward sweep are plotted together, all offset rightward by 0.5. The E_x map for the first plateau is shown at the top-right for sample 1 at 40 mK in the first cooldown. (b), The numbers of pinch-off devices (n_p), quantised 1D devices (n_{1D}), and $n_{0.7}$, $n_{1.7}$, $n_{2.7}$ for MUX sample 1-5 in 12 cooldowns respectively for the forward V_G sweep. $n_{0.7}$, $n_{1.7}$, and $n_{2.7}$ count 1D devices that have a parabolic potential barrier and show the 0.7 anomaly for the first three plateaus respectively.

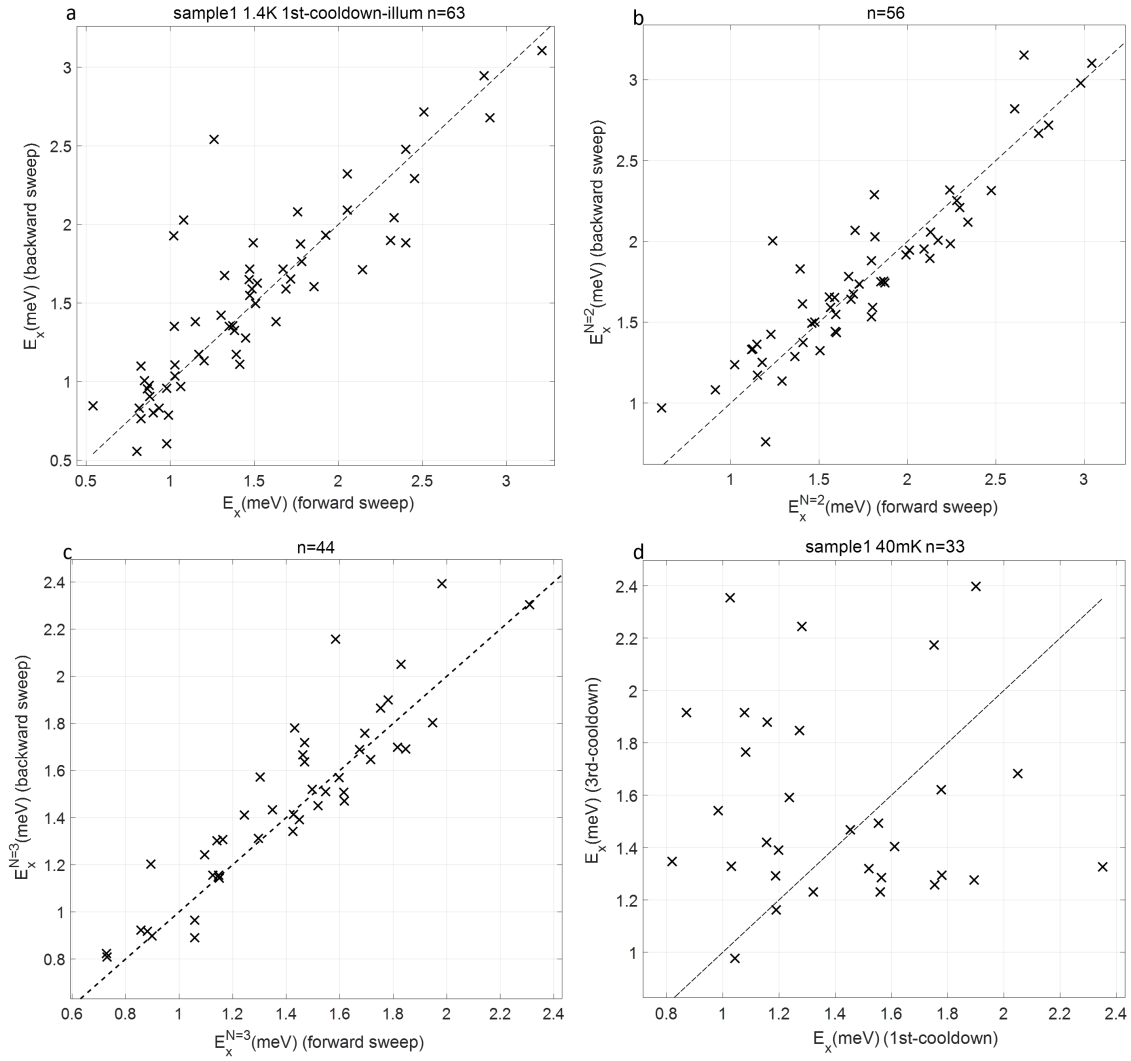

Figure 4.11: (a-c), Scatter plots of E_x^N between the forward (X axis) and backward (Y axis) V_G sweeps for the first three plateaus respectively, for sample 1 at 1.4 K after illumination. (d), Scatter plot of E_x between the first (X axis) and third (Y axis) cooldowns for sample 1 at 40 mK. In each panel, n counts the device number. The dashed line (gradient=1) provides a guide to eye.

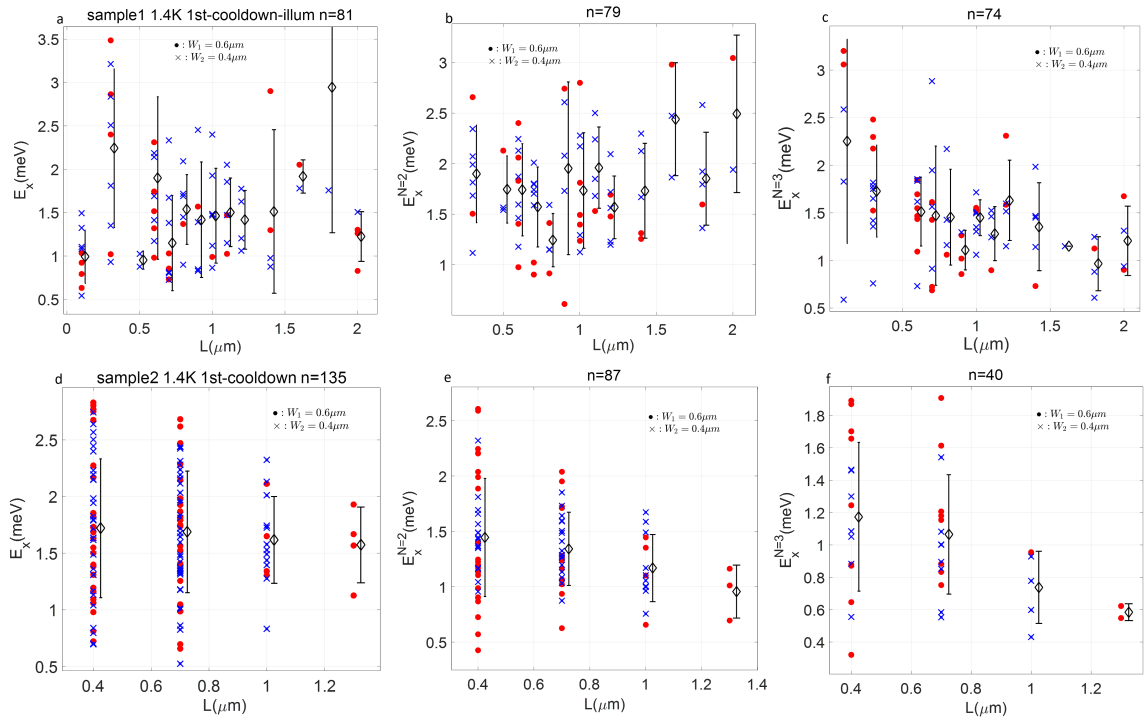

Figure 4.12: Geometry dependence of E_x^N for the first three plateaus respectively, for sample 1 (a-c) and 2 (d-f) at 1.4 K. In each panel, n counts the device number. The red dots and blue crosses represent devices with width $W_1 = 0.6\mu m$ and $W_2 = 0.4\mu m$ respectively. The error bar represents the mean ± standard deviation for the devices at each length, offset horizontally by 0.025 for clarity. E_x^N is hardly correlated with geometry.

4.5 Potential confinement curvature

With regard to the potential confinement curvature $E_y(=\hbar\omega_y)$, it is equal to the subband spacing for a parabolic confinement. Fig. 4.13a,b shows the DC bias spectroscopy before (a) and after (b) illumination respectively for a device D(10,11), sample 1 at 40 mK. The drop of applied DC bias voltage on series resistance is corrected using Eq. 3.2. The first three subband spacings ($\Delta E_{N,N+1}$) and corresponding lever arms ($\alpha_{N,N+1}$) are acquird as marked. $\Delta E_{N,N+1}$ greatly increase after illumination. Fig. 4.13c,d shows the statistics of the first three subband spacings (c) and lever arms (d) in 9 cooldowns at 40 mK or 1.4 K, in the order of decreasing V_d^{mean}. In Fig. 4.13c, the cooldowns with a more negative V_d^{mean} (which means a higher carrier density n_{2D}) tend to have larger subband spacings. In particular, the 8th and 9th cooldowns are after illumination, and have the largest means of $\Delta E_{N,N+1}$. The map of $\Delta E_{1,2}$ is shown at the top-right, for sample 1 at 1.4 K in the first cooldown after illumination. In addition, both $\Delta E_{N,N+1}$ and $\alpha_{N,N+1}$ decrease as N increases, implying the potential confinement is not a perfect parabolic.

Fig. 4.14a-c shows scatter plots of $\Delta E_{N,N+1}$ between the first and second cooldowns for sample 1 at 40 mK, for the first three subband spacings respectively. A repetitive trend exhibits for each plateau, which is different from that for E_x. Fig. 4.14d-f shows scatter plots of $\Delta E_{N,N+1}$ between before and after illumination for sample 1 at 40 mK in the second cooldown. All the subband spacings are almost double after illumination. Thus, illumination results in a stronger confinement, which can effectively amplify the interaction strength U and therefore U_{eff}^{max} according to Eq. 2.2.

Considering how to tune E_y by geometry, in Fig. 4.15, Koop et al. calculate E_y as a function of length and width respectively. Qualitatively, E_y is negatively correlated with both length and width, so short and narrow QPCs yield the strongest confinement. Quantitatively, Koop et al. state that the calculated values are significantly larger than the experimental values because of the type of calculations they used. In Fig. 4.15b, E_y has a maximum at $W \approx 3d$ (d is the depth of 2DEG beneath the wafer surface, which is 90 nm for our case) [5].

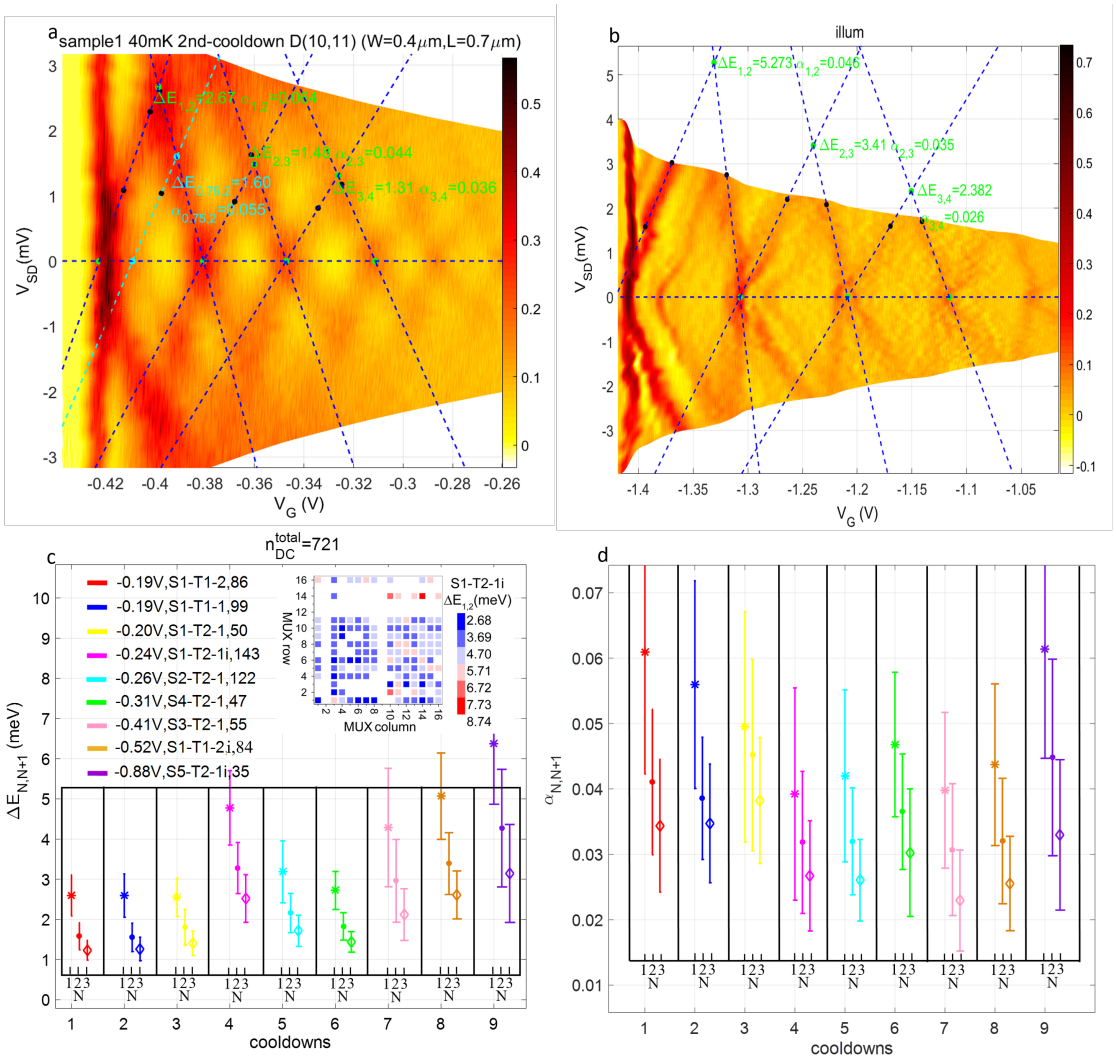

Figure 4.13: (a,b), DC bias spectroscopy with $\Delta E_{N,N+1}$ and $\alpha_{N,N+1}$ as marked before (a) and after (b) illumination for D(10,11), sample 1 at 40 mK. The DC-bias-induced 0.75 anomaly marked with the cyan dashed line will be discussed in Chapter 7. (c,d), Statistics of $\Delta E_{N,N+1}$ (c) and $\alpha_{N,N+1}$ (d) in 9 cooldowns at 40 mK or 1.4 K in the order of decreasing V_d^{mean}. In (c), in the sub-plot for each cool-down, the error-bars in the same colour show the statistics of $\Delta E_{N,N+1}$ as a function of N. The map of $\Delta E_{1,2}$ is shown at the top-right, for sample 1 at 1.4 K in the first cooldown after illumination. In the legend, for instance, the symbol '-0.19V, S1-T1-2, 86' refers to 'mean definition voltage V_d^{mean}=-0.19 V, for sample 1-at 40 mK-in the 2^{nd} cooldown in the dark, with n_{DC}=86 DC-bias spectroscopies'. The symbol '-0.24V, S1-T2-1i, 143' refers to 'V_d^{mean}=-0.24 V, for sample 1-at 1.4 K-in the 1^{st} cooldown after illumination, with n_{DC}=143 DC-bias spectroscopies'. Total n_{DC}^{total}=721 spectroscopies (sum of n_{DC}) have been acquired in 9 cooldowns.

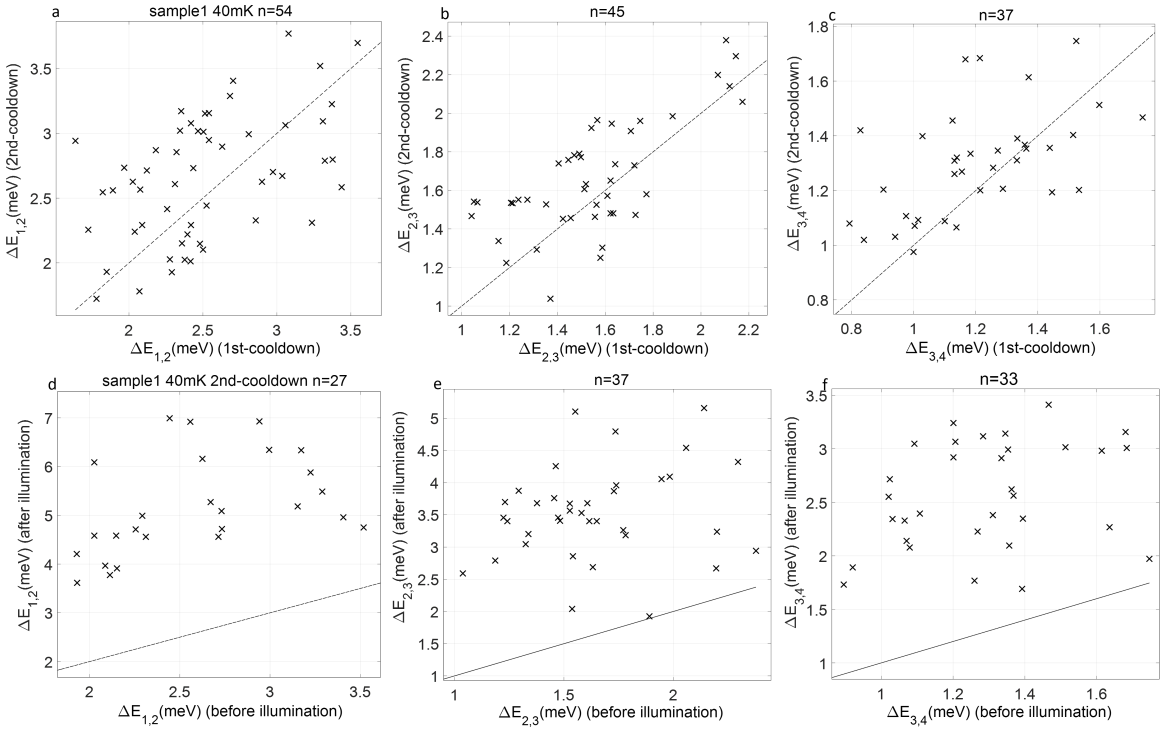

Figure 4.14: (a-c), Scatter plots of $\Delta E_{N,N+1}$ between the first (X axis) and second (Y axis) cooldowns for sample 1 at 40 mK, for the first three subband spacings respectively. (d-f), Scatter plots of $\Delta E_{N,N+1}$ between before (X axis) and after (Y axis) illumination for sample 1 at 40 mK in the second cooldown, for the first three subband spacings respectively. In each panel, n counts the device number. The dashed line (gradient=1) provides a guide to eye.

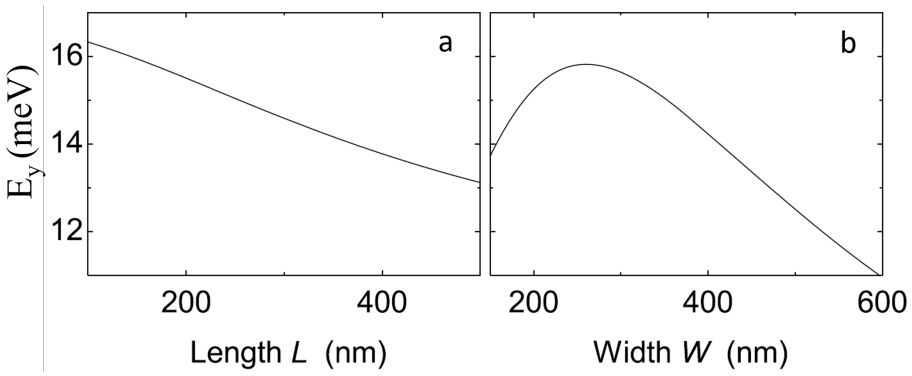

Figure 4.15: Calculated E_y as a function of length (a) and width (b), based on an electrostatic modelling of a saddle-point potential. Adapted from Ref. [5].

Fig. 4.16 shows the geometry dependence of $\Delta E_{N,N+1}$ for type-1 MUX sample 1 and 2 at 1.4 K. For length dependence, the mean $\Delta E_{N,N+1}$ has a weak negative correlation with length. For width dependence, the red dots (devices with width 0.6 μm) tend to be below the blue crosses (devices with width 0.4 μm), indicating a larger width could result in smaller E_y. In a word, E_y is negatively correlated with both length and width respectively, which accords with the calculations in Fig. 4.15. Unlike E_x which is difficult to adjust, E_y can be adjusted to some extent by geometry. In this way, we can realise the control of U_{eff}^{max}. Appendix Fig. A.7 shows the cases for type 2 MUX sample 3 and 4 at 1.4 K.

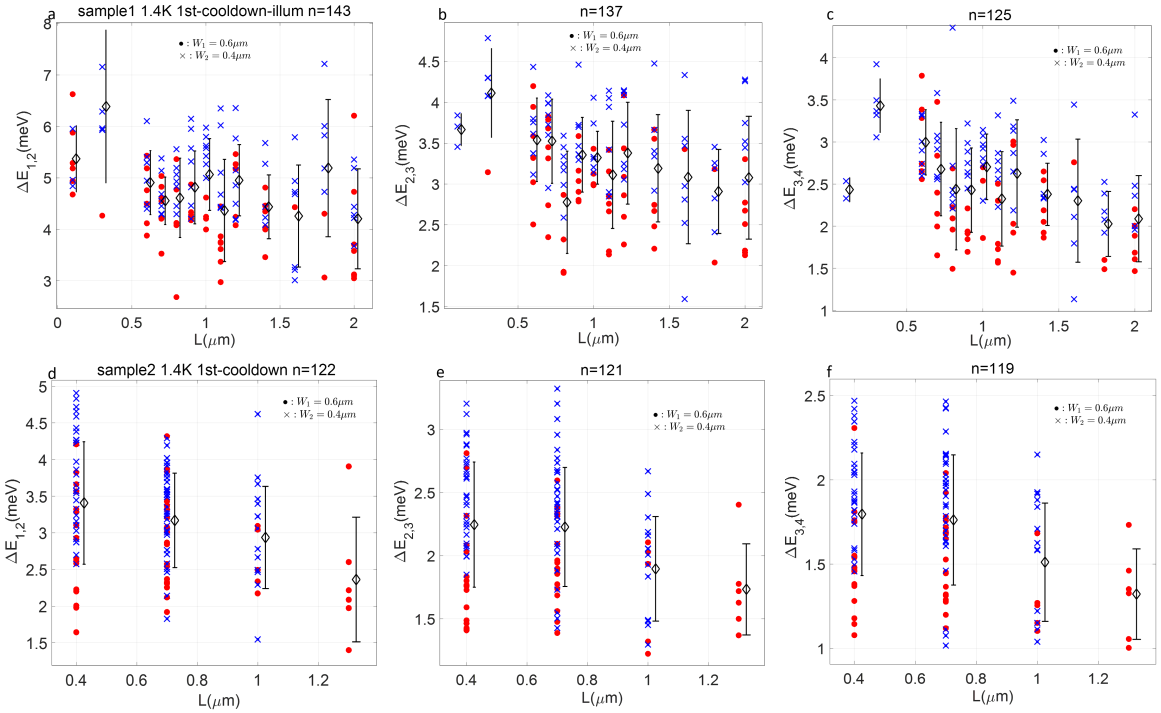

Figure 4.16: Geometry dependence of $\Delta E_{N,N+1}$ for type-1 MUX sample 1 (a-c) and 2 (d-f) at 1.4 K respectively. In each panel, n counts the device number. The red dots and blue crosses represent devices with width $W_1 = 0.6\mu m$ and $W_2 = 0.4\mu m$ respectively. The error bar represents the mean ± standard deviation for the devices at each length, offset horizontally by 0.025 for clarity. $\Delta E_{N,N+1}$ is negatively correlated with both length and width respectively.

Furthermore, it is meaningful to discuss the geometry dependence of lever arm, since lever arm is an important factor to convert V_G to κ in Eq. 1.15, also to process the g^*. Fig. 4.17 shows the geometry dependence of lever arm $\alpha_{N,N+1}$ for the first three plateaus respectively, for sample 1 (a-c) and 2 (d-f) at 1.4 K. In each panel, it is interesting to see most red dots (devices with width 0.6 μm) are below blue crosses (devices with width 0.4 μm) for each length, indicating the devices with a larger width have a relatively lower ability to change the potential energy by sweeping V_G. By contrast, $\alpha_{N,N+1}$ seems to be independent of length. Thus, the geometric origin of lever arm seems to be the width. For cases for sample 3 and 4 at 1.4 K, see the Appendix Fig. A.8.

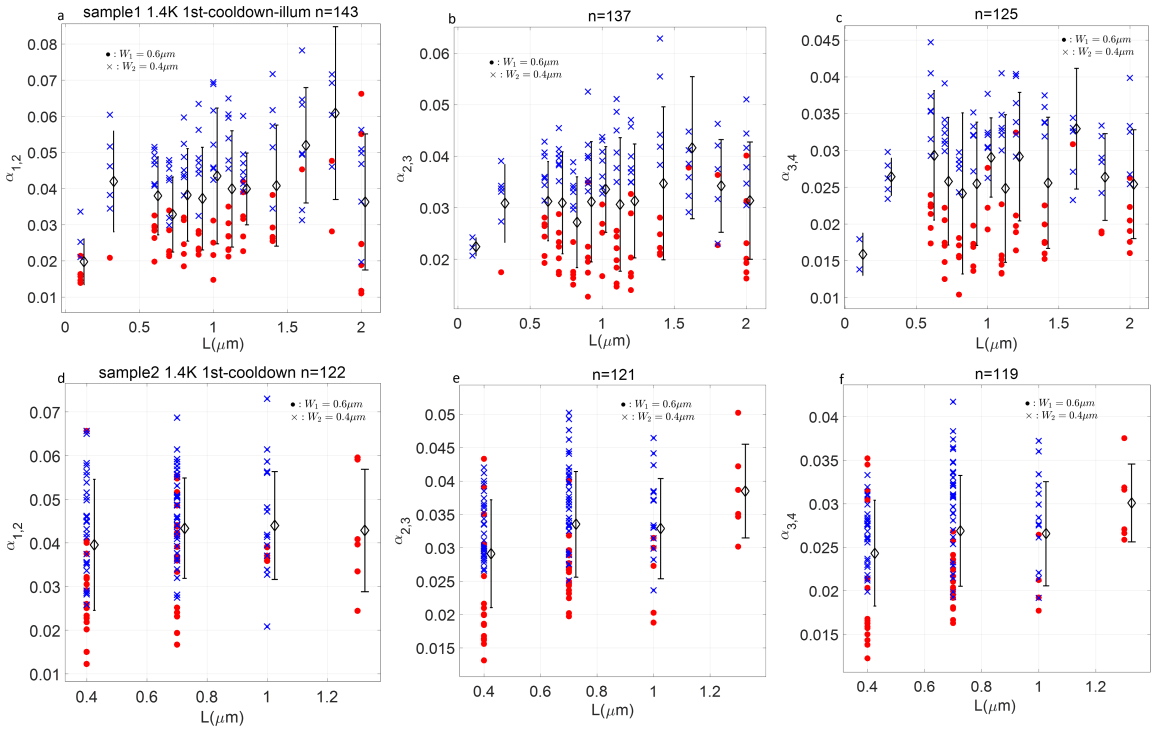

Figure 4.17: Geometry dependence of $\alpha_{N,N+1}$ for sample 1 (a-c) and 2 (d-f) at 1.4 K. In each panel, n counts the device number. The red dots and blue crosses represent devices with width $W_1 = 0.6\mu m$ and $W_2 = 0.4\mu m$ respectively. The error bar represents the mean $\pm$ standard deviation for the devices at each length, offset horizontally by 0.025 for clarity. A larger width could result in smaller $\alpha_{N,N+1}$.

4.6 Two definitions of the 0.7 anomaly

Based on Eq. 3.26 (though treated only to first order) in Ref. [6], $1-U_{eff}$ is equal to differential of the effective Hartree barrier height ($\widetilde{V}_c^h$) with respect to the bare central barrier height $\widetilde{V}_c$:

$$1-U_{eff}=\frac{d\widetilde{V}_c^h}{d\widetilde{V}_c} \tag{4.4}$$

Then we can deduce

$$1-U_{eff}(\kappa)=\frac{d\widetilde{V}_c^h}{d\widetilde{V}_c}=\frac{d\kappa^h}{d\kappa}=\frac{dG_{SD}/d\kappa}{dG_{SD}/d\kappa^h}\approx\frac{dG_{SD}/d\kappa}{dG^0/d\kappa}=\frac{TC_{SD}}{TC^0}=S_{TC}(\kappa) \tag{4.5}$$

where the source-drain transconductance $TC_{SD}=dG_{SD}/d\kappa$ (TC_{SD} is acquired by the differential of smoothed G_{SD}, since differential will greatly amplify any little oscillations); and the non-interacting transconductance $TC^0=dG^0/d\kappa$; and the transconductance suppression $S_{TC}(\kappa)$ is the ratio of $TC_{SD}(\kappa)$ with $TC^0(\kappa)$.

Eq. 4.5 directly links the effective interaction strength $U_{eff}(\kappa)=U\cdot LDOS(\kappa)$ with $S_{TC}(\kappa)$. We can use '1-$S_{TC}(\kappa)$' to mimic the effective LDOS shape $LDOS(\kappa)$ approximately.

According to Eqs. 2.2 and 4.5, due to the strongest effect of U_{eff}^{max} at the $LDOS_{max}$ of van Hove ridge, S_{TC} will be strongest and has the minimum value (we say the suppression is stronger at a lower value). Thus, we can define the 0.7 anomaly related with the transconductance: the strongest S_{TC} is defined as 'the 0.7 anomaly transconductance suppression' ($S_{TC}^{0.7}$), and the κ position and conductance of $S_{TC}^{0.7}$ is defined as $\kappa_{TC}^{0.7}$ and $G_{TC}^{0.7}$ respectively.

$$1-U\cdot LDOS_{max}=1-U_{eff}^{max}\approx S_{TC}^{0.7} \tag{4.6}$$

We can see the 0.7 anomaly is directly caused by the strongest U_{eff}^{max}. Thus, U_{eff}^{max} can be characterised by '1-$S_{TC}^{0.7}$'. The κ position of $LDOS_{max}$- $\kappa_{LDOS_{max}}$ should be the same as $\kappa_{TC}^{0.7}$.

In a similar manner, for the conductance suppression $S_G(\kappa)=G_{SD}/G^0$, there is also a strongest S_G during sweeping κ. We can also define the 0.7 anomaly related with S_G, although this is a phenomenological definition. The κ position and conductance at the minimum of S_G are defined as $\kappa^{0.7}$ and $G^{0.7}$ respectively. To consider an overall suppression of conductance, we define 'the 0.7 anomaly conductance suppression' ($S^{0.7}$) as the ratio of two areas beneath G_{SD} and G^0 curves respectively, across the whole part of positive κ.

Fig. 4.18a shows representative curves of $S_G(\kappa)$ and $S_{TC}(\kappa)$, for a device D(16,15), sample 1 at 40 mK. It is interesting to see that the 0.7 anomaly has already developed at a temperature as low as 40 mK, which indicates U_{eff}^{max} still plays a role at 40 mK. This is same as the previous measurements shown in Fig. 2.1 that the 0.7 anomaly exists at 50 and 70 mK in Fig. 2.1a,b respectively. There is also a possibility that the 0.7 anomaly suppression at 40 mK is caused by a large ac excitation voltage 0.1 mV we use. In Ref. [7], Bauer et al. state a larger source-drain voltage results in a stronger 0.7 anomaly suppression. The ac excitation energy 0.1 meV we use is much larger than the thermal energy of 40 mK, which may reinforce the 0.7 anomaly suppression.

The 0.7 anomaly has a special temperature behaviour that it becomes more pronounced as the temperature increases. Bauer et al. state that the higher thermal energy results in the stronger conductance suppression with a quadratic relation [7]. Fig. 4.18b compares $S_{TC}(\kappa)$ curves for the same device at 40 mK and 1.4 K, both before and after illumination respectively. S_{TC} at 1.4 K is stronger than that at 40 mK, which accords with the model prediction. Furthermore, S_{TC} becomes stronger after illumination at both temperatures, since illumination increases E_y but not E_x, thus resulting in larger U_{eff}^{max}. In fact, illumination has a similar effect with applying a positive top gate voltage in Ref. [7], since both methods could increase U_{eff}^{max} by increasing E_y. With regard to the conductance suppression S_G, the stronger $S_{TC}^{0.7}$, the stronger $S^{0.7}$, and $\kappa^{0.7}$ is larger than $\kappa_{TC}^{0.7}$ for each cooldown. This implies the origin of S_G is S_{TC}.

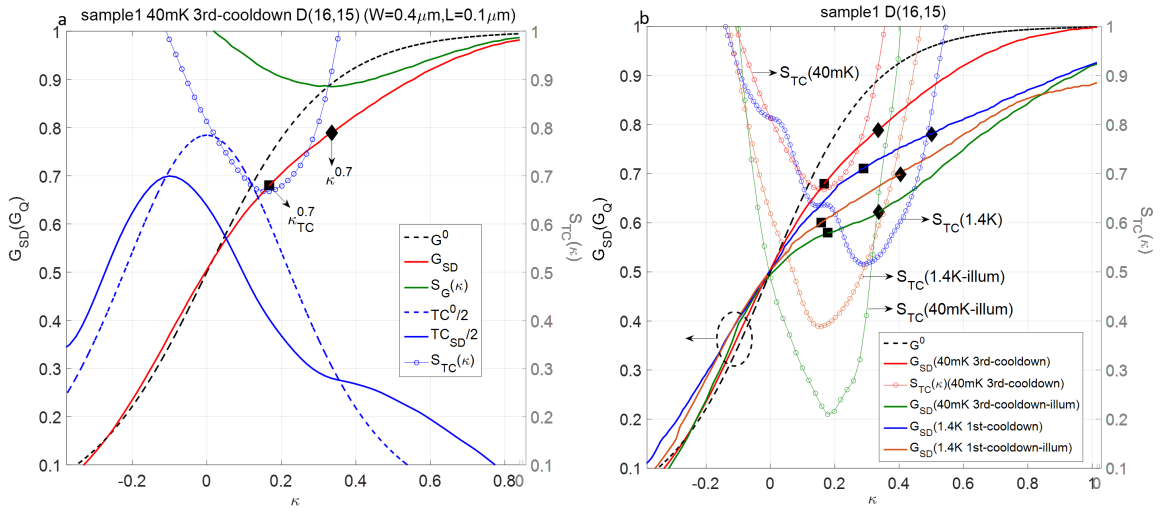

Figure 4.18: (a) Representative curves of $S_G(\kappa) = G_{SD}/G^0$ and $S_{TC}(\kappa) = TC_{SD}/TC^0$ for a device D(16,15), sample 1 at 40 mK. V_G axis is transformed into κ using Eq. 1.15. For S_G, TC^0, TC_{SD} and S_{TC} curves, read the right axis. The $\kappa^{0.7}$ and $\kappa^{0.7}_{TC}$ positions are marked with diamonds and squares respectively in G_{SD} curve. (b) Comparisons of $S_{TC}(\kappa)$ curves (circle-marked) for the same device at 40 mK and 1.4 K, before and after illumination respectively. S_{TC} is stronger after illumination than before illumination, at both 40 mK and 1.4 K respectively.

In fact, the role of E_x on the conductance and transconductance suppressions already exist in the non-interacting regime. Fig. 4.19 shows the non-interacting calculations at 1.4 K using the Landauer-Buttiker formula Eq. 4.3. Both S_G^0 in Fig. 4.19a, and S_{TC}^0 in Fig. 4.19b become stronger with decreasing E_x.

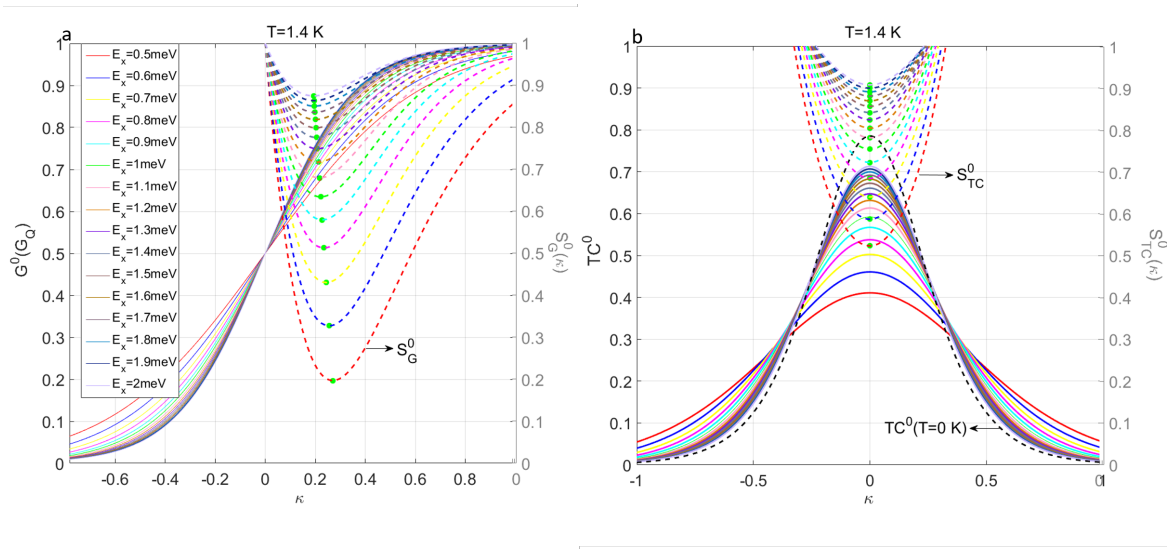

Figure 4.19: Non-interacting effects of E_x on S_G^0 (a) and S_{TC}^0 (b) at 1.4 K. In (a), as E_x decreases, S_G^0 (dashed lines) becomes stronger, at larger $\kappa_{0.7}^0$ (marked with green dots) and smaller $G_{0.7}^0$. In (b), as E_x decreases, S_{TC}^0 (dashed lines) also becomes stronger with smaller $S_{TC}^{0.7,0}$ (marked with green dots). The black dashed line represents TC^0 at 0 K for a reference. The typical $S_{TC}^{0.7,0}$=0.75 for E_x=1 meV.

4.7 Statistics of the 0.7 anomaly suppressions

With regard to the higher plateau case, Fig. 4.20a compares S_{TC} curves for the first three plateaus for a device D(8,3), sample 1 at 40 mK. Compared with $S_{TC}^{N=1}$, $S_{TC}^{N=2}$ is weaker and $S_{TC}^{N=3}$ is much weaker for the higher plateaus. This is because the screening almost limits the interactions in the first three 1D subbands only. As the channel becomes wider, the density increases in each sub-open regime, and U_{eff}^{max} drops almost to zero for the third plateau. Fig. 4.20b-d shows the statistics of $S_{TC}^{0.7,N}$, $\kappa_{TC}^{0.7,N}$, and $G_{TC}^{0.7,N}$ in 12 cooldowns at 40 mK or 1.4 K. In Fig. 4.20b, $S_{TC}^{0.7}$ is stronger than $S_{TC}^{1.7}$ and $S_{TC}^{2.7}$ in each cooldown, confirming that the suppression is strongest for the first plateau. $S_{TC}^{0.7,N}$ tends to be stronger in the cooldowns after illumination. In Fig. 4.20c, three plateaus have similar positions of $\kappa_{TC}^{0.7,N}$. This is because the 0.7 anomaly originates from similar LDOS shapes for each plateau respectively.

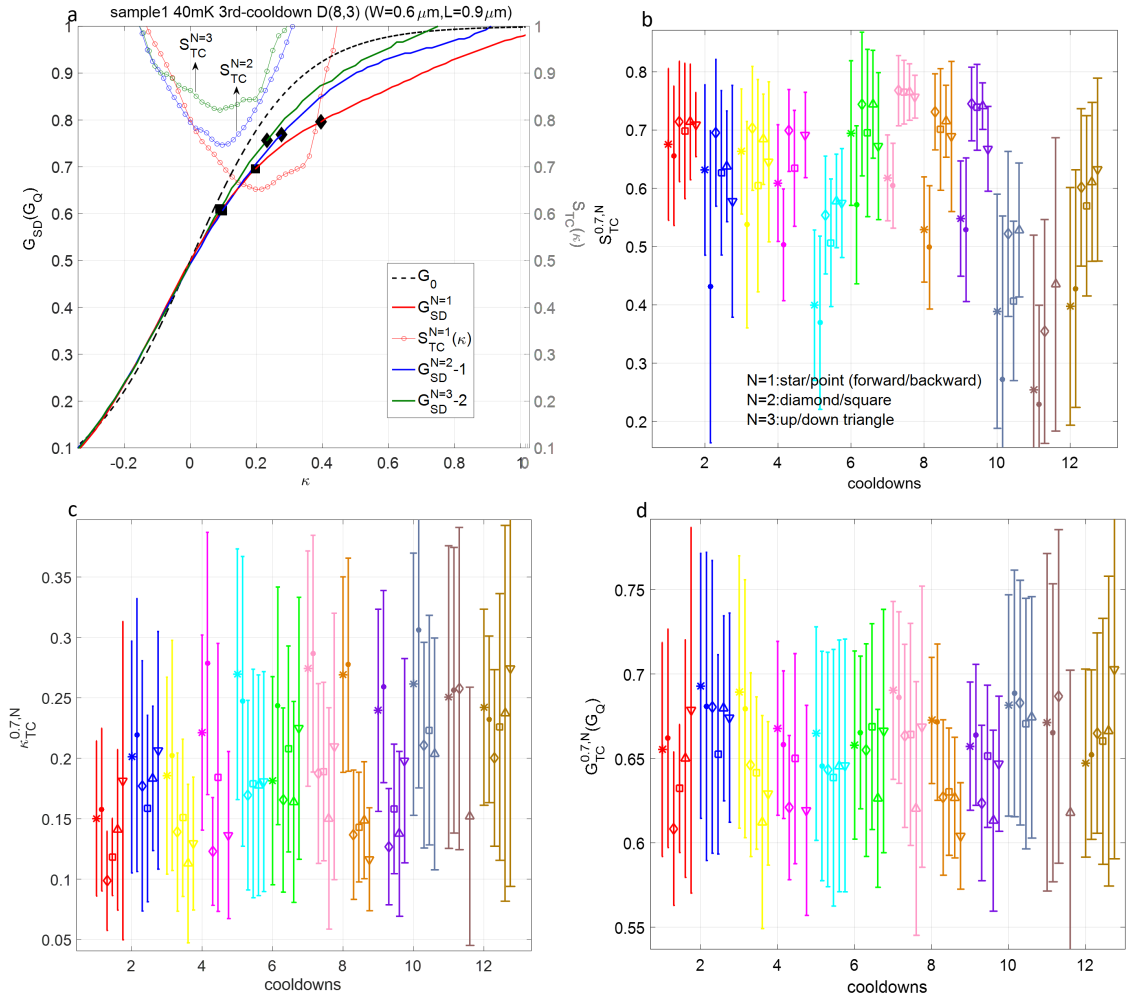

Figure 4.20: (a), Comparisons of $S_{TC}(\kappa)$ curves for the first three plateaus for a device D(8,3), sample 1 at 40 mK. S_{TC} is weak for the higher plateaus ($G_{SD}^{N=2}$ and $G_{SD}^{N=3}$ are vertically offset to the first plateau position). (b-d), Statistics of $S_{TC}^{0.7,N}$ (b), $\kappa_{TC}^{0.7,N}$ (c), and $G_{TC}^{0.7,N}$ (d) for the first three plateaus in 12 cooldowns at 40 mK or 1.4 K. For 12 cooldown information, read the legend in Fig. 4.10. The error bars for the forward or backward V_G sweep are plotted in the same way as Fig. 4.10. In (d), $G_{TC}^{1.7}$ and $G_{TC}^{2.7}$ are offset to the first plateau position.

Next, Fig. 4.21 shows scatter plots of $S_{TC}^{0.7,N}$, $\kappa_{TC}^{0.7,N}$ and $G_{TC}^{0.7,N}$ between the forward and backward V_G sweeps, for sample 1 at 1.4 K in the first (a-c) and second (d-f) plateaus respectively. The good repetitions demonstrate that our definitions of the transconductance 0.7 anomaly are reliable.

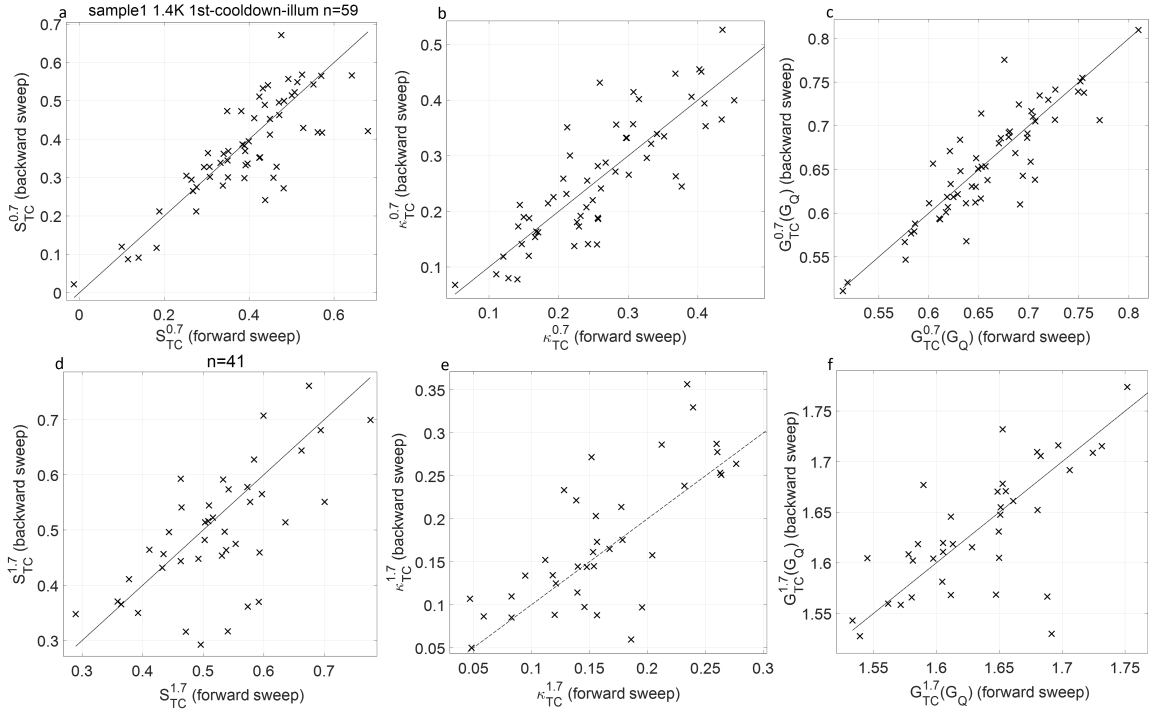

Figure 4.21: Scatter plots of $S_{TC}^{0.7,N}$, $\kappa_{TC}^{0.7,N}$, and $G_{TC}^{0.7,N}$ between the forward and backward V_G sweeps, for sample 1 at 1.4 K in the first (a-c) and second (d-f) plateaus respectively, showing reliable repetitions of our 0.7 anomaly definitions in terms of transconductance. In each panel, n counts the device number. The dashed line (gradient=1) provides a guide to eye.

In a more straightforward way, Fig. 4.22a-c shows statistics of the 0.7 anomaly in terms of conductance-$S^{0.7,N}$, $\kappa^{0.7,N}$, and $G^{0.7,N}$ respectively in those 12 cooldowns. In Fig. 4.22c, it is understandable that $S^{0.7}$ is significantly stronger than $S^{1.7}$ and $S^{2.7}$. $S^{1.7}$ and $S^{2.7}$ are also quite weak. For a comparison, Fig. 4.22d-f compares the statistics of $S^{0.7}$, $\kappa^{0.7}$, $G^{0.7}$ (star-marked error bars), with $S^{0.7}_{TC}$, $\kappa^{0.7}_{TC}$, $G^{0.7}_{TC}$ (diamond-marked error bars) respectively, for the first plateau.

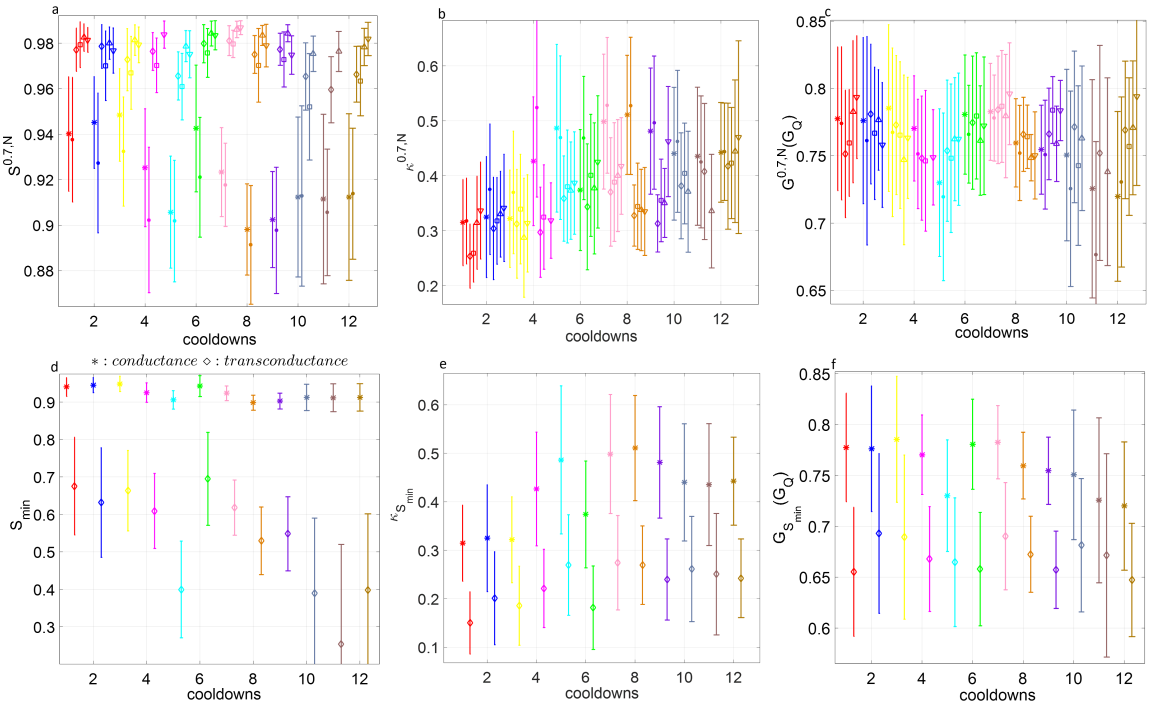

Figure 4.22: (a-c), Statistics of $S^{0.7,N}$ (a), $\kappa^{0.7,N}$ (b), and $G^{0.7,N}$ (c) in 12 cooldowns. (d-f), Comparisons of $S^{0.7}$ (d), $\kappa^{0.7}$ (e), $G^{0.7}$ (f), with $S^{0.7}_{TC}$, $\kappa^{0.7}_{TC}$, $G^{0.7}_{TC}$ respectively, for the first plateau. The 0.7 anomaly definitions in terms of conductance and transconductance are marked with stars and diamonds respectively.

Moreover, Fig. 4.23 compares the 0.7 anomaly definitions in terms of conductance with those in terms of transconductance, for sample 1 at 1.4 K for the first three plateaus respectively. In Fig. 4.23a,d,g, the devices with stronger $S_{TC}^{0.7,N}$ also have stronger $S^{0.7,N}$ for the first three plateaus respectively, which makes it clear that $S_G(\kappa)$ is a result of $S_{TC}(\kappa)$. In Fig. 4.23b,e,h, $\kappa^{0.7,N}$ follows $\kappa_{TC}^{0.7,N}$ at larger values, resulting in larger $G^{0.7,N}$ than $G_{TC}^{0.7,N}$ as shown in Fig. 4.23c,f,i.

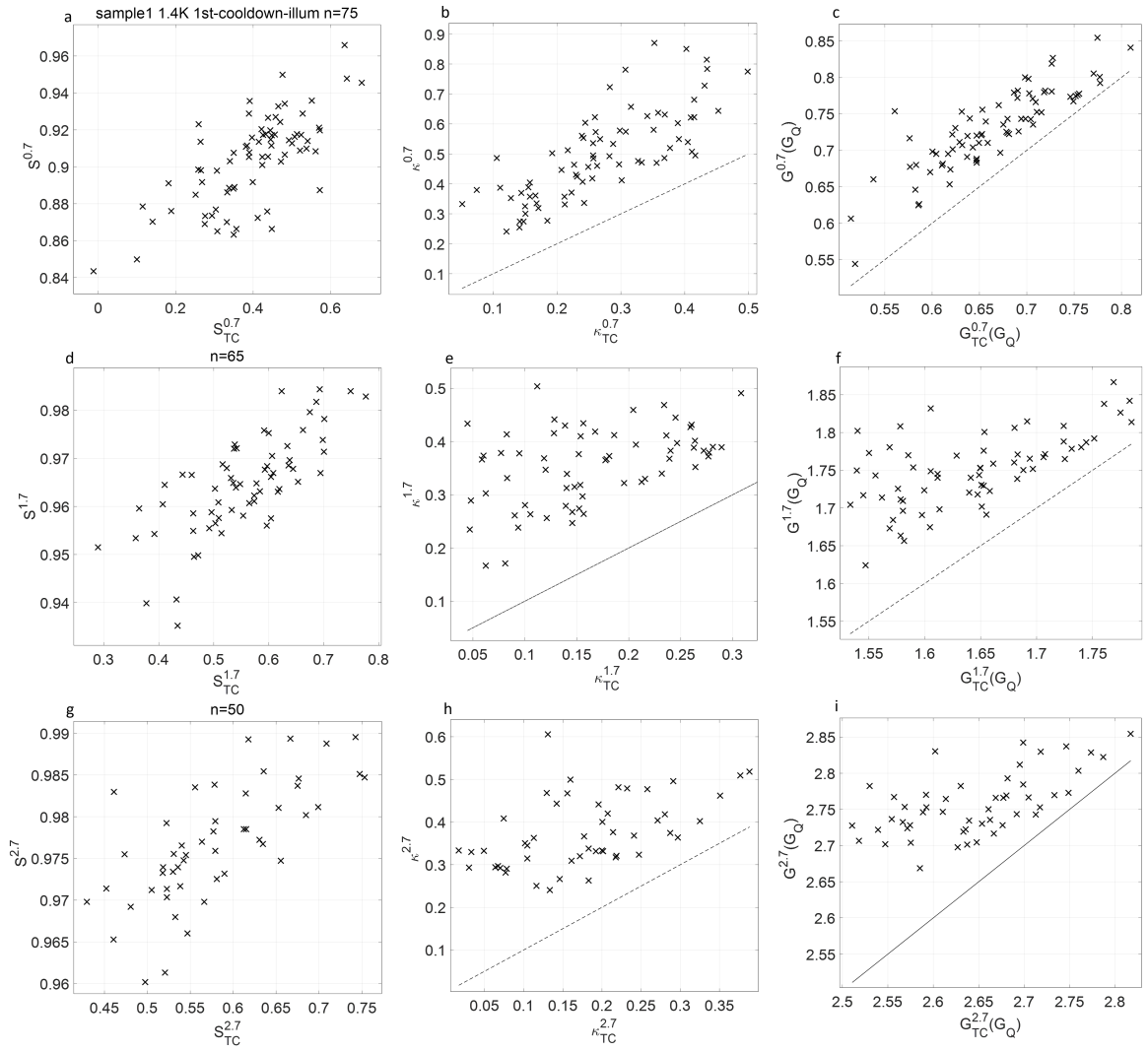

Figure 4.23: Scatter plots of $S^{0.7,N}$, $\kappa^{0.7,N}$, $G_{TC}^{0.7,N}$, with $S_{TC}^{0.7,N}$, $\kappa_{TC}^{0.7,N}$, $G^{0.7,N}$, for sample 1 at 1.4 K for the first three plateaus respectively. In each panel, n counts the device number. The dashed line (gradient=1) provides a guide to eye.

4.8 The role of effective LDOS

Here, we discuss how E_x influences S_{TC} by modifying the $LDOS$ in experiments. With regard to the $LDOS$, in Fig. 4.24a, Heyder et al. provide the analytic non-interacting $LDOS^0$ as a function of the longitudinal position, for a parabolic barrier at the chemical potential in the barrier centre [6]. Fig. 4.24b shows the analytic $LDOS^0$ shape as a function of the barrier height (i.e. κ for our symbol). The van-Hove singularity of a homogeneous system is smeared and shifted by the inhomogeneous barrier, forming the ridge-like $LDOS^0$. In particular, $LDOS^0_{max}$ scales with $1/\sqrt{E_x}$, and is shifted to analytic $\kappa^0_{LDOS_{max}} \approx 0.2$, as shown in Fig.4.24b. In Fig.4.24c-e, Heyder et al. show calculated $LDOS^0$ in a realistic model. In Fig.4.24d, $\kappa^0_{LDOS_{max}} \approx 0.28$.

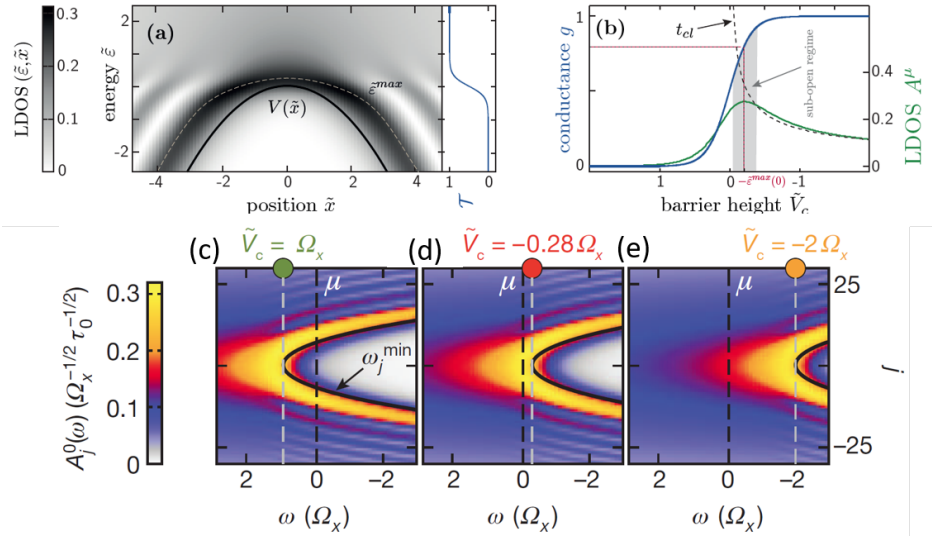

Figure 4.24: (a-b), Analytic $LDOS^0$ as a function of the longitudinal position (a) and κ (b) respectively. (c-e), Calculated $LDOS^0$ in a realistic model. Ω_x is E_x, and $-\widetilde{V}_c/\Omega_x$ is κ for our symbols. Adapted from Refs. [6, 7].

In reality, $LDOS^0$ and interaction strength U affect each other in an iterative way, forming the effective $LDOS$ and U_{eff}. In Fig. 4.25, Heyder et al. show the interacting calculations of conductance (a) and $LDOS$ (b) as a function of the barrier height (i.e. κ for our symbol) respectively [6]. With the increasing steps of U_{eff}^{max}, conductance is more suppressed as shown in Fig. 4.25a, and $LDOS_{max}$ is moving upwards as shown in Fig. 4.25b (as the arrow shows), indicating both $LDOS_{max}$ and $\kappa_{LDOS_{max}}$ are increasing.

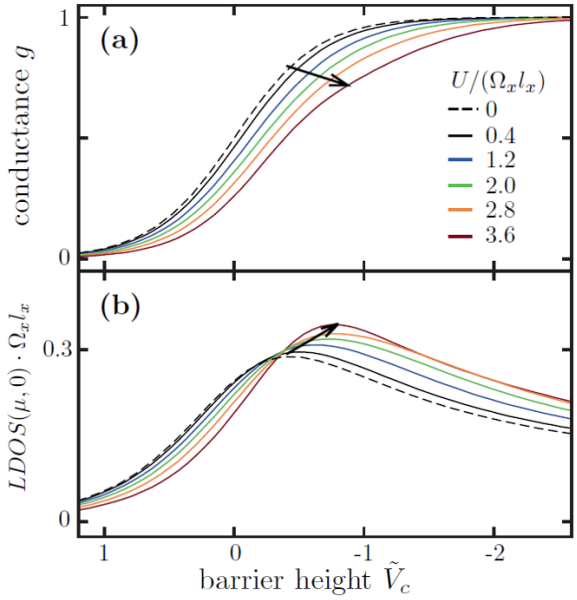

Figure 4.25: Interacting calculations of conductance (a) and effective $LDOS$ (b) as a function of the barrier height (i.e. κ for our symbol) respectively. In the legend in (a), $U/(\Omega_x l_x)$ is U_{eff}^{max} for our symbol. Adapted from Ref. [6].

Since $LDOS_{max}$ and $\kappa_{LDOS_{max}}$ increase with U_{eff}^{max} in Fig. 4.25b, based on 1-$S_{TC}^{0.7} \approx U_{eff}^{max}$ in Eq. 4.6, 1-$S_{TC}^{0.7}$ and $\kappa_{TC}^{0.7}$ should also increase with U_E (=E_y/E_x, to characterise U_{eff}^{max}) in experiments. Fig. 4.26 shows 1-$S_{TC}^{0.7}$ as a funciton of $\sqrt{U_E}$ (a), and $\kappa_{TC}^{0.7}$ as a funciton of U_E (b) respectively, for sample 1 at 1.4 K with 65 devices. In Fig. 4.26a, 1-$S_{TC}^{0.7}$ is positively correlated with $\sqrt{U_E}$, which obeys $1 - S_{TC}^{0.7} \approx \sqrt{U_E}$ combining Eq. 4.2 and Eq. 4.6. In Fig. 4.26b, $\kappa_{TC}^{0.7}$ is positively correlated with U_E, which agrees with the prediction in Fig. 4.25b.

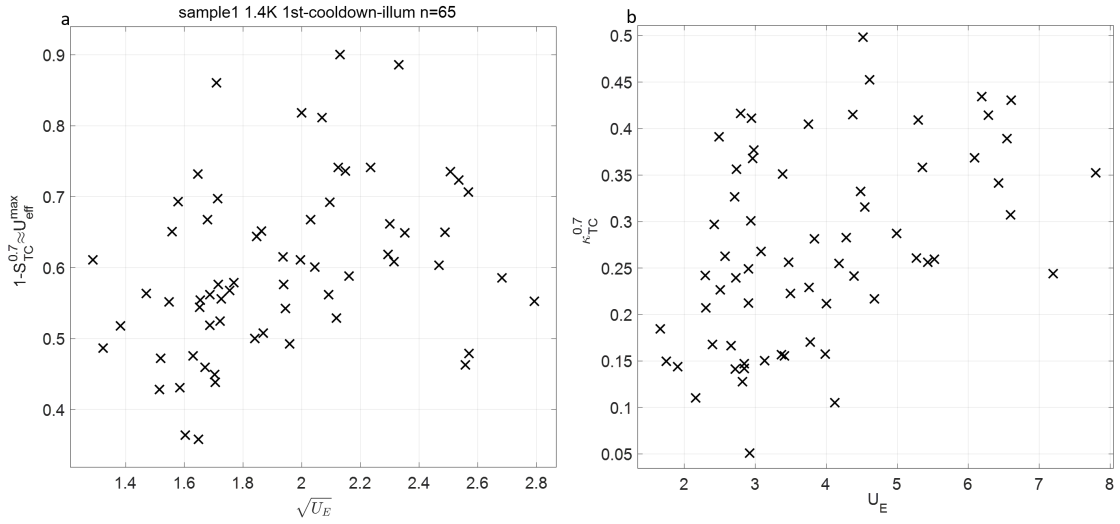

Figure 4.26: 1-$S_{TC}^{0.7}$ as a funciton of $\sqrt{U_E}$ (a), and $\kappa_{TC}^{0.7}$ as a funciton of U_E (b) respectively, for sample 1 at 1.4 K with 65 devices.

Based on Eq. 4.6, we can use '1-S_{TC}' curve to mimic the effective $LDOS$ ridge, although this mimic is defective since $S_{TC}(\kappa)$ carries a great deal of amplified noise. In Fig. 4.27, we plot together '1-S_{TC}' curves as a function of κ for the first three plateaus, for sample 1 at 40 mK (a-c), and sample 2 (d-f) and 3 (g-i) at 1.4 K respectively. Clearly, the second and third plateaus show similarly weak transconductance suppression. The count of S_{TC} curves decreases with increasing N, showing a decreasing probability of showing the 0.7 anomaly for the higher subbands.

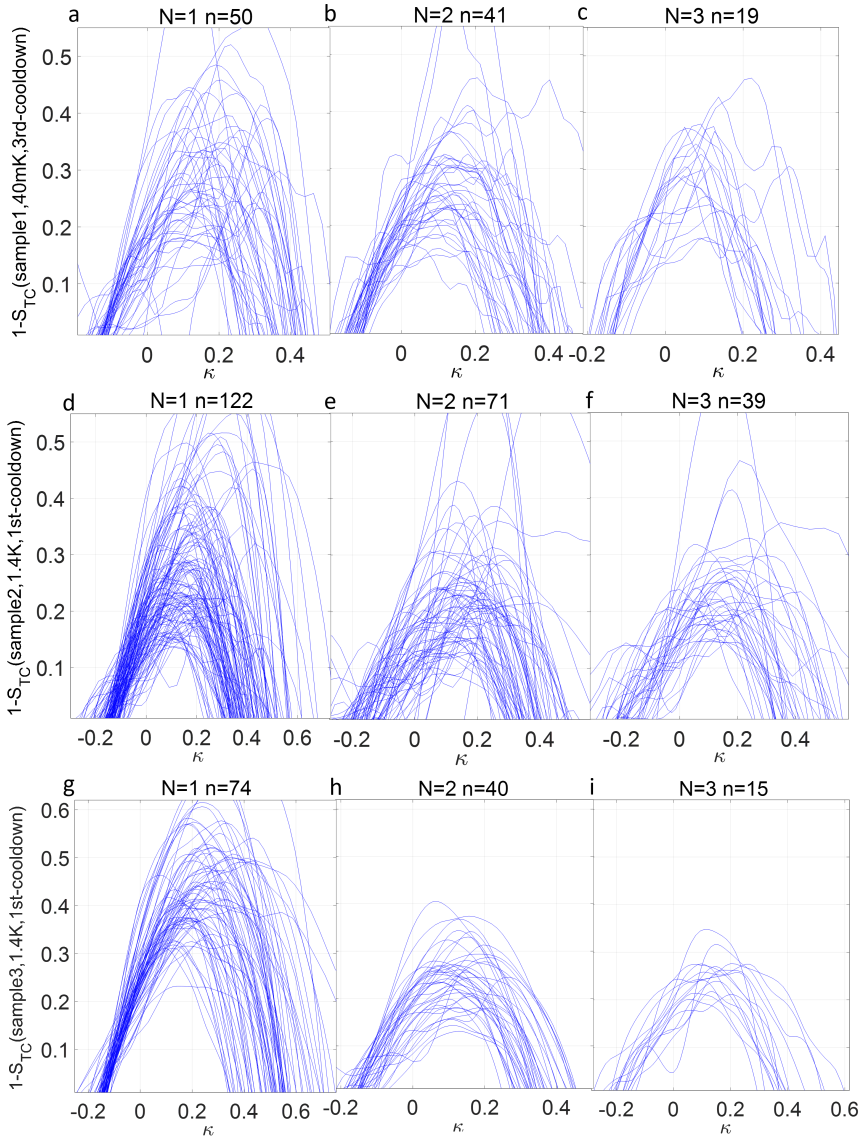

Figure 4.27: '1-S_{TC}' curves as a function of κ for the first three plateaus, for sample 1 at 40 mK (a-c), and sample 2 (d-f) and 3 (g-i) at 1.4 K respectively. In each panel, n counts the device number.

4.9 The origin of spontaneous risers-splitting

Here we explain the origin of spontaneous risers-splitting for transconductance. Fig. 4.28a illustrates a typical case of risers-splitting for a device D(10,11), sample 1 at 40 mK. After illumination, the 0.7 anomaly transconductance is suppressed further with $S_{TC}^{0.7}$ decreasing from a value 0.439 to a value as low as 0.118, which gives rise to a local minimum and forms the risers-splitting in TC_{SD} curve (star-marked green line) as arrowed in Fig. 4.28a. Hence, we arrive at a conclusion that the risers-splitting is a direct result of a strongly suppressed transconductance for the 0.7 anomaly. If we multiplying the lever arm, and convert the V_G distance of two risers into energy (called ΔE_{rs}^{0T}), we can compare with the measurements by Thomas et al. In our measurements, ΔE_{rs}^{0T}=1.37 meV in Fig. 4.28a. In their measurements, ΔE_{rs}^{0T}=1.1 and 0.43 meV for the first and second plateaus respectively in Fig. 2.1a. They regard ΔE_{rs}^{0T} as an evidence of the spin-gap of spontaneously polarised spins. However, this argument is not convincing because the risers-splitting does not always appear and actually has a very low probability of occurrence, whereas the 0.7 anomaly suppression is always there. Hence, a statistical test of measuring numerous devices is desired, and our multiplexer technique has the ability to realise it.

We sort out the devices that show spontaneous risers-splitting in the TC_{SD} curve. Fig. 4.28b compares yields of risers-splitting ($Y_{rs}^{0.7}$) and transconductance suppression ($Y_{TC}^{0.7}$) in 1D devices. Remarkably, $Y_{rs}^{0.7}$ is much lower than $Y_{TC}^{0.7}$ in 12 cooldowns. Also $Y_{rs}^{0.7}$ is higher in those cooldowns after illumination, since a stronger suppression after illumination makes the risers-splitting more likely to happen. For instance, comparing the 1st and 10th cooldowns, $Y_{rs}^{0.7}$ increases from 9.23% before illuminaiton, to 29.47% after illumination, for sample 1 at 40 mK in the second cooldown. This supports that the risers-splitting is a direct result of the transconductance suppression, rather than the spontaneous spin polarisation.

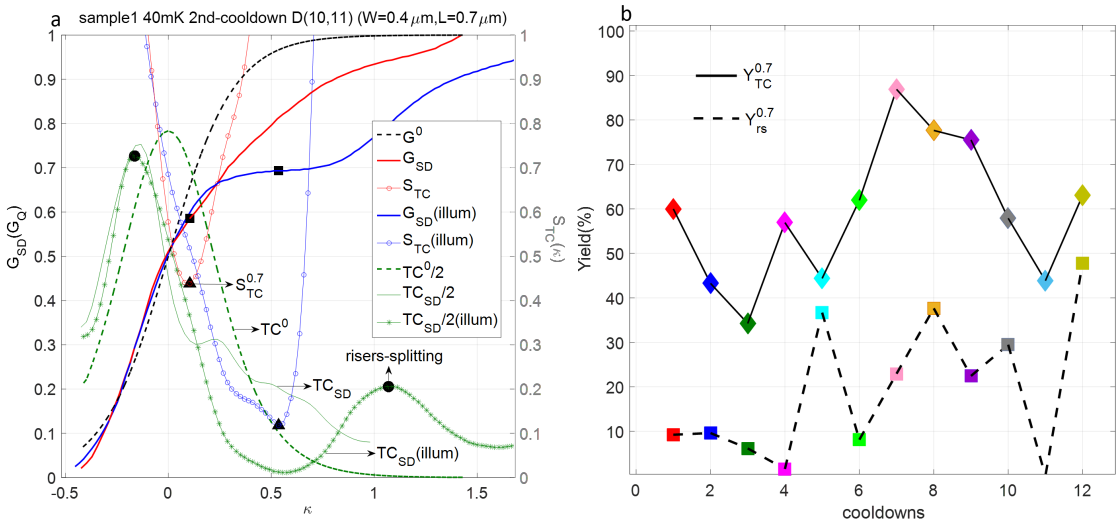

Figure 4.28: (a), Spontaneous risers-splitting for TC_{SD} curve for a device D(10,11), sample 1 at 40 mK. For TC^0, TC_{SD} and $S_{TC} = TC_{SD}/TC^0$ curves, read the right axis. $S_{TC}^{0.7}$ is marked with triangles for S_{TC} curves before and after illumination respectively. After illumination, due to the strongly suppressed S_{TC} curve (circle-marked blue line), two split-risers (marked with dots) appear in TC_{SD} curve (star-marked green line). (b), Comparisons of $Y_{rs}^{0.7}$ (dashed line) with $Y_{TC}^{0.7}$ (solid line) for sample 1-5 in 12 cooldowns. $Y_{rs}^{0.7}$ ($Y_{TC}^{0.7}$) is the yield of devices showing risers-splitting (transconductance suppression) in 1D devices. For each cooldown information, see the legend in Fig. 4.10.

4.10 Summary

In this Chapter, first, we show the distribution map of definition voltage for different multiplexer samples, which can be used to approximate the local distribution of density. We then show geometry dependence of pinch-off voltage, and find a shorter or wider QPC results in a more negative pinch-off voltage. Second, we find in all the 1D devices for a MUX sample in a cooldown, some devices show a variable series resistance, which increases with decreasing subband index. We suspect this may be caused by the poor insulation of polyimide beneath the bar-gate. There is also a possibility that this is caused by an impurity that happens to be in the channel. Afterwards, we provide different solutions for correcting the variable series resistance in following Chapters.

Second, we link the effective interaction strength with the ratio E_y/E_x. We show how to fit E_x using Landauer-Büttiker formula. We then show statistics and geometry dependence of E_x for the first three plateaus respectively, for different MUX samples, in different cooldowns at 40 mK or 1.4 K, before or after illumination respectively. We find E_x is highly influenced by potential background fluctuations, and is almost independent of QPC geometry. For E_y, we acquire it in a DC-bias spectroscopy. We show statistics and geometry dependence of E_y for the first three plateaus respectively. We find E_y shows a roughly negative correlation with width and length respectively.

Third, since the 0.7 anomaly shows the strongest suppressions of transconductance and conductance respectively, we propose two definitions of the 0.7 anomaly, in terms of transconductance and conductance respectively. We shows statistics of the 0.7 anomaly suppressions, in terms of transconductance and conductance respectively. We find the 0.7 anomaly transconductance suppression is stronger at 1.4 K than that at 40 mK, and is stronger for the first plateau than that for the higher plateaus. We explain the spontaneous risers-splitting in transconductance, which is caused by a very strong suppression of transconductance . We also use the transconductance curve to mimic the $LDOS$ shape for a QPC.

5

Dependence of Conductance on the Effective Interaction Strength

5.1 Introduction

In the last Chapter, we focus on the effect of U_{eff}^{max} on the 0.7 anomaly suppressions. In this Chapter, we discuss how the whole part of conductance suppression $S_G(\kappa)$ is affected by U_{eff}^{max} at fixed κ positions in multiplexed devices, in the absence or presence of magnetic fields. It is chosen to investigate $S_G(\kappa)$ instead of $S_{TC}(\kappa)$, since S_G is first-hand data and more reliable than S_{TC} which has much more noise.

5.2 Interaction effects on conductance suppression at fixed κ

First, we look at the role of E_x on non-interacting S_G^0. Fig. 5.1 shows S_G^0 as a function of E_x at each κ step at 1.4 K, based on Eq. 4.3. S_G^0 becomes stronger with decreasing E_x. By contrast, Fig. 5.2 shows interacting calculations in Ref. [7]. The conductance becomes more suppressed with decreasing E_x (a) or increasing U (b) respectively.

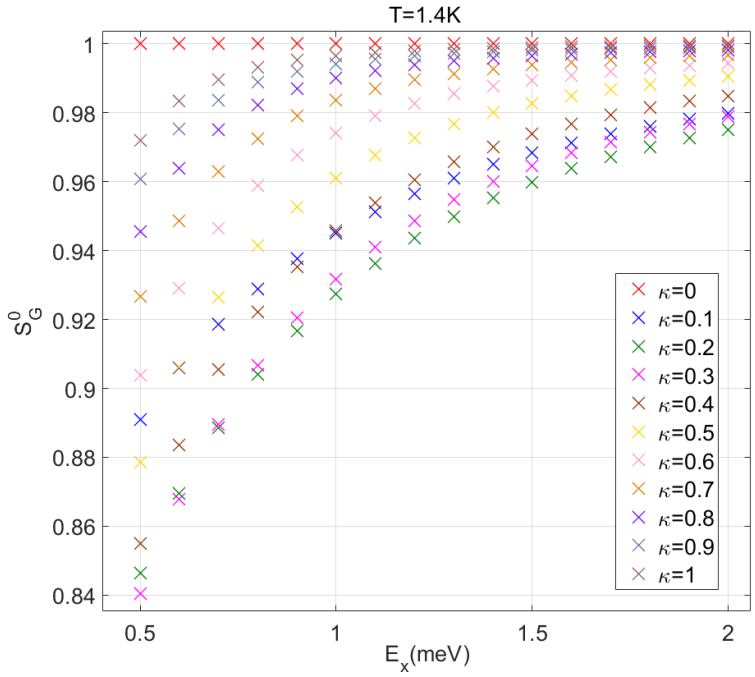

Figure 5.1: Non-interacting S_G^0 as a function of E_x at each κ step at 1.4 K.

In experiments, we can testify that both E_x and E_y have a role on U_{eff}^{max} based on Eq. 2.2, by checking whether or not S_G is more correlated with $1/U_E = E_x/E_y$ than E_x.

In Fig. 4a, we plot together the first steps for 62 1D devices for sample 1 at 40 mK. The curves assemble together in the half step below 0.5 G_Q. The 0.7 anomaly manifests different suppression levels compared with G^0 in the sub-open regime. Fig. 5.3b shows E_x dependence of G_{SD} for the devices in Fig. 5.3a, at fixed positive κ steps (see vertical coloured lines in Fig. 5.3a). It can be seen that G_{SD} decreases with decreasing E_x. This is same as the pioneering work by Smith et al. [61] as shown in Fig. 2.2. However, it is flawed that they simply use G_{SD} instead of S_G to conclude the

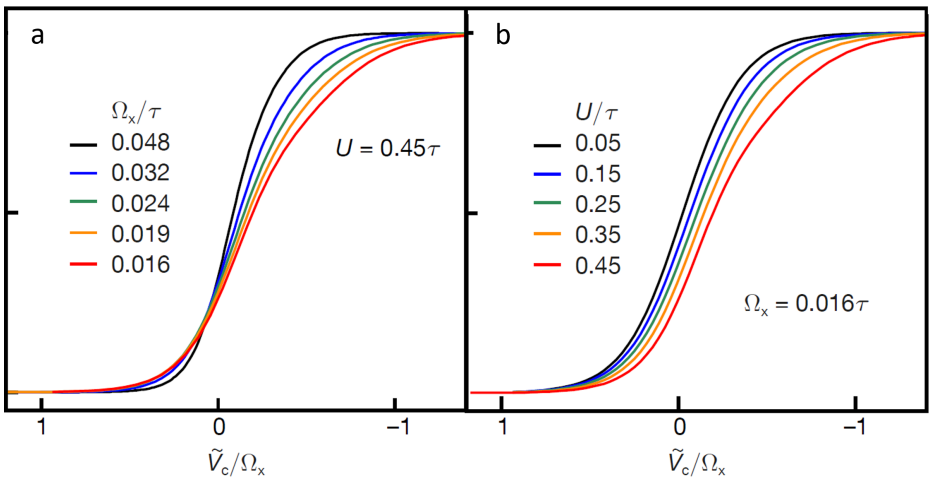

Figure 5.2: Interacting effects of E_x (a) and U (b) on the conductance suppression respectively. Ω_x is E_x, and $-\widetilde{V}_c/\Omega_x$ is κ for our symbols. Adapted from Ref. [7].

role of E_x at 1.4 K, because decreasing G_{SD} does not mean decreasing S_G. Based on Eq. 4.3, the thermal broadening at 1.4 K makes G^0 decrease with decreasing E_x. In fact, G_{SD} can only represent S_G at low temperatures like 40 mK, at which temperature G^0 is nearly equal to G^0 at 0 K (i.e. G_0 in Eq. 1.17), which is independent of E_x. Therefore, it is necessary to refer to S_G rather than G_{SD} to reflect the role of U_{eff}^{max} on the 0.7 anomaly.

Next, Fig. 5.3c,d shows the dependence of S_G on E_x (c) and $1/U_E$ (d) respectively. We can see S_G not only decreases with decreasing E_x, but also decreases with decreasing $1/U_E$. However, it is difficult to distinguish the correlation strength of S_G with E_x and $1/U_E$ respectively. We will clarify this by comparing Pearson product-moment correlation coefficients-$\rho(S_G, E_x)$ and $\rho(S_G, 1/U_E)$.

Fig. 5.4a compares $\rho(S_G, E_x)$ with $\rho(S_G, 1/U_E)$ in 6 cooldowns at 40 mK or 1.4 K. Fig. 5.4b shows $\rho(S_G, E_x)$ for the backward V_G sweep for a comparison (here there is no correlation of S_G with $1/U_E$, since we only measured E_y in the forward V_G sweep). First, it is noticeable that at the low κ range below 0.3, $\rho(S_G, E_x)$ (dot-marked) is negative in the cooldowns at 1.4 K in both forward and backward sweeps. However, in Fig. 5.4a, $\rho(S_G, E_x)$ (diamond-marked) is positive at those κ positions. This reinforces the point that the change of G_{SD} does not represent the change of S_G at a high temperature 1.4 K. Second, as κ increases, $\rho(S_G, E_x)$ and $\rho(S_G, 1/U_E)$ are rising in all the cooldowns, indicating that the effect of U_{eff}^{max} on the 0.7 anomaly is strengthening. This is because the role of U_{eff}^{max} starts manifesting, and the conductance suppression starts broadening as κ increases from zero. Third, in Fig. 5.4a, it is clear to see

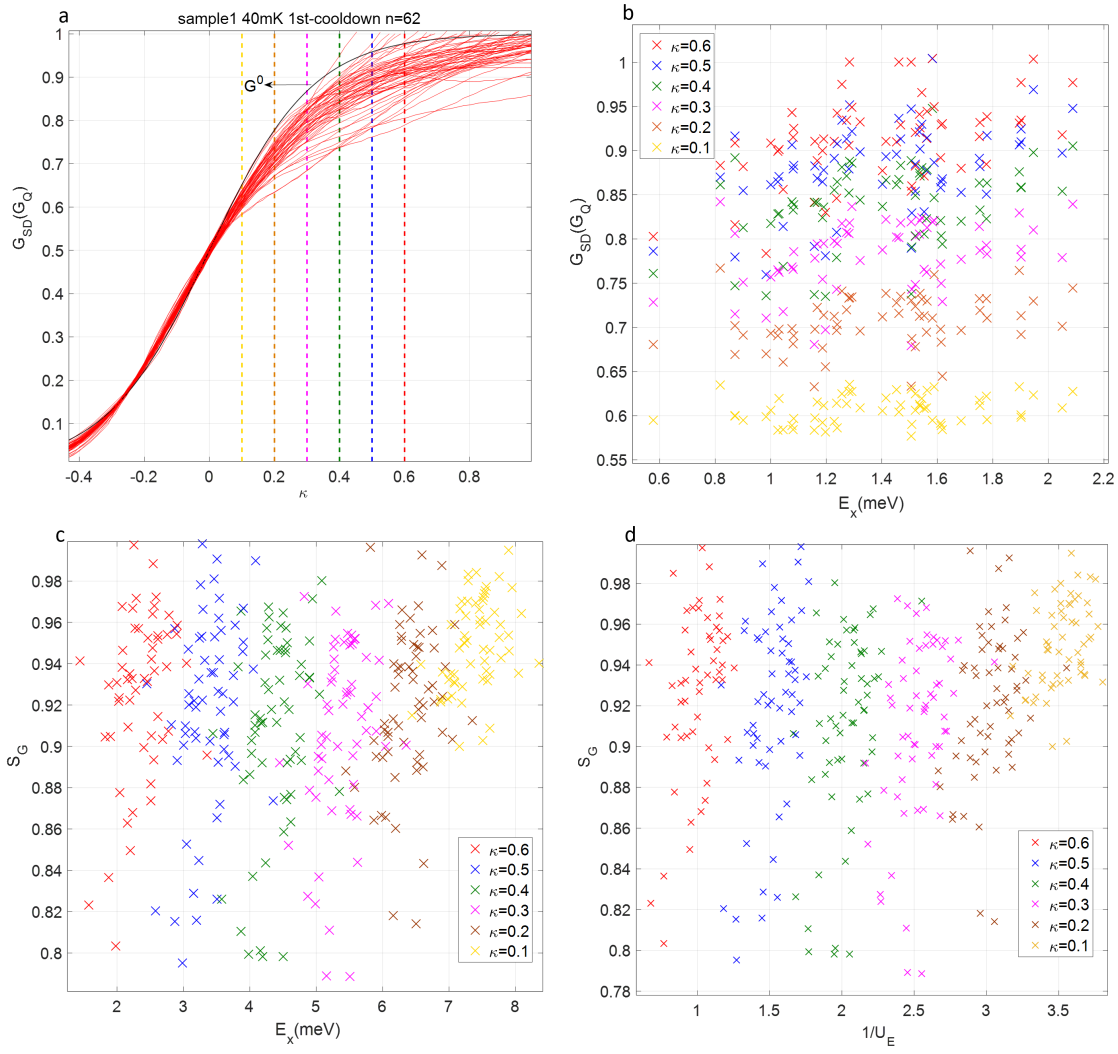

Figure 5.3: (a), The first steps for 62 devices for sample 1 at 40 mK. (b), E_x dependence of G_{SD} at fixed κ steps (vertical coloured lines in (a)). (c,d), Dependence of S_G (offset to the right equally by 0.5 in turn for clarity) on E_x (c) and $1/U_E$ (d) respectively at fixed κ.

diamond-marked lines are above dot-marked lines (i.e. $\rho(S_G, 1/U_E) > \rho(S_G, E_x)$) for each cooldown in the same colour, which testifies that S_G is more dependent on $1/U_E$ than E_x. This underlines the fact that the role of E_y on S_G should be considered as same as that of E_x.

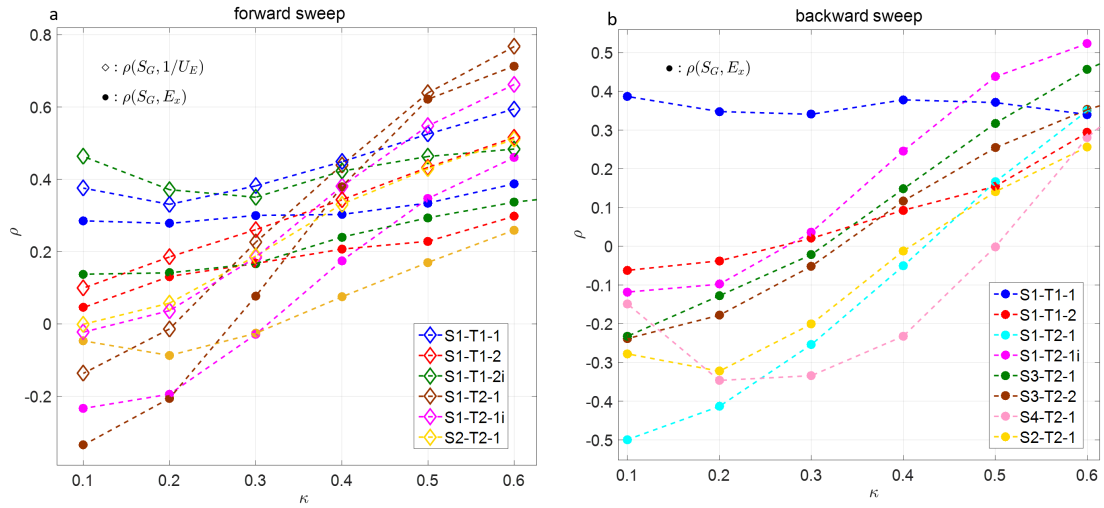

Figure 5.4: (a), Comparisons of $\rho(S_G, 1/U_E)$ (marked with diamonds) with $\rho(S_G, E_x)$ (marked with dots) as a function of the κ steps in 6 cooldowns at 40 mK or 1.4 K, for the forward V_G sweep. The diamonds are above the dots in each cooldown (in the same colour), verifying $\rho(S_G, 1/U_E) > \rho(S_G, E_x)$. (b), $\rho(S_G, E_x)$ as a function of κ in 8 cooldowns, for the backward V_G sweep. In the legend, for instance, the symbol 'S1-T1-1' refers to sample 1-at 40 mK-in the 1^{st} cooldown in the dark. The symbol 'S1-T2-1i' refers to sample 1-at 1.4 K-in the 1^{st} cooldown after illumination.

Furthermore, it is interesting to see how S_G changes as a function of $1/U_E$ in a different cooldown, at a different temperature, and after illumination, for a same MUX sample. Fig. 5.5a shows S_G as a function of $1/U_E$ in the first (crosses) and second (diamonds) cooldowns respectively, for sample 1 at 40 mK. The crosses and diamonds nearly overlap each other, showing the repeatability of S_G as a function of U_E between different cooldowns. Fig. 5.5b shows S_G as a function of $1/U_E$, for sample 1 at 40 mK (crosses) and 1.4 K (diamonds) respectively. The diamonds tend to be below the crosses particularly at large κ steps, meaning S_G is stronger at 1.4 K than that at 40 mK even though both cooldowns have similar values of U_E. This confirms the role of temperature on U_{eff}^{max} and S_G again, implying U_{eff}^{max} is not only a function of E_x and E_y, but also a function of temperature. Fig. 5.5c,d shows S_G as a function of $1/U_E$ before (crosses) and after (diamonds) illumination respectively, for sample 1 at 40 mK (c) and 1.4 K (d) respectively. Remarkably, the diamonds are situated at the bottom-left

compared to the crosses at both 40 mK and 1.4 K, demonstrating again illumination could significantly strengthen U_{eff}^{max} and S_G, by enlarging E_y (E_y enlargement in Fig. 5.5c is shown in Fig. 4.14d).

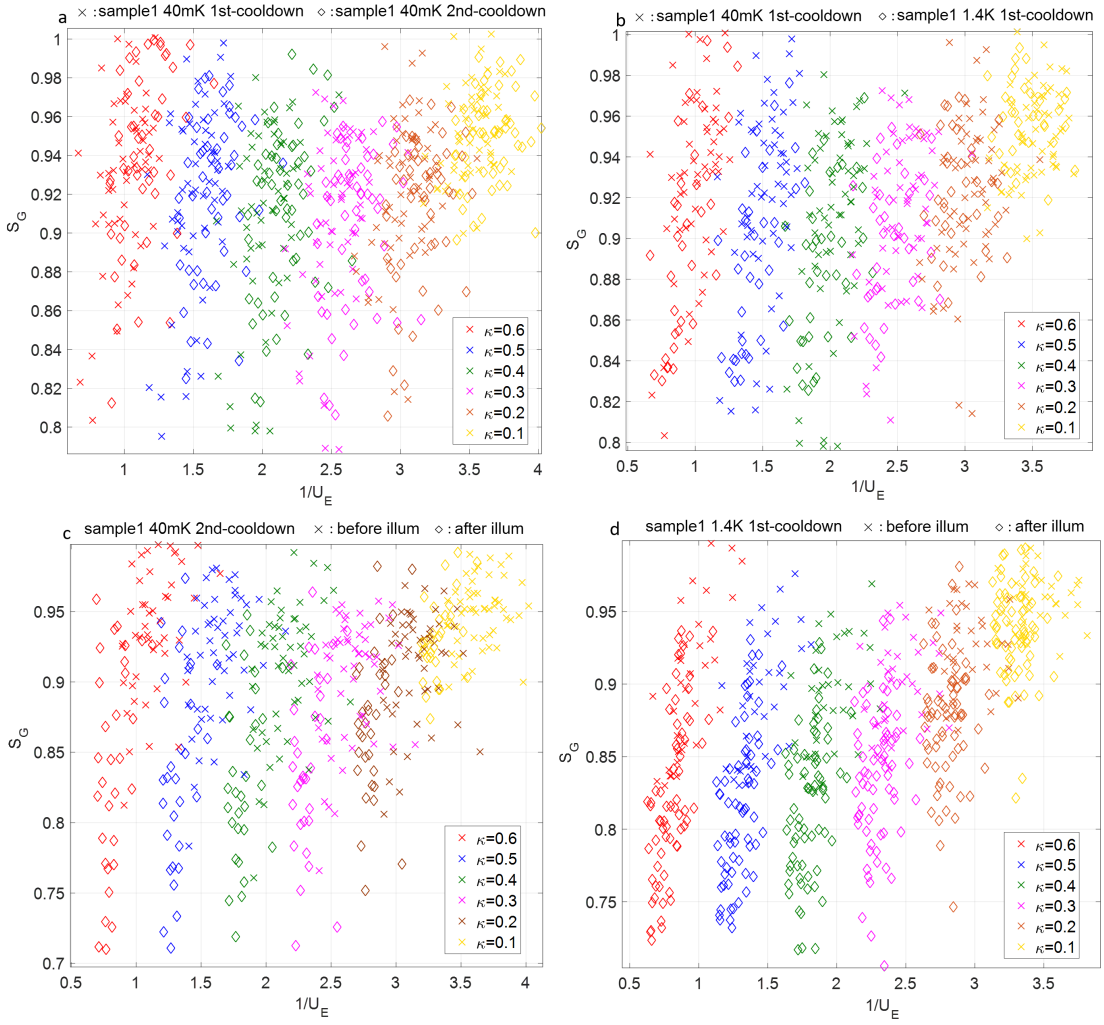

Figure 5.5: S_G (offset rightward in turn by 0.5 for clarity) as a function of $1/U_E$: (a), in the first (crosses) and second (diamonds) cooldowns respectively, for sample 1 at 40 mK; (b), for sample 1 at 40 mK (crosses) and 1.4 K (diamonds) respectively; (c,d), before (crosses) and after (diamonds) illumination respectivley, for sample 1 at 40 mK (c) and 1.4 K (d).

5.3 Extend to the higher plateaus

We here discuss the dependence of S_G on $1/U_E^N$, where $U_E^N = \Delta E_{N,N+1}/E_x^N$ for the higher plateaus. Fig. 5.6a-c shows the first three steps for multiplexed devices for sample 1 at 1.4 K respectively. Fig. 5.6d-f shows dependence of S_G on $1/U_E^N$ for corresponding devices in Fig. 5.6a-c respectively. Appendix Fig. A.9 shows the case for sample 2 at 1.4 K.

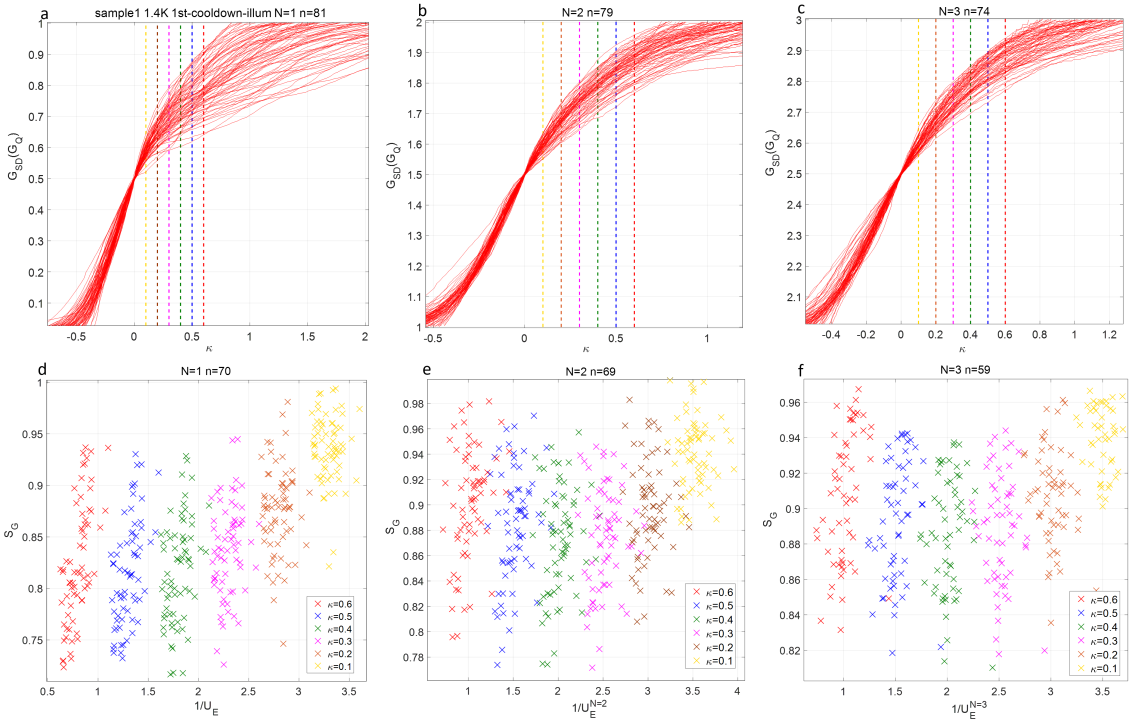

Figure 5.6: (a-c), First three steps for the devices for sample 1 at 1.4 K respectively. (d-f), Dependence of S_G (offset rightward in turn by 0.5 for clarity) on $1/U_E^N$ at fixed κ positions, for the first three plateaus for devices in (a-c) respectively.

Next, Fig. 5.7 compares $\rho(S_G, E_x^N)$ with $\rho(S_G, 1/U_E^N)$ in different cooldowns for the second (a) and third plateaus (c) respectively. Similar with Fig. 5.4, ρ is rising with increasing κ, and $\rho(S_G, 1/U_E^N) > \rho(S_G, E_x^N)$ in most cooldowns. In a word, Fig. 5.6 and 5.7 demonstrate again the conductance suppression for the higher plateaus is analogous to that for the first plateau.

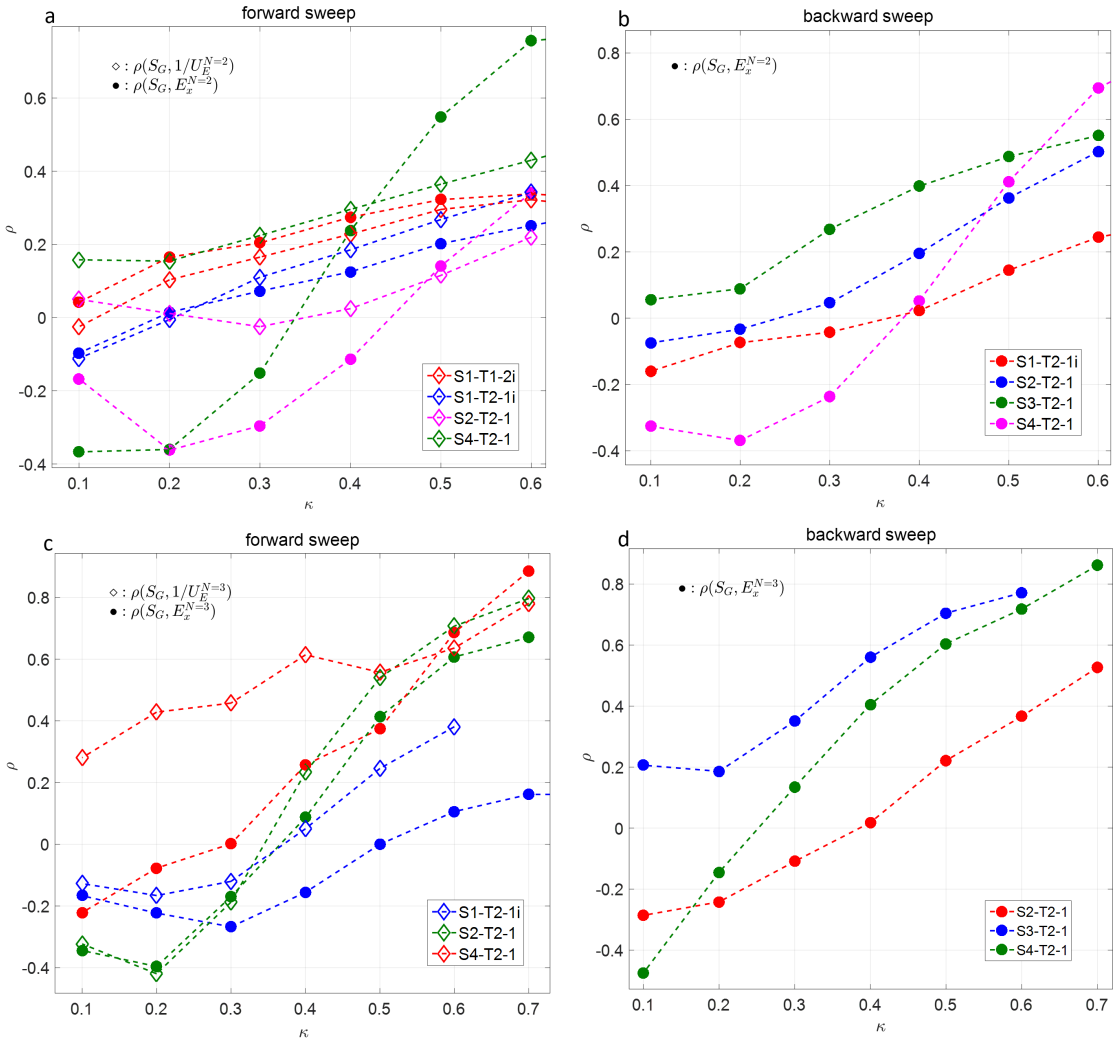

Figure 5.7: (a,c), Comparisons of $\rho(S_G, 1/U_E^N)$ (marked with diamonds) with $\rho(S_G, E_x^N)$ (marked with dots) for the second (a) and third (c) plateaus respectively, in the forward V_G sweep. (b,d), $\rho(S_G, E_x^N)$ as a function of κ for the second (b) and third (d) plateaus respectively, in the backward V_G sweep for a comparison. In the legend, for instance, the symbol 'S2-T2-1' refers to sample 2-at 1.4 K-in the 1^{st} cooldown in the dark. The symbol 'S1-T1-2i' refers to sample 1-at 40 mK-in the 2^{nd} cooldown after illumination.

5.4 Equations of interaction effects on the magnetoconductance suppression

In this section, we discuss the behaviours of magnetoconductance G_B. Bauer et al. propose that the magnetoconductance suppression $S_B(B)$ (defined as the ratio of G_B with zero-B-field conductance G_{0T}) depends on B fields quadratically at fixed κ positions in the sub-open regime at low B fields [7]. The quadratic coefficient is called B_*, which is inversely proportional to the local spin fluctuations [33]. B_* has a minimum value B_*^{min} (implying the strongest S_B), at the κ position $\kappa_{B_*^{min}}$, where the $LDOS$ is maximum and the exchange-driven U_{eff}^{max} is strongest [7]. In our experiments, the magnetoconductance behaviours are verified at both 40 mK and 1.4 K, in low in-plane magnetic fields (perpendicular to the transport direction).

Bauer et al. state that the quadratic dependence of S_B on B fields has a non-interacting origin as expressed in Eq. S27 in Ref. [7], which is written here in our symbols:

$$\frac{G_B^0(\widetilde{B},\widetilde{T},\widetilde{V}_{SD})}{G^0} = 1 - (\frac{\widetilde{T}}{\widetilde{T}_*^0})^2 - (\frac{\widetilde{B}}{\widetilde{B}_*^0})^2 - (\frac{\widetilde{V}_{SD}}{\widetilde{V}_{SD*}^0})^2 \tag{5.1}$$

We modify Eq. 5.1 into Eq. 5.2 here by further expanding G_B^0 to the quartic term more precisely:

$$S_B^0 = \frac{G_B^0}{G^0} \approx 1 + \frac{T_r^{(2)}(0)}{T_r^{(0)}(0)}(\frac{\widetilde{B}^2}{8} + \frac{\pi^2\widetilde{T}^2}{6}) + \frac{T_r^{(4)}(0)}{T_r^{(0)}(0)}(\frac{\widetilde{B}^4}{384} + \frac{\pi^2\widetilde{B}^2\widetilde{T}^2}{48} + \frac{7\pi^4\widetilde{T}^4}{360}) \tag{5.2}$$

where $T_r^{(0)}(0)(=G^0/G_Q)$, $T_r^{(2)}(0)$ and $T_r^{(4)}(0)$ are coefficients of the zero, second and fourth order differential of the transmission probability at μ respectively. Usng Eq. 5.2, we can achieve a better fitting of $B_*^{0,fit}$ as expressed in Eq. 5.3, compared to the B_*^0 expression in Eq. S32a in Ref. [7], which is written here in Eq. 5.4 with our symbols.

$$\widetilde{B}_*^{0,fit} = \sqrt{-\frac{8T_r^{(0)}(0)}{T_r^{(2)}(0)}} \tag{5.3}$$

$$\widetilde{B}_*^0/E_x = \frac{\sqrt{2}}{\pi}\sqrt{coth(\pi\kappa)}e^{\pi\kappa} \tag{5.4}$$

We make non-interacting calculations of G_B^0 based on Eq. 1.18. Fig. 5.8a shows '1-S_B^0' as a function of B at fixed κ for E_x=1 meV and T=1.4 K on a log-log scale. At low B fields, $1 - S_B^0$ changes little with increasing B fields, since it is dominated by

the thermal energy at 1.4 K. At high B fields, $1 - S_B^0$ increases almost quadratically with B fields. Fig. 5.8b shows B_*^0 as a function of κ (black line) based on Eq. 5.4 on a log-linear scale. We compare the fitting results of $B_*^{0,fit}$ using modified Eq. 5.2 at 0 K (red crosses) and 1.4 K (blue crosses) respectively, to that using Eq. 5.1 (i.e. Eq. S27 in Ref. [7]) at 0 K (green crosses). The red and blue crosses all lie on the black line at κ positions larger than 0.4, whereas there is some error for the green crosses compared to the black line, which justifies the improvement of modified Eq. 5.2 than Eq. 5.1. $\widetilde{B}_*^0/E_x$ is independent of E_x, and has a minimum value 1.09 at $\kappa_{B_*^{min}} = 0.14$. G_{0T} at $\kappa_{B_*^{min}}$ (called $G^0_{B_*^{min}}$) is 0.707 G_Q. Thus, $\widetilde{B}_*^{min,0}$ is directly proportional to E_x: $\widetilde{B}_*^{min,0}/E_x = 1.09$ (e.g. $\widetilde{B}_*^{min,0} = 18.8T$ for $E_x = 1meV$). In a word, the exponential dependence of B_* on κ, and the minimum of B_* with the strongest S_B, have non-interacting origins.

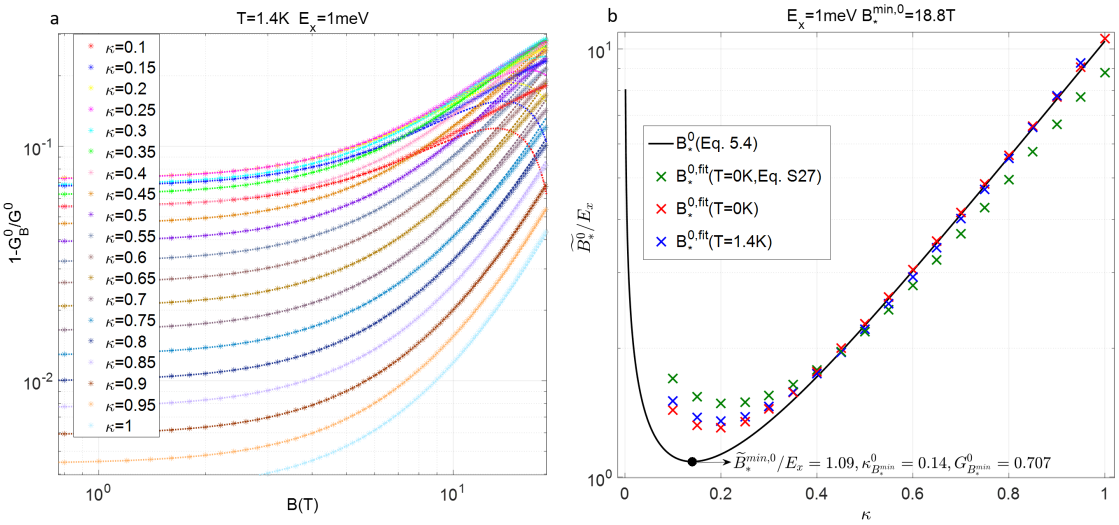

Figure 5.8: (a), Quadratic dependence of '1-S_B^0' on B fields for E_x=1 meV at 1.4 K on a log-log scale. At each κ step, a series of S_B^0 are shown with stars, and the expression in Eq. 5.2 with fitted $B_*^{0,fit}$ are shown with lines. The lines cross most stars, showing a good fitting of $B_*^{0,fit}$ using Eq. 5.2. (b), Exponential dependence of B_*^0 on κ on a log-linear scale. The black line shows the expression of $\widetilde{B}_*^0/E_x$ in Eq. 5.4. $B_*^{0,fit}$ is fitted using modified Eq. 5.2 at 0 K (red crosses) and 1.4 K (blue crosses), and using Eq. 5.1 (i.e. Eq. S27 in Ref. [7]) at 0 K (green crosses) respectively. $\widetilde{B}_*^0/E_x$ is independent of E_x, and has a minimum value 1.09 at $\kappa_{B_*^{min}} = 0.14$. G_{0T} at $\kappa_{B_*^{min}}$ (called $G^0_{B_*^{min}}$) is 0.707 G_Q.

In Fig. 5.9a,b, Bauer et al. perform calculations of G_B as a function of κ (in our symbol) at different B steps, using either the functional renormalization group (FRG, a) or the second-order perturbation theory (SOPT, b) approach. Fig. 5.9c shows

measured G_B as a function of κ. To deal with S_B, in Fig. 5.9d, they directly plot G_B/G_{0T} as a function of B fields to verify the quadratic relation.

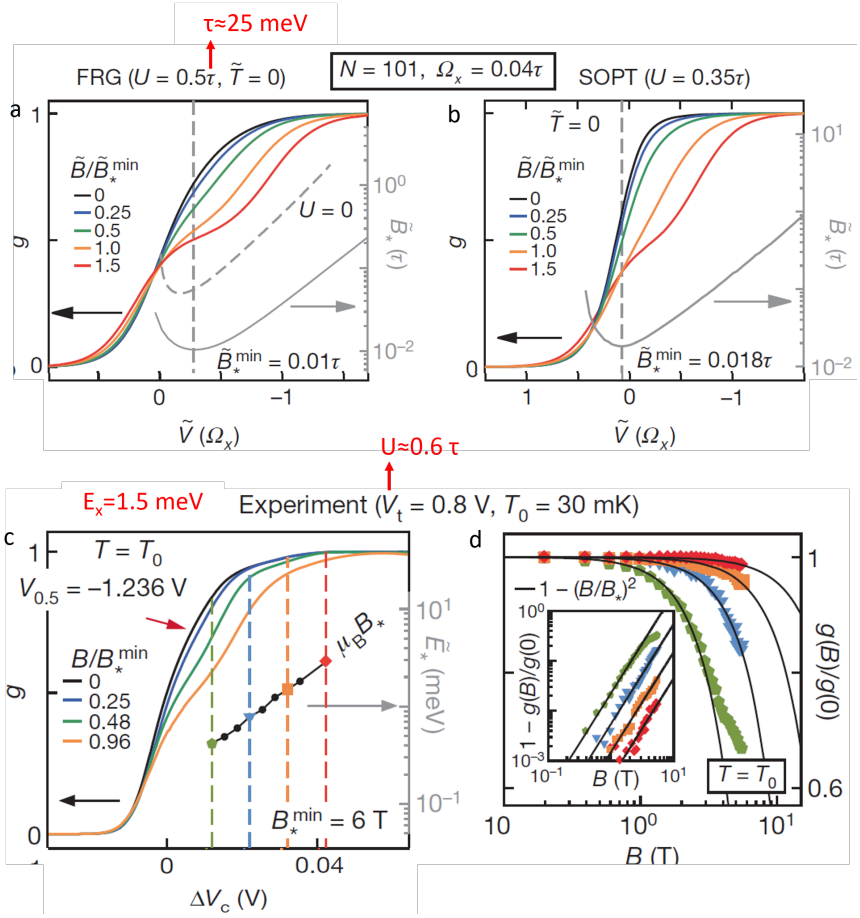

Figure 5.9: (a,b),Calculated G_B as a function of κ (in our symbol), using a FRG (a) or SOPT (b) approach. (c), Measured G_B as a function of κE_x (in our symbol) at 30 mK. (d), G_B/G_{0T} as a function of B fields. Ω_x is E_x; $-\tilde{V}_c/\Omega_x$ is κ; g(B) is G_B; g(0) is G_{0T}, for our symbols. τ is the hopping amplitude. V_t is a top gate voltage. Adapted from Ref. [7].

However, to calculate S_B using the single G_{0T} may be a risk, if there is any oscillation for G_{0T} curve. We make a little improvement to calculate S_B in Eq. 5.5. For a series of measured G_B at fixed κ at each B step, we use Eq. 5.5 to fit G_{0T}^{fit} and B_*^{fit}. We do not use G_{0T} directly, but compare G_{0T}^{fit} to G_{0T} to check, which could be a better method.

$$S_B(B) = G_B/G_{0T}^{fit} \approx 1 - (B/B_*^{fit})^2 \tag{5.5}$$

Moreover, we find Eq. 5.5 is applicable not only at 40 mK, but also at a higher temperature 1.4 K. In fact, Bauer et al. show that the temperature dependence of

S_G also follows a quadratic relation [7]. We regard the effect of temperature on S_G is already included into the suppression of G_{0T} (i.e. the 0.7 anomaly at 0 T). At a constant temperature, the further suppression S_B from G_{0T} to G_B depends on B fields quadratically, as described in Eq. 5.5. Therefore, even though G_{0T} shows a stronger suppression at 1.4 K than that at 40 mK, S_B at 1.4 K still follows Eq. 5.5.

Regarding the B_* behaviour, in Fig. 5.10, Bauer et al. show the effect of U on B_* in the large κ regime follows Eq. S35a, which is written here in our symbols

$$\widetilde{B}_*(\kappa)/E_x \approx e^{\pi\kappa - U_{eff}^{max}} \tag{5.6}$$

We can see B_* depends on κ exponentially, which has a non-interacting origin described in Eq. 5.4. B_* also experiences an exponential suppression due to the effect of U_{eff}^{max}. As shown in Fig. 5.10, with increasing U, the curves moves towards the bottom, showing a smaller B_*^{min}.

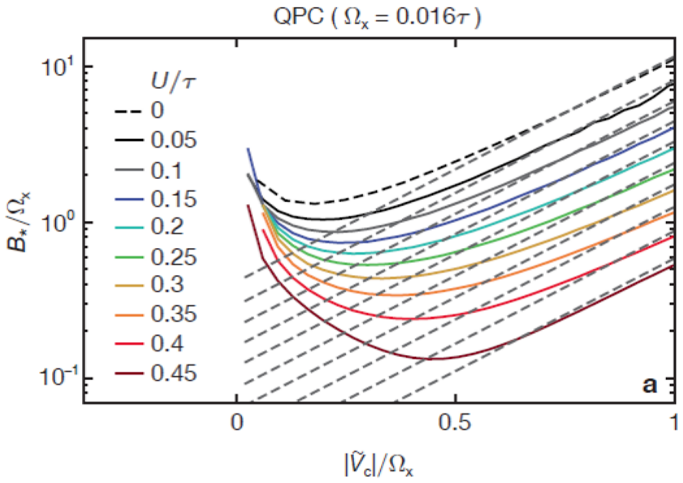

Figure 5.10: Calculated $\widetilde{B}_*/E_x$ as a function of κ (in our symbols) for different steps of U in a log-linear scale. Adapted from Ref. [7]. U_{eff}^{max} is fitted by the dashed lines.

For a quantitative comparison with theoretical calculations, we attempt to make a prediction of experimental values of U in units of hopping amplitude τ. In Ref. [67], $\tau \approx 25meV$ and lattice spacing $a = \sqrt{\hbar^2/2\tau m} \approx 5nm$. We regard the suppression of B_*^{min} as the suppression of B_* approximately, and substitute $\tau \approx 25meV$ into calculated results in Fig. 5.9a,b (with $E_x \approx 1meV$) and Fig. 5.10 (with $E_x \approx 0.4meV$). For the measurements of Bauer et al. in Fig. 5.9c,d with E_x=1.5 meV and B_*^{min}=6 T, we can predict that their experimental $U \approx 0.6\tau$ by applying a top gate voltage 0.8 V.

5.5 Magnetoconductance suppression and B_* in representative devices

In our experiments, G_B is measured in low in-plane B fields below 8 T at a step of 0.2 T (perpendicular to the transport direction), for sample 1 at 40 mK and 1.4 K respectively. In Fig. 5.11, we use a typical device to illustrate behaviours of S_B and B_*^{fit} at 40 mK. Fig. 5.11a shows G_B curves from 0 T (red bold line) to 8 T (blue bold line) at a step of 0.2 T. G_B already has an evident suppression at 0 T, and suppresses further with increasing B fields. Fig. 5.11b demonstrates the quadratic dependence of S_B on B fields. In Fig. 5.11c, G_{0T}^{fit} values (blue stars) basically lie on G_{0T} curve (solid red line), showing a reliability of the G_{0T}^{fit} method in Eq. 5.5. In Fig. 5.11d, compared to the non-interacting case in Fig. 5.8b, B_*^{fit}/E_x also has a minimum B_*^{min}/E_x at $\kappa_{B_*^{min}}$. Appendix Fig. A.10-A.12 show behaviours of S_B and B_*^{fit} for three more representative devices at 40 mK.

In the same way as Fig. 5.11, Fig. 5.12 shows similar behaviours of S_B and B_*^{fit} for a typical device at 1.4 K. For cases of another three devices at 1.4 K, see Appendix Fig. A.13-A.15.

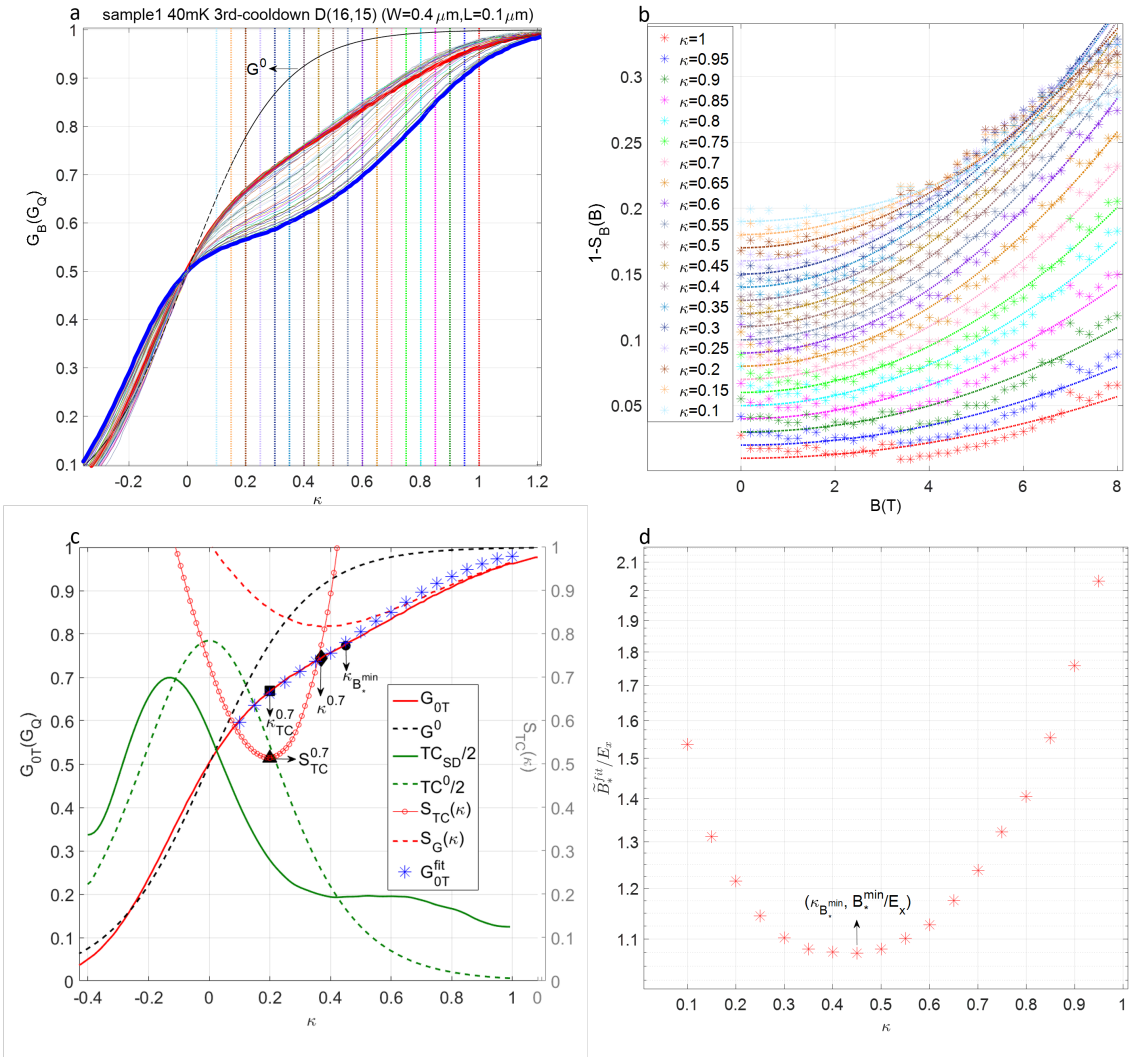

Figure 5.11: Behaviours of S_B and B_*^{fit} for a device D(16,15), sample 1 at 40 mK. (a), The first steps of G_B from 0 T (red bold line) to 8 T (blue bold line) with a step of 0.2 T. The series resistance is corrected individually at each B step by aligning the first plateau to G_Q, since the 2DEG conductance decreases (i.e. the series resistance increases) with increasing B fields. We get a series of G_B at fixed κ positions from 0.1 to 0.8 (step=0.05, vertical coloured lines), and fit G_{0T}^{fit} and B_*^{fit} according to Eq. 5.5. (b), '1-S_B' (stars, shifted upward in turn by 0.01 for clarity) as a function of B fields at each κ step. The dashed lines shows the expression $1-(B/B_*^{fit})^2$. The stars spread along the dashed lines, indicating the fitting is within the margin of error. (c), $\kappa_{B_*^{min}}$ (dot-marked) is compared with $\kappa_{TC}^{0.7}$ (square-marked) and $\kappa^{0.7}$ (diamond-marked) for G_{0T} curve. $\kappa_{TC}^{0.7}$ is always smallest among the three. (d), $\tilde{B}_*^{fit}/E_x$ (red stars) as a function of κ steps on a log-linear scale. There is a minimum B_*^{min}/E_x at $\kappa_{B_*^{min}}$.

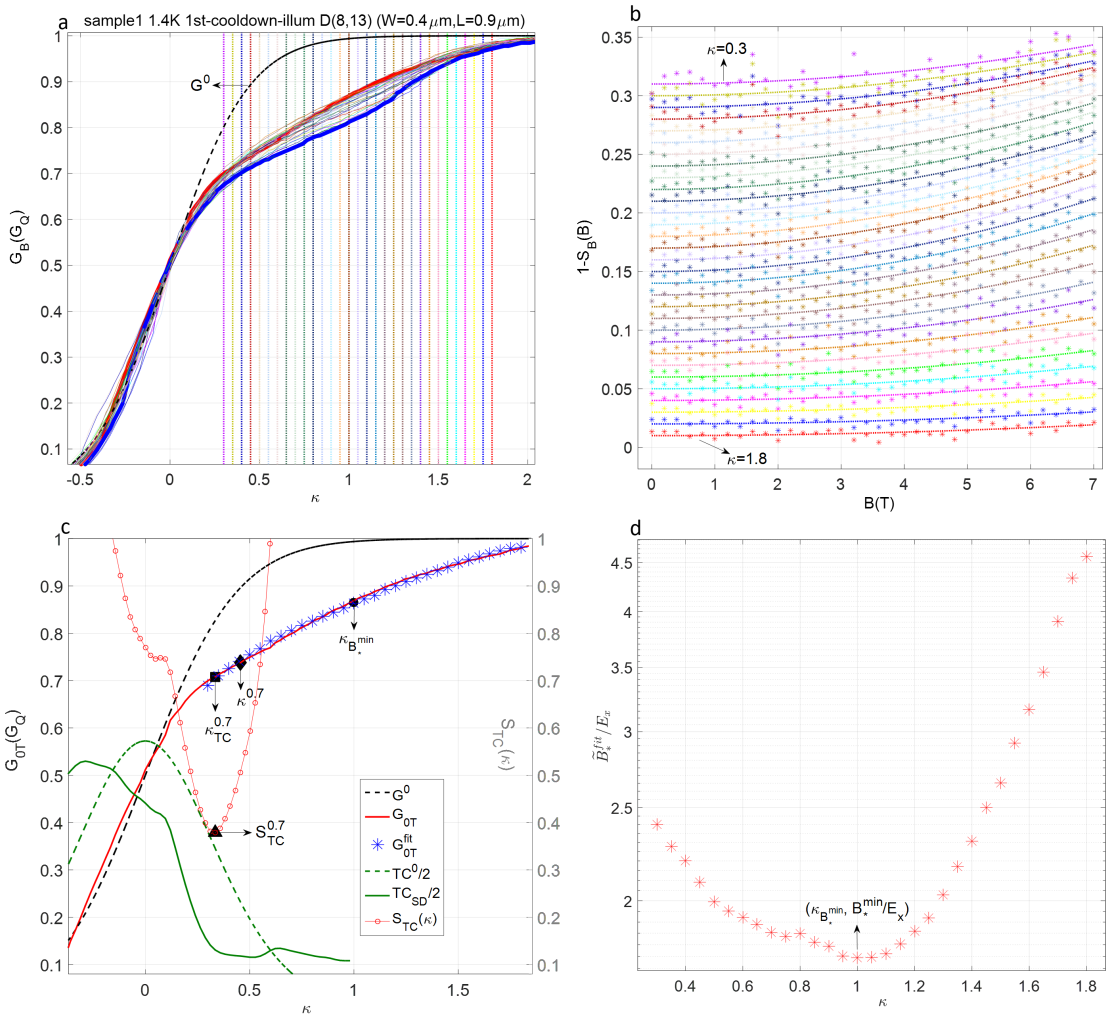

Figure 5.12: Behaviours of S_B and B_*^{fit} for a device D(8,13), sample 1 at 1.4 K. (a), The first steps of G_B from 0 T (red bold line) to 7 T (blue bold line) with a step of 0.2 T. We get a series of G_B at fixed κ positions from 0.3 to 1.8 (step=0.05, vertical coloured lines), and fit G_{0T}^{fit} and B_*^{fit} according to Eq. 5.5. (b), '1-S_B' (stars, shifted upward in turn by 0.01 for clarity) as a function of B fields at each κ step. The dashed lines shows the expression $1-(B/B_*^{fit})^2$. The stars spread along the dashed lines, indicating the fitting is within the margin of error. (c), $\kappa_{B_*^{min}}$ (dot-marked) is compared with $\kappa_{TC}^{0.7}$ (square-marked) and $\kappa^{0.7}$ (diamond-marked) for G_{0T} curve. (d), $\widetilde{B}_*^{fit}/E_x$ (red stars) as a function of κ steps on a log-linear scale. There is a minimum B_*^{min}/E_x at $\kappa_{B_*^{min}}$.

5.6 Statistic behaviours of B_*

Fig. 5.13 plots together the fitted G_{0T}^{fit} and B_*^{fit}/E_x as a function of κ steps, for 16 devices at 40 mK (a,b), and 18 devices at 1.4 K (c,d) respectively in the order of increasing U_E. In Fig. 5.13a,c, all devices show a good alignment of G_{0T}^{fit} with G_{0T} curve. The inset shows that $\kappa_{B_*^{min}}$ follows $\kappa_{TC}^{0.7}$ at larger values with a positive correlation, implying the κ position of strongest S_B follows $\kappa_{LDOS_{max}}$.

In Fig. 5.13b,d, all devices show a B_*^{min}/E_x at $\kappa_{B_*^{min}}$ where the exchange-driven U_{eff}^{max} is strongest. Based on Eq. 5.6, B_*^{min}/E_x should be smaller than non-interacting $B_*^{min,0}/E_x$=1.09, and decreases with increasing U_{eff}^{max}. However, in Fig. 5.13b,d at 40 mK and 1.4 K respectively, most devices show B_*^{min}/E_x above 1.09, and B_*^{min}/E_x does not decrease with increasing U_E as shown in the inset. The reason may lies in that, at the basis of G_{0T} which is considerably suppressed at 40 mK (which may be caused by a large ac excitation voltage 0.1 meV we use at 40 mK), the further suppression S_B could be less affected by Zeeman energy than that in the non-interacting regime. This results in a much larger (rather than reduced) B_* than B_*^0.

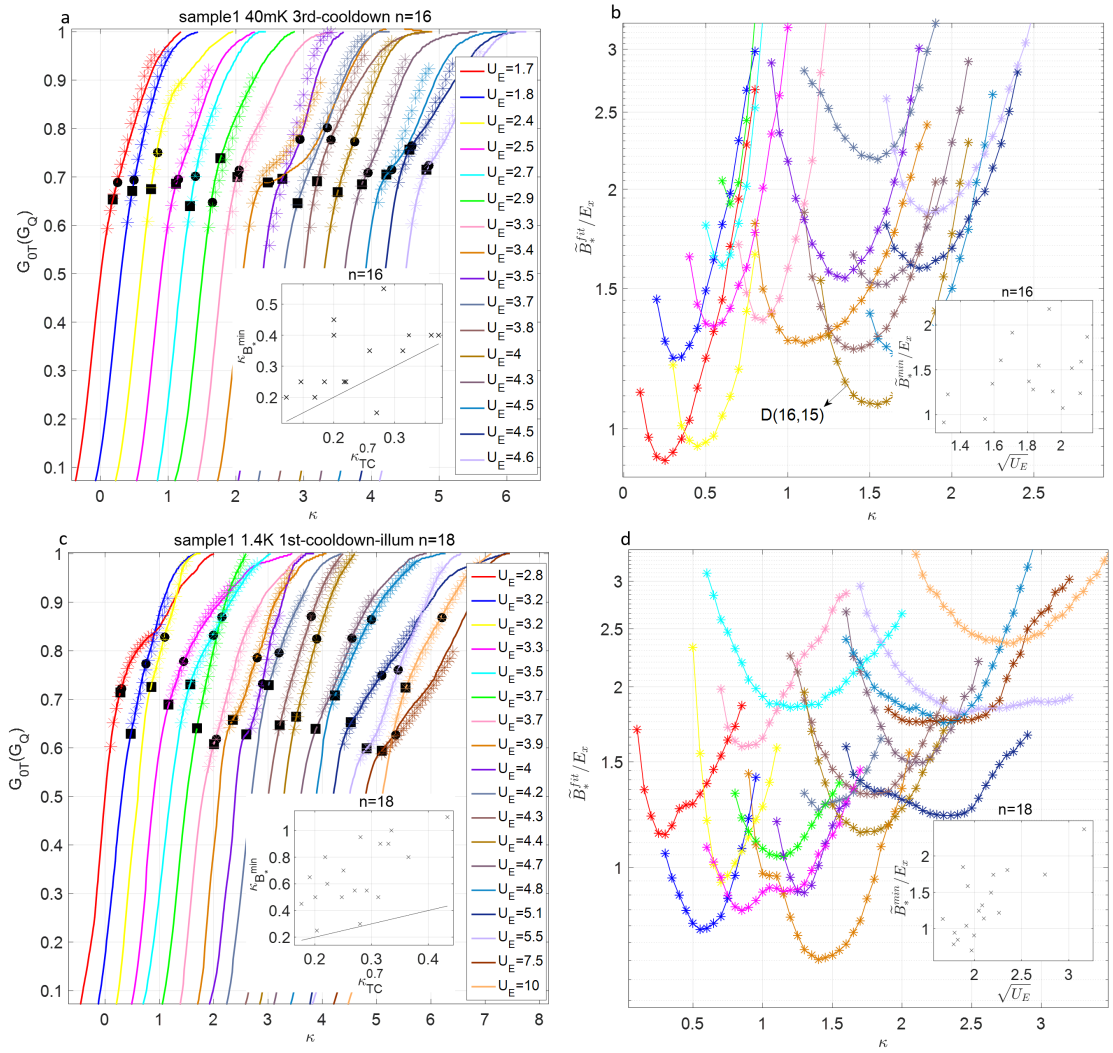

Figure 5.13: G_{0T}^{fit} (stars, offset rightward in turn by 0.3) and B_*^{fit} (stars, offset rightward in turn by 0.1) as a function of κ steps in the order of increasing U_E, for 16 devices at 40 mK (a,b) and 18 device at 1.4 K (c,d) respectively. In (a,c), for each G_{0T} curve, the positions of $\kappa_{TC}^{0.7}$ and $\kappa_{B_*^{min}}$ are marked with squares and dots respectively. The inset shows the correlation of $\kappa_{B_*^{min}}$ with $\kappa_{TC}^{0.7}$. The dashed line with gradient=1 provides a guide to eye. In (b,d), the inset shows the correlation of B_*^{min}/E_x with $\sqrt{U_E}$.

We measured G_B for 19 devices at 40 mK, and 66 devices at 1.4 K. However, as shown in Fig. 5.13, we found the quadratic dependence of S_B on B fields for 16 devices at 40 mK and only 18 devices at 1.4 K respectively. For the other devices, G_B is almost constant or decreases slightly with increasing B fields. Fig. 5.13 illustrates two such devices that show almost constant G_B with B fields increasing from 0 to 8 T, for sample 1 at 40 mK (a) and 1.4 K (b) respectively. The percentage of devices showing a constant G_B is much higher at 1.4 K. This is because that G_{0T} is more strongly suppressed and S_B could be much less affected by B fields at 1.4 K than that at 40 mK. In a word, for the statistics of our measurements, there are only some devices that follow Eq. 5.5, and the other devices show constant G_B independent of B fields. B_*^{min}/E_x is mostly larger than 1.09, which does not fit with Eq. 5.6.

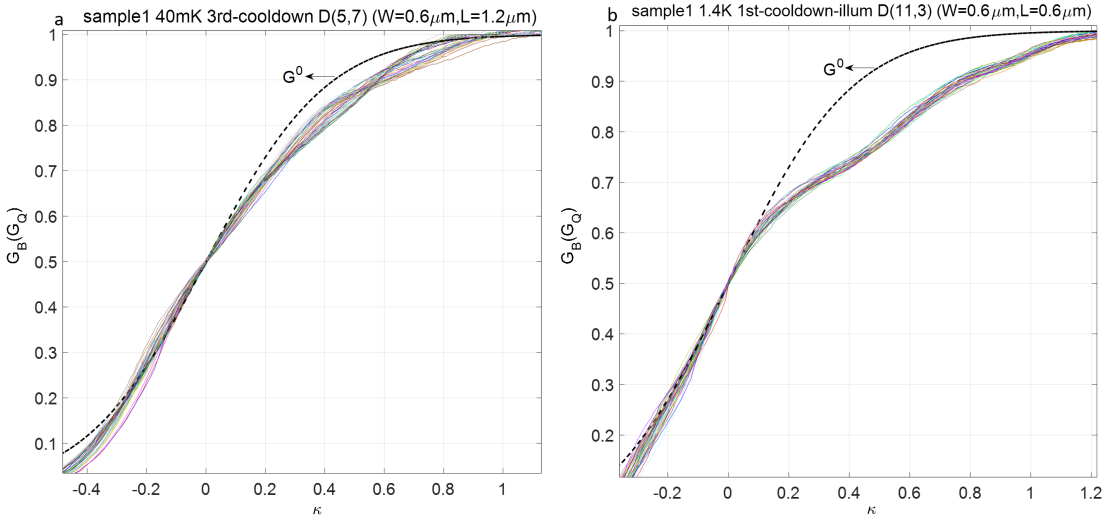

Figure 5.14: Two typical devices that show almost constant G_B with B fields increasing from 0 to 8 T, at 40 mK (a) and 1.4 K (b) respectively.

5.7 Summary

In this Chapter, first, we discuss interaction effects on the conductance suppression at fixed κ positions for different multiplexed devices in a cooldown. We find the conductance suppression is negatively correlated with E_x and E_x/E_y respectively, and is more correlated with E_x/E_y than that with E_x for the first three plateaus respectively, for different MUX samples in different cooldowns. This verifies the role of effective interaction strength on the 0.7 anomaly.

Second, we further verify the quadratic dependence of magnetoconductance suppression on B fields, at both 40 mK or 1.4 K respectivley. However, we do not verify the exponential suppression of B_* due to the effective interaction strength. This may be attributed to the already considerable conductance suppression at 0 T.

6

Statistics of Effective g Factors

6.1 Introduction

In a QPC, electron interactions are known to cause the 0.7 anomaly and an enhancement of the effective g factor g^*. As commonly reported, g^*=0.75-1.5 under in-plane B fields for GaAs QPCs [5, 28, 29, 53, 69, 70]. QPCs have also shown a promising candidate as the building block for spintronic applications where electron spin is used to store and process logical information [71]. For QPC operating as a spin injector and detector [72, 73], a magnetic field is commonly needed to break the spin degeneracy. This makes maximising g^* highly desirable, which reduces the B field needed to resolve the spin.

In Fig. 6.1a, Thomas et al. show g^* increases from the bulk value 0.44 (dashed line) for N=25, to around 1 for N<4 in GaAs [29]. In Fig. 6.1b-e, Burke et al. show g^* versus 2DEG carrier density by changing the top-gate voltage for 3 GaAs/AlGaAs QPCs [74]. They used the Cambridge W191 wafer, with a density of $1.8 \times 10^{11} cm^{-2}$ and a mobility of $2.7 \times 10^6 cm^2 V^{-1} s^{-1}$, which is similar to our wafer. In each panel, the red dashed square shows g^* for two QPCs without applying a top-gate voltage. These g^* inside the squares are basically stable with the increasing subband index.

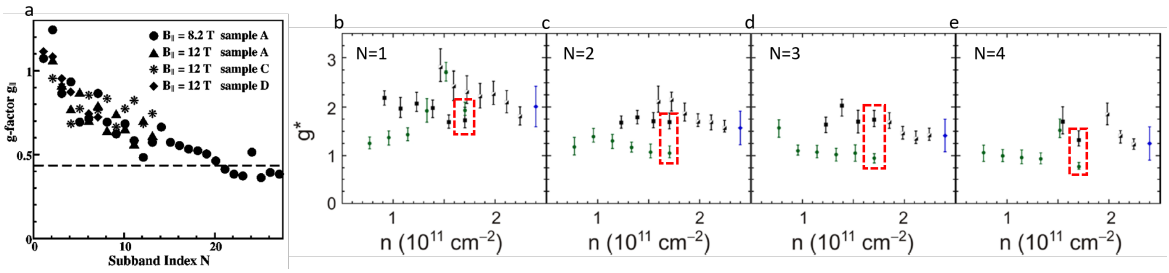

Figure 6.1: (a), In-plane g^* as a function of subband index N for GaAs/AlGaAs QPCs. Adapted from Ref. [29]. (b-e) g^* versus 2DEG carrier density by changing the top-gate voltage for 3 GaAs/AlGaAs QPCs, for the first four subbands respectively. In each panel, the red dashed square shows g^* for two QPCs without applying a top-gate voltage. Adapted from Ref. [74].

When extracting g^* by the linear fitting of the subband splitting energy (ΔE_{ss}) with B fields, there is an intercept, which is called the high-field offset (ΔE^{hfo}) by Koop et al. [5]

$$\Delta E_{ss} = g^* \mu_B B + \Delta E^{hfo} \tag{6.1}$$

where $\Delta E_Z = g^* \mu_B B$ is the Zeeman energy. In Fig. 6.2, Bauer et al. show both g^* and ΔE^{hfo} increase with U in both experiments (a-c) and theories (d-f).

Here, we realise measurements of g^* and ΔE^{hfo} in a number of QPCs in a single cooldown at 40 mK, using sample 1 (with QPC length varying from 0.1 to 2 μm and width fixed at 0.4 or 0.6 μm). We use $\Delta E_{N,N+1}$ to characterise U, and explore effects of $\Delta E_{N,N+1}$ on g^* and ΔE^{hfo} respectively in a statistical way. We measured $g^*_\perp$ and $\Delta E^{hfo}_\perp$ in the 2^{nd} cooldown, under in-plane magnetic fields perpendicular to the transport direction ($B_\perp$). We also measured the anisotropic $g^*_\parallel$ and $\Delta E^{hfo}_\parallel$ in the 3^{rd} cooldown, under in-plane magnetic fields parallel to the transport direction ($B_\parallel$).

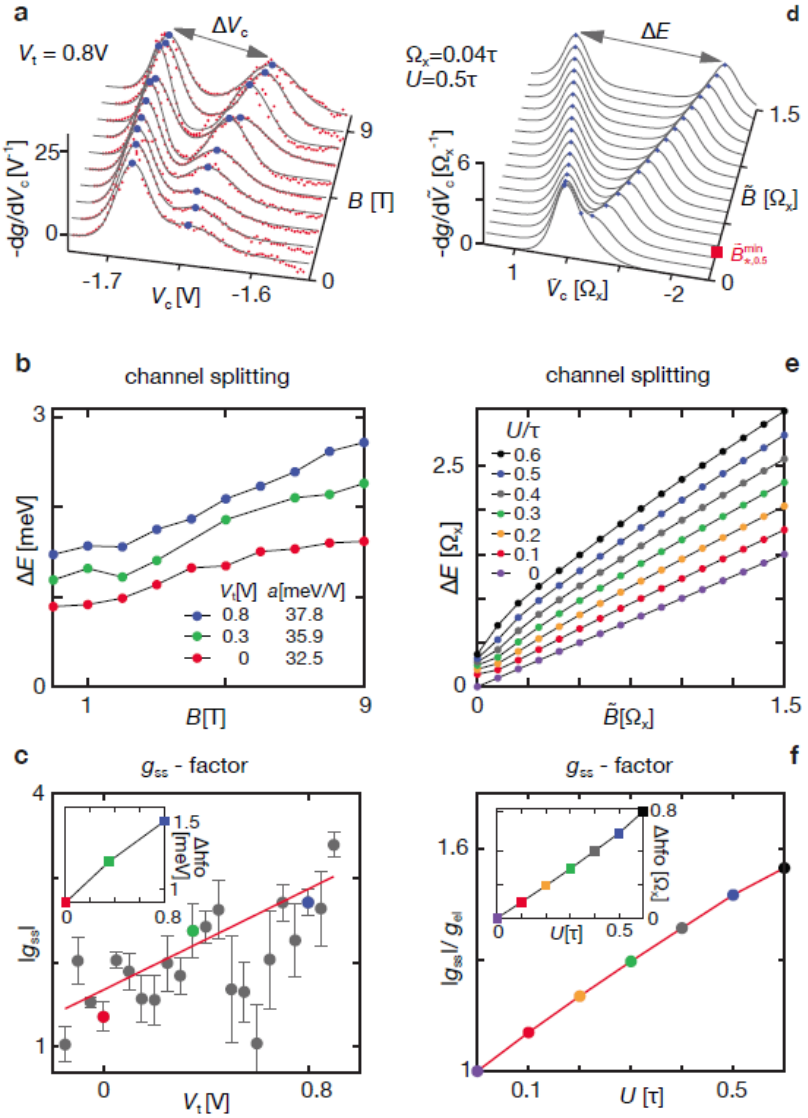

Figure 6.2: Interacting effects of U on g^* and ΔE^{hfo} in experiments (a-c) and theories (d-f). In (a-c), U is changed by applying a positive top gate voltage. In (f), the calculations show both g^* and ΔE^{hfo} (shown in the inset) increase with U. Adapted from [7].

6.2 Treatment of ΔE_{ss}

To extract the value of g^*, a common method was developed by Patel et al.[69], to find the V_G distance for splitting risers of TC_{SD}-ΔV_G^{rs}. $\Delta E_{rs} = \alpha \Delta V_G^{rs}$ is regarded as the subband splitting energy ΔE_{ss} in Eq. 6.1. In experiments, Fig. 6.3a shows the TC_{SD} map for a typical device D(6,11), sample 1 at 40 mK in the 2^{nd} cooldown. We can see the risers have been spin-resolved and split further apart with increasing B fields for each plateau. Fig. 6.3b shows G_B curves from 8 to 11.8 T. For each G_B curve for the first plateau, ΔE_{rs} is acquired by finding V_G^{rs} (marked with black dots) at the peaks of TC_{SD}. Fig. 6.3c shows the linear fitting of ΔE_{rs} as a function of $\widetilde{B}$ to extract $g_\perp^*$ and $\Delta E_\perp^{hfo}$ for different plateaus respectively. Fig. 6.3d shows acquired $g_\perp^*$ (read the left axis) and $\Delta E_\perp^{hfo}$ (read the right axis) as a function of subband index N.

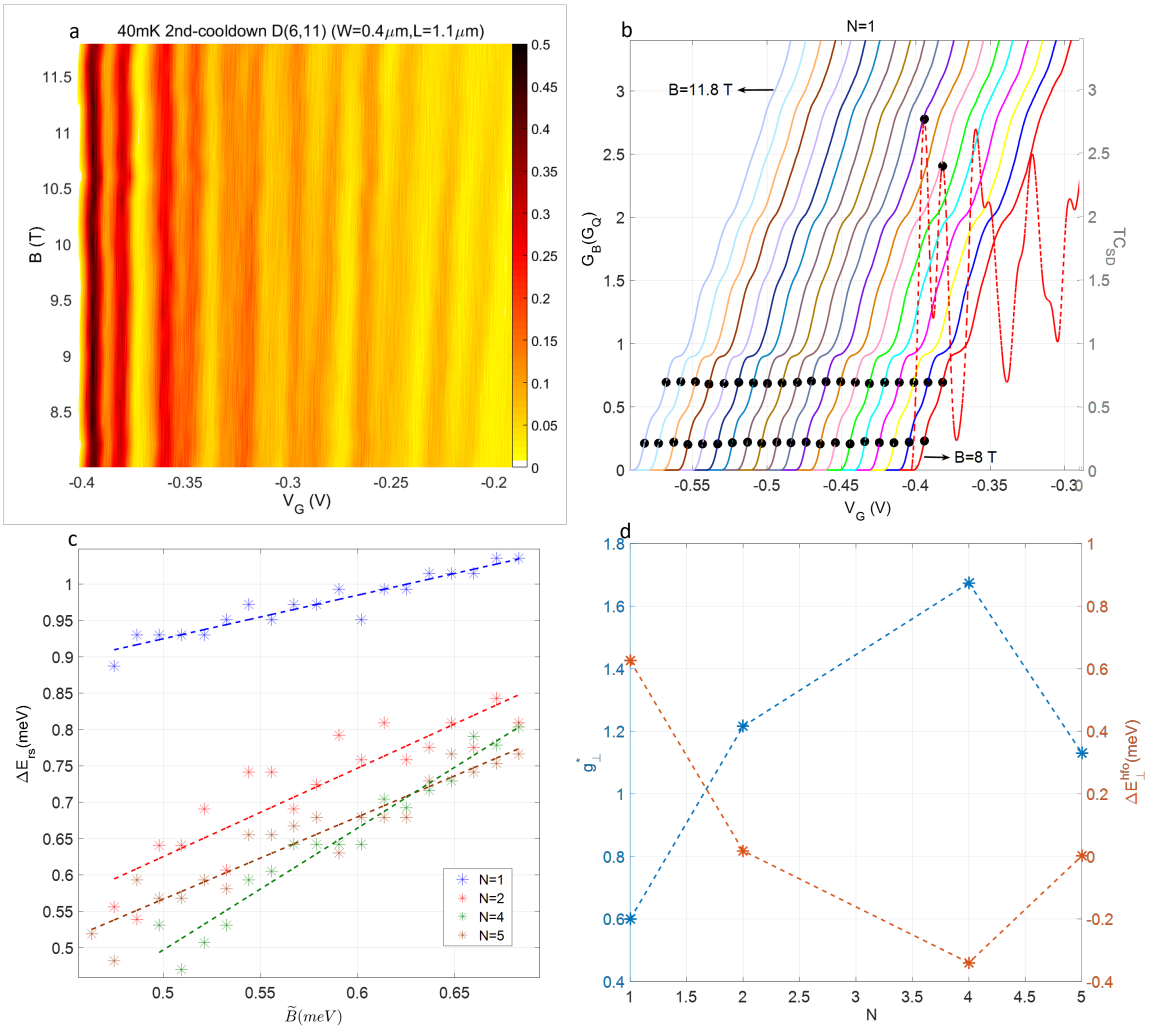

Figure 6.3: Extracting $g^*_\perp$ and $\Delta E^{hfo}_\perp$ for a typical device D(6,11), sample 1 at 40 mK in the 2^{nd} cooldown. (a), TC_{SD} map as a function of V_G and B fields from 8 to 11.8 T. (b), G_B curves (offset to the left in turn by 0.01 for clarity) from 8 to 11.8 T. The red dashed line shows TC_{SD} curve (read the right axis) at 8 T. For each G_B curve for the first plateau, V^{rs}_G positions are marked with black dots at the local peaks of TC_{SD}. (c), Linear fitting of ΔE_{rs} as a function of $\widetilde{B}$ for different plateaus respectively. (d), Acquired $g^*_\perp$ (read the left axis) and $\Delta E^{hfo}_\perp$ (read the right axis) as a function of N.

6.3 Comparisons of B_{ls} with B_{rs}

Fig. 6.4 shows calculated G_B^0 and TC^0 curves at each B step using Eq. 1.18, for $E_x = 1meV$ at 0 K (a,b) and 1.4 K (c,d) respectively. In Fig. 6.4a, the risers start splitting at 7.4 T (bold red line), which B field is called B_{rs}. The inset shows an almost linear dependence of B_{rs} on E_x at 0 K (red stars) and 1.4 K (blue stars) respectively. Larger E_x makes the risers split later at higher B_{rs}. Also, the thermal broadening at 1.4 K results in higher B_{rs} than that at 0 K. Fig. 6.5 shows calculated TC^0 maps for E_x=1 or 1.5 meV, at 0 or 1.4 K respectively.

Fig. 6.6a shows TC_{SD} map for a typical device D(16,15) at 40 mK in the 3^{rd} cooldown. Fig. 6.6b shows G_B curves from 3 to 9.6 T. Fig. 6.6c shows the Zeeman splitting of ΔE_{rs} as a function of $\widetilde{B}$ for the first plateau from 3 to 9.6 T. The linear Zeeman splitting starts at 3 T, which B field is called B_{ls}. The inset shows G_{0T} as a function of κ with $E_x = 0.93meV$. Thus $B_{rs} = 6.9T$ based on the expression of B_{rs} at 0 K (which is basically the same as B_{rs} at 40 mK) in Fig. 6.4a. This implies the risers already split at a lower $B_{ls} = 3T$ than $B_{rs} = 6.9T$. Fig. 6.6d shows comparisons of B_{ls} with B_{rs} for 11 devices, sample 1 at 40 mK in the 3^{rd} cooldown, for the first plateau. First, B_{ls} is positively correlated with B_{rs}, which is attributed to the role of E_x. Second, B_{ls} is smaller than B_{rs} for each device, because the interaction-induced magnetoconductance suppression makes the risers split at a lower B_{ls} than the non-interacting B_{rs}. Appendix Fig. A.16 compares B_{ls} with B_{rs} for another device.

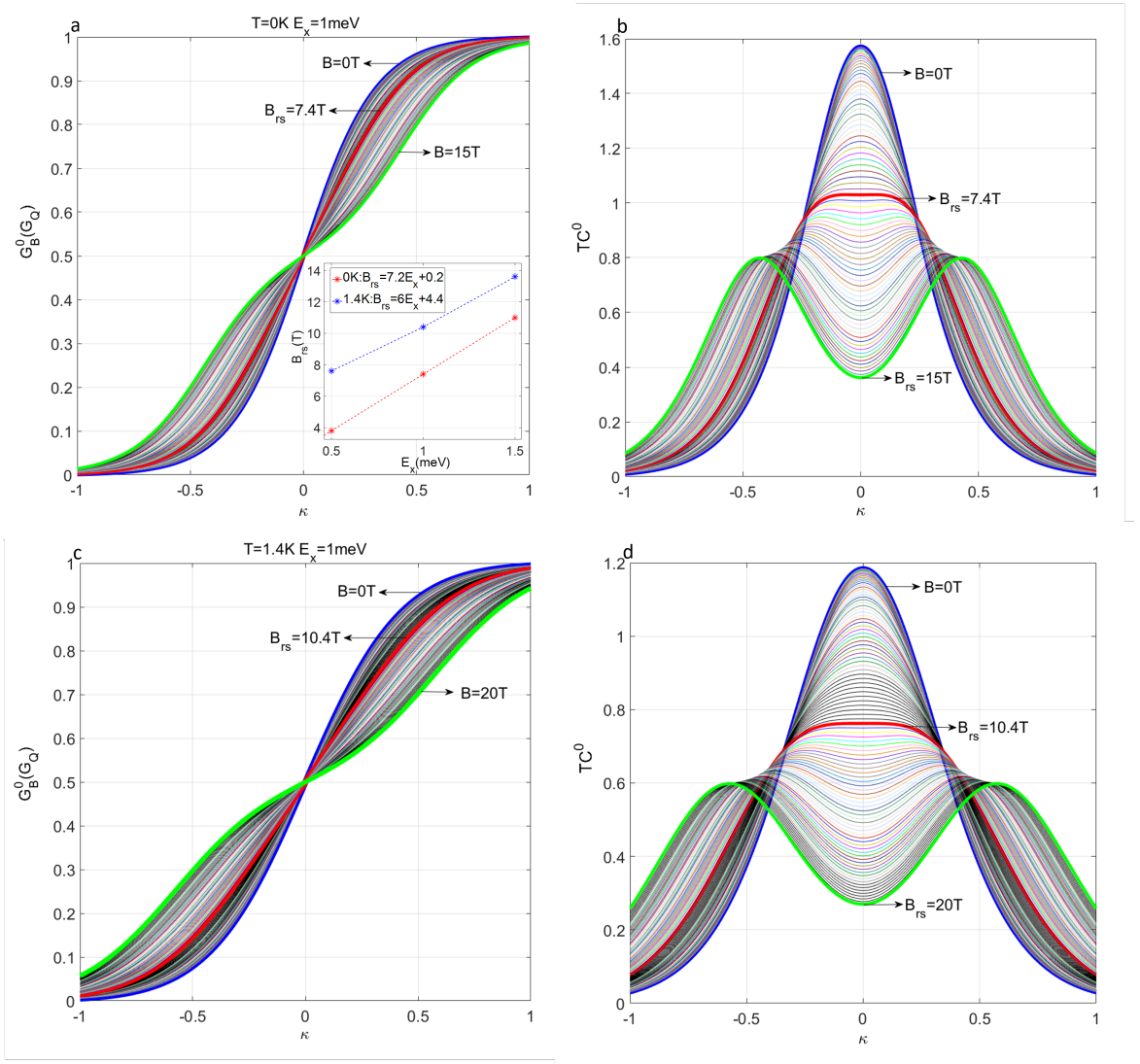

Figure 6.4: (a,b), Calculated G_B^0 (a) and TC^0 (b) as a function of κ from 0 to 15 T (bold green line), for $E_x = 1meV$ at 0 K. The risers start splitting at $B = B_{rs}$ (bold red line). The inset shows an almost linear dependence of B_{rs} on E_x at 0 K (red stars) and 1.4 K (blue stars) respectively. (c,d), Calculated G_B^0 (c) and TC^0 (d) for $E_x = 1meV$ at 1.4 K.

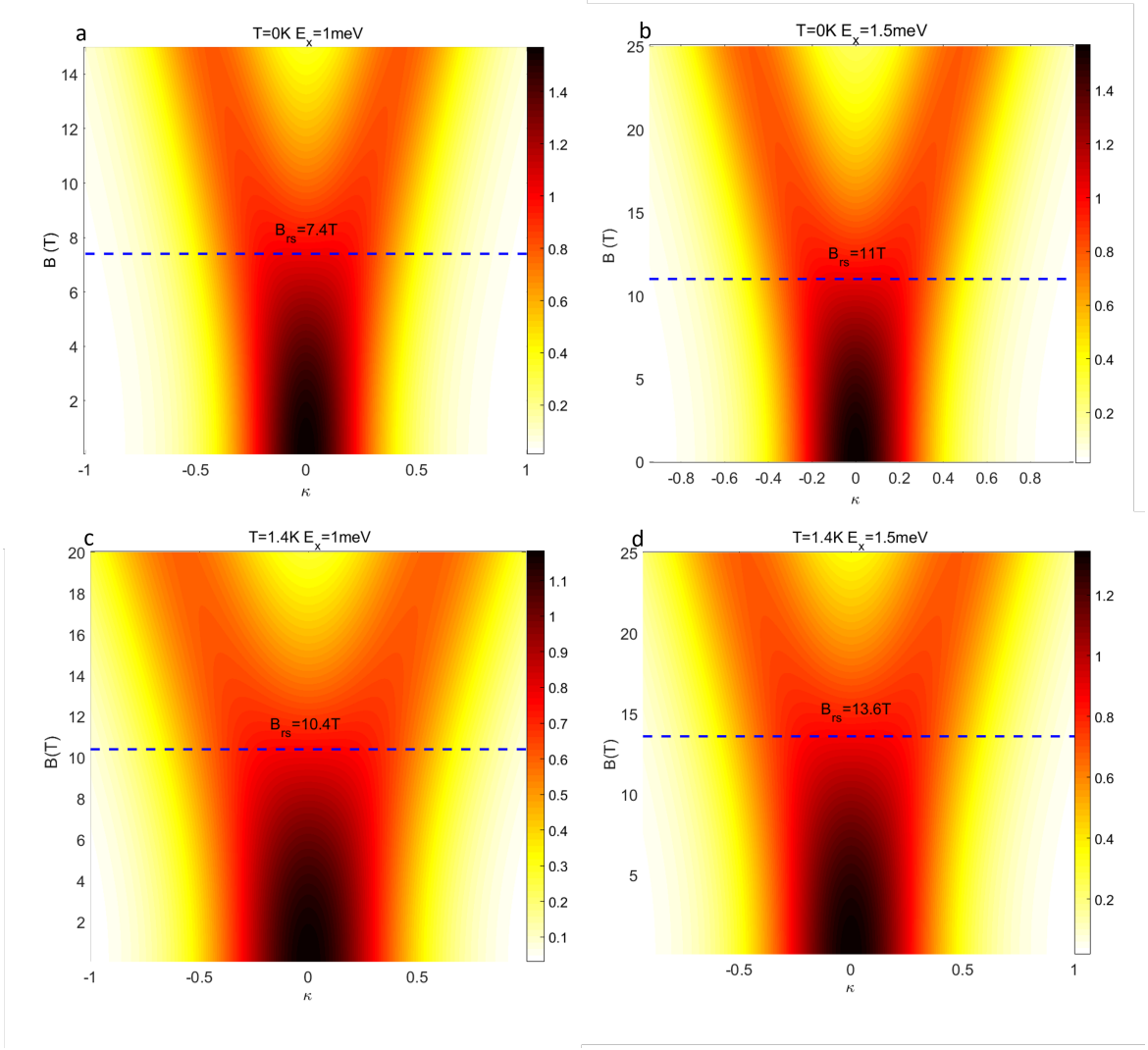

Figure 6.5: Calculated TC^0 as a function of κ and B for E_x=1 or 1.5 meV, at 0 or 1.4 K respectively. B_{rs} is marked with a dashed blue line in each panel.

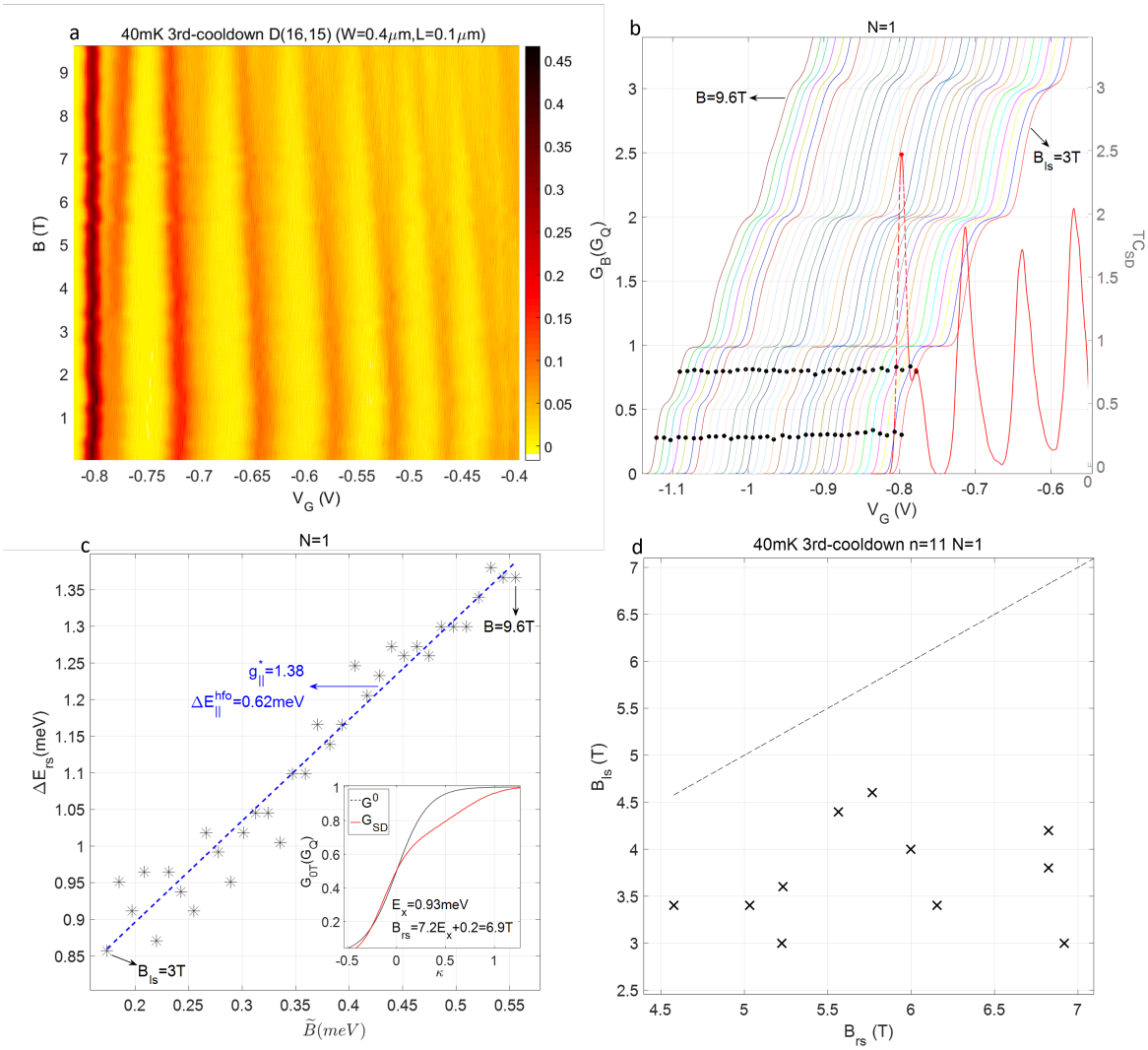

Figure 6.6: (a), TC_{SD} map for a device D(16,15), sample 1 at 40 mK in the 3^{rd} cooldown. (b), G_B curves (offset to the left in turn by 0.02) from $B_{ls} = 3T$ to 9.6 T. The red dashed line shows TC_{SD} curve (read the right axis) at 3 T. For each G_B curve for the first plateau, V_G^{rs} positions are marked with black dots at the local peaks of TC_{SD}. (c), Linear Zeeman splitting of ΔE_{rs} as a function of $\widetilde{B}$ for the first plateau from $B_{ls} = 3T$ to 9.6 T. The results of $g_{\|}^{*}$ and $\Delta E_{\|}^{hfo}$ are arrowed in the panel. The inset shows G_{0T} as a function of κ with $E_x = 0.93meV$. Thus $B_{rs} = 6.9T$. (d), Comparisons of B_{ls} with B_{rs} for 11 devices, sample 1 at 40 mK in the 3^{rd} cooldown, for the first plateau. The dashed line with gradient=1 provides a guide to eye. B_{ls} is positively correlated with B_{rs}. Each device has a lower B_{ls} than B_{rs}.

6.4 Comparisons of ΔE^{hfo} with ΔE_{rs}^{0T}

To understand the origin of ΔE^{hfo}, Fig. 6.7a shows TC_{SD} map for a typical device D(10,11), sample 1 at 40 mK in the 3^{rd} cooldown. The device shows the spontaneous risers-splitting at 0 T for the first plateau. The spontaneous risers-splitting is caused by the interaction-induced 0.7 anomaly transconductance suppression, since there is no spin polarisation at zero B field. Fig. 6.7b shows G_B curves from 0 to 8 T. The risers already split at 0 T for TC_{SD} curve (red dashed line, read the right axis). Fig. 6.7c shows ΔE_{rs} as a function of $\widetilde{B}$ for the first plateau from 0 to 11.8 T. ΔE_{rs} at 0 T is called ΔE_{rs}^{0T}. It is interesting to see ΔE_{rs} fluctuates around ΔE_{rs}^{0T} from 0 T. After $B = B_{ls}$, Zeeman splitting dominates, and ΔE_{rs} starts increasing linearly with B fields.

The inset in Fig. 6.7c compares $\Delta E_{\|}^{hfo}$ with ΔE_{rs}^{0T} for 7 devices that show the spontaneous risers-splitting, for sample 1 at 40 mK in the 3^{rd} cooldown for the first plateau. Appendix Fig. A.17 show ΔE_{rs} as a function of $\widetilde{B}$ from 0 T for the other 7 devices. $\Delta E_{\|}^{hfo}$ is positively correlated with ΔE_{rs}^{0T}, which is reasonable since both ΔE^{hfo} and ΔE_{rs}^{0T} increase with interaction strength U. We note that ΔE^{hfo} is not ΔE_{rs}^{0T}, and is smaller than ΔE_{rs}^{0T} as shown in the inset. This point is supported by the statistics of ΔE_{rs}^{0T} in 10 cooldowns at 40 mK or 1.4 K, as shown in Fig. 6.7d. The mean ΔE_{rs}^{0T} ranges from around 0.8 to 1.3 meV, which is much larger than the mean $\Delta E_{\|}^{hfo}$=0.5 meV for the first plateau.

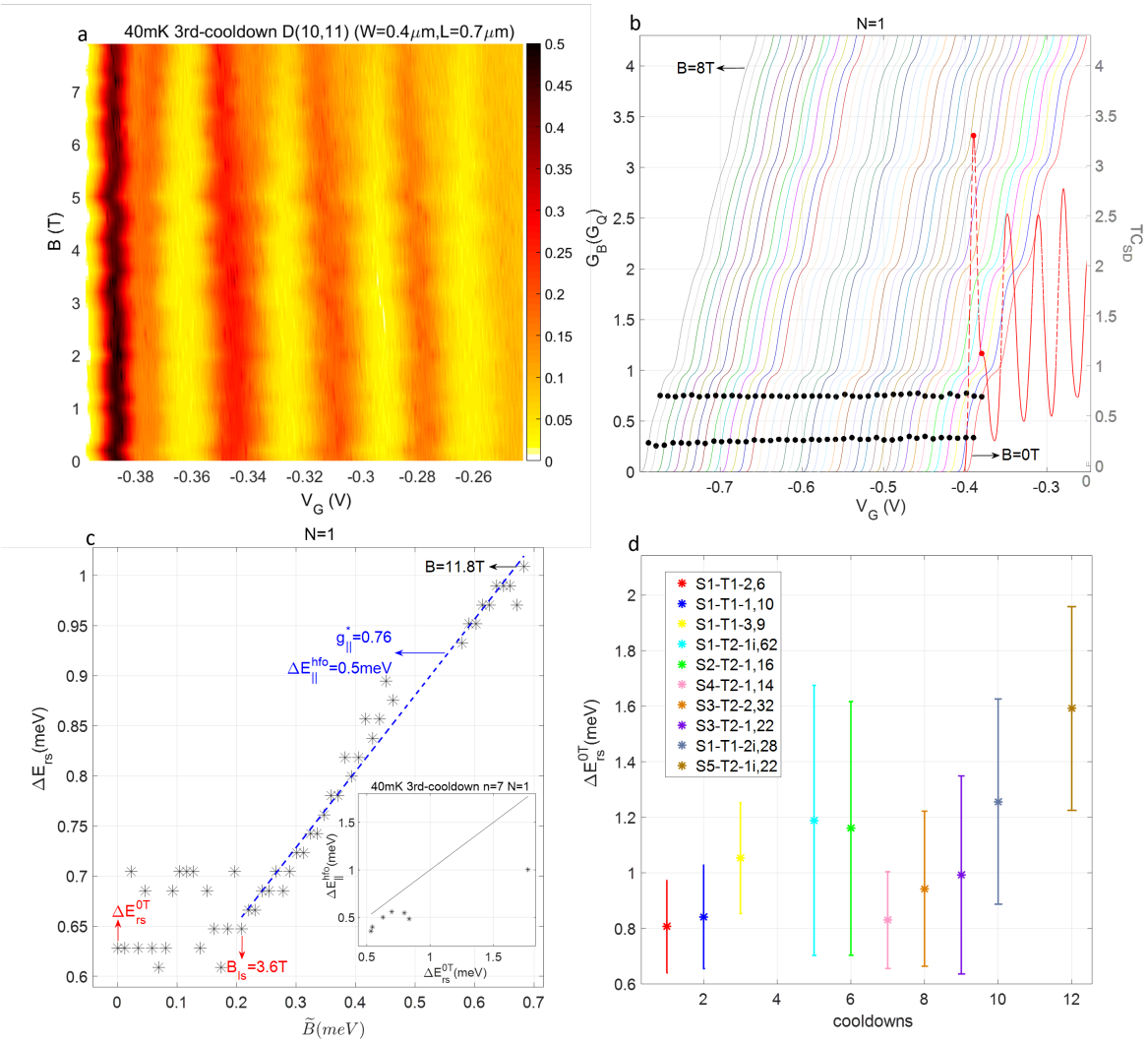

Figure 6.7: (a), TC_{SD} map for a typical device D(10,11), sample 1 at 40 mK in the 3^{rd} cooldown. The device shows the spontaneous risers-splitting at 0 T for the first plateau. (b), G_B curves from 0 to 8 T. The risers already split at 0 T for TC_{SD} curve (red dashed line, read the right axis). (c), ΔE_{rs} as a function of $\widetilde{B}$ for the first plateau from 0 to 11.8 T. ΔE_{rs} fluctuates around ΔE_{rs}^{0T} as arrowed from B=0 T, and starts increasing linearly with B fields from $B = B_{ls}$. The inset shows the positive correlation of ΔE^{hfo} with ΔE_{rs}^{0T} for 7 devices that show the spontaneous risers-splitting, for sample 1 at 40 mK in the 3^{rd} cooldown for the first plateau. Each device show smaller ΔE^{hfo} than ΔE_{rs}^{0T}. (d), Statistics of ΔE_{rs}^{0T} in 10 cooldowns at 40 mK or 1.4 K. In the legend, for instance, the symbol 'S1-T1-2, 6' refers to sample 1-at 40 mK-in the 2^{nd} cooldown in the dark-with 6 1D devices that show spontaneous risers-splitting. The symbol 'S1-T2-1i, 62' refers to sample 1-at 1.4 K-in the 1^{st} cooldown after illumination-with 62 1D devices that show spontaneous risers-splitting. The error bar represents the mean ± standard deviation for each cooldown.

6.5 Statistics of g^* and ΔE^{hfo}

For sample 1 at 40 mK, we obtain $g^*_\perp$ and $\Delta E^{hfo}_\perp$ for 22 devices in the 2^{nd} cooldown, and anisotropic $g^*_\parallel$ and $\Delta E^{hfo}_\parallel$ for 20 devices in the 3^{rd} cooldown, for the first four subbands respectively. Note that those devices show constant series resistence as a function of subband index. Appendix Fig. A.18 and A.19 show the extracting of $g^*_\perp$ and $\Delta E^{hfo}_\perp$ for 2 device in the 2^{nd} cooldown, and $g^*_\parallel$ and $\Delta E^{hfo}_\parallel$ for 2 device in the 3^{rd} cooldown respectively. Fig. 6.8a,b show statistics of $g^*_\perp$ and $\Delta E^{hfo}_\perp$ (in red colour), and $g^*_\parallel$ and $\Delta E^{hfo}_\parallel$ (in blue colour) for the first four subbands respectively. In Fig. 6.8a, the black error bar shows the error of linear fitting for $g^*_\perp$ for D(1,11). In Fig. 6.8b, the black error bar shows the error of linear fitting for $\Delta E^{hfo}_\perp$ for D(6,15).

First, anisotropic $g^*_\parallel$ and $\Delta E^{hfo}_\parallel$ have similar values with $g^*_\perp$ and $\Delta E^{hfo}_\perp$ respectively, which is the same as the measurements by Thomas et al [29]. Second, the means of g^* do not vary much for different plateaus. This is similar to the results of Burke et al. in Fig. 6.1. However, for a same plateau, g^* varies significantly in different devices with a standard deviation of around 0.4. This could be attributed to a broad variation of the potential confinement (measured by $\Delta E_{N,N+1}$) in different devices. Third, interestingly, the mean ΔE^{hfo} is largest for the first plateau, and drops fast for the higher plateaus. This agrees with the role of U on Δ^{hfo}, since U is only considerable for the first plateau, and is very weak for the higher plateaus.

Fig. 6.8c-h further shows correlations of $g^*_\perp$ (c-e) and $\Delta E^{hfo}_\perp$ (f-h) with the first three subband spacings respectively. Devices with a larger subband spacing $\Delta E_{N,N+1}$ roughly have larger $g^*_\perp$ (c-e) and $\Delta E^{hfo}_\perp$ (f-h) for the first three plateaus respectively. This supports the prediction that both g^* and ΔE^{hfo} increase with U.

Note that ΔE_{rs} is an approximation of ΔE_{ss}. ΔE_{rs} is almost equal to ΔE_{ss} at high B fields. However, ΔE_{rs} is smaller than ΔE_{ss} at low B fields, which causes an error of the fitted g^*. The reason lies in that the risers of transconductance TC are not at the same positions as the risers of $TC_\downarrow$ and $TC_\uparrow$ respectively. To cope with this, Bauer et al. use a pair of Gaussians to fit $TC_\downarrow$ and $TC_\uparrow$ [7]. We justify this method using non-interacting calculations in the Appendix Fig. A.20. For a comparison with the results using ΔE_{rs} in Fig. 6.8, we attempt to extract g^* and ΔE^{hfo} for the devices in Fig. 6.8 using the Gaussian method, as shown in the Appendix Fig. A.21 and A.22.

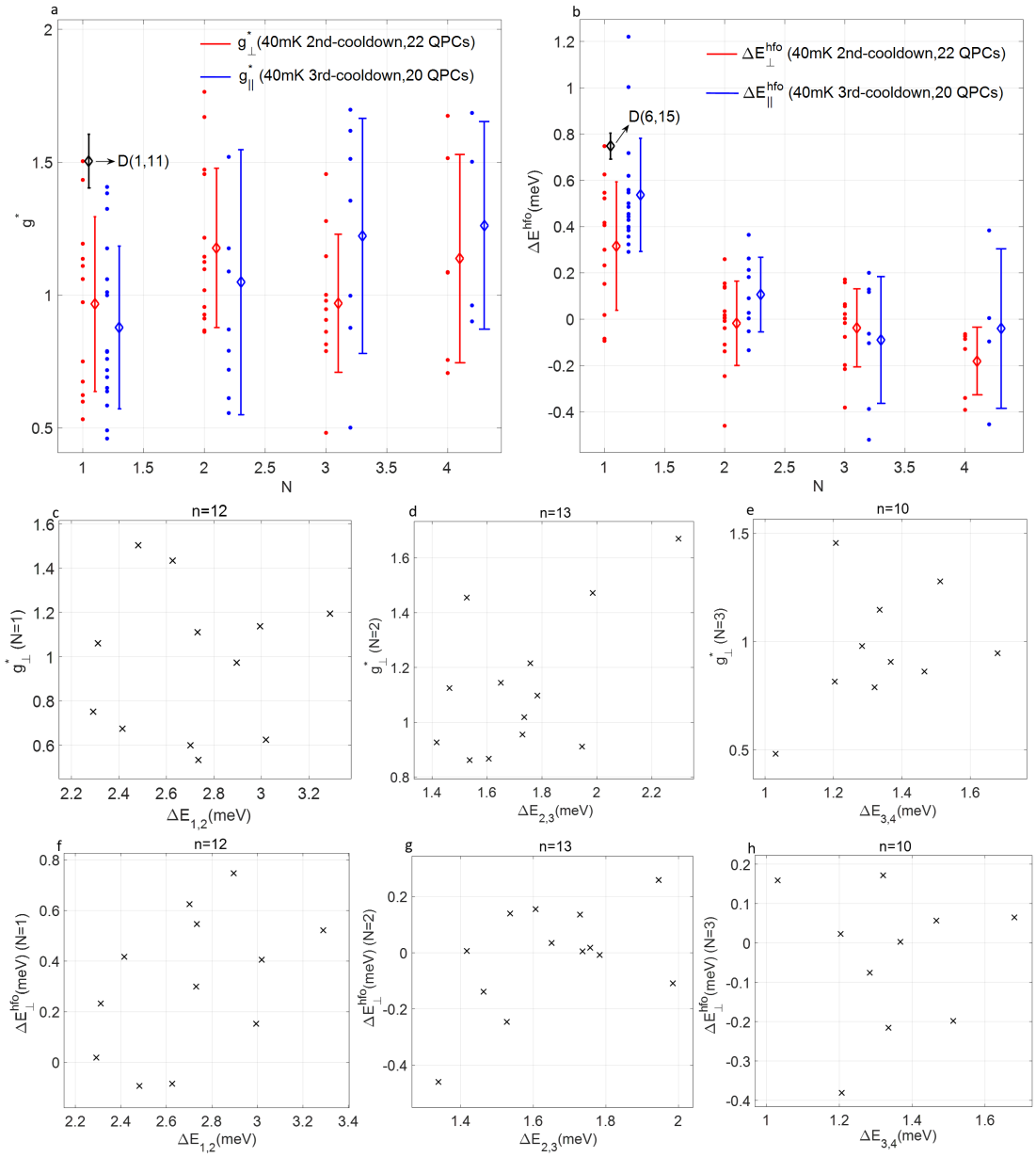

Figure 6.8: (a,b), Statistics of $g^*_\perp$ and $\Delta E^{hfo}_\perp$ (red symbols) for 22 devices in the 2^{nd} cooldown, and $g^*_\parallel$ and $\Delta E^{hfo}_\parallel$ (blue symbols, offset horizontally by 0.2 than red symbols) for 20 devices in the 3^{rd} cooldown, for sample 1 at 40 mK for the first four subbands respectively. The dot represents a value for each device. The error bar (offset horizontally by 0.1) represents the mean ± standard deviation. The two black error bars provide the fitted error of $g^*_\perp$ for D(1,11) in (a), and $\Delta E^{hfo}_\perp$ for D(6,15) in (b) respectively. (c-h), Positive correlations of $g^*_\perp$ (c-e) and $\Delta E^{hfo}_\perp$ (f-h) with the first three subband spacings respectively.

6.6 Summary

In this Chapter, first, we calculate the magnetic field B_{rs} at which the risers start splitting in transconductance. We show B_{rs} increases with E_x linearly at 0 K and 1.4 K respectively. In experiments, we find the magnetic field B_{ls}, at which the linear Zeaman splitting starts showing, is lower than B_{rs}. This implies the risers already split at a lower B field than B_{rs}, which is due to the interaction effect.

Second, we compare the high-field-offset ΔE^{hfo} with the zero-B-field ΔE_{rs}^{0T}. We find ΔE^{hfo} is smaller than ΔE_{rs}^{0T} in values, showing they are not a same physical quantity.

Third, we show the statistics of g^* and ΔE^{hfo} in $B_\perp$ and $B_\parallel$ fields respectively, for a number of devices for the first four plateaus. g^* shows a considerable range between devices for the same plateau, but the means of g^* does not change much for different plateaus. For ΔE^{hfo}, it is largest for the fist plateau, and drops fast for higher plateus. We further show that both g^* and ΔE^{hfo} have possitive correlatons with the potential confinement, which agrees with the prediction that g^* and ΔE^{hfo} increase with interaction strength.

7

DC-bias-induced 0.75 and 0.25 Anomalies

7.1 Introduction

Compared to the 0.7 anomaly, the 0.75 and 0.25 anomalies were discovered in the non-linear transport regime [29, 69]. For GaAs QPCs, Thomas et al. found the anomalies occur at around 0.85 and 0.3 G_Q [29], and Chen et al. found the DC-bias-induced anomalies occur at around 0.85 and 0.25 G_Q respectively [64–66]. Furthermore, the anomalies also occur in the narrow-gap materials. For $In_{0.75}Ga_{0.25}As$ QPCs, Simmonds et al. found the DC-bias-induced anomalies occur at around 0.75 and 0.25 G_Q [75], and Martin et al. found the DC-bias-induced anomalies occur at around 0.8 and 0.25 G_Q respectively [76], implying the anomalies are universal properties for 1D transport under a DC bias. People proposed a model that the DC-bias-induced anomalies are caused by the spin-splitting of the first 1D subband [64–66, 77]. In this way, QPC could be used as an all-electrical spin injection and detection without ferromagnetic contacts or applied magnetic fields, where the 0.25 anomaly under a DC bias is regarded as a spin-polarised current [78].

In this Chapter, we will discuss the statistical behaviours of the 0.75 and 0.25 anomalies in a large number of devices, and propose a DC-bias-induced spin-splitting model to explain the formation and development of the anomalies.

7.2 DC-bias-induced spin-splitting model

The 0.75 and 0.25 anomalies can be observed in a DC bias spectroscopy. Fig. 7.1a shows a DC bias spectroscopy for a typical device D(16, 10), sample 1 at 40 mK, at a DC bias V_{DC} from -4 to 4 mV (step=0.2 mV). Fig. 7.1b shows the differential conductance G_{ac} (i.e. G_{SD}) at positive V_{DC} steps. We can see the 0.7 anomaly suppression at V_{DC}=0 (red curve). We note that the 0.75 anomaly is only formed after a DC bias is applied, which has a different origin with the 0.7 anomaly occurring in the linear regime. The 0.75 and 0.25 anomalies start showing up (by observing the local minimum of TC_{SD}), at V_{DC}=0.6 mV (called 0.75 anomaly start bias $V_{DC}^{0.75s}$) and 1.4 mV (called 0.25 anomaly start bias $V_{DC}^{0.25s}$) respectively. As the DC bias increases, the 0.75 anomaly disappears and the 0.25 anomaly develops gradually to a lower value of differential conductance, accompanying with the 1.25 anomaly appearing. By contrast, Fig. 7.1c shows G_{ac} curves at negative V_{DC} steps, showing $V_{DC}^{0.75s}$=-0.6 meV and $V_{DC}^{0.25s}$=-1.4 meV.

We also calculate the corrected source-drain dc conductance G_{dc} using Eq. 3.2, which can be used to track the subband energy. G_{ac} (G_{dc}) values of the 0.75 and 0.25 anomalies at the minimum of dG_{ac}/dV_G (dG_{dc}/dV_G) are called $G_{ac}^{0.75}$ and $G_{ac}^{0.25}$ ($G_{dc}^{0.75}$ and $G_{dc}^{0.25}$) respectively. In a similar way, G_{ac} and G_{dc} values of the 0.75 (0.25) anomaly when the anomaly starts showing up at $V_{DC}^{0.75s}$ ($V_{DC}^{0.25s}$), are called $G_{ac}^{0.75s}$ and $G_{dc}^{0.75s}$ ($G_{ac}^{0.25s}$ and $G_{dc}^{0.25s}$) respectively. In Fig. 7.1d, $G_{ac}^{0.75}$ and $G_{ac}^{0.25}$ ($G_{dc}^{0.75}$ and $G_{dc}^{0.25}$) are arrowed in the black solid (dashed) curve at V_{DC}=2 mV. $G_{ac}^{0.75s}$ and $G_{ac}^{0.25s}$ positions are also marked at $V_{DC}^{0.75s}$=0.6 mV (red curve) and $V_{DC}^{0.25s}$=1.4 mV (blue curve) respectively.

To explain the anomaly behaviours, we come up with a phenomenological model in Fig. 7.2, which is modified from the spontaneous spin polarisation model [64–66, 77]. First, in Fig. 7.1a, it is interesting to see the first riser does not split immediately once applying the DC bias, whereas the second and third risers split normally. This is a common phenomenon in every DC bias measurement at 40 mK or 1.4 K. To explain this, we propose the first assumption: when sweeping V_G in the backward direction to increase the conductance from zero, once the first subband edge crosses the higher chemical potential (supposed at source, μ_s), its subband energy experiences a sudden drop with a value ΔE_{drop}. This means the first subband energy decreases swiftly only within a few steps in V_G. As a result, the first riser does not split until $e|V_{DC}|$ is larger than ΔE_{drop}. This speculation has also been proposed in Ref. [79]. Second, to explain how the DC bias causes the spin splitting, we make the second assumption: the pinning mechanism. After the first spin-degenerate subband passes though μ_s during a sudden drop, the spin-up subband (1↑) pins at μ_s until the spin-down subband (1↓) passes

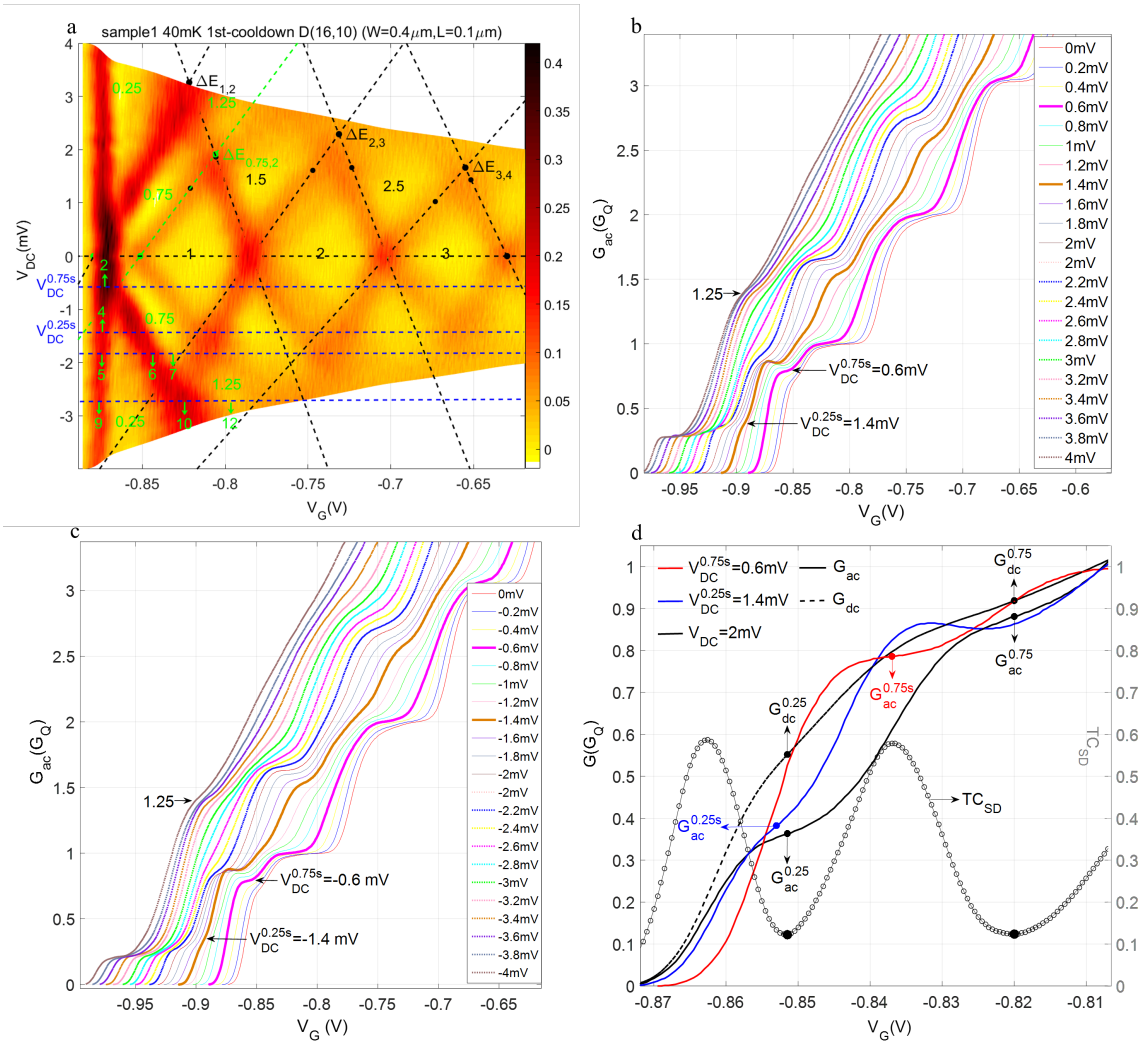

Figure 7.1: The 0.75 and 0.25 anomalies in a DC bias spectroscopy for a device at 40 mK. (a), DC bias spectroscopy for a device D(16,10), sample 1 at 40 mK. The conductance of normal and anomalous plateaus are shown with black and green numbers in units of G_Q respectively. (b,c), G_{ac} curves from V_{DC}=0 to 4 mV (offset to the left in turn by 0.005 for clarity) at positive (b) and negative (c) V_{DC} steps respectively. G_{ac} at the steps of $V_{DC}^{0.75s}$ and $V_{DC}^{0.25s}$ are shown in bold colours, for which the 0.75 and 0.25 anomalies start showing up respectively. (d), G_{ac} (black solid curve, $G_{ac}^{0.75}$ and $G_{ac}^{0.25}$ are arrowed) and G_{dc} (black dashed curve, $G_{dc}^{0.75}$ and $G_{dc}^{0.25}$ are arrowed) at V_{DC}=2 mV. G_{ac} curves at $V_{DC}^{0.75s}$ (red curve, $G_{ac}^{0.75s}$ is arrowed) and $V_{DC}^{0.25s}$ (blue curve, $G_{ac}^{0.25s}$ is arrowed) respectively.

though the lower drain chemical potential (μ_d), resulting in the opening of an spin gap. Afterwards, 1↓ passes through μ_d and 1↑ passes through μ_s simultaneously, resulting in a DC-bias-induced spin gap (called ΔE_{DC}) being just equal to $e|V_{DC}|$.

Fig. 7.2(1-5) shows the schematic of the subband positions when 1↓ has dropped downward by a value ΔE_{drop} below μ_s, with the increasing V_{DC}. Fig. 7.2(1-5) corresponds to the positions along the riser line of the 0.25 anomaly at around the same V_G position as arrowed in Fig.7.1a.

In Fig. 7.2(1), at a small DC bias, although 1↓ and 1↑ already have a spin gap $\Delta E_{DC} = e|V_{DC}|$, the first riser does not split, since both 1↓ and 1↑ have crossed μ_d after the sudden drop.

Fig. 7.2(2) shows the formation of the 0.75 anomaly after the sudden drop, when V_{DC} increases to be $e|V_{DC}^{0.75s}| = \Delta E_{drop}/2$, which corresponds to $V_{DC}^{0.75s} = -0.6mV$ as marked in Fig. 7.1a. Fig. 7.2(3) shows the subbands of the 0.75 anomaly with $G_{ac}^{0.75} = 0.75G_Q$. μ_s and μ_d both populating 1↓ contributes 0.5 G_Q, and μ_s populating 1↑ contributes 0.25 G_Q to $G_{ac}^{0.75}$.

Fig. 7.2(4) shows the formation of the 0.25 anomaly after the sudden drop, when V_{DC} increases further to be $e|V_{DC}^{0.25s}| = \Delta E_{drop}$, which corresponds to $V_{DC}^{0.25s} = -1.4mV$ as marked in Fig. 7.1a. We can see the 0.25 anomaly starts with the differential conductance $G_{ac}^{0.25s} = 0.5G_Q$. μ_d crossing the edge of 1↓ contributes 0.375 G_Q, and μ_s crossing the edge of 1↑ contributes 0.125 G_Q to $G_{ac}^{0.25s}$. Fig. 7.2(5) shows the subbands of the 0.25 anomaly with $G_{ac}^{0.25} = 0.375G_Q$. Since $e|V_{DC}| > \Delta E_{drop}$, after the sudden drop, 1↓ has not arrived at μ_d yet (contributing 0.25 G_Q to $G_{ac}^{0.25}$), and the edge of 1↑ pins at μ_s until 1↓ crosses μ_d (contributing 0.125 G_Q to $G_{ac}^{0.25}$), which gives rise to the 0.25 anomaly.

Thus, the 0.25 anomaly is formed at the differential conductance 0.5 G_Q as shown in Fig. 7.2(4), and evolves to 0.375 G_Q with the increasing V_{DC} as shown in Fig. 7.2(5). This explains why the 0.25 anomaly moves from around 0.5 to 0.3 G_Q in Fig. 7.1b. In addition, combining $e|V_{DC}^{0.75s}| = \Delta E_{drop}/2$ in Fig. 7.2(2) and $e|V_{DC}^{0.25s}| = \Delta E_{drop}$ in Fig. 7.2(4), the value of $V_{DC}^{0.25s}$ should be twice that of $V_{DC}^{0.75s}$. Thus, we can check $V_{DC}^{0.25s}/V_{DC}^{0.75s}$ in experiments for a verification. In Fig. 7.1b, $V_{DC}^{0.25s}/V_{DC}^{0.75s}$=1.4 mV/0.6 mV=2.3, which is satisfactory considering the DC-dependence measurement is performed at a step size of 0.2 mV.

Compared to G_{ac} that only changes in quantised steps when the subband intercepts μ_s or μ_d, however, G_{dc} changes gradually when the subband moves between μ_s and μ_d, which records the information of subband energy. For the 0.75 anomaly depicted in Fig. 7.2(3), we can refer to $G_{dc}^{0.75}$ to track the subband energy of 1↑ with reference

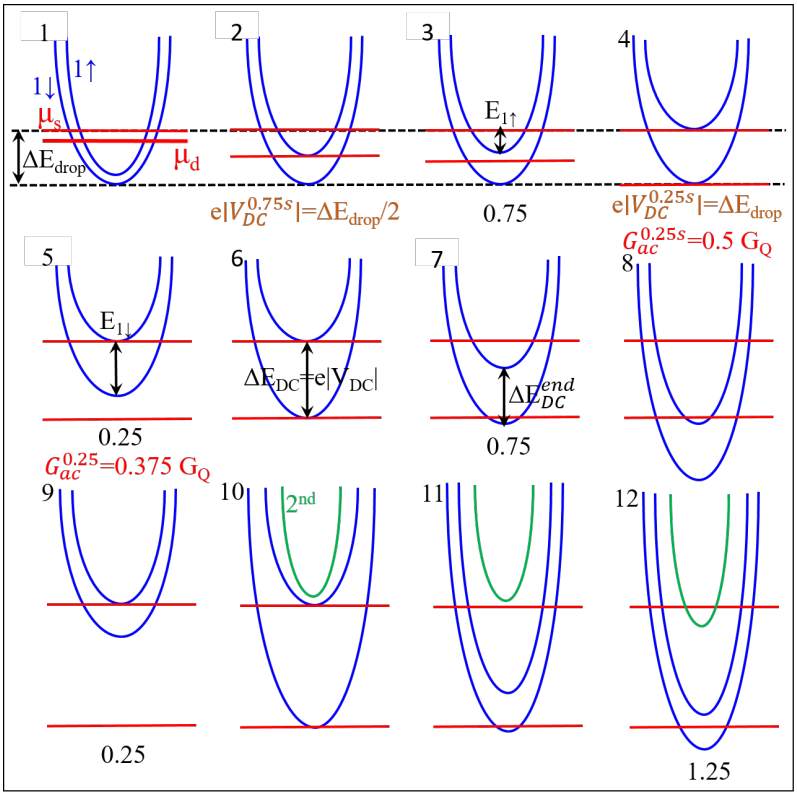

Figure 7.2: Schematic of a DC-bias-induced spin-splitting model. (1-5), Schematic of subband positions with the increasing V_{DC}, after the sudden drop of ΔE_{drop} for 1↓. The positions of (1-5) in a spectroscopy are arrowed in Fig. 7.1a. In (1), at a small V_{DC}, the risers does not split. In (2), the 0.75 anomaly is formed after the sudden drop at $e|V_{DC}^{0.75s}| = \Delta E_{drop}/2$. (3) shows the subbands for the 0.75 anomaly. $G_{dc}^{0.75}$ can be used to track the subband energy of 1↑: $E_{1\uparrow} = e|V_{DC}|(2G_{dc}^{0.75}/G_Q - 1)$. In (4), the 0.25 anomaly is formed with the differential conductance $G_{ac}^{0.25s} = 0.5G_Q$ after the sudden drop, at $e|V_{DC}^{0.25s}| = \Delta E_{drop}$. (5) shows the subbands for the 0.25 anomaly with the differential conductance $G_{ac}^{0.25} = 0.375G_Q$. $G_{dc}^{0.25}$ can be used to track the subband energy of 1↓: $E_{1\downarrow} = e|V_{DC}|(2G_{dc}^{0.25}/G_Q)$. (6-8), The subband movements with the increasing V_G, at the same DC bias as (5). In (1-6), the DC-bias-induced spin gap ΔE_{DC} is equal to $e|V_{DC}|$. In (7), after a pinning-energy-release drop for 1↑, the final DC-bias-induced spin gap ΔE_{DC}^{end} returns to be ΔE_{drop}. As the DC bias increases further, (9-12) shows how the 1.25 anomaly is formed with the increasing V_G at a same DC bias.

to μ_s (called $E_{1\uparrow}$, as marked in Fig. 7.2(3)): $E_{1\uparrow} = e|V_{DC}|(2G_{dc}^{0.75}/G_Q - 1)$ [64]. Similarly, for the 0.25 anomaly depicted in Fig. 7.2(5), the subband energy of $1\downarrow$ with reference to μ_s (called $E_{1\downarrow}$, as marked in Fig. 7.2(5)) can be measured using $G_{dc}^{0.25}$: $E_{1\downarrow} = e|V_{DC}|(2G_{dc}^{0.25}/G_Q)$ [64].

Next, at the same DC bias as Fig. 7.2(5), Fig. 7.2(6-8) (see corresponding markers in Fig.7.1a) shows the movement of subbands with the increasing V_G. In Fig. 7.2(6), as V_G increases, $1\downarrow$ moves downward to μ_d and $1\uparrow$ keeps pinning at μ_s (for an energy range of $e|V_{DC}| - \Delta E_{drop}$), the spin gap is enlarged to be $\Delta E_{DC} = e|V_{DC}|$ again. Thus, at a large DC bias, the spin gap first opens from zero to be ΔE_{drop} after the sudden drop, and then increases to be $e|V_{DC}|$ along with the backward sweep of V_G during the 0.25 plateau region. To summarise, in Fig. 7.2(1-6), $\Delta E_{DC} = e|V_{DC}|$ with increasing V_{DC}, implying that the pinning mechanism could enable a continuous manipulation of spin gap simply by applying a DC bias voltage.

In Fig. 7.2(7), as V_G increases further, $1\downarrow$ and $1\uparrow$ pass through μ_s and μ_d simultaneously, and the 0.75 plateau is formed (see the corresponding marker in Fig.7.1a). Then Fig. 7.2(8) shows the formation of the first plateau after $1\uparrow$ had passed through μ_d. In Fig. 7.1a, it is interesting to see the riser line of the 0.75 plateau is almost parallel to that of the first plateau (green dashed line). This parallel distance of V_G in energy (called ΔE_{DC}^{end}) is basically equal to $\Delta E_{1,2} - \Delta E_{0.75,2}$ as marked in Fig. 7.1a. This means that $1\uparrow$ moves downward with a same potential distance, from crossing μ_s (riser of the 0.75 plateau) to arrive at μ_d (riser of the first plateau). However, this is contradictory with the fact that the potential distance between μ_s and μ_d (i.e. $e|V_{DC}|$) is changing. To explain this, we propose the third assumption: when $1\uparrow$ crosses μ_s after pinning there for an energy range of $e|V_{DC}| - \Delta E_{drop}$, it will release that pinning energy and drop downward by the same $e|V_{DC}| - \Delta E_{drop}$, as shown in Fig. 7.2(7). After the drop, the final DC-bias-induced spin gap ΔE_{DC}^{end} (as marked in Fig. 7.2(7)) returns to be ΔE_{drop}, which accounts for the fact that two riser lines are parallel. Combining $e|V_{DC}^{0.25s}| = \Delta E_{drop}$ in Fig. 7.2(4) and $\Delta E_{DC}^{end} = \Delta E_{drop}$ in Fig. 7.2(7), we can compare ΔE_{DC}^{end} to $e|V_{DC}^{0.25s}|$ in experiments to verify this assumption. In Fig. 7.1a, $\Delta E_{DC}^{end} \approx \Delta E_{1,2} - \Delta E_{0.75,2}$=3.264 mV-1.909 mV=1.355 mV, which is almost equal to $e|V_{DC}^{0.25s}|$=1.4 mV, showing an evidence of the assumption above.

Moreover, in Fig. 7.1b,c, we can see the 0.25 anomaly is directly followed by the 1.25 anomaly at a large DC bias. Fig. 7.2(9-12) illustrates the formation of 1.25 anomaly at a same DC bias with the increasing V_G (see corresponding markers in the spectroscopy in Fig.7.1a). Fig. 7.2(9) shows the riser of the 0.25 anomaly after the sudden drop. In Fig. 7.2(10), as V_G increases, since the large $e|V_{DC}|$ is almost

comparable to the first subband spacing, 1↑ pins at μ_s for a long energy range and the second subband edge already moves close to μ_s. In Fig. 7.2(11), after 1↑ crosses μ_s after the pinning-energy-release drop, the second subband arrives at μ_s almost at the same time. Then Fig. 7.2(l2) shows the 1.25 plateau is formed after the second subband passes through μ_s (1↓ and 1↑ contribute 0.75 G_Q, and the second subband contributes 0.5 G_Q to the 1.25 anomaly respectively).

7.3 Statistical behaviours for the formation and development of the 0.75 and 0.25 anomalies

In experiments, Fig. 7.3 shows the formation and development of the 0.75 and 0.25 anomalies at positive and negative V_{DC} steps respectively, for two typical devices for smaple 1 at 40 mK. In Fig. 7.3b,c,e,f, there is no obvious 0.7 anomaly at zero DC bias whereas the 0.75 anomaly always shows up at $V_{DC}^{0.75s}$, supporting the model that the 0.75 anomaly does not develop from the 0.7 anomaly.

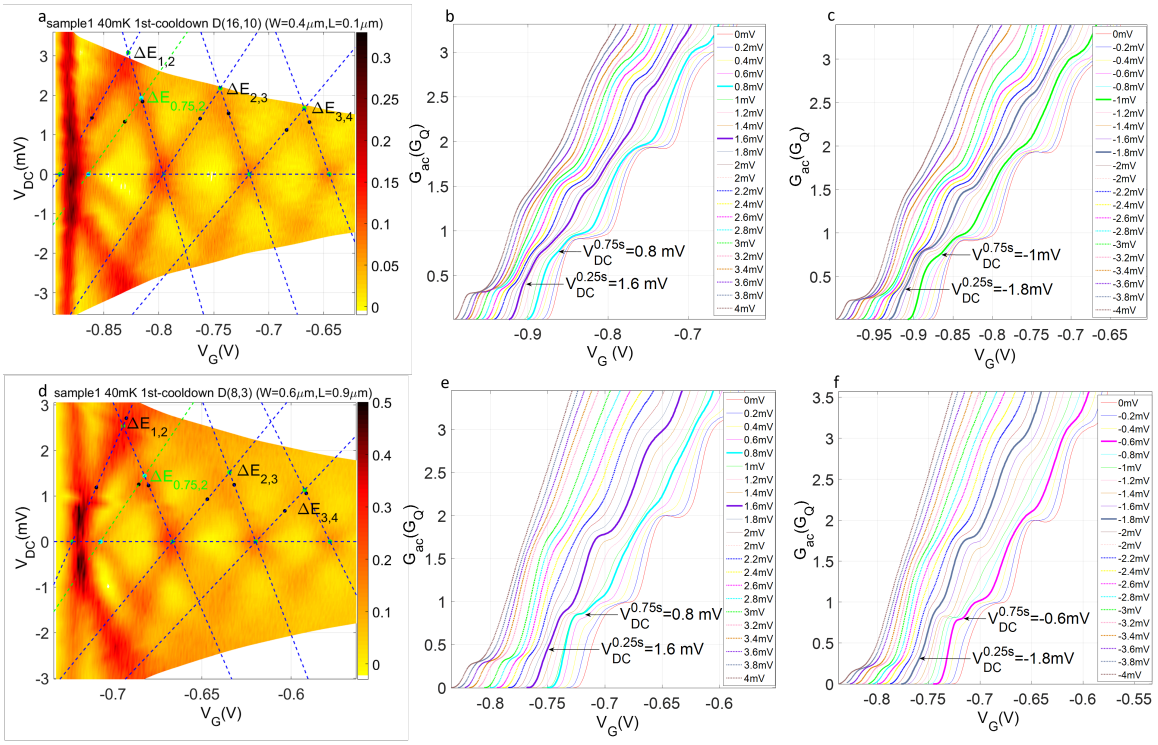

Figure 7.3: Spectroscopy maps (a,d); and formation and development of the 0.75 and 0.25 anomalies at positive (b,e) and negative (c,f) V_{DC} steps for D(16,15) and D(8,3), sample 1 at 40 mK. In (b,c,e,f), G_{ac} at $V_{DC}^{0.75s}$ and $V_{DC}^{0.25s}$ are shown in bold lines, for the formation of the 0.75 and 0.25 anomalies respectively.

With regard to the statistical behaviours for the conductance development of the anomalies with increasing V_{DC}, Fig. 7.4a shows statistics of $G_{ac}^{0.75}$ (diamond-marked error bars) and $G_{dc}^{0.75}$ (square-marked error bars) at $V_{DC} = \pm 1$, ± 2 and ± 3 mV respectively, for sample 1 at 40 mK with 100 spectroscopies. For statistics of $G^{0.75}$, we only processed partial spectroscopies in which the 0.75 anomaly can be observed clearly, thus $Y^{0.75}$ (the ratio of acquired $G^{0.75}$ count with spectroscopy count 100, read

the right axis) is not high at each V_{DC}. We can see the means of $G_{ac}^{0.75}$ and $G_{dc}^{0.75}$ are basically stable at 0.75-0.85 G_Q, and are overall symmetrical at positive and negative V_{DC} respectively.

For statistics of $G^{0.25}$, we processed all spectroscopies since the 0.25 anomaly is more evident to observe than the 0.75 anomaly. Fig. 7.4b shows the statistics of $G_{ac}^{0.25}$ (diamond-marked error bars) and $G_{dc}^{0.25}$ (square-marked error bars) at $V_{DC} = \pm 2$, ± 3 and ± 4 mV for the same 100 spectroscopies. We can see the yield of the 0.25 anomaly ($Y^{0.25}$, the ratio of acquired $G^{0.25}$ count with spectroscopy count 100) commonly increases to almost 100% with increasing V_{DC}, implying the realisation of a complete spin-polarised current at a large DC bias. For the case of positive V_{DC}, $G_{ac}^{0.25}$ mostly falls from around 0.45 to 0.3 G_Q with increasing V_{DC}, which fits well with the model that $G_{ac}^{0.25}$ starts at 0.5 G_Q and develops to 0.375 G_Q as shown in Fig. 7.2(4,5). However, for the case of negative V_{DC}, $G_{ac}^{0.25}$ is lower than the counterpart at the symmetrical value of positive V_{DC}. In addition, $G_{dc}^{0.25}$ changes from around 0.5 to 0.3 G_Q with increasing V_{DC}, indicating that $1\downarrow$ moves from a position at around μ_d, to a position below μ_s around 0.6 $e|V_{DC}|$ based on the $E_{1\downarrow}$ expression in Fig. 7.2(5). Appendix Fig. A.23-A.28 shows the statistical behaviours for the conductance development of the 0.75 and 0.25 anomalies, in more DC-dependence measurements for sample 1-5 at 40 mK or 1.4 K.

Fig. 7.4c,d shows statistics of conductance (c) and DC bias (d) when the anomalies start showing up for samples 1-5 in 9 cooldowns at 40 mK or 1.4 K. In Fig. 7.4c, first, for $G_{ac}^{0.75s}$ (star-marked error bars), the means are about 0.7-0.8 G_Q. Second, for $G_{dc}^{0.75s}$ (dot-marked error bars), the means are about 0.7-0.8 G_Q, indicating $1\uparrow$ is populated below μ_s about 0.4-0.6 $e|V_{DC}|$ (around in the middle of μ_s and μ_d) as shown in Fig. 7.2(3). Third, for $G_{ac}^{0.25s}$ (diamond-marked error bars), it is interesting to see the means are slightly lower than 0.5 G_Q in most cooldowns, proving the conductance prediction in Fig. 7.2(4). However, at the negative DC bias (see the last three cooldowns), the means are relatively lower-less than 0.4 G_Q, showing the 0.25 anomaly conductance is not completely symmetrical at the positive and negative DC bias respectively. Fourth, for $G_{dc}^{0.25s}$ (square-marked error bars), the means are more or less 0.5 G_Q, which indicates $1\downarrow$ populates at around μ_d. This accords with the position of $1\downarrow$ for the formation of the 0.25 anomaly as the model predicts in Fig. 7.2(4).

In Fig. 7.4d, it is clear to see the means of $2V_{DC}^{0.75s}$ (star-marked error bars) and $V_{DC}^{0.25s}$ (dot-marked error bars) almost have same values at around 1.5-2 mV. The means of $V_{DC}^{0.25s}/V_{DC}^{0.75s}$ (diamond-marked error bars) are around two in most cooldowns. This verifies the $e|V_{DC}^{0.25s}| = 2e|V_{DC}^{0.75s}| = \Delta E_{drop}$ as predicted in Fig. 7.2(2,4). Furthermore,

to check $e|V_{DC}^{0.25s}| = \Delta E_{DC}^{end} = \Delta E_{drop}$ as predicted in Fig. 7.2(4,7), Fig. 7.4d also shows statistics of ΔE_{DC}^{end} (square-marked error bars). However, the means of ΔE_{DC}^{end} are not equal to, but lower than $e|V_{DC}^{0.25s}|$ generally, and the means vary much in different cooldowns. The changeable ΔE_{DC}^{end} may be due to the fact that $1\uparrow$ drops randomly when it releases the pinning energy.

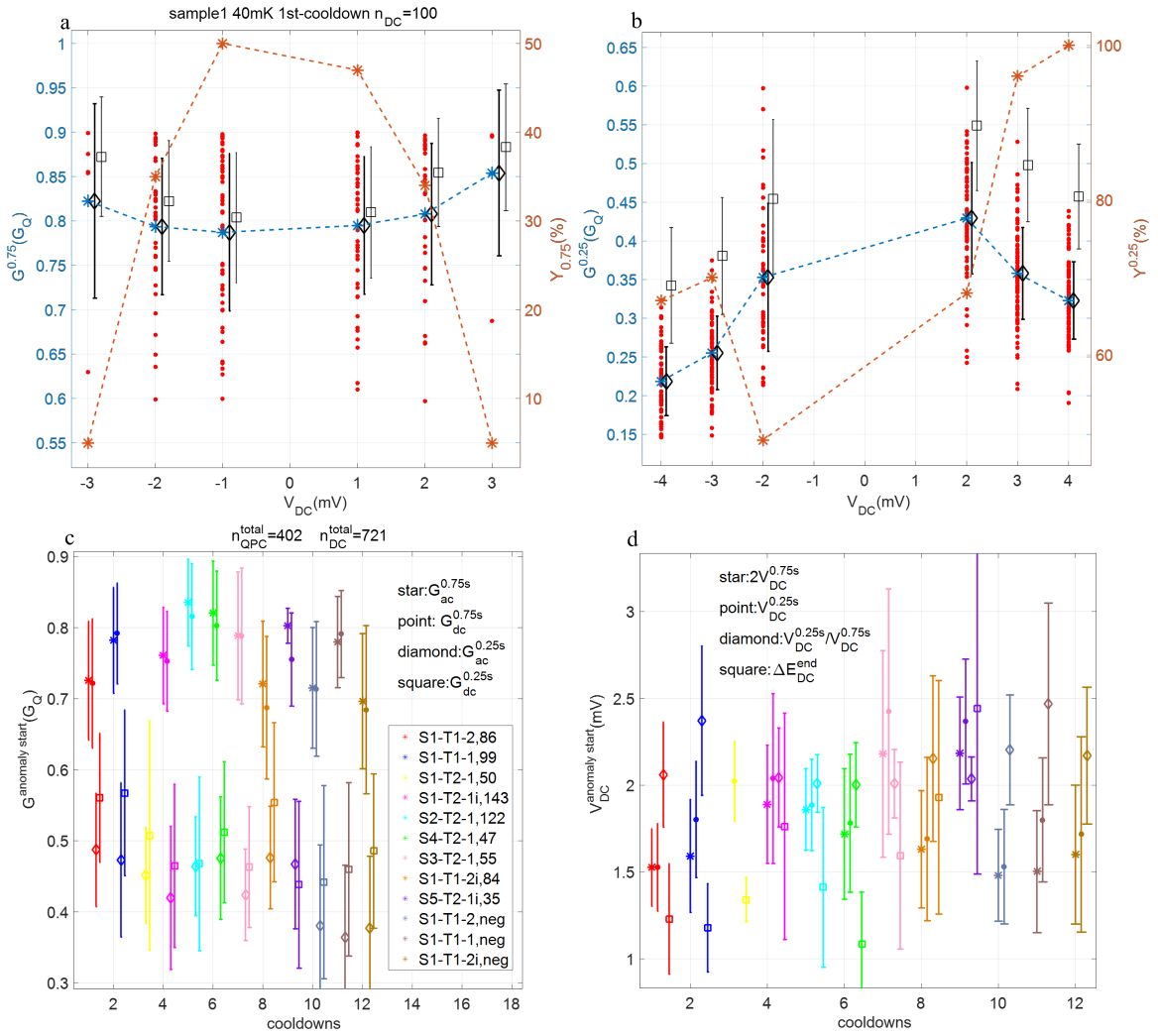

Figure 7.4: Statistical behaviours for the formation and development of the 0.75 and 0.25 anomalies. (a), Statistics of $G_{ac}^{0.75}$ (diamond-marked, offset horizontally by 0.1) and $G_{dc}^{0.75}$ (square-marked, offset horizontally by 0.2) at $V_{DC} = \pm 1$, ± 2 and ± 3 mV respectively in 100 spectroscopies for sample 1 at 40 mK. (b), Statistics of $G_{ac}^{0.25}$ (diamond-marked) and $G_{dc}^{0.25}$ (square-marked) for the same 100 spectroscopies. The orange dashed line shows $Y^{0.75}$ and $Y^{0.25}$ (read the right axis) at each V_{DC}. (c,d), Statistics of conductance (c) and DC bias (d) when the anomalies start showing up for sample 1-5 in 9 cooldowns at 40 mK or 1.4 K. The legend shows the count of DC-bias spectroscopies n_{DC}. We achieve spectroscopies from a maximum of $n_{QPC}^{total} = 402$ QPCs: 143, 122, 55, 47 and 35 for sample 1-5 measured at 1.4 K respectively. Total $n_{DC}^{total} = 721$ spectroscopies (sum of n_{DC}) have been acquired in 9 cooldowns. For statistics in cooldown 1-9, the measurements are perfomed at the positive DC bias. For statistics in cooldown 10-12, the measurements are perfomed at the positive DC bias. In (c), the error bars for statistics of $G_{ac}^{0.75s}$, $G_{dc}^{0.75s}$, $G_{ac}^{0.25s}$ and $G_{dc}^{0.25s}$ are marked with stars, dots, diamonds and squares respectively (offset horizontally in turn by 0.1). In (d), the error bars for statistics of $2V_{DC}^{0.75s}$, $V_{DC}^{0.25s}$ (which are absolute values for the negative DC bias), $V_{DC}^{0.25s}/V_{DC}^{0.75s}$ (use the same axis, dimensionless), and ΔE_{DC}^{end} (use the same axis with unit 'meV') are marked with stars, dots, diamonds and squares respectively (offset horizontally in turn by 0.1).

7.4 The 0.75 and 0.25 anomalies in a magnetic field

We further perform the DC-dependence measurements at a magnetic field 11.8 T using sample 1 at 40 mK, and find similar developments of the anomalies with increasing V_{DC}. To explain this, Fig. 7.5a shows the schematic of model with increasing V_{DC}, for already spin-split subbands with a spin gap ΔE_Z in a magnetic field.

In Fig. 7.5a1, at a small V_{DC}, both 1↓ and 1↑ have crossed μ_s and μ_d after the sudden drop, so there is no risers-splitting. Fig. 7.5a2 shows the formation of the 0.75 anomaly that 1↑ just arrives at μ_d after the sudden drop at $V_{DC}^{0.75s}$. We can see $e|V_{DC}^{0.75s}| = \Delta E_{drop} - \Delta E_Z$, which differs from $e|V_{DC}^{0.75s}| = \Delta E_{drop}/2$ at 0 T in Fig. 7.2(2). Fig. 7.5d3 shows the schematic of the 0.75 anomaly, which is the same as that at 0 T in Fig. 7.2(3). In Fig. 7.5d4, as the DC bias increases further, at $e|V_{DC}| \geq \Delta E_Z$, 1↑ pins at μ_s until 1↓ crosses μ_d during the drop, thus the spin gap opens further from ΔE_Z to be $e|V_{DC}|$ eventually. In a word, $\Delta E_{DC} = \Delta E_Z$ at $e|V_{DC}| < \Delta E_Z$; and $\Delta E_{DC} = e|V_{DC}|$ at $e|V_{DC}| \geq \Delta E_Z$. Then, Fig. 7.5d5 shows the formation of the 0.25 anomaly when the DC bias increases further to $e|V_{DC}^{0.25s}| = \Delta E_{drop}$, which is the same as Fig. 7.2(3). Furthermore, combining Fig. 7.5a2 and a5, the model predicts $e|V_{DC}^{0.25s}| - e|V_{DC}^{0.75s}| = \Delta E_Z$, thus we can compare $e|V_{DC}^{0.25s}| - e|V_{DC}^{0.75s}|$ to ΔE_Z in experiments to check the model. The g^*_{mean} is measured to be around 0.9 for the first plateau in Fig. 6.8, thus $\Delta E_Z \approx 0.6meV$ at B=11.8 T.

In experiments, Fig. 7.5b-g shows the formation and development of the 0.75 and 0.25 anomalies at positive (c, f) and negative (d, g) V_{DC} steps respectively, for two typical devices for sample 1 at T=40 mK and B=11.8 T. For another three devices, see Appendix Fig. A.29. In Fig. 7.5b,e, we can see the spin-split plateaus at zero DC bias. The 0.25 anomaly remains the same in a magnetic field, which reinforces the model that the 0.25 anomaly at 0 T is already spin-split due to a large DC bias. To check $e|V_{DC}^{0.25s}| - e|V_{DC}^{0.75s}| = \Delta E_Z$ as predicted in the model, compared to $\Delta E_Z \approx 0.6meV$, Fig. 7.5c,d,f,g shows $e|V_{DC}^{0.25s}| - e|V_{DC}^{0.75s}|$=1, 0.6, 0.6 and 1 meV respectively.

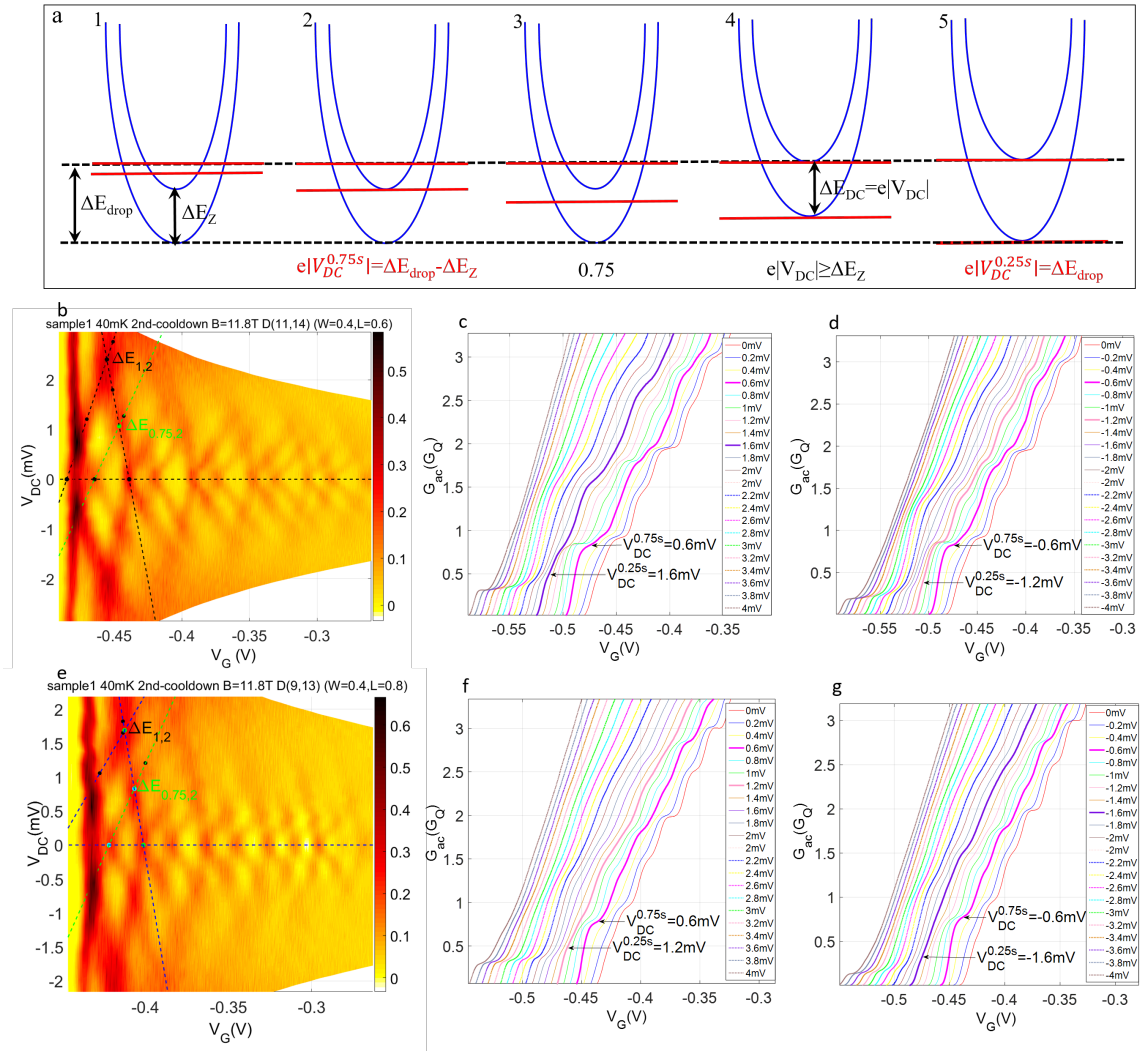

Figure 7.5: (a), Schematic of the DC-bias-induced spin-splitting model in a magnetic field. In (a1), at a small DC bias, the risers does not split. In (a2), at $e|V_{DC}^{0.75s}| = \Delta E_{drop} - \Delta E_Z$, the 0.75 anomaly starts showing up. (a3) shows the subbands of the 0.75 anomaly. In (a4), at $e|V_{DC}| \geq \Delta E_Z$, the spin gap splits further from ΔE_Z to be $e|V_{DC}|$. In (a5), at $e|V_{DC}^{0.25s}| = \Delta E_{drop}$, the 0.25 anomaly stars showing up. (b-g), Formation and development of the 0.75 and 0.25 anomalies at positive (c, f) and negative (d, g) steps of V_{DC} respectively, for two typical devices for sample 1 at T=40 mK and B=11.8 T. In (c,d,f,g), G_{ac} at the steps of $V_{DC}^{0.75s}$ and $V_{DC}^{0.25s}$ are shown in bold colours, for which the 0.75 and 0.25 anomalies start showing up respectively.

Next, Fig. 7.6 shows statistical behaviours for the formation and development of 0.75 and 0.25 anomalies, for sample 1 at T=40 mK and B=11.8 T with 63 spectroscopies. Fig. 7.6a shows statistics of $G_{ac}^{0.75}$ (diamond-marked) and $G_{dc}^{0.75}$ (square-marked) at $V_{DC} = \pm 1$, ± 2 and ± 3 mV respectively. Fig. 7.6b shows statistics of $G_{ac}^{0.25}$ (diamond-marked) and $G_{dc}^{0.25}$ (square-marked) at $V_{DC} = \pm 2$, ± 3 and ± 4 mV respectively. The 0.75 and 0.25 anomalies have similar developments of conductance as that at 0 T with increasing V_{DC}. Fig. 7.6c shows statistics of $G_{ac}^{0.75s}$ (star-marked), $G_{dc}^{0.75s}$ (dot-marked), $G_{ac}^{0.25s}$ (diamond-marked) and $G_{dc}^{0.25s}$ (square-marked, offset horizontally in turn by 0.15), at positive (red error-bars) and negative (blue error-bars) V_{DC} respectively. The means of $G_{ac}^{0.75s}$ and $G_{ac}^{0.25s}$ are around 0.75 G_Q and 0.5 G_Q respectively, fitting with the model predictions. Fig. 7.6d shows the statistics of $V_{DC}^{0.75s}$ (star-marked), $V_{DC}^{0.25s}$ (dot-marked), $V_{DC}^{0.25s} - V_{DC}^{0.75s}$ (diamond-marked) and ΔE_{DC}^{end} (square-marked, offset horizontally in turn by 0.15) at positive (red error-bars) and negative (blue error-bars) V_{DC} respectively. The mean and standard deviation of $e|V_{DC}^{0.25s}| - e|V_{DC}^{0.75s}|$ are around 0.7 and 0.3 meV respectively at both positive and negative V_{DC}. The model predicts $e|V_{DC}^{0.25s}| - e|V_{DC}^{0.75s}| = \Delta E_Z$, thus $V_{DC}^{0.25s} - V_{DC}^{0.75s} \approx 0.7 \pm 0.3meV$ is in accordance with $\Delta E_Z \approx 0.6meV$, considering different devices have different ΔE_Z due to variant g^*. Furthermore, the mean ΔE_{DC}^{end} is basically equal to the mean $e|V_{DC}^{0.25s}|$ as the model predicts.

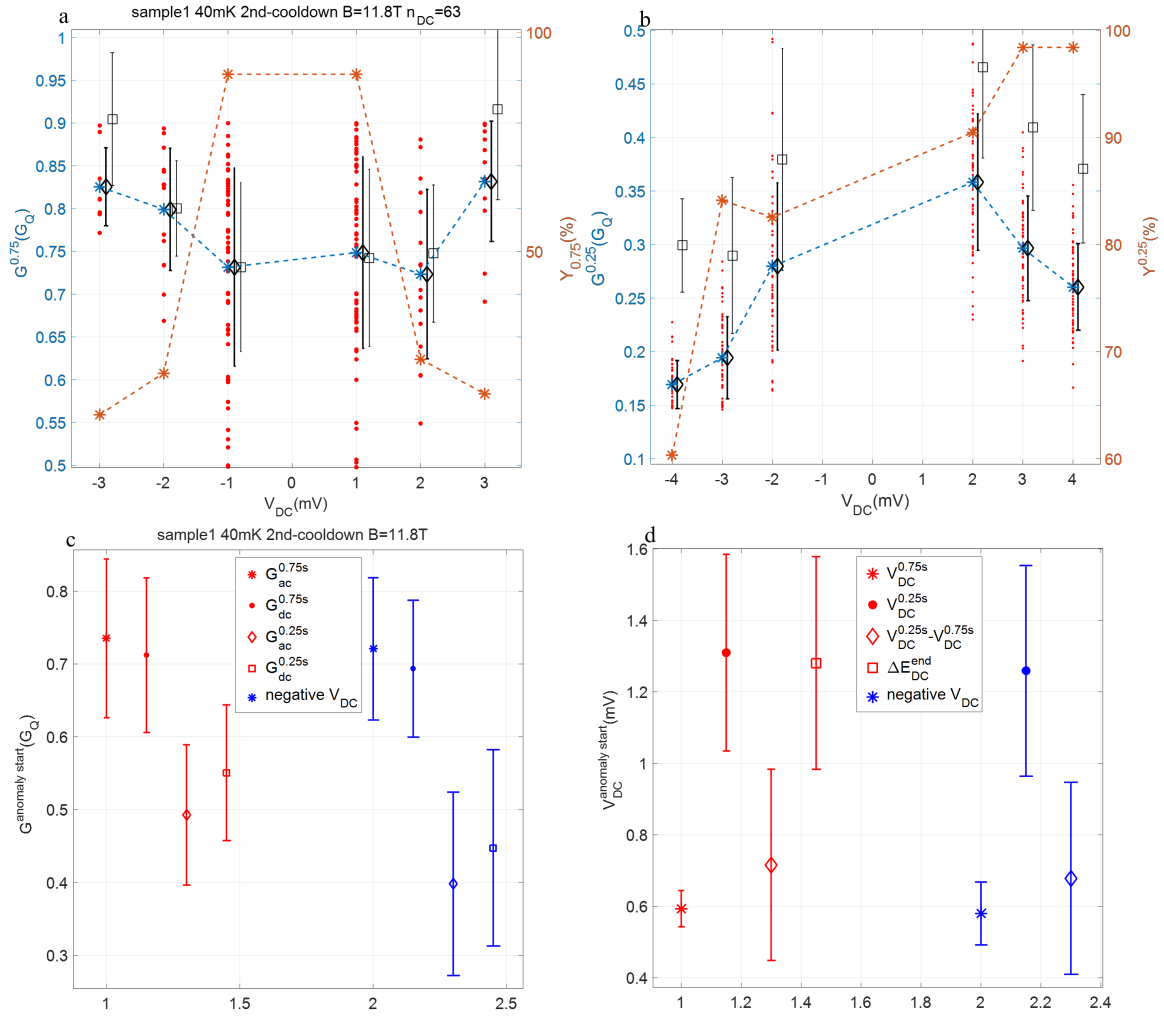

Figure 7.6: Statistical behaviours for the formation and development of the 0.75 and 0.25 anomalies, with 63 spectroscopies for sample 1 at T=40 mK and B=11.8 T. (a), Statistics of $G_{ac}^{0.75}$ (diamond-marked) and $G_{dc}^{0.75}$ (square-marked) at $V_{DC} = \pm 1$, ± 2 and ± 3 mV respectively. (b), Statistics of $G_{ac}^{0.25}$ (diamond-marked) and $G_{dc}^{0.25}$ (square-marked) at $V_{DC} = \pm 2$, ± 3 and ± 4 mV respectively. (c), Statistics of $G_{ac}^{0.75s}$ (star-marked), $G_{dc}^{0.75s}$ (dot-marked), $G_{ac}^{0.25s}$ (diamond-marked) and $G_{dc}^{0.25s}$ (square-marked, offset horizontally in turn by 0.15) at positive (red error-bars) and negative (blue error-bars) V_{DC} respectively. (d), Statistics of $V_{DC}^{0.75s}$ (star-marked), $V_{DC}^{0.25s}$ (dot-marked), $V_{DC}^{0.25s} - V_{DC}^{0.75s}$ (diamond-marked) and ΔE_{DC}^{end} (square-marked, offset horizontally in turn by 0.15), at the positive (red error-bars) and negative (blue error-bars, absolute value of V_{DC} is shown) V_{DC} respectively.

7.5 Summary

In this Chapter, first, we shows the 0.75 and 0.25 anomalies in a DC spectroscopy. We find the 0.75 anomaly shows up first and later the 0.25 anomaly with increasing DC bias. We define the differential conductance of those anomalies at the local minimum of transconductance. We also define the DC bias voltage at which the 0.75 and 0.25 anomalies just come into being.

Second, to explain such behaviours of the 0.75 and 0.25 anomalies, we come up with a DC-bias-induced spin splitting model. In the model, we propose three assumptions regarding the movement of subbands, including the sudden drop of subbands once crossing the higher chemical potential, the pinning mechnism of spin-up subband, and the pinning-energy-release drop of spin-up subband. The model predicts the 0.75 anomaly has a differential conductance 0.75 G_Q, and the 0.25 anomaly moves from 0.5 to 0.375 G_Q with increasing DC bias. The model also predicts the DC-bias-induced spin gap is equal to the DC bias energy applied

Third, we show the statistics for the formation and development of the 0.75 and 0.25 anomalies for different MUX samples in different cooldowns. The conductance developments of the 0.75 and 0.25 anomalies with increasing DC bias agrees with the model predictions. The DC bias voltage for the formation of the 0.25 anomaly is around twice that for the formation of the 0.75 anomaly, which also supports the model prediciton.

Fourth, we also measure the DC-bias induced 0.75 and 0.25 anomalies in a magnetic field 11.8 T, showing similar developments of anomaly conductance. We use the model to explain those anomaly behaviours in a magnetic field. We further show the statistics for the formation and development of the 0.75 and 0.25 anomalies in a cooldown at 40 mK and 11.8 T

8

Conclusion and Future Work

8.1 Conclusion

In Chapter 4, we statistically explore the 0.7 anomaly on the first three plateaus in 571 1D devices. The statistics of E_x and E_y are investigated. We highlight that the potential curvature ratio E_y/E_x governs the 0.7 anomaly. Since E_x is about 1 meV, while E_y is more than 2 meV, E_x is more sensitive and dominated by the potential background than geometry, while E_y is more geometry-dependent. We find the 0.7 anomaly shows the transconductance suppression, which is consistent with the van Hove model where it is caused by the LDOS-modified effective interactions. The spontaneous risers-splitting is an extreme case of the transconductance suppression. We also find the 0.7 anomaly transconductance suppression is strongest for the first plateau, and is stronger at 1.4 K than that at 40 mK.

In Chapter 5, the van Hove theory is further verified, including the negative correlation of S_G on U_{eff}^{max}, and quadratic dependence of S_B on B fields, at fixed κ. When dealing with electron interactions in theories, there are a variety of models, sometimes conflicting. In this way, our experimental results at both T=40 mK and 1.4 K statistically and quantitatively support the van Hove framework using a 1D tight-binding model with short-ranged screenings [7].

In Chapter 6, we obtained the statistics of g^* and ΔE^{hfo} for a number of devices at 40 mK, under in-plane B fields perpendicular and parallel to the transport direction respectively. Our experimental results statistically reveal that both g^* and ΔE^{hfo} could be enhanced by a stronger potential confinement. This also implies that g^* and ΔE^{hfo} could serve as measures of the interaction strength. Thus, using a quantum multiplexer, simply by tuning the QPC geometry (make it short and narrow) to achieve a strong potential confinement, we could realise a high g^*, which has implications in integrated spintronics without resorting to narrow-gap materials.

In Chapter 7, we statistically investigate the formation and development of the DC-bias-induced 0.75 and 0.25 anomalies in 402 QPCs. We propose a model in which the DC bias could result in the spin splitting and adjust the spin gap of the first subband. The split-gates could be applied as a spin-polariser, for which the 0.75 and 0.25 anomalies are partially and fully spin-polarised current respectively. This is an all-electric manipulation of spin polarisation, which has implications for the development of spintronic devices and future quantum computation.

8.2 Future work

First, Bauer et al. use an on-site interaction in the model, which is the most extreme case of short-ranged interactions (with screening length smaller than twice the lattice spacing)[7]. In reality, the interactions should have a range in vicinity of the barrier top, which length depends on the harmonic oscillator length of the barrier, and is about ten sites compared with the on-site model [6]. Therefore, the longer-ranged calculations with a more delicate treatment of the screening effect is meaningful and left for future theoretical work. It would be interesting to see whether the short-range results in Ref. [7] could still be established in long-ranged interactions for a same parabolic QPC.

Second, we only focus on QPCs showing a parabolic barrier in this work. Nevertheless, for some QPCs, it is possible that the electrostatic potential has a flatter-than-parabolic barrier shape. It would be interesting to investigate the interaction effects in the crossover regime from a parabolic barrier to a wide, flat barrier. In particular, in the limit of a wide and flat barrier, the central constriction would be a long 1D wire with a low density, which may realise a spin-incoherent Luttinger liquid [47]. Again, in the regime of a flatter-than-parabolic barrier, it would be important to consider the long-ranged interactions, since the screening length increases with the decreasing density. To realise in experiments, the effective barrier shape can be tuned smoothly by using the side-gates in the same way as in Ref. [7].

Third, for the current multiplexer, interaction strength U depends on E_y for each device and can not be changed unless using illumination. It will be interesting to design a top-gate multiplexer to allow U to be tuned. For an individual device with a typical E_x, U can be adjusted by changing the top-gate voltage, which enables the measurements of U dependence. Furthermore, we can tune g^* and ΔE^{hfo} by controlling the top gate voltage, which enables the quantitative investigation of the interaction effects on g^* and ΔE^{hfo}.

Fourth, our explanation for the 0.25 anomaly at a large DC bias is phenomenological. Bauer et al. only perform calculations to explain zero-bias-anomlay at a small bias excitation [7]. It would be challenging to settle down whether the 0.25 anomaly is related to spins or electron-electron interactions, which will enrich the fundamental physics of a QPC.

References

[1] H. Al-Taie, "Cryogenic on-chip multiplexer for the statistical study of quantum transport in low-dimensional devices," *PhD Thesis, University of Cambridge*, 2014.

[2] A. C. Graham, "Many-body interactions in quantum wires," *PhD Thesis, University of Cambridge*, 2003.

[3] W. K. Hew, "Interacting electrons in a weakly-confined quantum wire," *PhD Thesis, University of Cambridge*, 2009.

[4] L. W. Smith, "Electron interaction effects in quasi one-dimensional quantum wires," *PhD Thesis, University of Cambridge*, 2011.

[5] E. Koop et al., "The influence of device geometry on many-body effects in quantum point contacts: signatures of the 0.7-anomaly, exchange and Kondo," *J. Supercond. Nov. Magn.*, vol. 20, pp. 433–441, 2007.

[6] J. Heyder, "The 0.7 anomaly in quantum point contacts: a microscopic model for the first conductance step," *PhD Thesis, Ludwig-Maximilians-Universität München*, 2014.

[7] F. Bauer et al., "Microscopic origin of the '0.7-anomaly' in quantum point contacts," *Nature*, vol. 501, pp. 73–78, 2013.

[8] G. E. Moore, "Cramming components onto integrated circuits," *Electronics*, vol. 38, 1965.

[9] N. Gershenfeld et al., "Quantum computing with molecules," *Scientific American*, 1998.

[10] H. Al-Taie et al., "Cryogenic on-chip multiplexer for the study of quantum transport in 256 split-gate devices," *Appl. Phys. Lett.*, vol. 102, p. 243102, 2013.

[11] K. v. Klitzing et al., "New method for high-accuracy determination of the fine-structure constant based on quantized Hall resistance," *Phys. Rev. Lett.*, vol. 45, p. 494–497, 1980.

[12] D. C. Tsui et al., "Two-dimensional magnetotransport in the extreme quantum limit," *Phys. Rev. Lett.*, vol. 48, p. 1559, 1982.

[13] B. J. van Wees et al., "Quantized conductance of point contacts in a two-dimensional electron gas," *Phys. Rev. Lett.*, vol. 60, pp. 848–850, 1988.

[14] D. A. Wharam et al., "One-dimensional transport and the quantisation of the ballistic resistance," *J. Phys. C*, vol. 21, pp. L209–L214, 1988.

[15] C. G. Smith et al., "The transition from one- to zero-dimensional ballistic transport," *J. Phys C: Solid State Phys.*, vol. 21, pp. L893–L898, 1988.

[16] T. J. Thornton et al., "One-dimensional conduction in the 2D electron gas of a GaAs-AlGaAs heterojunction," *Phys. Rev. Lett.*, vol. 56, pp. 1198–1201, 1986.

[17] M. Büttiker et al., "Quantized transmission of a saddle-point constriction," *Phys. Rev. B*, vol. 41, p. 7906(R), 1990.

[18] B. J. van Wees et al., "Quantum ballistic and adiabatic electron transport studied with quantum point contacts," *Phys. Rev. B*, vol. 43, pp. 12431–12453, 1991.

[19] L. Martin et al., "Non-linear conductance of a saddle-point constriction," *J. Phys.: Condens. Matter*, vol. 4, pp. 1323–1333, 1992.

[20] A. B. Fowler et al., "Conductance in restricted-dimensionality accumulation layers," *Phys. Rev. Lett.*, vol. 48, pp. 196–199, 1982.

[21] C. C. Dean and M. Pepper, "The transition from two- to one-dimensional electronic transport in narrow silicon accumulation layers," *J. Phys. C: Solid State Phys.*, vol. 15, pp. L1287–L1297, 1982.

[22] H. L. Stormer et al., "Two dimensional electron gas at a semiconductor-semiconductor interface," *Solid State Commun.*, vol. 29, pp. 705–709, 1979.

[23] H. C. Casey and M. B. Panish, "Heterojunction lasers," *New York: Academic press*, pp. 191–193, 1978.

[24] M. A. Herman et al., "Molecular beam epitaxy: fundamentals and current status," *Springer-Verlag*, 1996.

[25] C. G. Smith, "Low-dimensional quantum devices," *Rep. Prog. Phys.*, vol. 59, pp. 235–282, 1996.

[26] J. R. Prance, "Cooling an electron gas using quantum dot based electronic refrigeration," *PhD Thesis, University of Cambridge*, 2009.

[27] D. R. Ward et al., "Integration of on-chip field-effect transistor switches with dopantless Si/SiGe quantum dots for high-throughput testing," *Appl. Phys. Lett.*, vol. 102, p. 213107, 2013.

[28] K. J. Thomas et al., "Possible spin polarization in a one-dimensional electron gas," *Phys. Rev. Lett.*, vol. 77, pp. 135–138, 1996.

[29] K. J. Thomas et al., "Interaction effects in a one-dimensional constriction," *Phys. Rev. B*, vol. 58, pp. 4846–4852, 1998.

[30] A. P. Micolich et al., "What lurks below the last plateau: experimental studies of the $0.7 \times 2e^2/h$ conductance anomaly in one-dimensional systems," *J. Phys. Condens. Matter*, vol. 23, p. 443201, 2011.

[31] A. P. Micolich et al., "Quantum point contacts: Double or nothing?," *Nat. Phys.*, vol. 9, pp. 530–531, 2013.

[32] M. J. Iqbal et al., "Odd and even Kondo effects from emergent localization in quantum point contacts," *Nature*, vol. 501, pp. 79–83, 2013.

[33] K. J. Heyder et al., "Relation between the 0.7 anomaly and the Kondo effect: geometric crossover between a quantum point contact and a Kondo quantum dot," *Phys. Rev. B*, vol. 92, p. 195401, 2015.

[34] C. K. Wang et al., "Spin splitting of subbands in quasi-one-dimensional electron quantum channels," *Phys. Rev. B*, vol. 54, p. R14257, 1996.

[35] C. K. Wang et al., "Local spin polarization in ballistic quantum point contacts," *Phys. Rev. B*, vol. 57, p. 4552, 1998.

[36] H. Bruus et al., "The anomalous 0.5 and 0.7 conductance plateaus in quantum point contacts," *Physica E*, vol. 10, pp. 97–102, 2001.

[37] A. C. Graham et al., "Energy-level pinning and the 0.7 spin state in one dimension: GaAs quantum wires studied using finite-bias spectroscopy," *Phys. Rev. B*, vol. 75, p. 035331, 2007.

[38] D. J. Reilly., "Density-dependent spin polarization in ultra-low-disorder quantum wires," *Phys. Rev. Lett.*, vol. 89, p. 246801, 2002.

[39] D. J. Reilly., "Phenomenological model for the 0.7 conductance feature in quantum wires," *Phys. Rev. B*, vol. 72, p. 033309, 2005.

[40] E. Wigner et al., "On the interaction of electrons in metals," *Phys. Rev.*, vol. 46, p. 1002, 1934.

[41] E. Wigner et al., "Effects of the electron interaction on the energy levels of electrons in metals," *Trans. Faraday Soc.*, vol. 34, p. 678–685, 1938.

[42] A. D. Klironomos et al., "Spontaneous spin polarization in quantum wires," *Europhys. Lett.*, vol. 74, p. 679, 2006.

[43] A. D. Klironomos et al., "Spin coupling in zigzag Wigner crystals," *Phys. Rev. B*, vol. 76, p. 075302, 2007.

[44] B. Spivak et al., "Ferromagnetic correlations in quasi-one-dimensional conducting channels," *Phys. Rev. B*, vol. 61, p. 16730, 2000.

[45] S. Tomonaga et al., "Remarks on Bloch's method of sound waves applied to many-fermion problems," *Prog. Theor. Phys.*, vol. 5, p. 544, 1950.

[46] J. M. Luttinger et al., "An exactly soluble model of a many fermion system," *J. Math. Phys.*, vol. 4, pp. 1154–1162, 1963.

[47] K. A. Matveev et al., "Conductance of a quantum wire in the Wigner-crystal regime," *Phys. Rev. Lett.*, vol. 92, p. 106801, 2004.

[48] K. A. Matveev et al., "Conductance of a quantum wire at low electron density," *Phys. Rev. B*, vol. 70, p. 245319, 2004.

[49] D. Goldhaber-Gordon et al., "Kondo effect in a single-electron transistor," *Nature*, vol. 391, p. 156–159, 1998.

[50] D. Goldhaber-Gordon et al., "From the Kondo regime to the mixed-valence regime in a single-electron transistor," *Phys. Rev. Lett.*, vol. 81, p. 5225–5228, 1998.

[51] S. M. Cronenwett et al., "A tunable kondo effect in quantum dots," *Science*, vol. 281, p. 540–544, 1998.

[52] M. Pustilnik et al., "Kondo effect in quantum dots," *J. Phys.: Condens. Matter*, vol. 16, p. R513, 2004.

[53] S. M. Cronenwett et al., "Low-temperature fate of the 0.7 structure in a point contact: a Kondo-like correlated state in an open system," *Phys. Rev. Lett.*, vol. 88, p. 226805, 2002.

[54] Y. Meir et al., "Kondo model for the 0.7 anomaly in transport through a quantum point contact," *Phys. Rev. Lett.*, vol. 89, p. 196802, 2002.

[55] K. Hirose et al., "Local moment formation in quantum point contacts," *Phys. Rev. Lett.*, vol. 90, p. 026804, 2003.

[56] A. Golub et al., "Suppression of shot noise in quantum point contacts in the 0.7 regime," *Phys. Rev. Lett.*, vol. 97, p. 186801, 2006.

[57] T. Rejec and Y. Meir, "Magnetic impurity formation in quantum point contacts," *Nature*, vol. 442, p. 900–903, 2006.

[58] B. Brun et al., "Wigner and Kondo physics in quantum point contacts revealed by scanning gate microscopy," *Nat. Commun.*, vol. 5, p. 4290, 2014.

[59] L. W. Smith et al., "Statistical study of conductance properties in one-dimensional quantum wires focusing on the 0.7 anomaly," *Phys. Rev. B*, vol. 90, p. 045426, 2014.

[60] L. W. Smith et al., "Dependence of the 0.7 anomaly on the curvature of the potential barrier in quantum wires," *Phys. Rev. B*, vol. 91, p. 235402, 2015.

[61] L. W. Smith et al., "Effect of split gate size on the electrostatic potential and 0.7 anomaly within quantum wires on a modulation-doped GaAs/AlGaAs heterostructure," *Phys. Rev. Applied*, vol. 5, p. 044015, 2016.

[62] K. L. Mittal, "Polyimide: synthesis, characterization and applications," *Plenum: New York*, vol. 1, p. 614, 1984.

[63] Y. Ozari et al., "A water sensitve thermomechanical transition in a Polyimide," *J. Appl. Polym. Sci.*, vol. 23, p. 11891201, 1979.

[64] T. M. Chen et al., "Spontaneous spin polarisation in one dimension under finite DC-bias," *Physica E*, vol. 40, pp. 1295–1297, 2008.

[65] T. M. Chen et al., "Bias-controlled spin polarization in quantum wires," *Phys. Rev. B*, vol. 89, p. 045128, 2014.

[66] T. M. Chen et al., "Direct observation of nonequilibrium spin population in quasi-one-dimensional nanostructures," *Phys. Rev. B*, vol. 89, p. 045128, 2014.

[67] K. J. Bauer et al., "Functional renormalization group approach for inhomogeneous interacting Fermi systems," *Phys. Rev. B*, vol. 89, p. 045128, 2014.

[68] A. M. Lunde et al., "Electron-electron interaction effects in quantum point contacts," *New J. Phys.*, vol. 11, p. 023031, 2009.

[69] N. K. Patel et al., "Evolution of half plateaus as a function of electric field in a ballistic quasi-one-dimensional constriction," *Phys. Rev. B*, vol. 44, pp. 13549–13555, 1991.

[70] S. M. Frolov et al., "Electrical generation of pure spin currents in a two-dimensional electron gas," *Phys. Rev. Lett.*, vol. 102, p. 116802, 2009.

[71] D. D. Awschalom and M. E. Flatte, "Challenges for semiconductor spintronics," *Nat. Phys.*, vol. 3, pp. 153–159, 2007.

[72] R. M. Potok et al., "Detecting spin-polarized currents in ballistic nanostructures," *Phys. Rev. Lett.*, vol. 89, p. 266602, 2002.

[73] J. A. Frolov et al., "A gate-controlled bidirectional spin filter using quantum coherence," *Science*, vol. 299, pp. 679–682, 2003.

[74] A. M. Burke et al., "Extreme sensitivity of the spin-splitting and 0.7 anomaly to confining potential in one-dimensional nanoelectronic devices," *Nano Lett.*, vol. 12, pp. 4495–4502, 2012.

[75] P. J. Simmonds et al., "Quantum transport in $In_{0.75}Ga_{0.25}As$ quantum wires," *Appl. Phys. Lett.*, vol. 92, p. 152108, 2008.

[76] T. P. Martin et al., "Enhanced Zeeman splitting in $Ga_{0.25}In_{0.75}As$ quantum point contacts," *Appl. Phys. Lett.*, vol. 93, p. 012105, 2008.

[77] H. Lind et al., "Electric-field control of magnetization in biased semiconductor quantum wires and point contacts," *Phys. Rev. B*, vol. 83, p. 075308, 2011.

[78] T. M. Chen et al., "All-electrical injection and detection of a spin-polarized current using 1D conductors," *Phys. Rev. Lett.*, vol. 109, p. 177202, 2012.

[79] A. C. Graham et al., "Anomalous spin-dependent behaviour of one-dimensional subbands," *Phys. Rev. B*, vol. 72, p. 193305, 2005.

A

In the same way as Fig. 4.3, Fig. A.1 shows another four histograms of V_d for sample 1-3 at 40 mK or 1.4 K.

In the same way as Fig. 4.5, Fig. A.2 shows dependence of V_p on length and G_d respectively, for geometry type 2 MUX sample 3 (a,b) and 4 (c,d) at 1.4 K. Considering that V_p is negatively correlated with width, but positively correlated with length in Fig. 4.5a,c, in Fig. A.2a,c, we can see increasing width and length together at a fixed ratio of L/W, results in a decreasing V_p. This means that width has a stronger effect on V_p than length. In Fig. A.2b,d, again a larger G_d results in a more negative V_p.

In the same way as Fig. 4.6, Fig. A.3 shows the histogram of constant R_s, and variable R_s^N as a function of N, for sample 1 at 40 mK before (a,b) and after (c,d) illumination respectively. In the same way as Fig. 4.7, Fig. A.4 shows the histogram of constant R_s, and variable R_s^N as a function of N, for sample 1 at 40 mK in the first (a,b) and third (c,d) cooldowns respectively.

Fig. A.5 shows the histogram of constant R_s (a), and variable R_s^N as a function of N (b), for sample 2 at 1.4 K in the first cooldown.

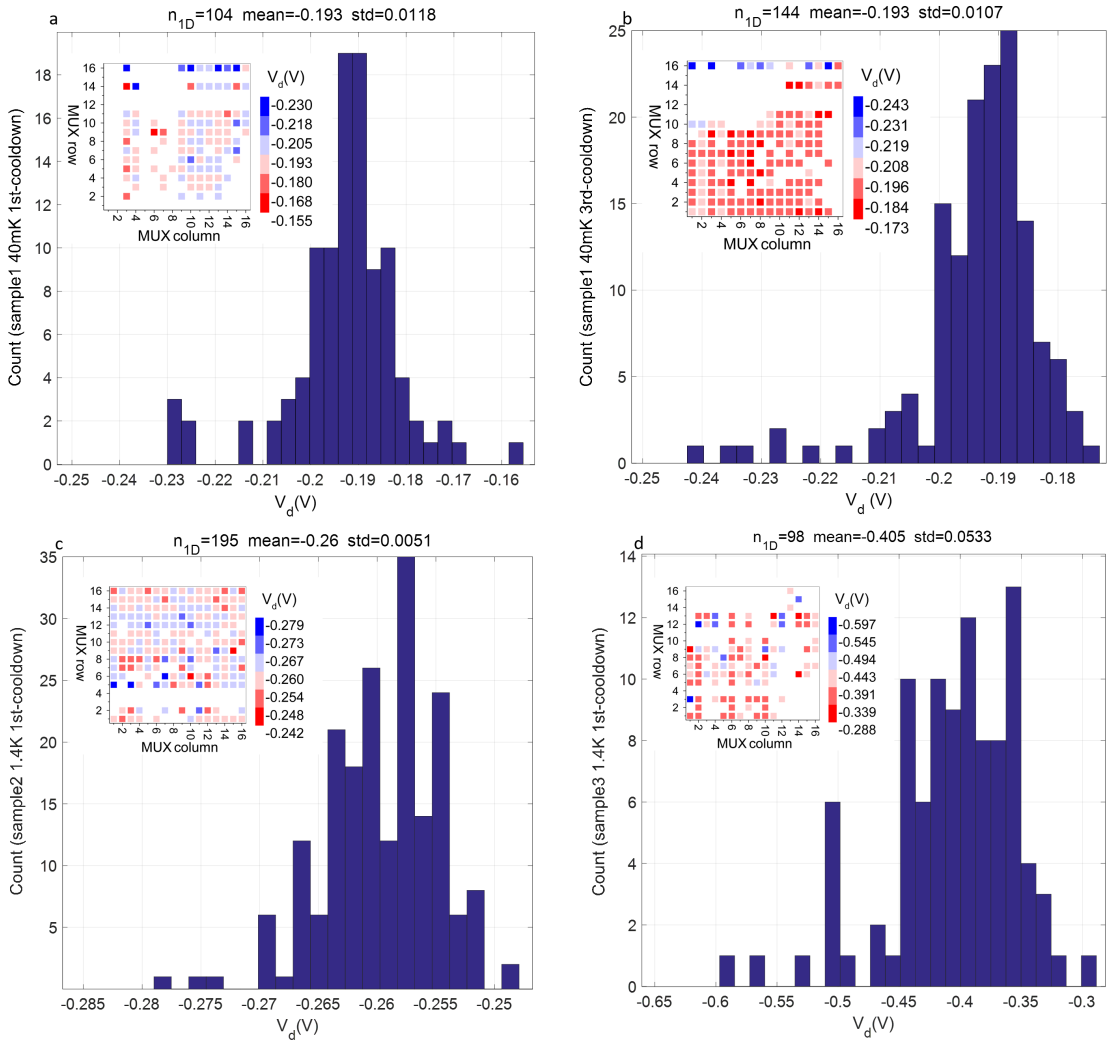

Figure A.1: V_d histograms for sample 1-3 at 40 mK or 1.4 K respectively. In each panel, the inset shows the V_d map of 1D devices achieved in the MUX sample.

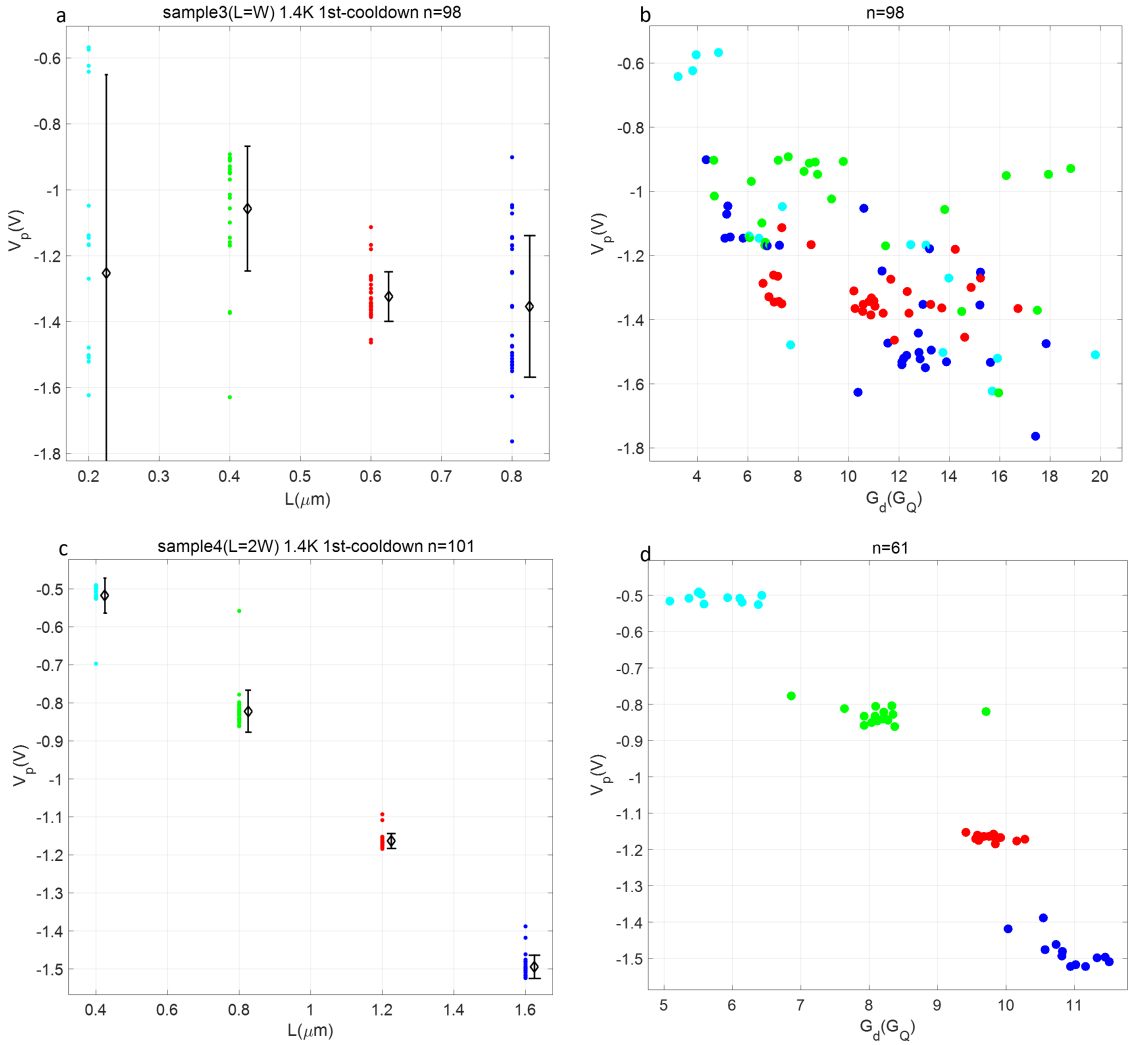

Figure A.2: Dependence of V_p on length and G_d respectively, for geometry type 2 MUX sample 3 and 4 at 1.4 K. Cyan, green, red and blue dots represent devices with width=0.2, 0.4, 0.6 and 0.8 μm respectively for geometry type 2 MUX samples.

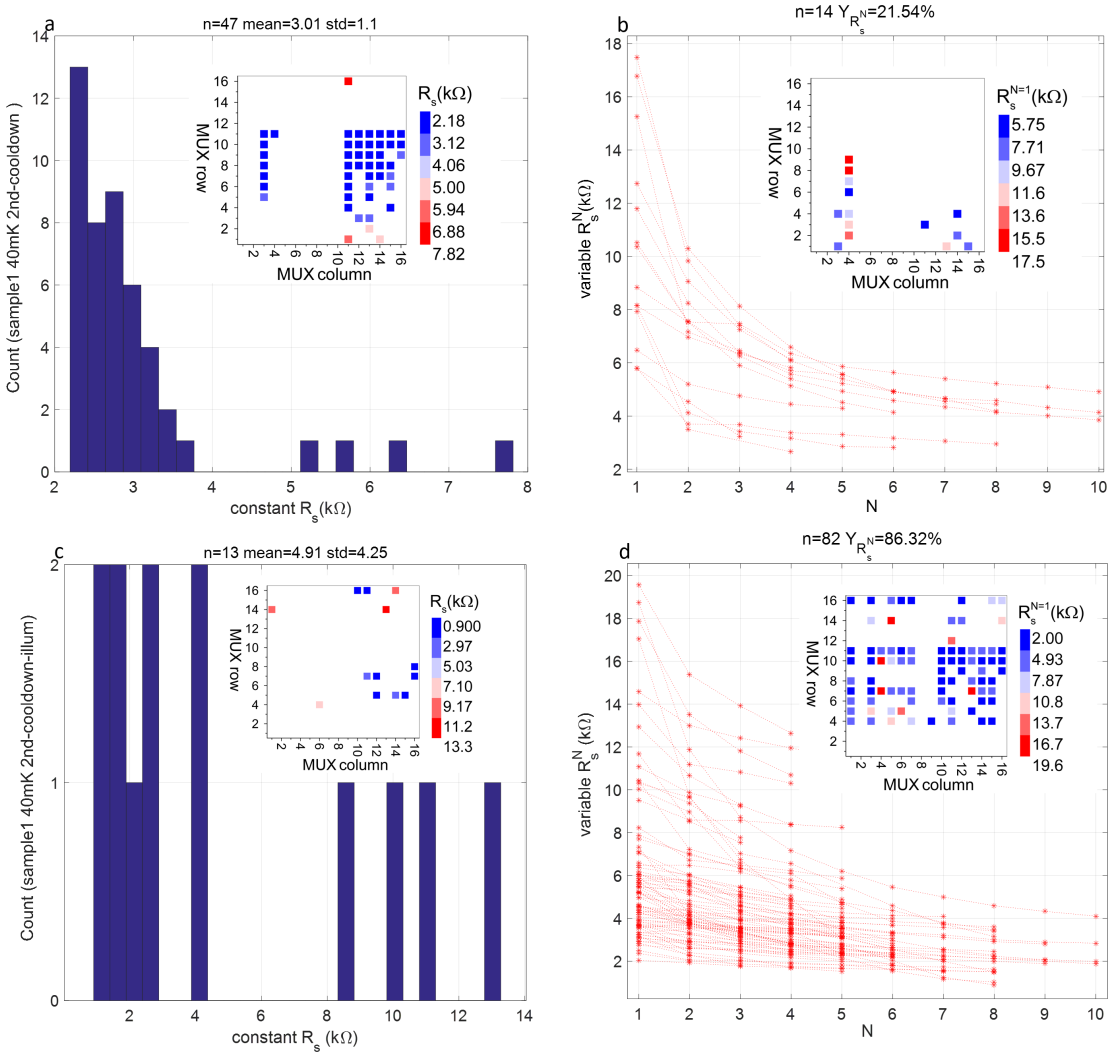

Figure A.3: Histogram of constant R_s, and variable R_s^N as a function of N, for sample 1 at 40 mK before (a,b) and after (c,d) illumination respectively

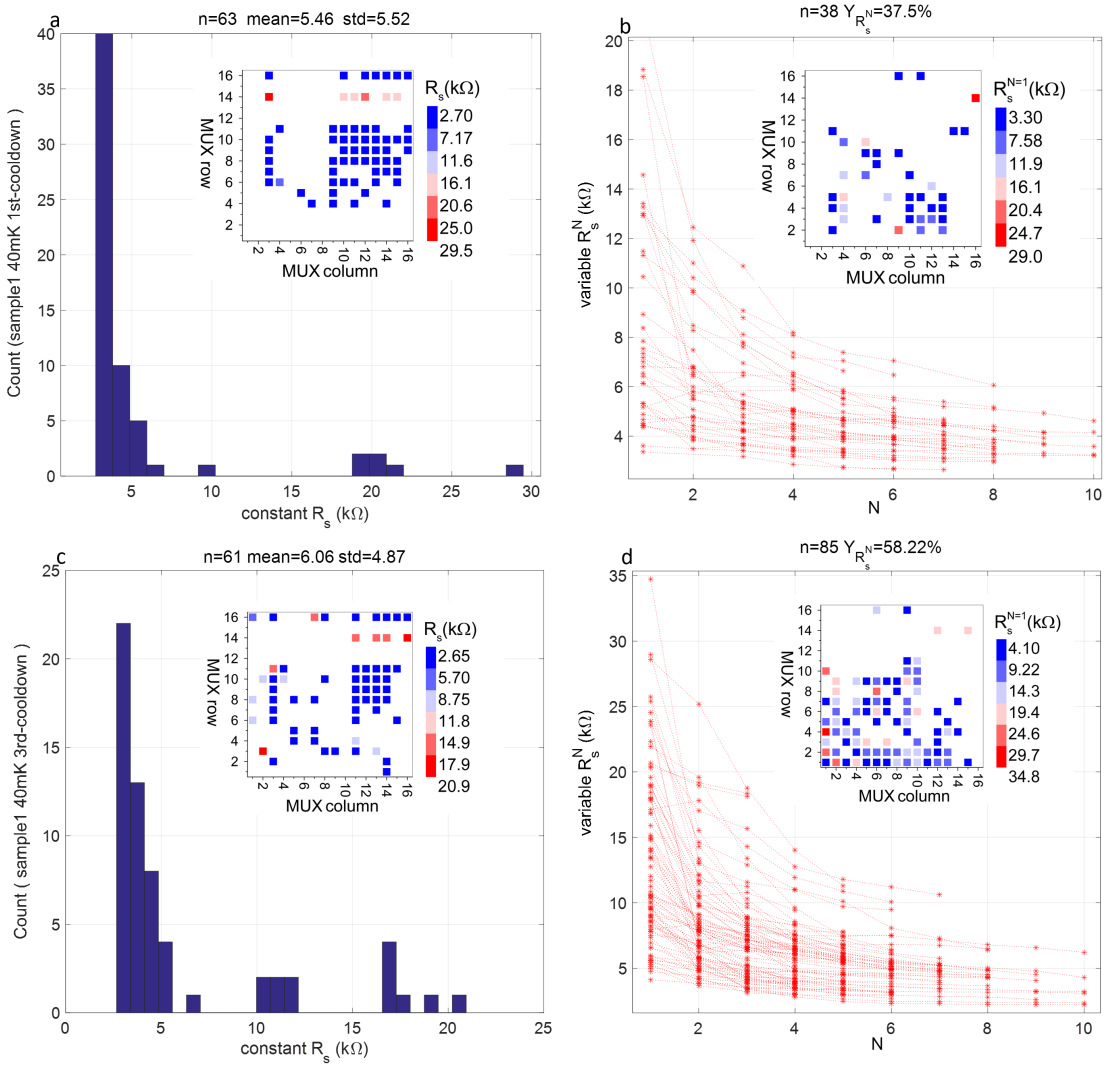

Figure A.4: Histogram of constant R_s, and variable R_s^N as a function of N, for sample 1 at 40 mK in the first (a,b) and third (c,d) cooldowns respectively.

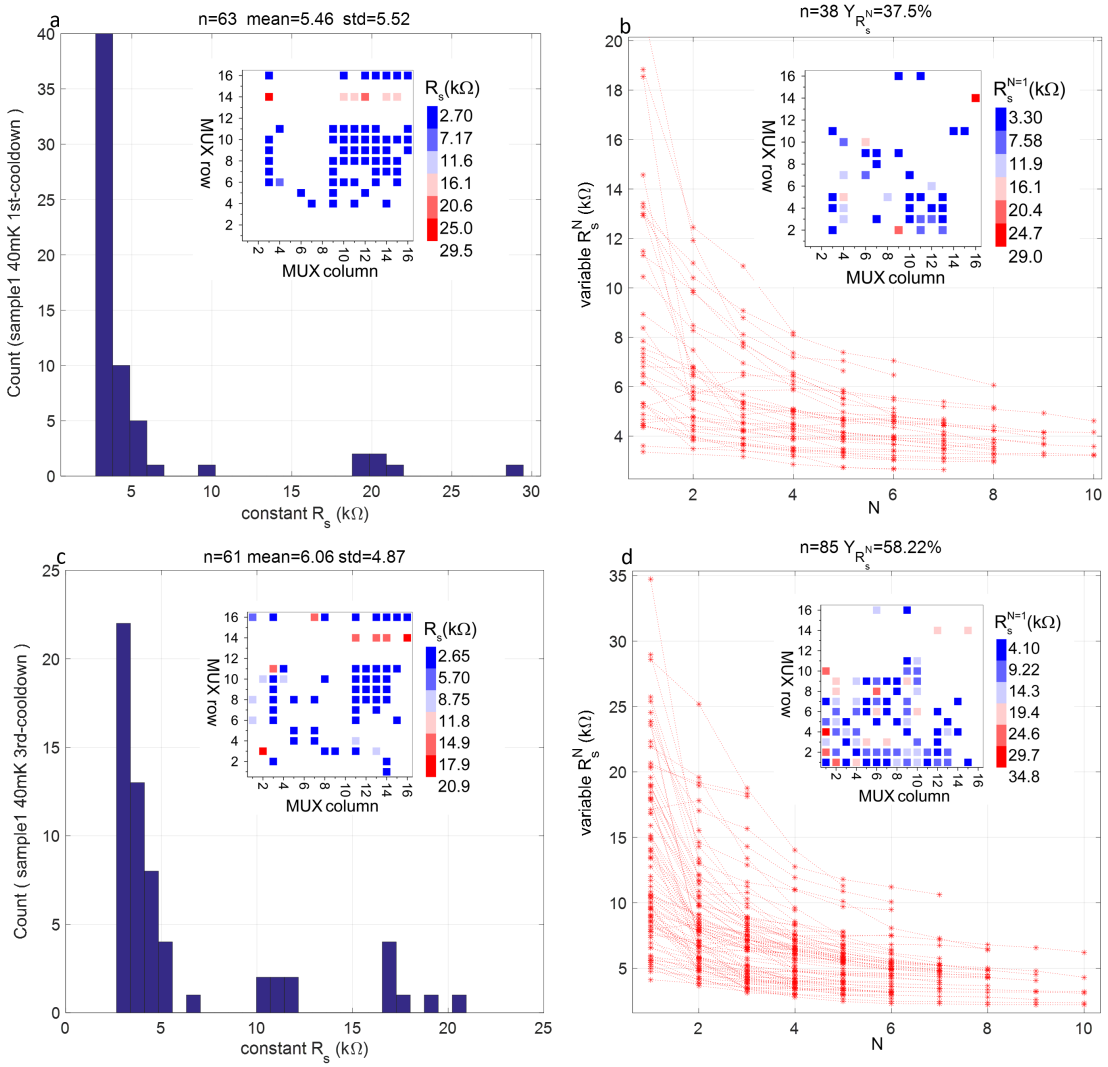

Figure A.5: Histogram of constant R_s (a), and variable R_s^N as a function of N (b), for sample 2 at 1.4 K in the first cooldown.

In the same way as Fig. 4.12, Fig. A.6 shows geometry dependence of E_x, for sample 1 at 40 mK in the first (a) and third (b) cooldowns respectively, and sample 3 (c) and 4 (d) at 1.4 K. Each panel shows a poor correlation of E_x on geometry.

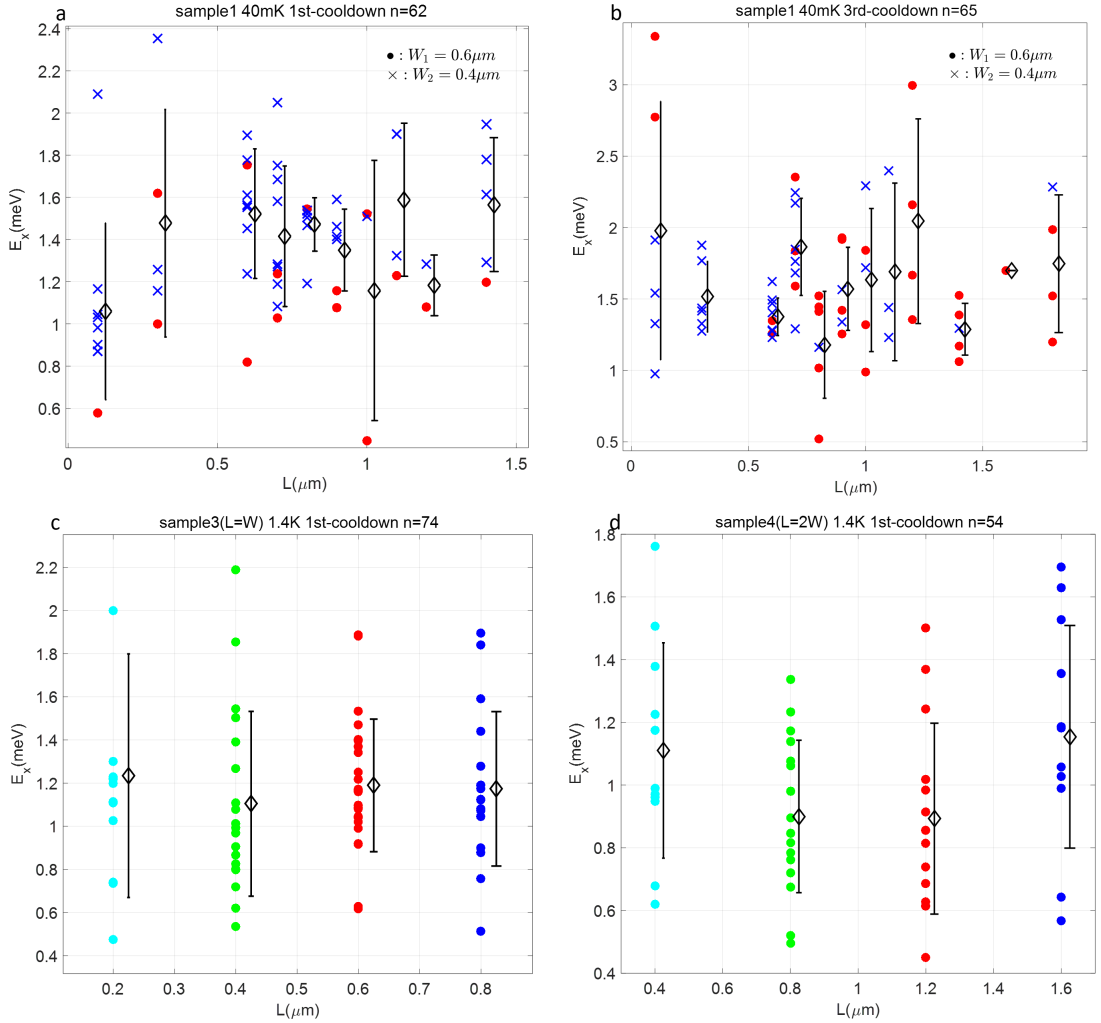

Figure A.6: Geometry dependence of the E_x, for sample 1 at 40 mK in the first (a) and third (b) cooldowns respectively, and sample 3 (c) and 4 (d) at 1.4 K.

In the same way as Fig. 4.16, Fig. A.7 shows geometry dependence of $\Delta E_{N,N+1}$ for type 2 MUX sample 3 (a-c, with L/W=1) and 4 (d-f, with L/W=2) at 1.4 K respectively. On the whole, $\Delta E_{N,N+1}$ shows weak downward trends as length and width increase together at a fixed L/W. However, $\Delta E_{N,N+1}$ for devices with width=0.4 μm (green error-bars) is comparable or even larger than that for devices with width=0.2 μm (cyan error-bars). This is reasonable considering E_y has a maximum at $W \approx 3d = 270nm$ ($d = 90$ nm for our wafers), based on the modelling in Fig. 4.15.

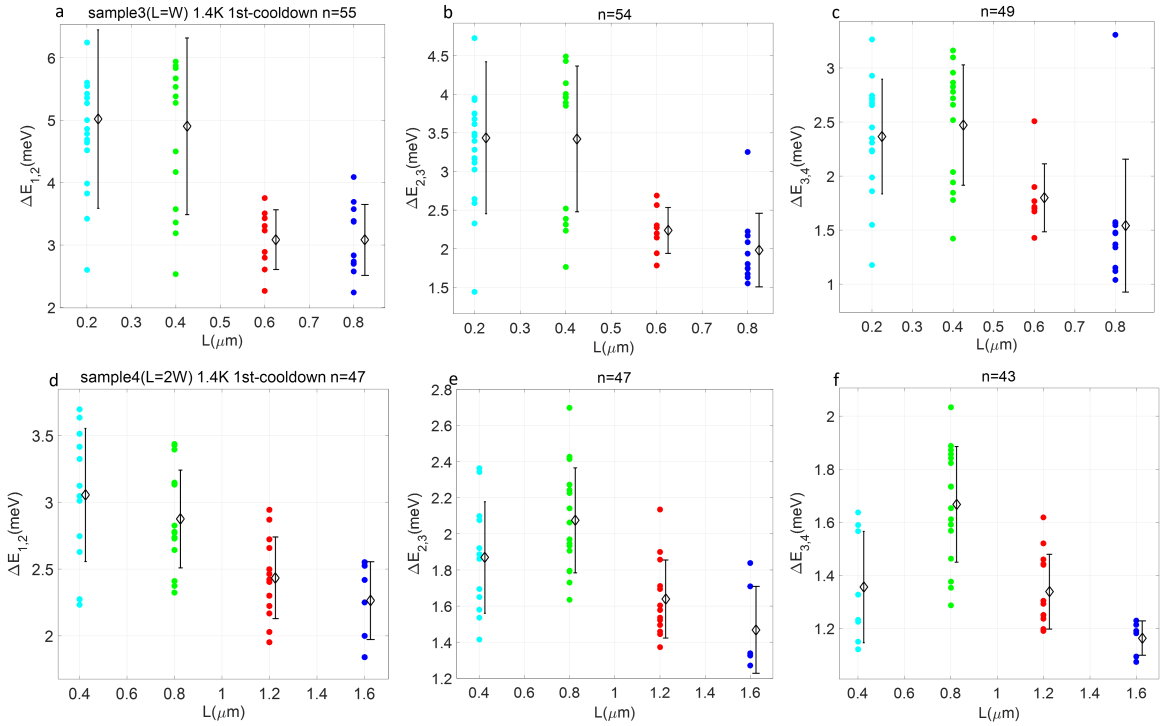

Figure A.7: Geometry dependence of $\Delta E_{N,N+1}$ for type 2 MUX sample 3 (a-c, with L/W=1) and 4 (d-f, with L/W=2) at 1.4 K respectively.

In the same way as Fig. 4.17, Fig. A.8 shows clearly $\alpha_{N,N+1}$ decreases as length and width increase together at a fixed L/W.

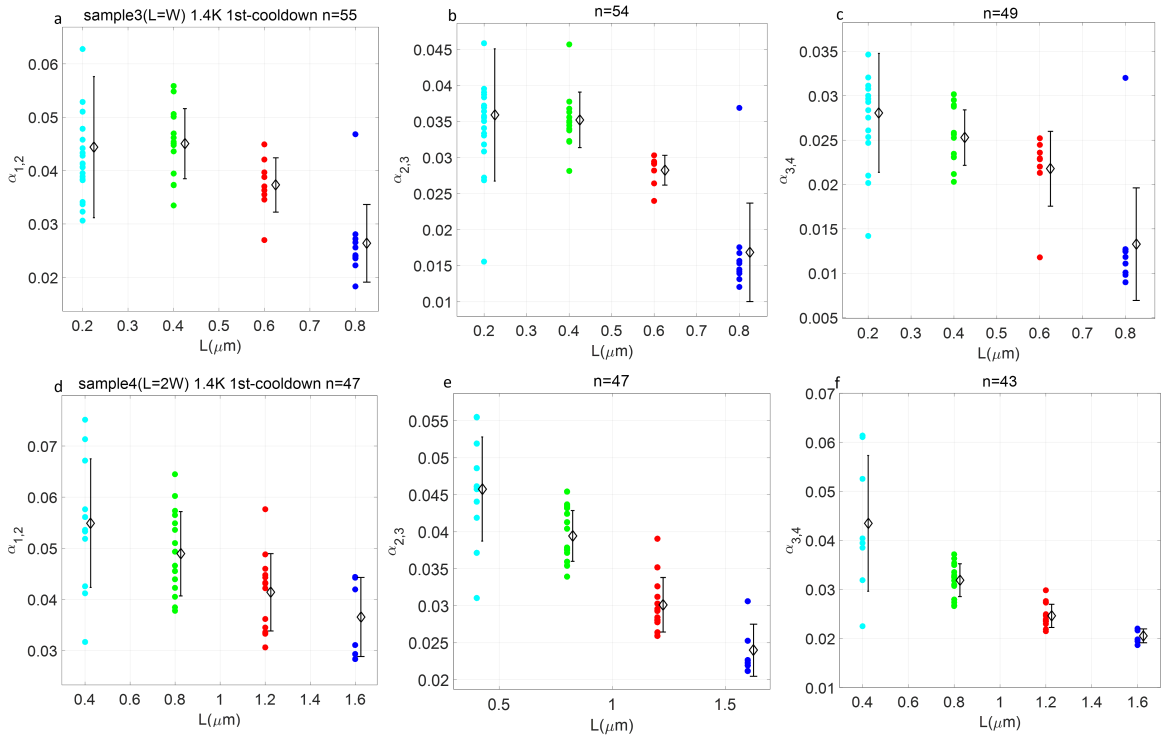

Figure A.8: Geometry dependence of $\alpha_{N,N+1}$ for type 2 MUX sample 3 (a-c, with L/W=1) and 4 (d-f, with L/W=2) at 1.4 K.

In the same way as Fig. 5.6, Fig. A.9 shows dependence of S_G on $1/U_E^N$ for sample 2 at 1.4 K, for the first three plateaus respectively.

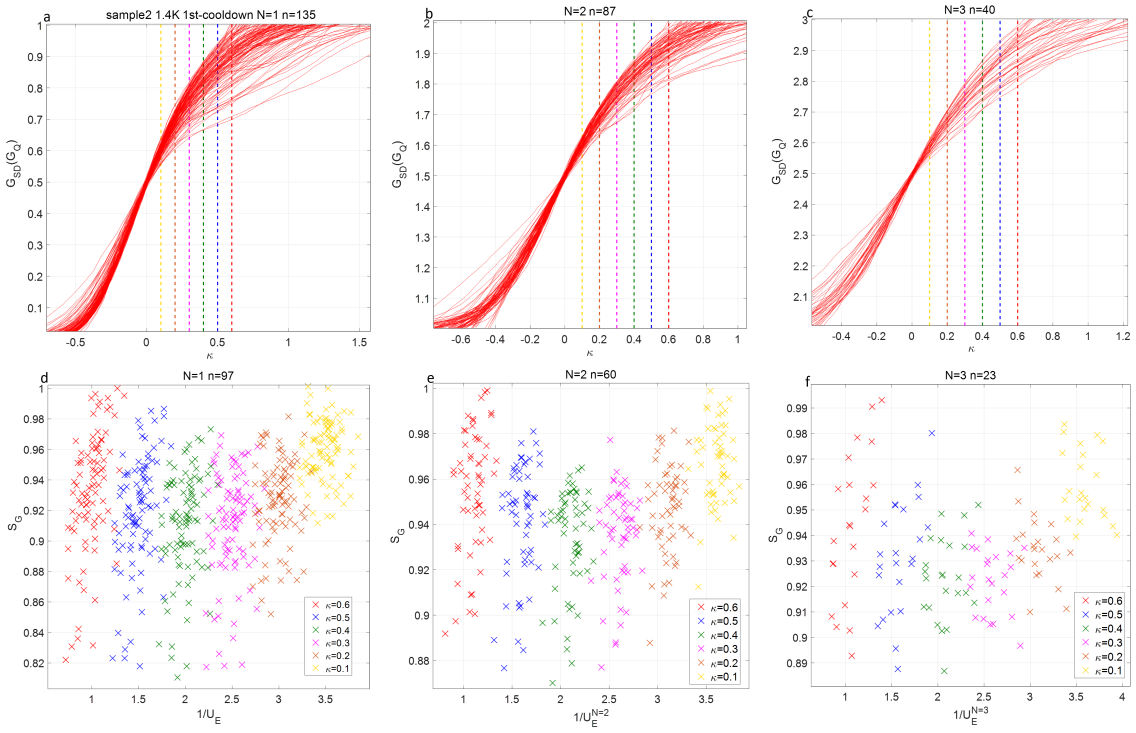

Figure A.9: (a-c), First three steps for the devices for sample 2 at 1.4 K respectively. (d-f), Dependence of S_G on $1/U_E^N$ at fixed κ, for the first three plateaus for devices in (a-c) respectively.

In the same way as Fig. 5.11, Fig. A.10-A.12 show behaviours of S_B and B_*^{fit} for three more devices at 40 mK.

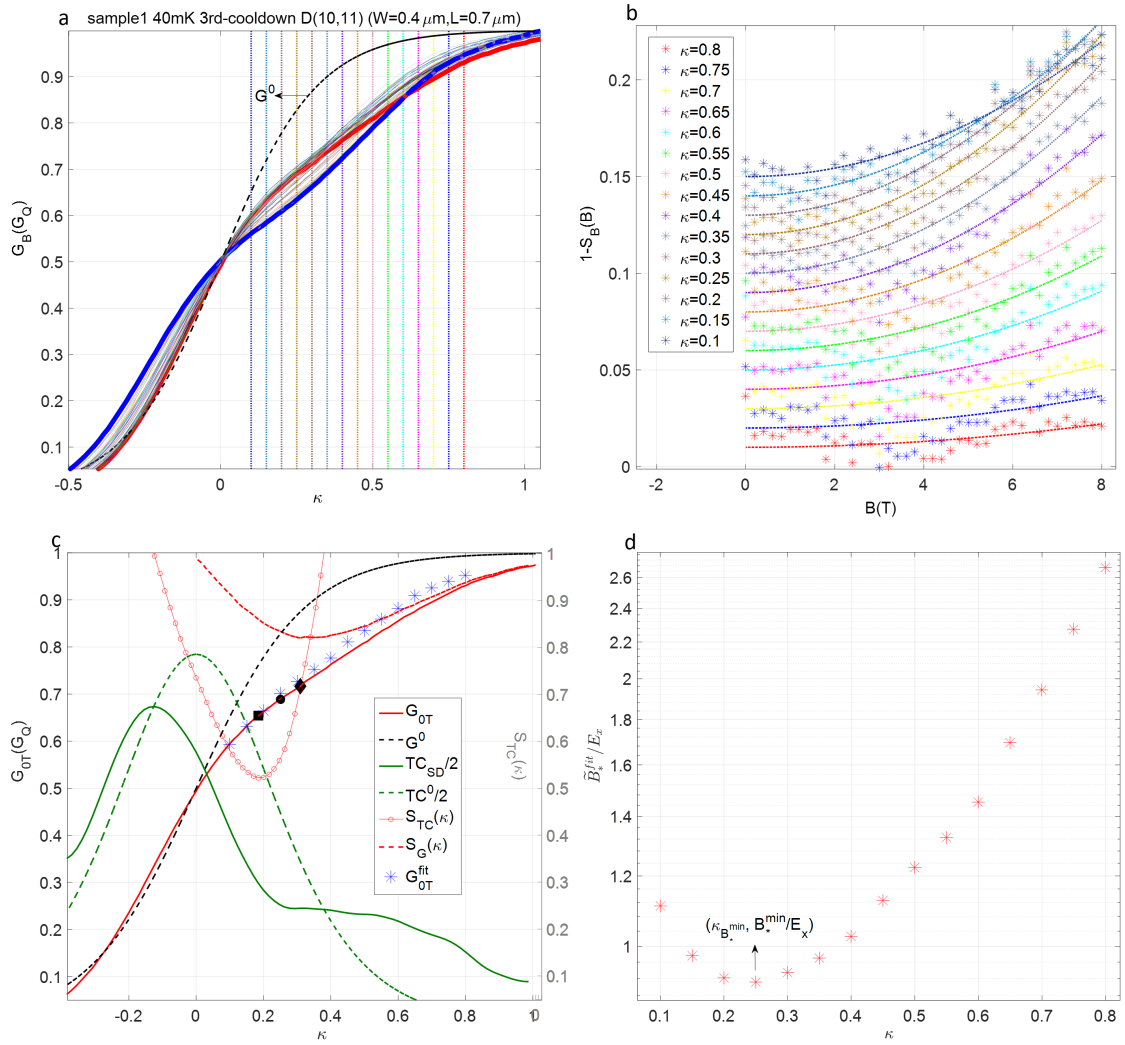

Figure A.10: Behaviours of S_B and B_*^{fit} for D(10,11), sample 1 at 40 mK. In (c), $\kappa_{TC}^{0.7}$, $\kappa^{0.7}$, and $\kappa_{B_*^{min}}$ are marked with squares, diamonds and dots respectively for G_{0T}.

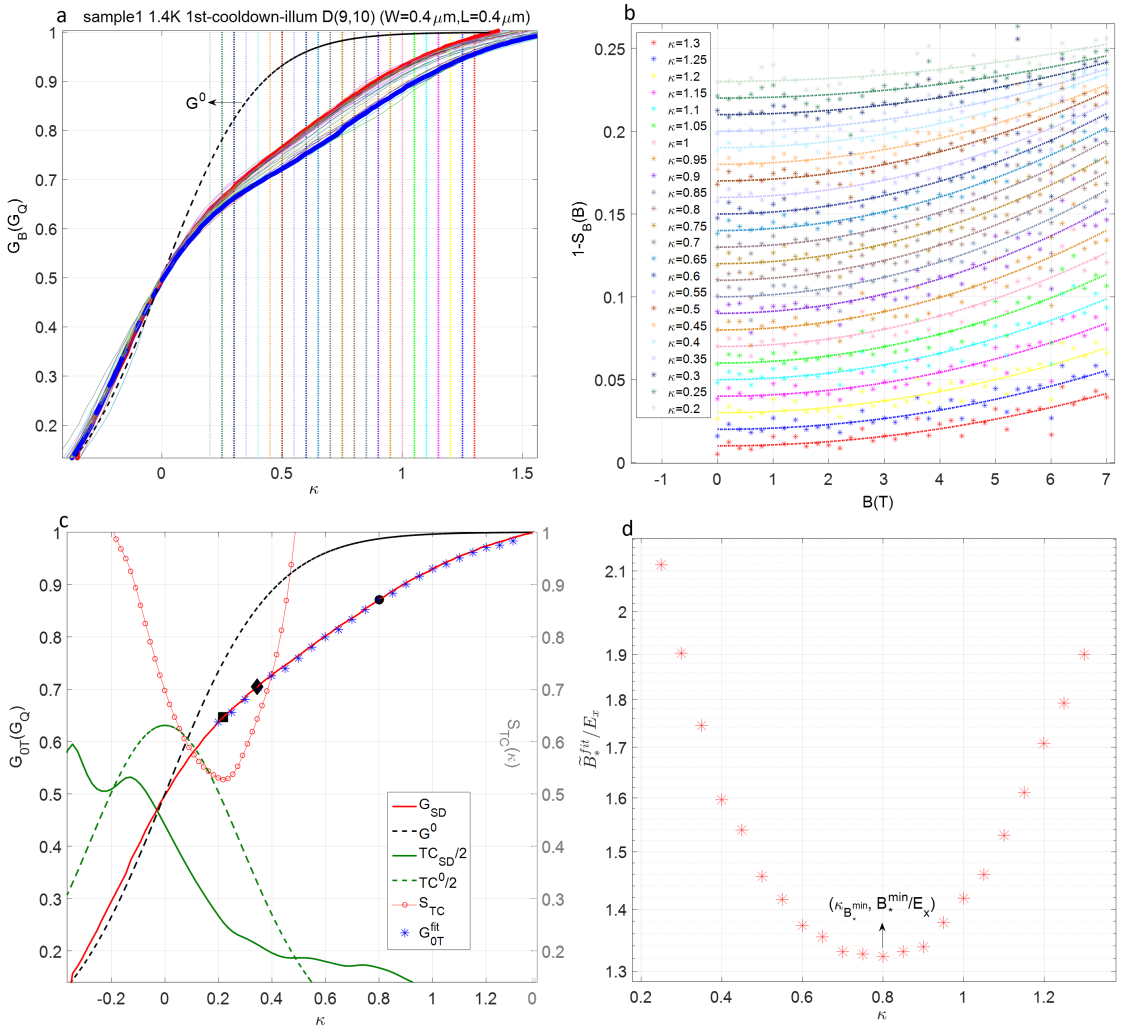

Figure A.11: Behaviours of S_B and B_*^{fit} for D(4,9), sample 1 at 40 mK.

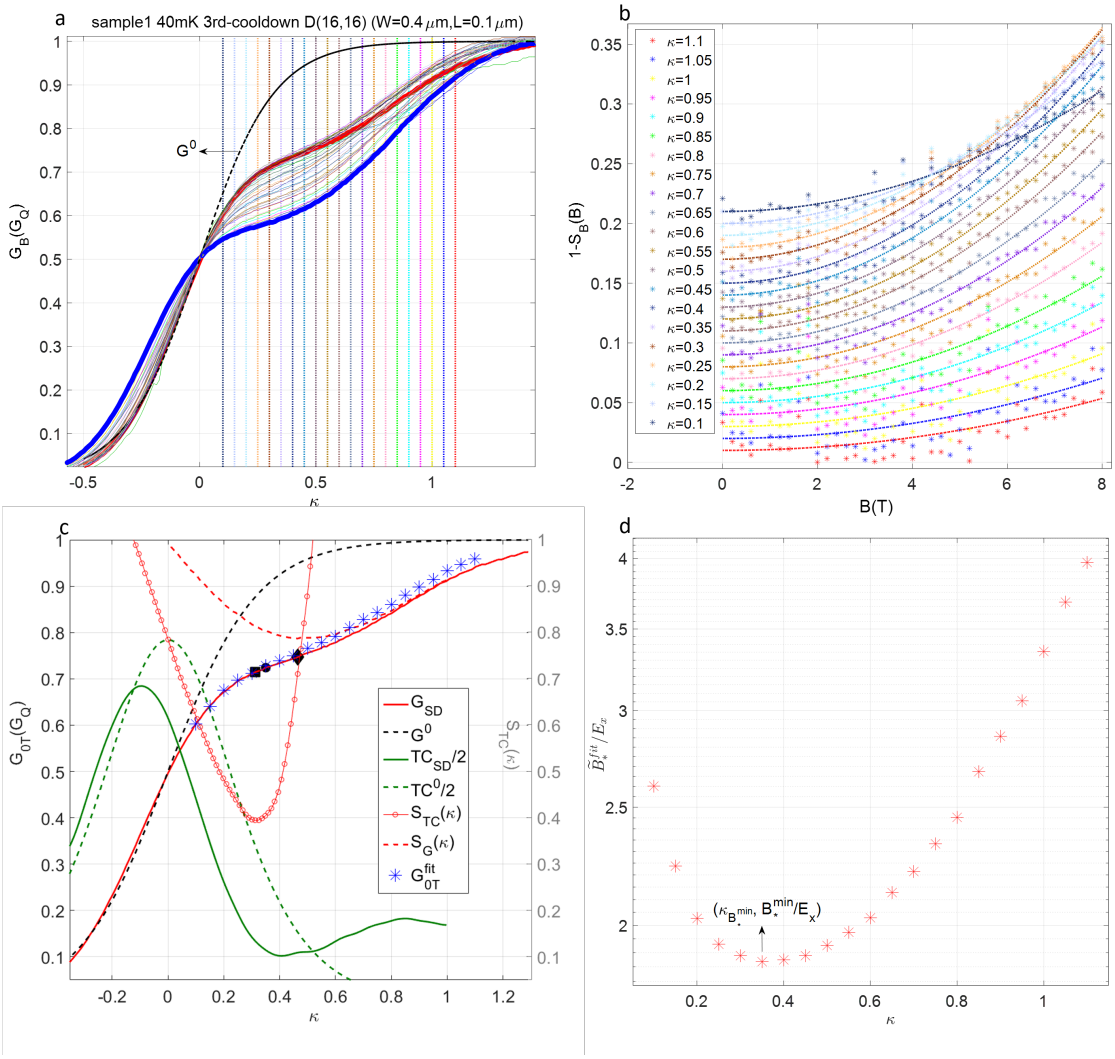

Figure A.12: Behaviours of S_B and B_*^{fit} for D(16,16), sample 1 at 40 mK.

In the same way as Fig. 5.12, Fig. A.13-A.15 show behaviours of S_B and B_*^{fit} for three more devices at 1.4 K.

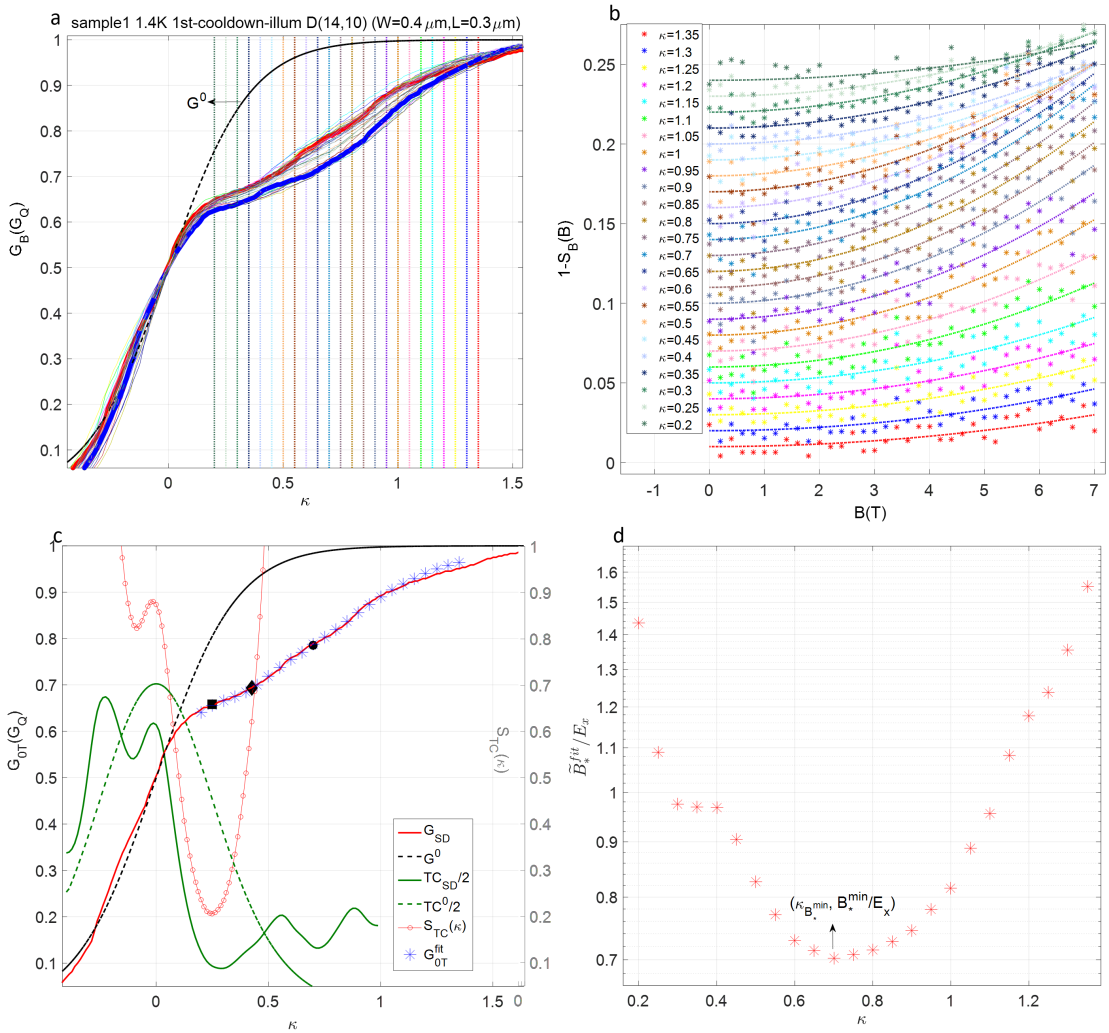

Figure A.13: Behaviours of S_B and B_*^{fit} for D(14,10), sample 1 at 1.4 K.

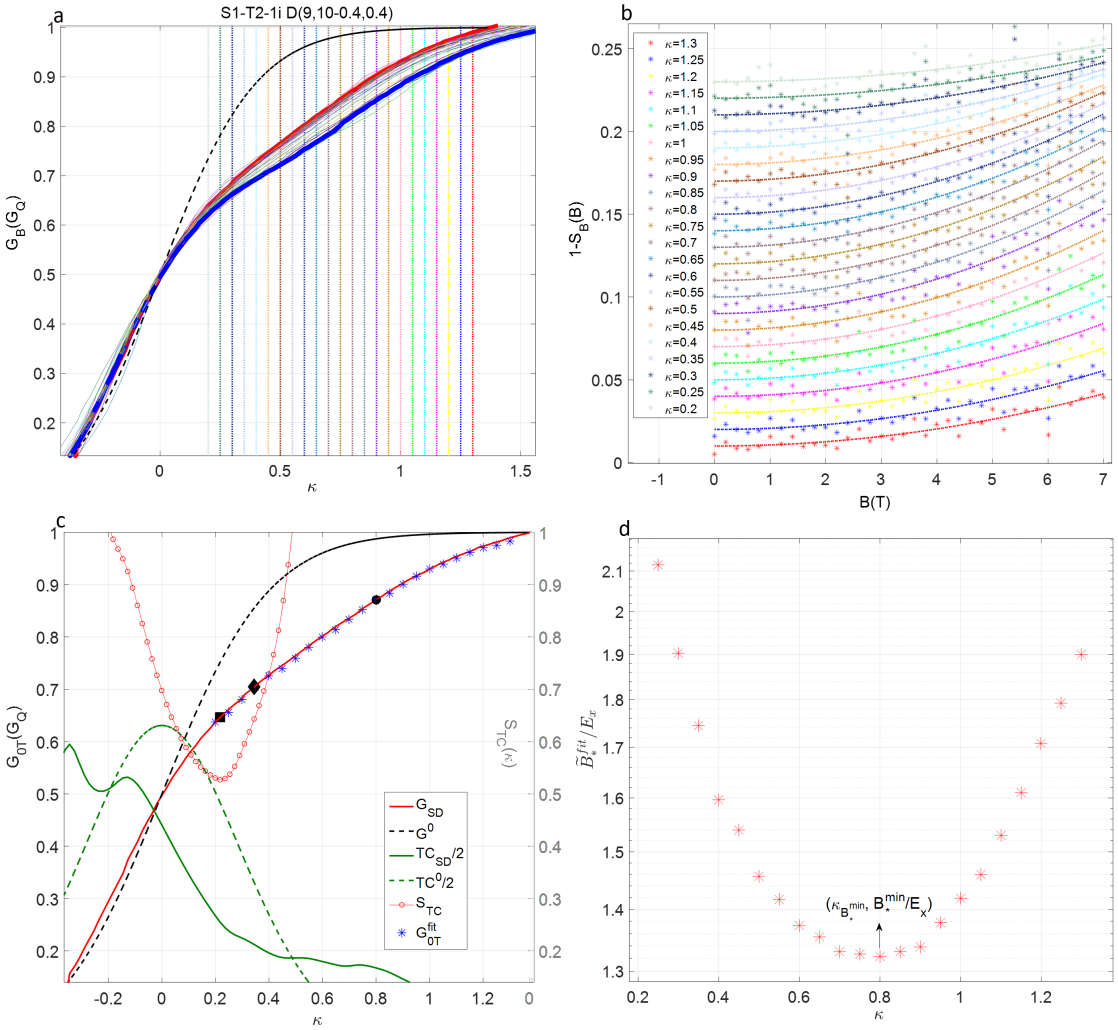

Figure A.14: Behaviours of S_B and B_*^{fit} for D(9,10), sample 1 at 1.4 K.

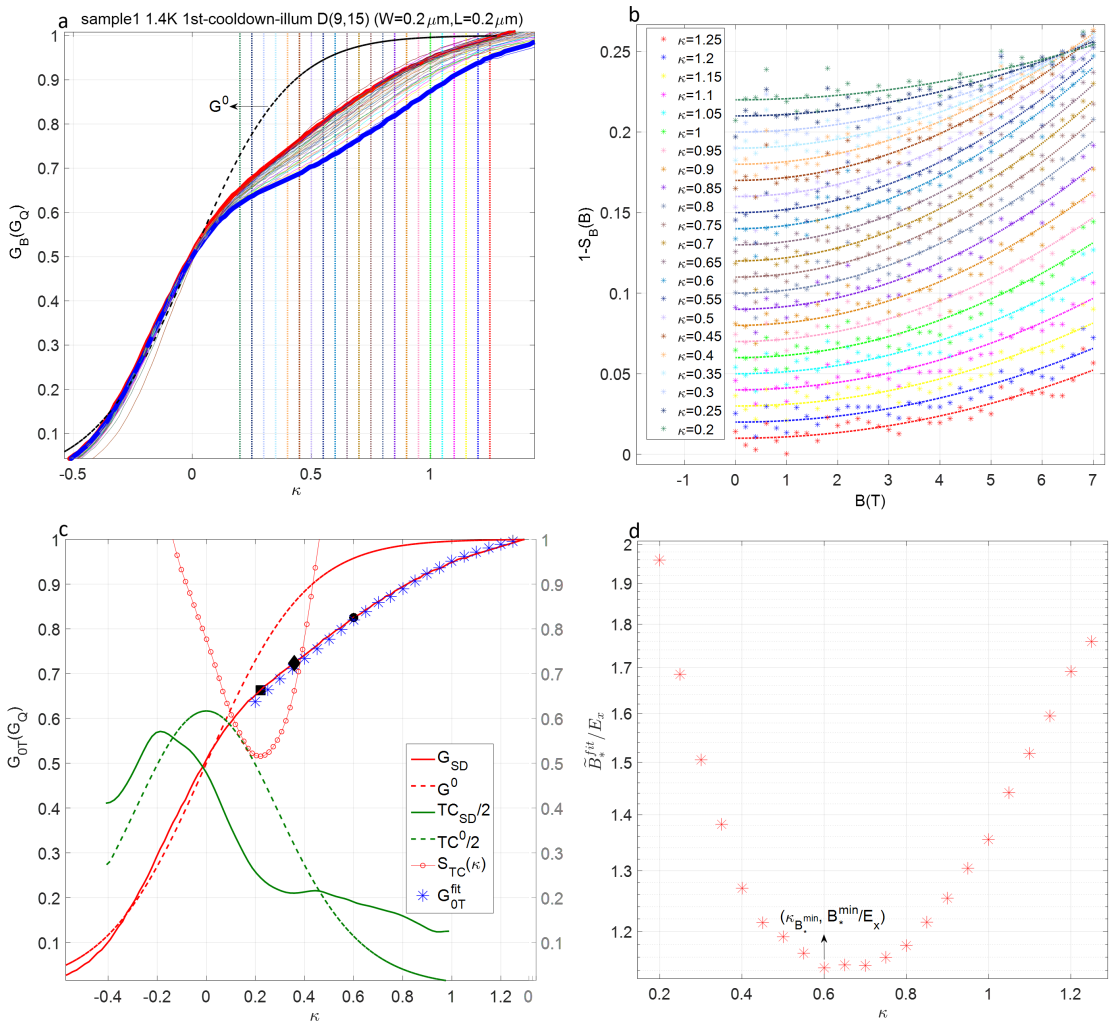

Figure A.15: Behaviours of S_B and B_*^{fit} for D(9,15), sample 1 at 1.4 K.

In the same way as Fig. 6.6, Fig. A.16 shows B_{ls}=4.2 T, which is smaller than B_{rs}=6.8 T (for E_x=0.92 meV for G_{0T}) for another device D(10,13), sample 1 at 40 mK in the 3^{rd} cooldown.

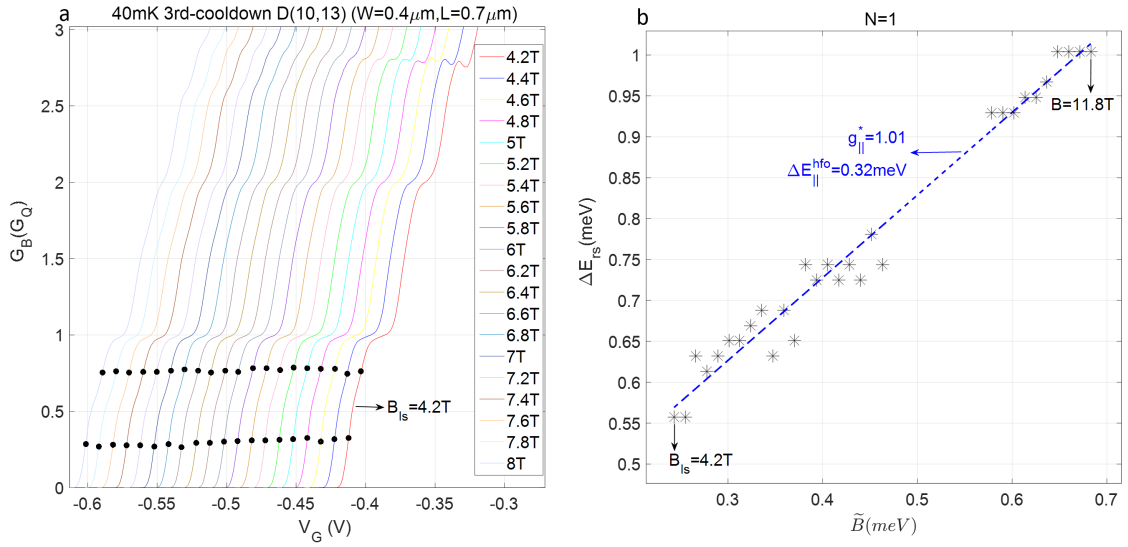

Figure A.16: Comparison of B_{ls}=4.2 T with B_{rs}=6.8 T for D(10,13), sample 1 at 40 mK in the 3^{rd} cooldown.

In the same way as Fig. 6.7c, Fig. A.17 compares $\Delta E_{\parallel}^{hfo}$ with ΔE_{rs}^{0T}, for another 6 devices that show spontaneous risers-splitting at 0 T for the first plateau, for sample 1 at 40 mK in the 3^{rd} cooldown.

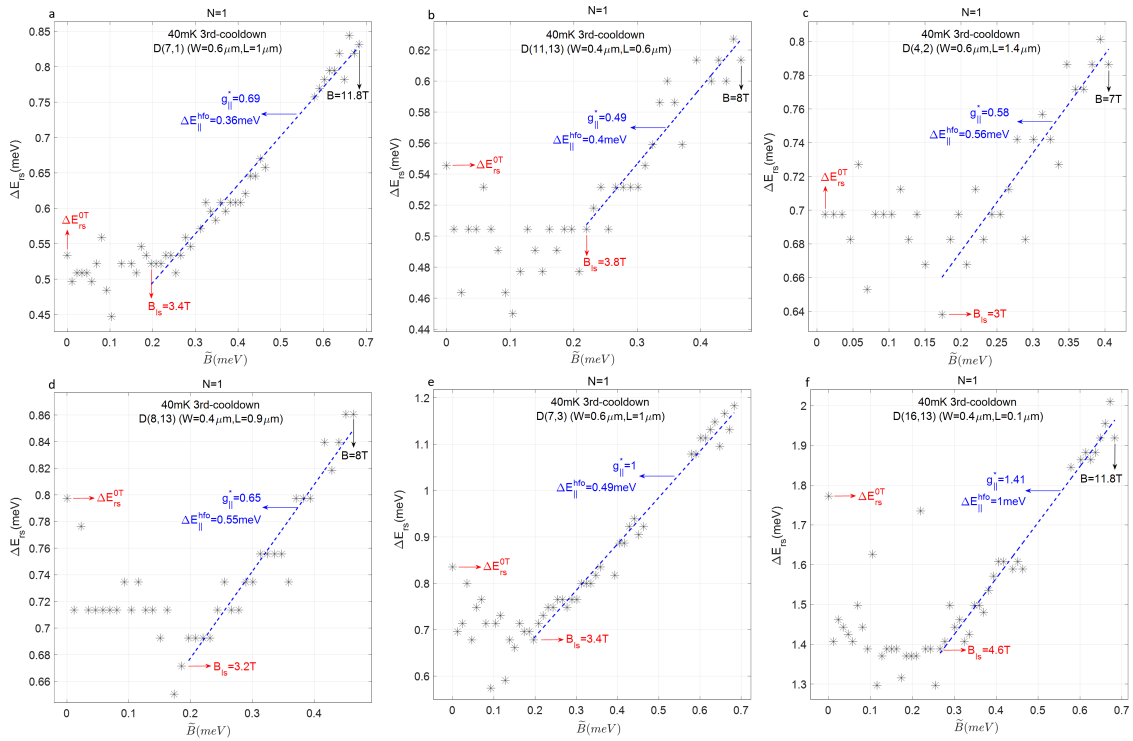

Figure A.17: ΔE_{rs} as a function of B fields from B=0 T for 6 devices that show spontaneous risers-splitting at 0 T for the first plateau, for sample 1 at 40 mK in the 3^{rd} cooldown.

Fig. A.18 and A.19 show the extracting of $g^*_\perp$ and $\Delta E^{hfo}_\perp$ for 2 device in the 2^{nd} cooldown, and $g^*_\parallel$ and $\Delta E^{hfo}_\parallel$ for 2 device in the 3^{rd} cooldown respectively, for sample 1 at 40 mK.

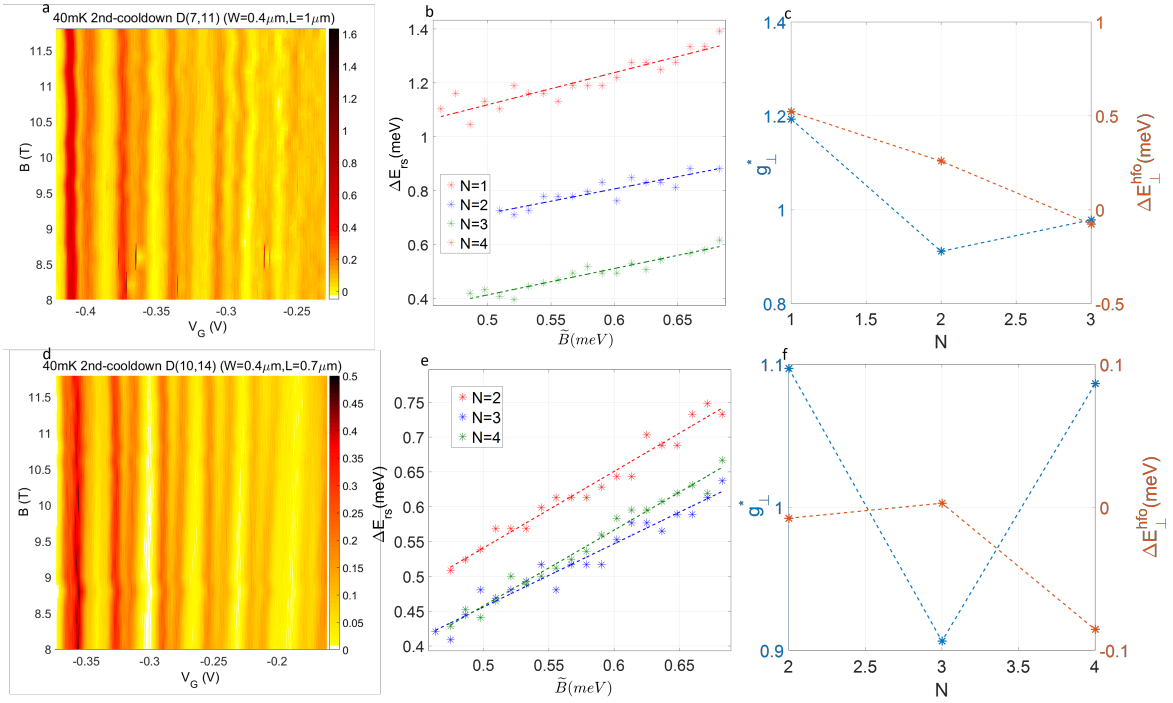

Figure A.18: Fitting of $g^*_\perp$ and $\Delta E^{hfo}_\perp$ for 2 devices respectively, for sample 1 in the 2^{nd} cooldown.

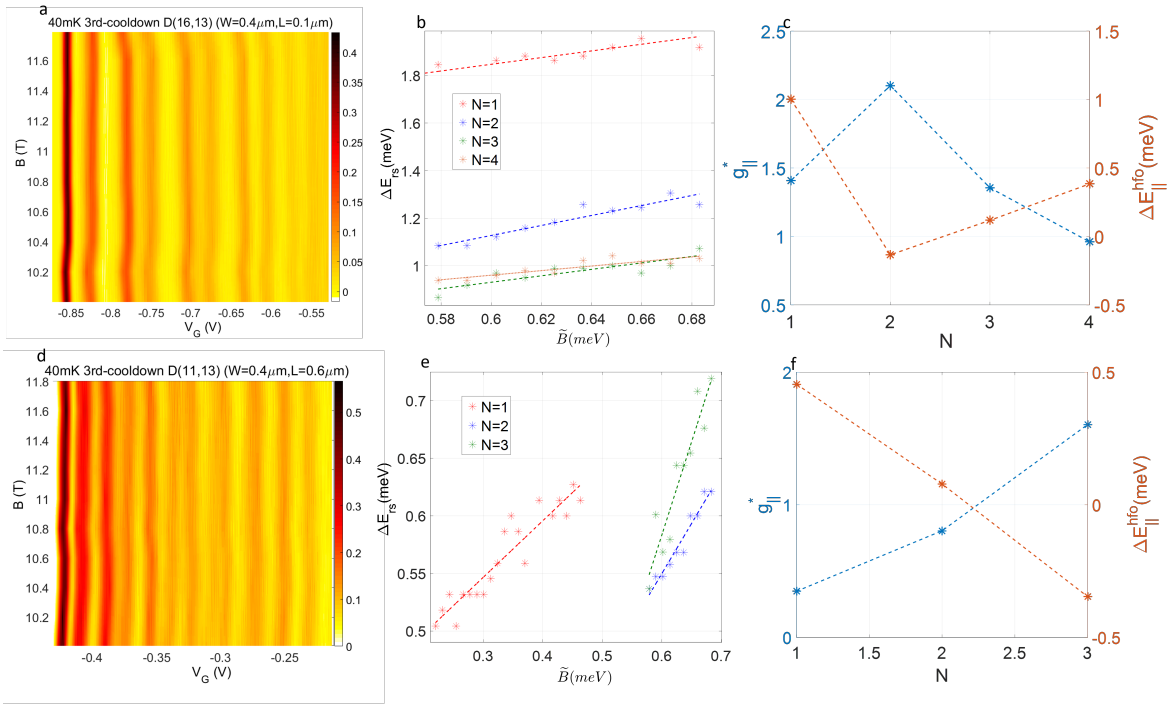

Figure A.19: Fitting of $g^*_{\parallel}$ and $\Delta E^{hfo}_{\parallel}$ for 2 devices respectively, for sample 1 in the 3^{rd} cooldown.

Fig. A.20a shows the non-interacting calculation of ΔE_{rs} for $E_x = 1meV$ at 0 K and 8 T using Eq. 1.18. It is clear to see ΔE_{rs} (distance for risers of TC^0 curve) is indeed smaller than ΔE_Z (distance for risers of $TC^0_\downarrow$ and $TC^0_\uparrow$), and the acquired g^* (called g^*_{rs}) has an error ($g^*_{rs} > g^*$) at low B fields. The reason lies in that the risers of TC^0 (red solid line) are not at same positions as the risers of $TC^0_\downarrow$ (red dashed line) and $TC^0_\uparrow$ (red dotted line) respectively.

To cope with this, in Fig. A.20a, we use a pair of Gaussians $Gau_\downarrow$ (blue dashed line) and $Gau_\uparrow$ (blue dotted line), by fitting $Gau = Gau_\downarrow + Gau_\uparrow$ with TC^0. The energy distance between the risers of $Gau_\downarrow$ and $Gau_\uparrow$ (called $\Delta E_{Gau} = \alpha \Delta V_G^{Gau}$), can be regarded as ΔE_Z reliably. Fig. A.20b demonstrates this by comparing ΔE_{Gau} (blue crosses) and ΔE_{rs} (red stars) with ΔE_Z (black line) respectively, from B_{rs}=7.4 T to B=15 T. It can be seen that ΔE_{rs} is smaller than ΔE_Z, while ΔE_{Gau} is basically situated on ΔE_Z at each B step.

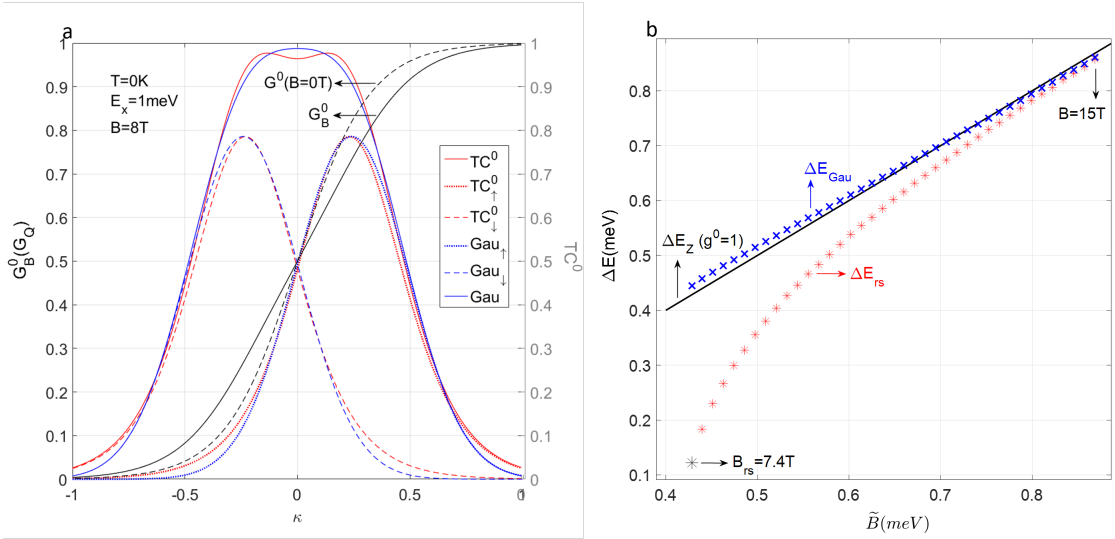

Figure A.20: Calculations of ΔE_{rs} and ΔE_{Gau} for $E_x = 1meV$ at T=0 K and B=8 T. G^0 at 0 T (black dashed line) is plotted together for a comparison with G^0_B (black solid line). ΔE_{rs} is acquired by finding the local peaks of TC^0 (red solid line). ΔE_{Gau} is the energy distance between the peaks of fitted $Gau_\downarrow$ (blue dashed line) and $Gau_\uparrow$ (blue dotted line). (b), Comparisons of ΔE_{Gau} (blue crosses) and ΔE_{rs} (red stars) with ΔE_Z (black line) at B steps from B_{rs}=7.4 T to B=15 T.

For a comparison with the results using ΔE_{rs} in Fig. 6.8, we attempt to extract g^* and ΔE^{hfo} using the Gaussian method ΔE_{Gau}. Fig. A.21a shows TC_{SD} map for the same device in Fig. 6.3. Fig. A.21b shows G_B and TC_{SD} as a function of V_G, for the first plateau at 8 T. We use a pair of Gaussians $Gau_\downarrow$ and $Gau_\uparrow$, to fit $Gau = Gau_\downarrow + Gau_\uparrow$ with TC_{SD}. ΔE_{Gau} is the energy distance between the peaks

(marked with black dots) of $Gau_{\downarrow}$ (green dashed line) and $Gau_{\uparrow}$ (brown dashed line). Fig. A.21c shows the processing of ΔE_{Gau} from 8 to 11.8 T for the first plateau. Fig. A.21d shows the linear fitting of ΔE_{Gau} with $\widetilde{B}$ for different plateaus respectively. The inset shows extracted $g^*_{\perp}$ and $\Delta E^{hfo}_{\perp}$ as a funtion of subband index N.

For a comparison with the statistics of fitted g^* and ΔE^{hfo} using ΔE_{rs} (called g^*_{rs} and ΔE^{hfo}_{rs}) in Fig. 6.8, Fig. A.22a,b shows the statistics of fitted g^* and ΔE^{hfo} using the Gaussian method (called g^*_{Gau} and ΔE^{hfo}_{Gau}), for the same devices in Fig. 6.8. Fig. A.22c-h shows correlations of g^*_{Gau} with g^*_{rs} (c-e), and correlations of ΔE^{hfo}_{Gau} with ΔE^{hfo}_{rs} (f-h), for the first three plateaus respectively, for devices at 40 mK in the 2nd cooldown. Fig. A.21c-h statically shows $g^*_{rs} > g^*_{Gau}$ and $\Delta E^{hfo}_{rs} < \Delta E^{hfo}_{Gau}$, which reveals the error of g^*_{rs} and ΔE^{hfo}_{rs} by regarding $\Delta E_{rs} = \Delta E_{ss}$.

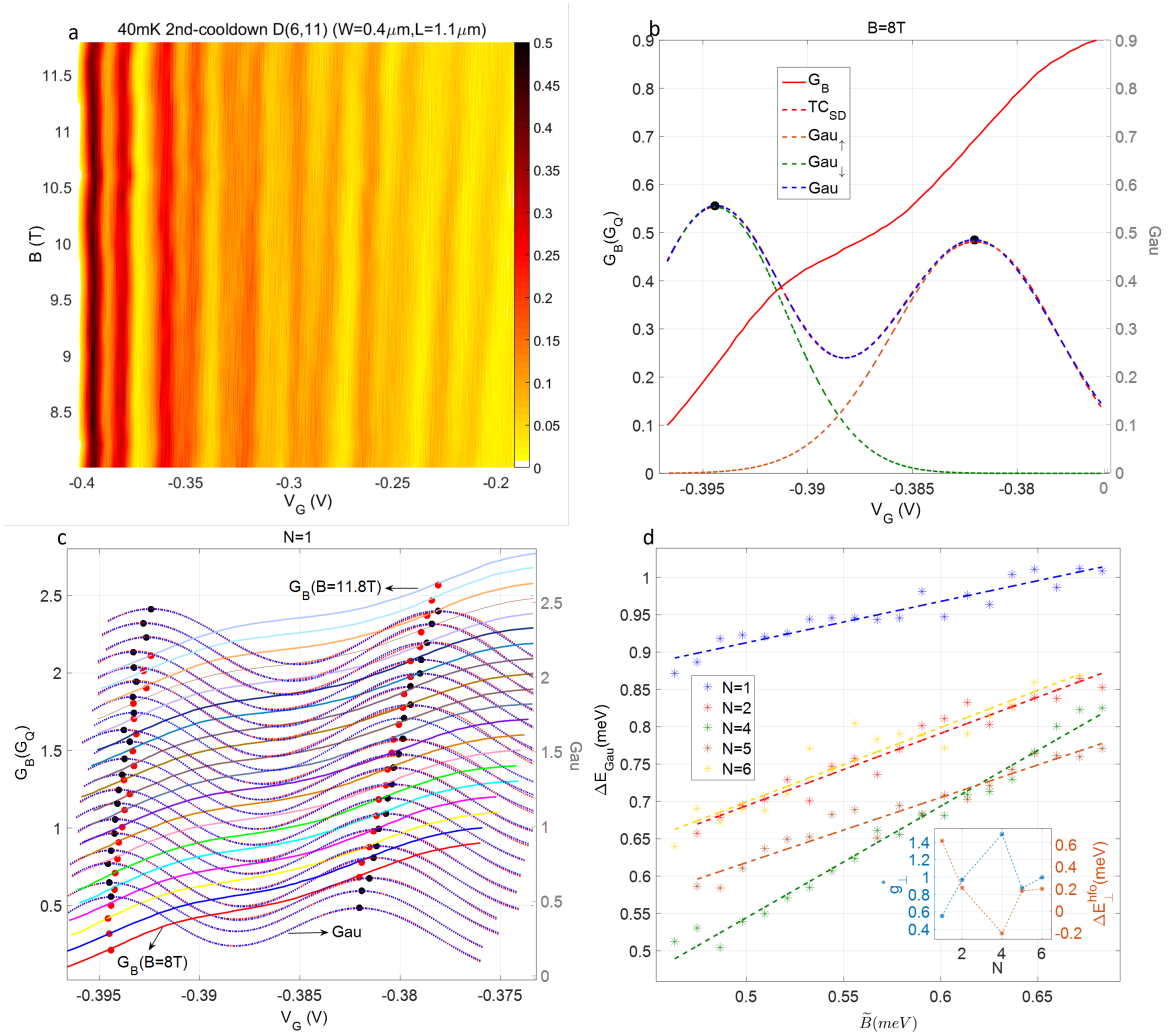

Figure A.21: Extracting $g^*_\perp$ and $\Delta E^{hfo}_\perp$ using the Gaussian method, for the same device in Fig. 6.3. (a), TC_{SD} map from 8 to 11.8 T. (b), Processing of ΔE_{Gau} at 8 T for the first plateau, by finding the peaks (black dots) of fitted $Gau_\downarrow$ (green dashed line) and $Gau_\uparrow$ (brown dashed line). (c), Processing of ΔE_{Gau} from 8 to 11.8 T for the first plateau. For G_B (coloured lines) and Gau (blue lines) curves (offset upward in turn by 0.1), the positions of V_G^{Gau} for the Gaussian peaks are marked with red and black dots respectively. (d), Linear fitting of ΔE_{Gau} with $\widetilde{B}$ for different plateaus respectively. The inset shows the acquired $g^*_\perp$ (left axis) and $\Delta E^{hfo}_\perp$ (right axis) as a function of subband index N.

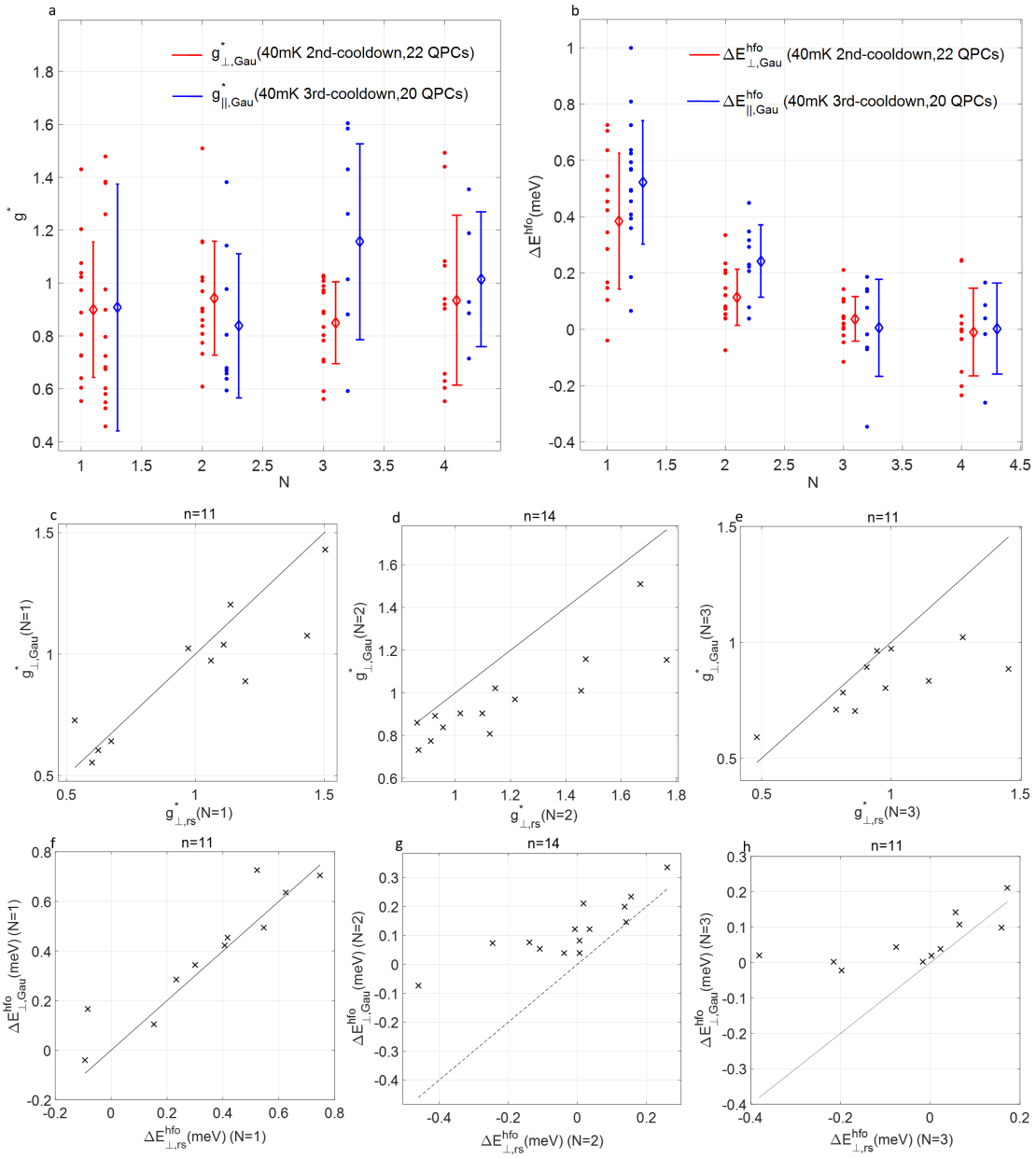

Figure A.22: (a,b), Statistics of g^*_{Gau} (a) and ΔE^{hfo}_{Gau} (b) using the Gaussian method, for the same devices in Fig. 6.8. (c-h), Correlations of g^*_{Gau} with g^*_{rs} (c-e), and correlations of ΔE^{hfo}_{Gau} with ΔE^{hfo}_{rs} (f-h), for the first three plateau respectively, for devices at 40 mK in the 2nd cooldown. In each panel, the dashed line (gradient=1) provides a guide to eye. Crosses are mostly situated below (c-e) and above (f-h) the dashed line respectively, statistically showing that $g^*_{rs} > g^*_{Gau}$ and $\Delta E^{hfo}_{rs} < \Delta E^{hfo}_{Gau}$.

In the same way as Fig. 7.3 and Fig. 7.4a,b, Fig. A.23-A.28 shows formations of the 0.75 and 0.25 anomalies for typical devices, and statistical development of conductance for the anomalies as a function of V_{DC}, for sample 1-5 at 40 mK or 1.4 K before or after illumination respectively. First, the data in Fig. A.24-A.28 are measured at 1.4 K, and the data in Fig. A.24 and A.28 are measured after illumination. The anomaly behaviours seem independent of QPC geometry or temperature. Second, $V_{DC}^{0.25s}$ is basically twice $V_{DC}^{0.75s}$ in all devices. This relation could be checked particularly using devices with exceptionally large $V_{DC}^{0.75s}$. In Fig. A.26c, $V_{DC}^{0.75s}$=1.6 mV and $V_{DC}^{0.25s}$=2.9 mV. In Fig. A.28d, $V_{DC}^{0.75s}$=1.4 mV and $V_{DC}^{0.25s}$=2.7 mV. Third, Fig. A.24d and Fig. A.26b,c show that the 0.25 anomaly is still robust at a large V_{DC}=10 mV and ±8 mV respectively.

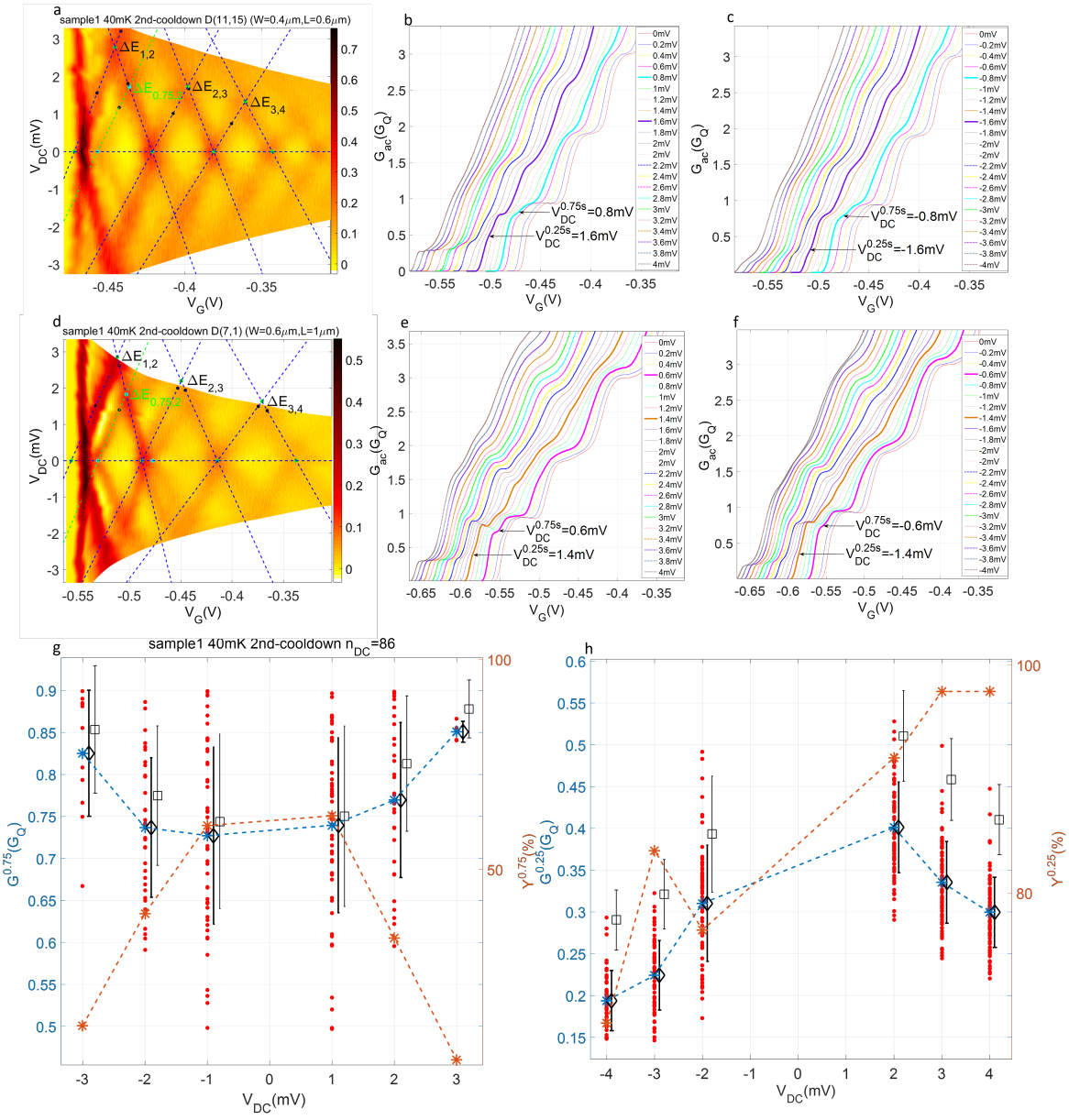

Figure A.23: Formation of the 0.75 and 0.25 anomalies for typical devices (a-f), and statistical development of conductance for the anomalies as a function of V_{DC} (g,h), for sample 1 at 40 mK in the second cooldown.

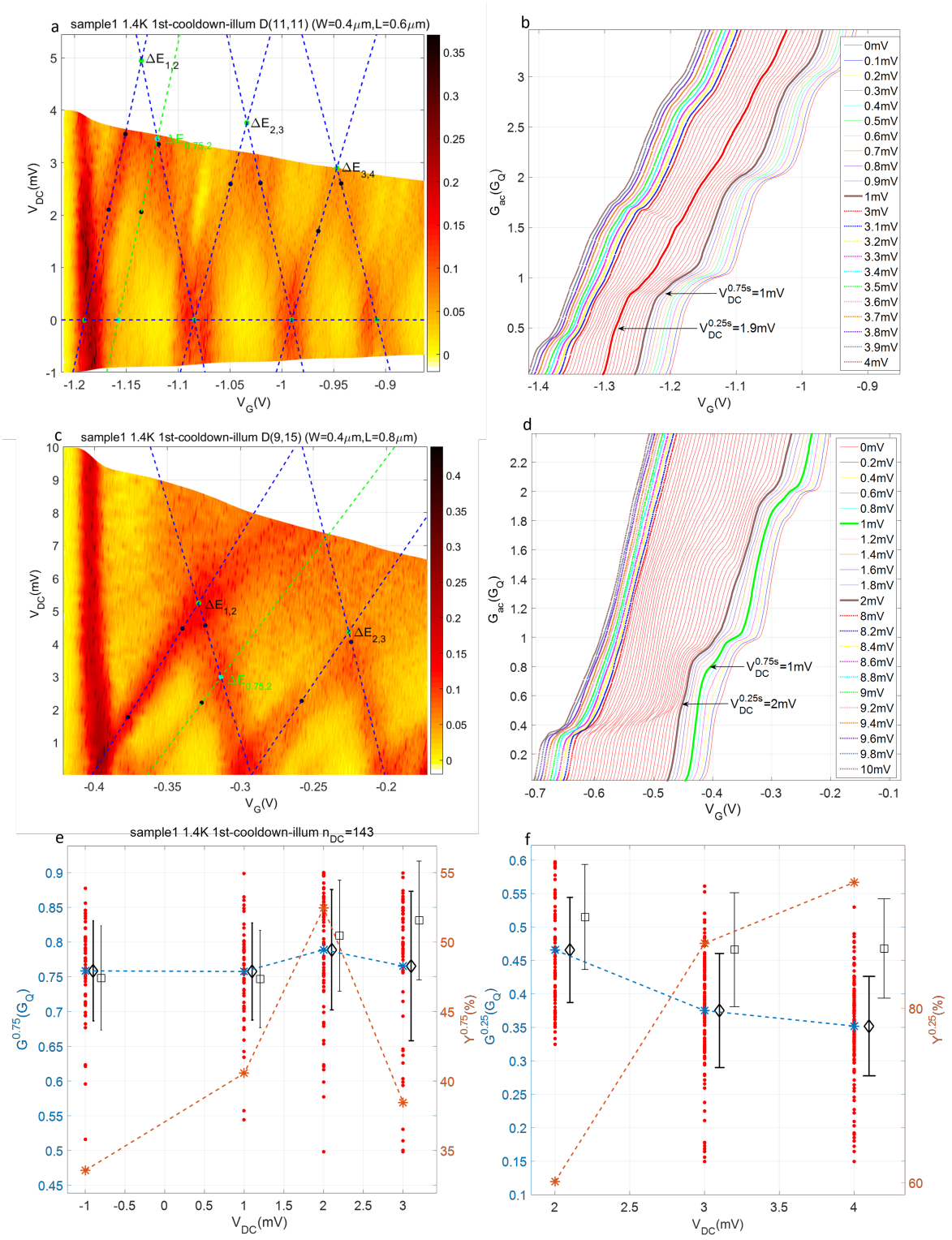

Figure A.24: Formation of the 0.75 and 0.25 anomalies for typical devices (a-d), and statistical development of conductance for the anomalies as a function of V_{DC} (e,f), for sample 1 at 1.4 K after illumination. In (d), the 0.25 anomaly is still robust at a large V_{DC}=10 mV.

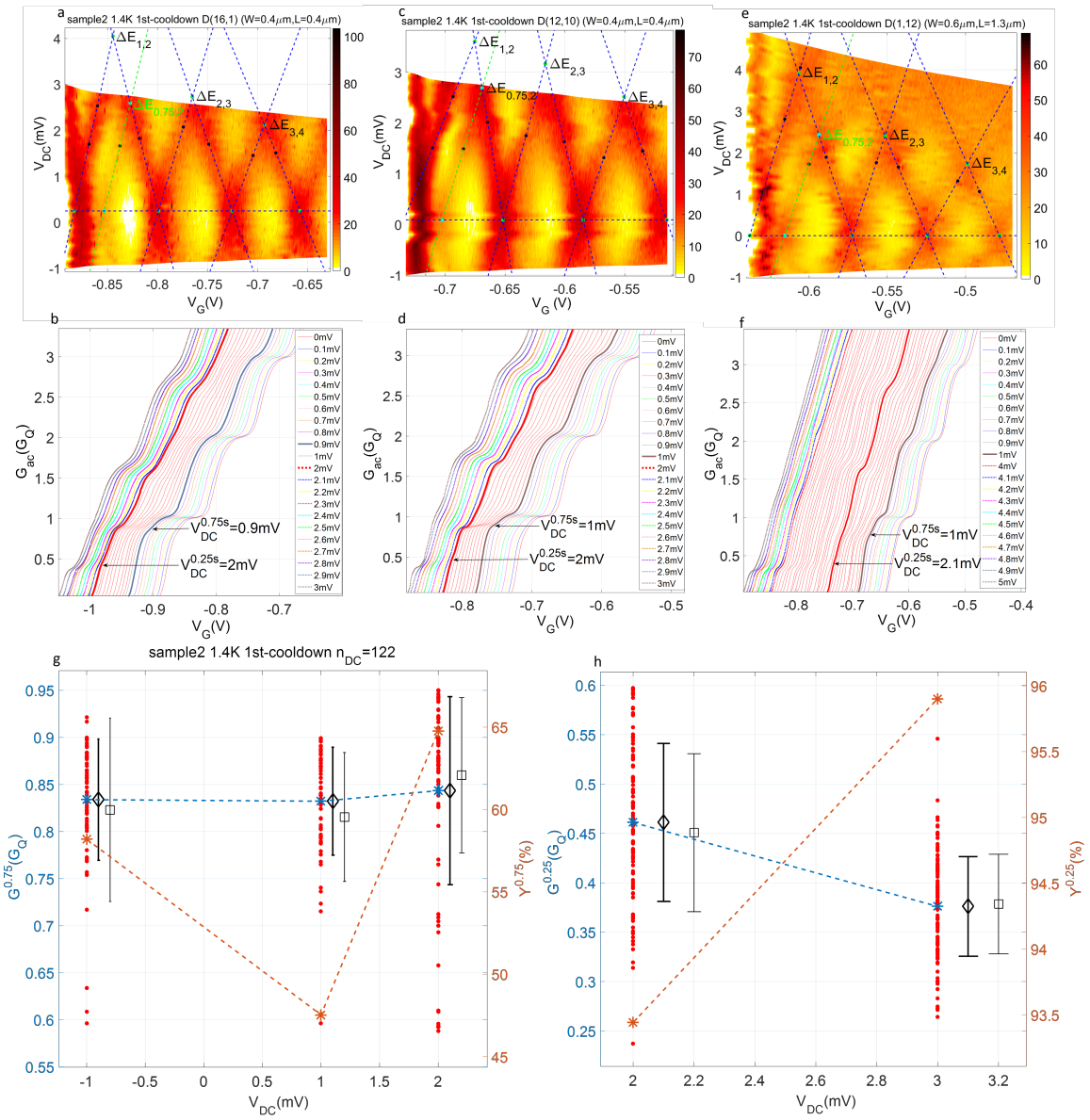

Figure A.25: Formation of the 0.75 and 0.25 anomalies for typical devices (a-f), and statistical development of conductance for the anomalies as a function of V_{DC} (g, h), for sample 2 at 1.4 K.

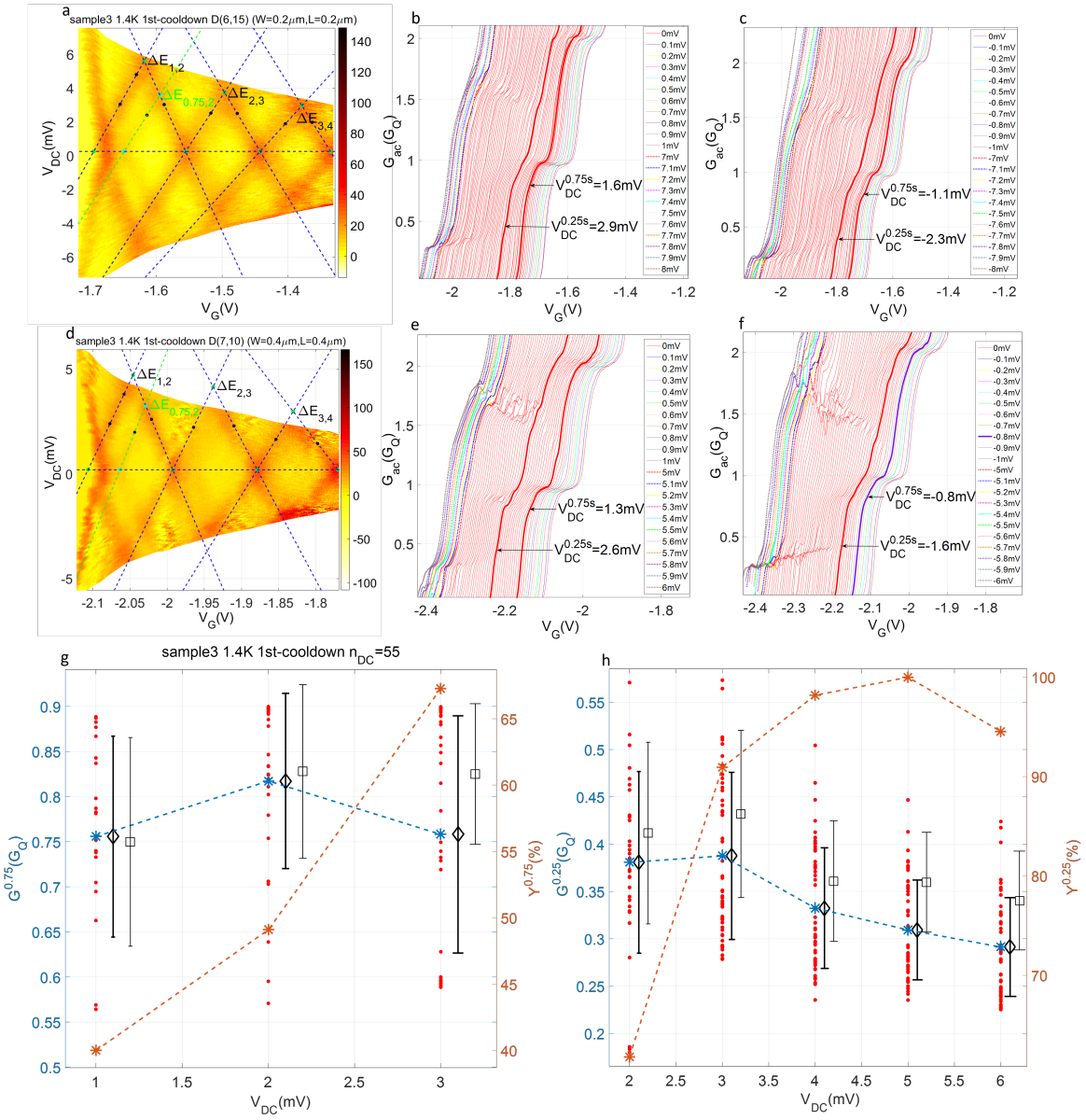

Figure A.26: Formation of the 0.75 and 0.25 anomalies for typical devices (a-f), and statistical development of conductance for the anomalies as a function of V_{DC} (g,h), for sample 3 at 1.4 K. In (b), for a large $V_{DC}^{0.75s}$=1.6 mV, $V_{DC}^{0.25s}$=2.9 mV, which still approximates twice $V_{DC}^{0.75s}$. In (b,c), the 0.25 anomaly is still robust at a large V_{DC}=±8 mV.

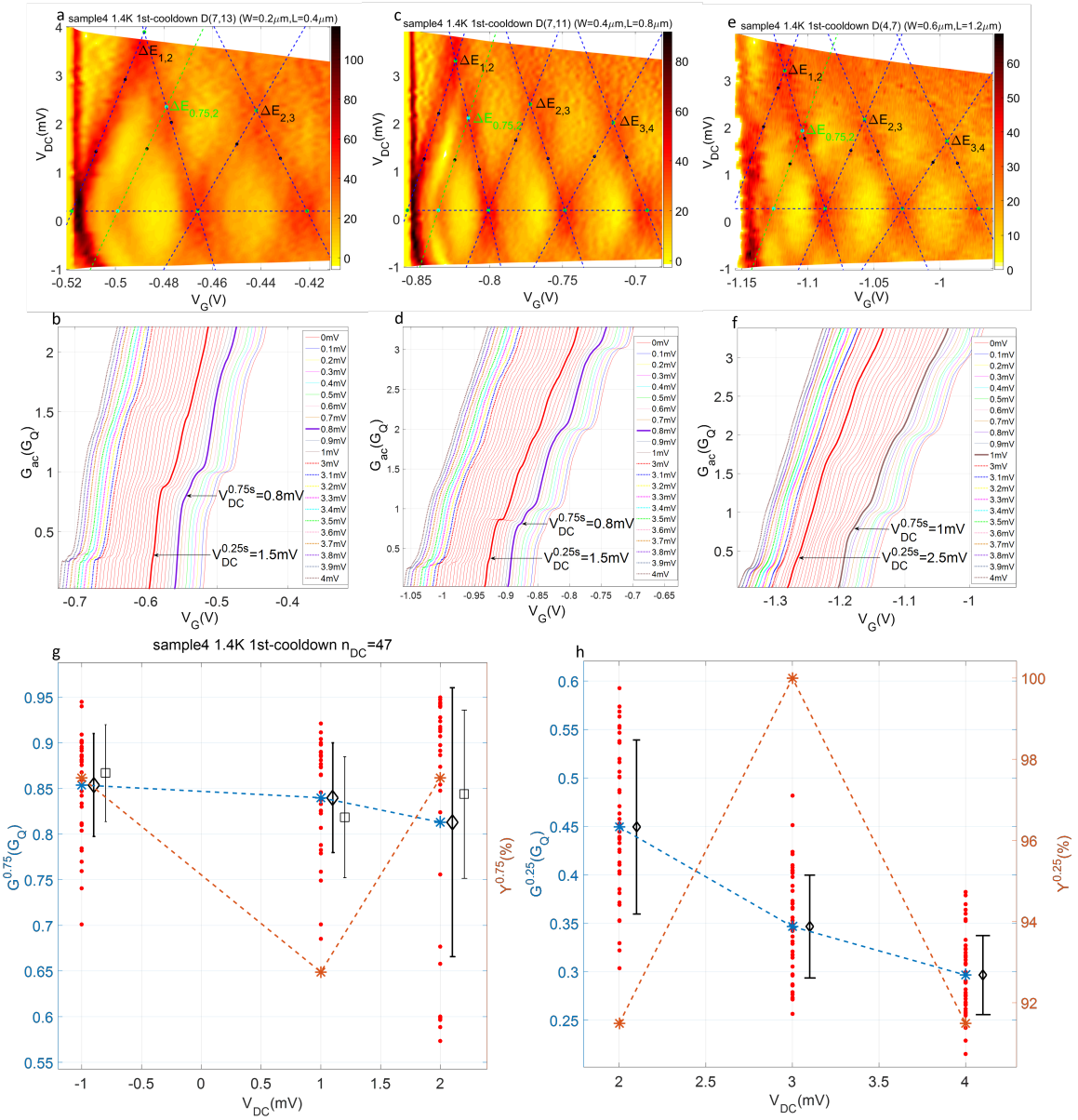

Figure A.27: Formation of the 0.75 and 0.25 anomalies for typical devices (a-f), and statistical development of conductance for the anomalies as a function of V_{DC} (g,h), for sample 4 at 1.4 K.

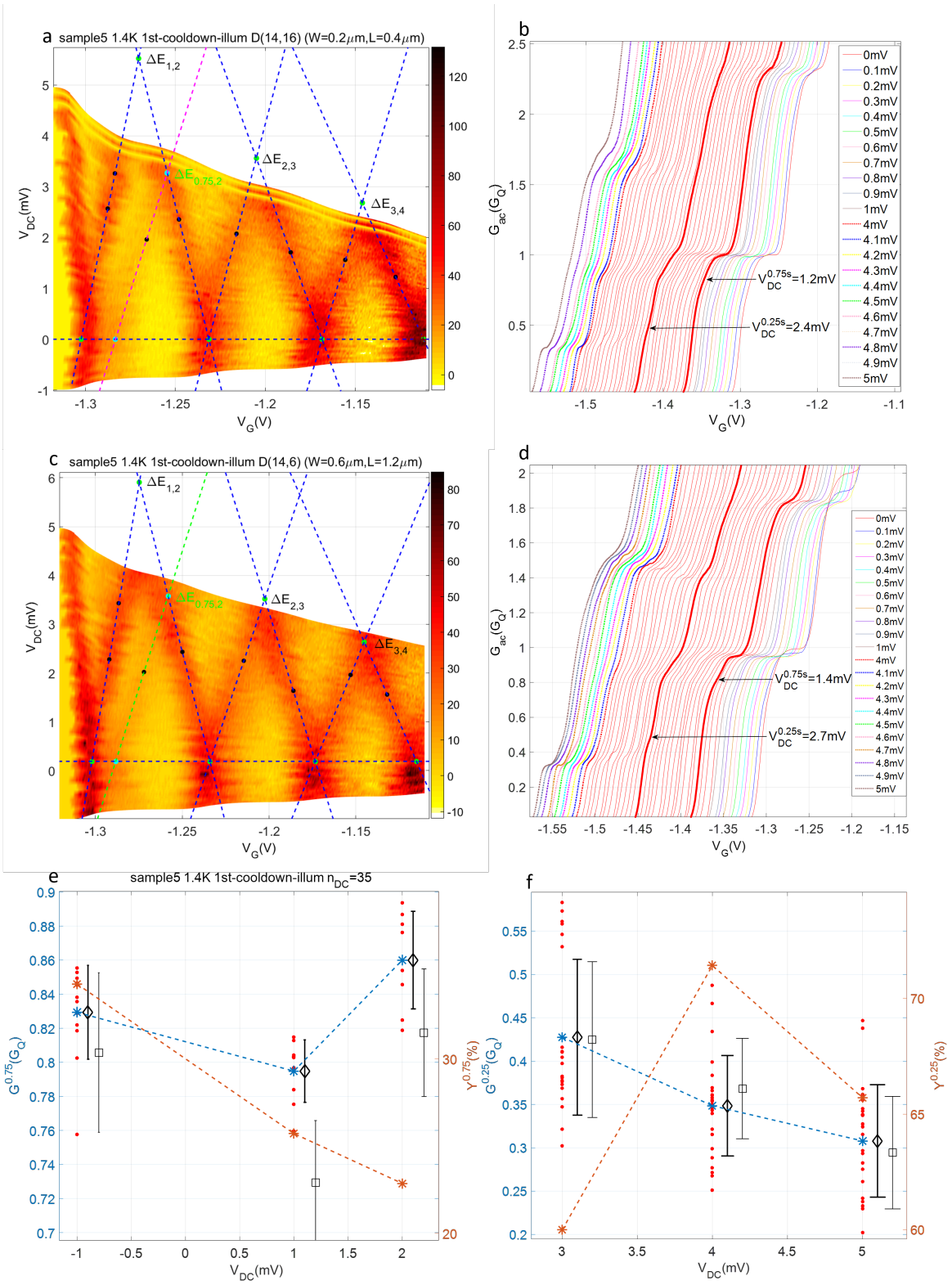

Figure A.28: Formation of the 0.75 and 0.25 anomalies for typical devices (a-d), and statistical development of conductance for the anomalies as a function of V_{DC} (e,f), for sample 5 at 1.4 K after illumination. In (d), for a large $V_{DC}^{0.75s}$=1.4 mV, $V_{DC}^{0.25s}$=2.7 mV, which still approximates twice $V_{DC}^{0.75s}$.

In the same way as Fig. 7.5b-g, Fig. A.29 shows formation and development of the 0.75 and 0.25 anomalies at positive V_{DC} steps, for three typical devices with the spectroscopy as shown in Fig. A.29a,c,e respectively, for sample 1 at T=40 mK and B=11.8 T. To check $e|V_{DC}^{0.25s}| - e|V_{DC}^{0.75s}| = \Delta E_Z$ as predicted in the model, compared to $\Delta E_Z \approx 0.6meV$, Fig. A.29b,d,f shows $e|V_{DC}^{0.25s}| - e|V_{DC}^{0.75s}|$=0.8, 0.6 and 0.8 meV respectively.

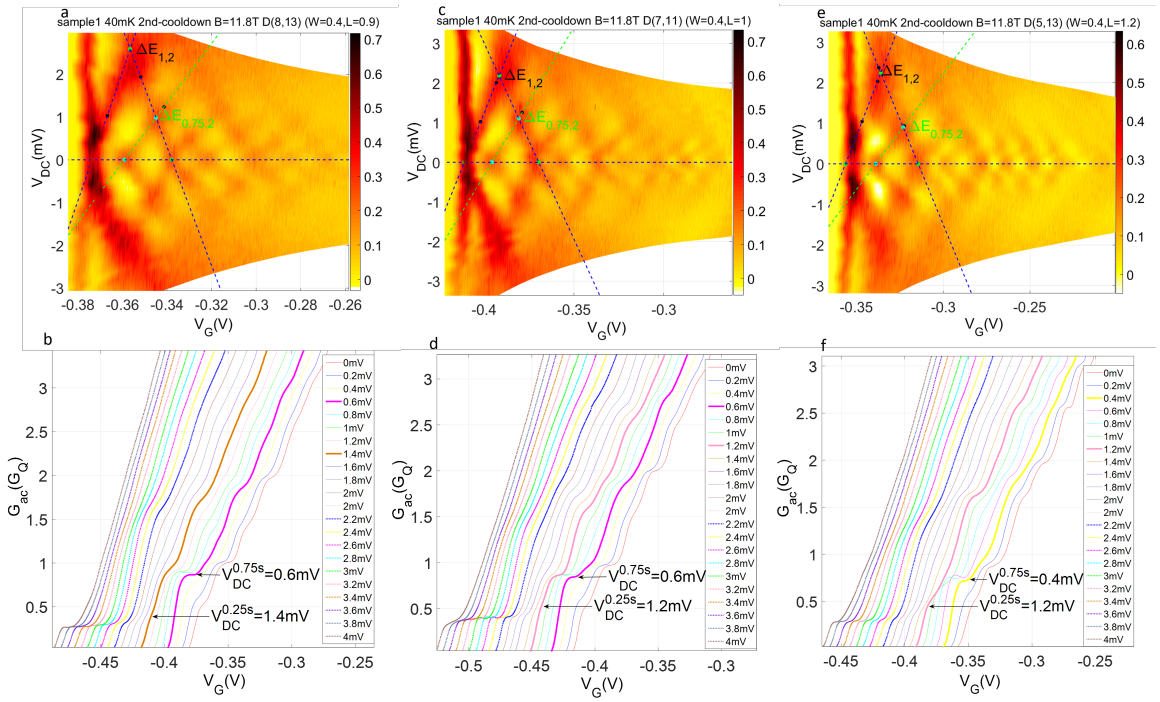

Figure A.29: Formation and development of the 0.75 and 0.25 anomalies for three typical devices for sample 1 at T=40 mK and B=11.8 T.